Reconstruction of wind turbine wake wind fields with long-range LiDAR measurements

Hauke Beck

Von der Fakultät für Mathematik und Naturwissenschaften der
Carl von Ossietzky Universität Oldenburg zur Erlangung des Grades und Titels eines

DOKTORS DER INGENIEURWISSENSCHAFTEN
DR. -ING.
angenommene Dissertation

von Hauke Beck
geboren in Bünde

CARL VON OSSIETZKY universität OLDENBURG

Gutachter:	Prof. Dr. Martin Kühn
Weitere Gutachter/in:	Prof. Dr. Torben Krogh Mikkelsen
Tag der Disputation:	14.02.2020

ABSTRACT

Wind turbine wake effects have a substantial influence on the operation and lifetime of wind turbines in wind farms. The interaction of the wake region with a wind turbine leads to a reduction in the energy yield, while the concomitant flow inhomogeneities in the downstream direction induced by the longitudinal wind speed deficit profile result in higher fatigue load. An exact understanding of the behaviour and the associated effects on the performance and loads of shaded turbines is essential for several applications ranging from the design of individual turbine components up to wind farm control strategies.

Spatial and temporal highly resolved inflow wind fields are needed in the design phase of wind turbines. The lack of suitable inflow data that can cope with the specific design criteria has the consequence that insufficient measurements have to be compensated by wind field modelling. So-called wake models estimate the wake characteristics. While the study of wake effects was only possible on a statistical level through point measurements (zero-dimensional) at meteorological masts and the wind turbines themselves, dynamic effects could only be recognised and considered explicitly with difficulties as such. In recent years, improved technical capabilities have led to the versatile remote sensing instruments LiDAR (Light Detect And Ranging) offering the possibility to capture flow conditions along the laser beam in a quasi-instantaneous manner. The outcome of (multi-dimensional) LiDAR measurements is used for the evaluation and the refinement of steady and dynamic wake model assumptions.

However, the modelling of wakes represents a source of inaccuracies within the aim to minimise the difference between calculated and real loads and energy yields. The associated need to further refine the current calculation possibilities implies a more precise mapping of the interaction reality of the inflow and the turbine, but above all, the analysis how far these differ. Within the framework of comparability of synthetic and real data, the objective is first, to reproduce the deterministic characteristics of the wind field measured in free-field on a wind turbine and afterwards, to compare and analyse the simulation results of the reconstructed synthetic wind field with the numerical model of the turbine against corresponding measured turbine data.

In this superordinated context, this thesis imparts the reconstruction of single turbine wake wind fields based on long-range LiDAR measurements and the data processing in order to be applicable not only for the comparison of aero-elastic load calculations against loads from free-field measurements but as well for measurement validation, wake characterisation and wake model evaluation. Therefore, the following questions will be addressed and answered:

- *How do LiDAR measurements need to be performed and processed to reconstruct dynamic 3D1C (three spatial dimensions, one flow component) wake wind fields?*
- *Which model assumption must be made for a 3D1C wake wind-field reconstruction?*
- *What are the characteristics of deviations in wake wind-field reconstruction?*

In order to answer these questions, processing and analysis methods were refined and developed to use planar and volumetric long-range LiDAR wake measurements. At different levels from the measurement conception up to the error evaluation, methods are presented and discussed, which imply the reconstruction of the longitudinal wind speed inside the wake.

First, LiDAR data must be processed in order to filter outliers and invalid measurements. Outliers arise from system-dependent behaviours, obstacles in the measuring area and for unknown technical reasons. The reconstruction of one-dimensional line-of-sight LiDAR data is realised with a dynamic filter concept based on the assumption of the self-similarity to provide maximum accuracy while maintaining maximum data availability for point and planar measurements. The effects of an insufficiently filtered data set can distort the analysis result in the sense of artefact structures within the scanned measurements.

Second, due to the functioning of long-range LiDARs, planar data can only be measured by scanning trajectories. This scanning behaviour induces a time difference within the measurement data, which can range from seconds to several minutes, depending on the parameterisation of the measurement. The reconstruction of the time-corrected scan was developed in order to achieve temporal high resolved wake wind fields. A temporal up-sampling is introduced as the prerequisite for accurate representation and synchronisation of LiDAR scans using a space-time conversion.

Third, the temporal up-sampling to a sub-measurement time scale is used to reconstruct planar wake flow characteristics. It is shown that the refinement of temporal resolution reduces the statistical mapping error. Further, it can be deduced that the inherent mapping error of scanned measurements can be minimised with suitable measurement parameters for specific flow situations. To evaluate the accuracy of the up-sampling, an evaluation within a synthetical framework was performed using a numerical LiDAR simulator and a LES wind field.

Fourth, the reconstruction of temporally and spatially high-resolved, dynamic 3D1C wake wind fields is shown. Therefore unsynchronised volumetric LiDAR measurements are temporally up-sampled and synchronised to determine the wake dynamics in the sense of the velocity deficit shape, the deficit position and the deficit intensity. These wake dynamics are used to reconstruct a dynamic 3D1C wake wind field under specific assumptions that are justified. The evaluation of the reconstruction quality and reconstruction characteristics is again performed with a data set of a synthetic wake wind field and a numerical LiDAR simulator.

On the way to minimising the deviations between modelled and real loads, the results of this work represent a further and essential step. It is shown that with appropriate data processing, wind field reconstructions can be performed on different levels with high accuracy. The first question will be dealt with in the first three named topics, while questions two and three will be answered in the fourth topic. The reconstruction of the LOS velocities by the presented LiDAR data filtering is an essential component of the process chain, that not only the flow statistics can be recalculated most accurately, but measurement artefacts can be filtered robustly. Through the temporal up-sampling, it is possible to reproduce the deterministic flow properties of scanned wind fields in time and to synchronise them with other measurements. This processing laid the foundation to increase the comparability of real and synthetic wind fields from a statistical to a direct level. The reconstruction of 3D1C wake wind fields is model-based and has its novelty in the mapping of multiple wake dynamics. Primarily by assuming a homogeneous wake behaviour along the flow direction, wind fields could be recreated, which represent the average wind speed with a deviation of 2.3% and the standard deviation with 0.18%. These results are not based on a statistical reproduction of the flow, but on a deterministic wind field propagation approach, which can represent specific flow events

ZUSAMMENFASSUNG

Nachlauf-Effekte von Windkraftanlagen haben einen erheblichen Einfluss auf den Betrieb und die Lebensdauer von Windkraftanlagen in Windparks. Durch Fluktuationen des longitudinalen Windgeschwindigkeitsdefizits, welches auf stromabwärts positionierte Anlagen trifft, entsteht eine Wechselwirkung der Nachlaufregion mit einer Windkraftanlagen, die zu einer Verringerung des Energieertrags und zu verstärkten Ermüdungsbelastungen führt. Ein genaues Verständnis dieses Verhaltens und der damit verbundenen Auswirkungen auf die Leistung und die Belastung von abschatteten Anlagen ist, angefangen von der Auslegung einzelner Anlagenkomponenten bis hin zu Steuerungsstrategien für Windparks, für eine Vielzahl von Anwendungen unerlässlich.

In der Entwurfsphase von Windkraftanlagen werden räumlich und zeitlich hochauflösende Einströmwindfelder benötigt. Das Fehlen geeigneter Einströmungsdaten, die den spezifischen Auslegungskriterien gerecht werden, hat zur Folge, dass unzureichende Messungen durch die Modellierung von Windfeldern innerhalb des Prozesses kompensiert werden müssen.

Im Rahmen dieser Modellierung werden verschiedene nachlaufspezifischen Strömungseigenschaften berechnet. Während die Analyse von Nachlaufeffekten bisher nur auf statistischer Basis mittels (nulldimensionaler) Punktmessungen an meteorologischen Masten und den Windkraftanlagen selbst möglich war, konnten dynamische Effekte nur mit Schwierigkeiten als solche explizit erkannt und berücksichtigt werden. In den letzten Jahren hat der technische Fortschritt zu dem vielseitigen Fernerkundungsinstrument LiDAR (Light Detect And Ranging) geführt, welches die Möglichkeit bietet, Strömungssituationen entlang des Laserstrahls quasi-instantan zu erfassen. Die Ergebnisse von (multidimensionalen) LiDAR-Messungen werden mittlerweile für die Evaluation und Verbesserung der Annahmen von statischen und dynamischen Nachlaufmodellen verwendet.

Die Modellierung von Nachläufen stellt, mit dem Ziel die Unterschiede zwischen realen und berechneten und Lasten und Energieerträgen zu minimieren, eine Quelle von Ungenauigkeiten dar. Die damit inhärente Notwendigkeit, die aktuellen Berechnungsmöglichkeiten weiter zu verfeinern, impliziert neben eine genauere Abbildung, vor allem die Analyse, inwieweit sich die realen Wechselwirkung der Einströmung und der Windkraftanlage von simulierten unterscheidet. Im Rahmen der Vergleichbarkeit von synthetischen und realen Daten geht es zunächst darum, die deterministischen Eigenschaften des im Freifeld gemessenen Windfeldes an einer Windkraftanlage zu reproduzieren und anschließend die Simulationsergebnisse der Kombination aus dem rekonstruierten, synthetischen Windfeldes und dem numerischen Modell der Anlage mit entsprechenden Turbinenmessdaten zu vergleichen und zu analysieren.

In diesem übergeordneten Kontext zeigt diese Arbeit wie die Rekonstruktion von Windfeldern einzelner Nachläufe mittels Langstrecken-LiDAR-Messungen durchgeführt werden kann. Spezieller Fokus wird auf die Datenverarbeitung gesetzt, um Windfelder zu rekonstruieren, die für den Vergleich von aeroelastischen Lastberechnungen, für die Messvalidierung, die Nachlaufcharakterisierung als auch für die Evaluation von Nachlaufmodellen genutzt werden können.

In diesem Zusammenhang adressiert und beantwortet diese Dissertation folgende Fragen:

- *Wie müssen LiDAR-Messungen durchgeführt und verarbeitet werden, um dynamische 3D1C(drei Raumdimensionen , eine Strömungskomponente)-Nachlauf-windfelder zu rekonstruieren?*
- *Welche Modellannahmen müssen für die Rekonstruktion eines 3D1C-Nachwindfeldes getroffen werden?*
- *Welche Charakteristiken zeigen die Abweichungen des rekonstruierten Windfeldes zu den Referenzdaten?*

Um diesen Fragen nachzukommen, wurden Verarbeitungs- und Analysemethoden entwickelt, um flächige und volumetrische Langstrecken-LiDAR-Nachlaufmessungen zu benutzen. Auf verschiedenen Ebenen, von der Messkonzeption bis zur Fehlerbewertung, werden Methoden vorgestellt und diskutiert, die die Rekonstruktion von Nachlaufwindfeldern thematisieren.

Dazu werden zuerst LiDAR-Daten verarbeitet, um Ausreißer und ungültige Messungen zu filtern. Invalide Daten entstehen durch gerätespezifisches Eigenheiten, Hindernisse im Messbereich und aus unbekannten technischen Gründen. Die Rekonstruktion der eindimensionalen LiDAR-Daten, in der sogenannten Sichtlinie, wird mit einem dynamischen Filterkonzept realisiert, welches maximale Genauigkeit mit möglichst maximaler Datenverfügbarkeit für Punkt- und Flächenmessungen gewährleistet. Zur Bestimmung der Gültigkeit einzelner Messpunkte wurde eine dynamische Filtermethode entwickelt, die auf der Annahme der Selbstähnlichkeit der Messdatenverteilung in einem multivariaten Bezugsrahmen basiert. Die Auswirkungen unzureichend gefilterter Geschwindigkeitsdaten können das Analyseergebnis mit Hinblick aus Artefaktstrukturen verfälschen.

Zweitens können bisher flächige Geschwindigkeitsdaten aufgrund der Funktionsweise von Langstrecken-LiDAR nur durch ein Rasterung des Messbereiches gewonnen werden. Diese Eigenschaft impliziert eine Zeitdifferenzen innerhalb der Messung, die je nach Parametrisierung der Messtrajektorie zwischen Sekunden und mehreren Minuten liegen kann. Um zeitlich hochaufgelöste Nachlaufwindfelder abbilden zu können, wird zuerst eine zeitkorrigierte Abbildung der Messung rekonstruiert. Als Voraussetzung für die zeitbereinigte Darstellung und zur späteren Synchronisierung verschiedener Messungen von mehreren LiDAR-Geräten, wird eine Methode zur nachträglichen Erhöhung der zeitliche Auflösung mittels einer Raum-Zeit-Konvertierung vorgestellt.

Drittens wird diese Verbesserung der zeitlichen Auflösung verwendet um flächige Nachlaufströmungseigenschaften zu rekonstruieren. Es wird gezeigt, dass die Verfeinerung der zeitlichen Auflösung den statistischen Abbildungsfehler reduzieren kann. Es lässt sich weiter ableiten, dass der inhärente Abbildungsfehler von gescannten Messungen für spezifische Strömungssituationen, durch die richtige Wahl der Messparameter, minimiert werden kann. Um die Genauigkeit der Raum-Zeit-Konvertierung zu überprüfen, wurde eine Evaluation innerhalb einer synthetischen Umgebung mit einem numerischen LiDAR-Simulator und einem LES-Windfeld durchgeführt.

Viertens wird die Rekonstruktion von zeitlich und räumlich hochaufgelösten, dynamischen 3D1C-Wake-Windfeldern gezeigt. Dafür werden nichtsynchronisierte volumetrische LiDAR-Messungen mit der zuvor eingeführten Raum-Zeit Konvertierung zeitlich aufbereitet und mit einander synchronisiert, um die Nachlaufdynamik in Form der Defizitform, der Defizitposition und der Defizitintensität zu bestimmen. Die ermittelte Nachlaufdynamik wird anschließend

verwendet, um unter eingeführten Annahmen ein dynamisches 3D1C-Nachlaufwindfeld zu erzeugen. Die Bewertung der Rekonstruktionsqualität und der Rekonstruktionseigenschaften erfolgt wiederum in einer kontrollierbaren Umgebung durch ein synthetischen Nachlaufwindfeldes und einem numerischen LiDAR-Simulator.

Auf dem Weg zur Minimierung der Abweichungen zwischen modellierten und realen Lasten stellen die Ergebnisse dieser Arbeit einen weiteren und wichtigen Schritt dar. Es wurde gezeigt, dass mit einer entsprechender Datenverarbeitung Windfelder auf verschiedenen Ebenen mit hoher Genauigkeit rekonstruiert werden können.

Die Erste Frage wird im Rahmen der ersten drei benannten Themenschwerpunkte behandelt, während die Fragen zwei und drei vom vierten Schwerpunkt beantwortet werden. Die Rekonstruktion der eindimensionalen Geschwindigkeiten durch die eingeführte LiDAR-Datenfilterung ist essentieller Baustein dieser Prozesskette um nicht nur Strömungsstatistik zu rekreieren, sondern um Messartefakte robust filtert zu können. Durch die Verbesserung der zeitlichen Auflösung ist es möglich die deterministischen Strömungseigenschaften von gescannten Windfelder zeitrein wiederzugeben und mit anderen Messungen zu synchronisieren, wodurch der Grundstein gelegt wurde die Vergleichbarkeit von realen und synthetischen Windfeldern von einem statistischen auf einen direkten Level zu heben. Die modellbasierte Rekonstruktion von 3D1C Nachlaufwindfeldern birgt in der Handhabung zuvor nicht berücksichtigter Nachlaufdynamiken und stellt somit ein Novum dar. Die hier gezeigte Datenverarbeitung ermöglicht die Rekonstruktion von Nachlaufwindfelder mit einer Abweichung der durchschnittliche Windgeschwindigkeit von 2,3% und eine Abweichung der Standardabweichung von 0,18%. Diese Ergebnisse der Rekonstruktion basieren dabei nicht auf einer Reproduktion der Strömungsstatistik in Form der ersten zwei zentralen Momente, sondern sind deterministisch durch den zuvor eingeführten Propagationsansatzes entstanden.

CONTENTS

LIST OF TABLES

LIST OF FIGURES

LIST OF ABBREVIATIONS

The following abbreviations are used in this manuscript:

ABL	Atmospheric Boundary Layer
Abs.	Absolute
ACL	Actuator Line Approach
ADE	Artificial Data Extension
AI	Artificial Intelligence
Avg.	Average
BEM	Blade Element Momentum
CFD	Computational Fluid Dynamics
CNR	Carrier-to-Noise Ratio
CW	Continuous-Wave
DBS	Doppler-Beam-Swing
DTW	Dynamic Time Warping
DWM	Dynamic Wake Meandering
EDPm	Extended Disk Particle model
FFoR	Fixed Frame of Reference
HDDR	High Data-Density Region
Iter.	Iterative
IQR	Interquartile-Range
LCE	Life-Cycle Earning
LES	Large-Eddy Simulation
LiDAR	Light Detection And Ranging
LLC	Life-Cycle Costs
LOS	Line-Of-Sight
MFoR	Meandering Frame of Reference
MUSCAT	Multiple-Doppler Synthesis and Continuity Adjustment Technique
PALM	Parallelised Large-Eddy Simulation Model
POD	Proper Orthogonal Decomposition
PPI	Plan Position Indicator
PTV	Particle Tracking Velocimetry
RaDAR	Radio Detection And Ranging
RHI	Range Height Indicator
RMS	Root-Mean-Square
RMSE	Root-Mean-Square Error
SCADA	Supervisory Control And Data Acquisition
SNR	Signal-to-Noise Ratio
Std.	Standard deviation
VAD	Vertical Azimuth Display
VD	Volumetric Deficit
VIC+	Vortex-In-Cell Plus

LIST OF FORMULA SYMBOLS

The following formula symbols are used in this manuscript:

Chapter 2

α	Carrier-to-Noise Ratio (CNR)
α_k	Single CNR measurement
$\alpha_k{}'$	Normalised single CNR measurement
$\overline{\alpha}_d^t$	Normalisation CNR value within the time interval t_{i-1} to t_i
α_{le}	Lower CNR limit
α_{ue}	Upper CNR limit
ΔT	Filtering time interval
Δt	Normalisation time interval
θ	Elevation angle
λ	Data availability
μ_r	Average radial line-of-sight velocity
σ_α	CNR bandwidth of the one-dimensional Gaussian kernel
σ_{u_r}	LOS bandwidth of the one-dimensional Gaussian kernel
σ_r	Standard deviation of the radial line-of-sight velocity
φ	Azimuth angle
d	Radial distance
D_A	Rotor diameter of Adwen turbine
D_S	Rotor diameter of Senvion turbine
f	Measurement frequency
h_{n_α}	CNR histogram bin width
$h_{n_{u_r}}$	LOS histogram bin width
h_A	Hub height of Adwen Turbine
h_S	Hub height of Senvion Turbine
IQR	Interquartile-range
K^T	Measurement validity within the time interval *T*
n	Standard deviation multiplier
n_d^t	Amount of measurements within the time interval from t_{i-1} to t_i
T	Time period
u	Longitudinal wind speed component
u_r	Radial line-of-sight velocity
u_{r_k}	Single line-of-sight velocity measurement
u'_{r_k}	Normalised Single line-of-sight velocity measurement
$u_{r,25}$	First quartile of the line-of-sight velocity
$u_{r,75}$	Third quartile of the line-of-sight velocity
$\overline{u_r}_d^t$	Normalisation LOS value within the time interval t_{i-1} to t_i
v	Vertical wind speed component
v^T	Normalised measurement validity within the time interval *T*
v_{th}	Filtering threshold of the measurement validity
V_L	LiDAR measurement volume
V_{USA}	Ultrasonic anemometer measurement volume

Chapter 3 & Chapter 4

$\alpha_\gamma, \alpha_\zeta$	Wake deficit intensity within the Gaussian fitting
$\beta_\gamma, \beta_\zeta$	Ambient longitudinal wind speed level within the Gaussian fitting
$\delta^{FFoR}, \delta_{VD}^{FFoR}$	Instantaneous wake velocity deficit in the fixed frame of reference
$\overline{\delta^{FFoR}}$	Averaged wake velocity deficit in the fixed frame of reference
δ^{MFoR}	Instantaneous wake velocity deficit in the meandering frame of reference
$\overline{\delta^{MFoR}}, \overline{\delta_{\mathrm{VD}}^{\mathrm{MFoR}}}$	Averaged wake velocity deficit in the meandering frame of reference
$\Delta\phi, \Delta\theta$	Total opening angle of PPI and RHI scan
$\varepsilon_{\bar{u}}$	Mean wind speed reconstruction error
ε_{σ_u}	Standard deviation reconstruction error
η_m	Measurement time efficiency
θ	Elevation angle
θ'	Difference angle of the vertical wind direction (Θ) and the elevation angle (θ)
Θ	Vertical wind direction
ϑ_{acc}	Measurement accumulation time
λ	Rotational weighting function
μ_γ, μ_ζ	Wake centre position within the Gaussian fitting
$\hat{v}_{LOS}$	Radial LiDAR velocity
$\sigma_\gamma, \sigma_\zeta$	Wake width within the Gaussian fitting
$\sigma_{\mathrm{VD}}^{\mathrm{MFoR}}$	Standard deviation of the wake wind speed in the meandering frame of reference
σ_m	Standard deviation of the measurement
τ	Radial distance within the $\gamma' - \zeta'$ coordinate system
ϕ	Azimuth angle
Φ	Horizontal wind direction
ϕ'	Difference angle of the horizontal wind direction (Φ) and the azimuth angle (ϕ)
$\omega_\phi, \omega_\theta$	Angular scan velocity
χ, γ, ζ	Fixed reference frame coordinate system in the Turbine ground point
χ, γ', ζ'	Meandering reference frame coordinate system
D	Rotor diameter
e	Maximum tolerable error
f_s	Measurement frequency
h_{HH}	Wind turbine hub height
I_0	Ambient turbulence intensity in the fixed frame of reference
$I_{\mathrm{VD}}^{\mathrm{MFoR}}$	Turbulence intensity in the meandering frame of reference
n_{pnt}	Number of measurements point within a scan
n_ϕ, n_θ	Number of angular measurements per scan
N_ϕ, N_θ	Number of scans per time interval
N_m	Required number of scans
r_γ, r_ζ	Radial position in transversal in-plane direction within the Gaussian fitting
$\mathcal{R}_\phi, \mathcal{R}_\theta$	Angular resolution of PPI and RHI scans
$s_{\mathrm{I_0}}^{\mathrm{MFoR}}$	Turbulence intensity scaling factor in the meandering frame of reference
s_γ	Horizontal spatial deficit shape scaling factor
s_ζ	Vertical spatial deficit shape scaling factor
s_δ	Velocity deficit intensity scaling factor
t	Point in time

t_r	Reset time
T	Set of all discrete measurement point in time t
T_ϕ, T_θ	Scan duration
u_o	Instantaneous ambient longitudinal wind speed
$\overline{u_o}$	Average ambient longitudinal wind speed
u_a	Instantaneous ambient longitudinal wind speed of synthetic wind field
$\overline{u_a}$	Average ambient longitudinal wind speed of synthetic wind field
$u_{\mathrm{fit,PPI}}$	Gaussian shaped wake wind speed profile within a PPI scan
$u_{\mathrm{fit,RHI}}$	Gaussian shaped wake wind speed profile within a RHI scan
u_{LES}	LES wind speed
$\overline{u_{\mathrm{VD}}^{\mathrm{MFoR}}}$	Averaged wind speed of wake in the meandering frame of reference
u_{PPI}	PPI wind speed
u_{RHI}	RHI wind speed
u_{RC}	Instantaneous ambient longitudinal wind speed of reconstructed wind field
u_{rot}	Rotated and weighted wind speed combination of RHI and PPI in the MFoR
u_t	Turbulent component of u_a
$\overline{v_0}$	Average ambient lateral wind speed
$\overline{w_0}$	Average ambient vertical wind speed
z	Confidence interval

PREAMBLE

Truth
is
a
reflection
of
what
we
perceive.

With this statement I would like to introduce the scientific investigation of this dissertation, which addresses the conscientious claim of finding new knowledge to approach the truth. The terms knowledge, truth and true are so closely linked that, in addition to the natural sciences, philosophy deals with this topic and, in conjunction, thematic areas arise that represent the overlapping of both. These include natural philosophy, epistemology and the philosophy of science.

For beings in a society or subgroups of this, the truth is seen as a congruence of statements with a subject matter, a fact or the correct reproduction of reality in the sense of perception [1, 2, 3]. Logically, a distinction must be made between truth and reality. Since people rarely reflect on their linguistic determinations, there are differences in the meaning of the general terms. Reality is absolute, its essence is not changeable in time – Since in this work often refers to dynamics (changes over time) the general concept of time and temporal perception is not explicitly questioned. Truth, on the other hand, is not subject to absoluteness and, in due course, is subject to revisions through the reflection of knowledge. Truth, from my perspective, is a fractal that calls on itself, since the true reproduction of perception requires preceding knowledge to be classified by the truth. The subsequent recitation of perception is thus filtered through personal knowledge and the resulting creation of a model of the observed process. Only through the repetition of a specific perception, this perception and personal knowledge can adapt, expand and become more detailed.

In the scientific context, the introduction and use of technical measuring instruments have complemented personal perception to decouple the limits of individual sensing and discrimination from a generally true statement to make it consistently sharable. The independence of perception as a key argument for knowledge formation corresponds to the claim of constant repeatability, but not yet to the search for truth. Personal perception and the cognitive focus nevertheless shift to a superordinated level of reflection as technology progresses. The more precisely we want to understand, or rather, the more accurately we want to define the truth, the more precisely we must perceive, the more precisely we need to quantify, the more precisely we should name, the more precisely we require to measure, the more precisely we have to conclude. This theoretically self-sustaining approach overcomes limitations through new measurement methods and/or the application of knowledge in order to generate opportunities for new knowledge findings.

Since this work is focused on real and synthetic measurements, the previously philosophised statements of perception are to be transferred to the technical measurement. A more accurate picture of the truth can only emerge if repeated perception is supplemented by a change of perspective.

1 INTRODUCTION

The following chapter is written in order to provide a general overview of the containing topics does not claim to be comprehensive. The including sub-chapters have been designed to supplement the contents of Chapter 2 to 4 and to minimise redundancy.

1.1 Wind Energy

Today, the term wind energy is understood less like the general use of wind as a resource than the conversion of kinetic energy from the wind into electrical energy that can be fed into the power grid. Necessary for this transformation is the physical and technical knowledge to make it usable for humankind. Today's wind turbines are technically complex machines which are mainly designed according to the criterion of safety and economy. The economic efficiency covers all costs of Life-Cycle Costs (LCC), which can be divided into costs in the manufacturing phase and costs in the operational phase [4, 5] and Life-Cycle Earning (LCE). The costs within the LCC must be considered separately in the financial report of costs and revenues since the owner in the operational phase bears these. Costs of the manufacturing phase are accounted in the acquisition price. LCC and LCE are interrelated since the site-dependent wind condition mainly determines both.

The decisive criterion for turbine design and the selection of a wind turbine according to a location mainly depend on the average wind speed and specific turbulence intensity that can be ascribed to certain wind classes [6]. The selection of a turbine is based on a turbine type designed for the corresponding wind class. An unsuitable selection for a site will have a weaker economic balance due to a low energy yield and/or due to potential failures for replacement and maintenance work. Since the main influencing factor for a wind turbine in the production and operational phases is wind speed, it becomes evident that it can only be operated efficiently and economically if the wind speed assumptions are highly representative.

With the trend towards increasing rotor diameters of wind turbines, the relative distances between clustered turbines are becoming smaller. This leads to considerably pronounced wake effects, since the wind speed recovery behind the rotor depends beside the atmospheric condition and the operating point of the turbine, on the downstream distance. The resulting losses are so

considerable that specific research is conducted on concepts to reduce wake effects in interaction with other turbines. Since the atmospheric conditions cannot yet be regulated actively [7, 8], the available space and mutual distance of turbines is determined by the rotor size, only the control of turbine operation within a wind farm remains as a regulating element. This comprises various strategies, such as induction control in which the trust and hence the energy extraction of upstream turbines is reduced to decrease the intensity of the average wind speed deficit [9, 10, 11] or active wake deflection by an intended yaw-misalignment of the rotor to the wind direction [12, 13, 14]. As promising as these approaches are, they will not be discussed in more detail within this thesis. However, for the investigation of specific control strategies of the wake behaviour and the interaction of wind turbines with wake flows, data, such as LiDAR measurements, is indispensable. Multiple of the data processing steps required in this context can as well be found in the following chapters.

1.2 Wind Turbine Wakes

The phenomenon of wakes is well known especially in fluid mechanics and generally occurs where fluids are obstructed from flowing undisturbed. Depending on the obstacle, altering areas of reduced velocity with increased fluctuation occur in turbulent flows [15]. By taking the kinetic energy from the flow through the rotor, a volume of affected wind speed is created behind the turbine in flow direction. This region is characterised by a characteristic longitudinal wind speed deficit and certain dynamics in relation to the turbine performance with concise shear and increased fluctuations. In contrast to the almost symmetrical structure of a wind turbine, this wake region is not completely symmetrical. Influencing factors that break the symmetry are the atmospheric boundary layer, the rotation of the rotor, the vortex shredding of the blade tips, the interaction of the wind with the turbine tower and the nacelle. The wake can therefore be regarded as a highly complex structure, which also exhibits complex dynamic behaviour due to the inhomogeneity of the inflow on different scales.

In research, a pragmatic division into near- and far-wake has been developed, which is characterised by the main effective processes [16]. In the near-wake, the flow is mainly characterised by the geometry of the turbine, rotor blades and the pressure relaxation. Within a stationary state, an axial symmetry can be seen in the far-wake, which can be assumed to be approximately Gaussian in its self-similarity with increasing downstream distance. As a result of the mixing processes, particularly due to shear flows by the wind speed deficit, a velocity recovery takes place as the distance to the turbine increases [17].

In the interaction of the wake with the atmospheric boundary layer, the phenomenon of the so-called wake meander becomes apparent. This meandering is visible in a horizontal and vertical transversal movement of the wake region in the downstream direction. It is assumed that the interaction of large scale inflow structures in the range of two to three rotor diameters and the turbines themselves causing this effect , which leads to continuously varying wake shading effects in wind farms. A comprehensive study of the wake meandering and the and the possibilities to measure and quantify them can be found in Trujillo's dissertation [18].

The wake is additionally influenced by the presence of the ground and the breaking of the symmetry by the rotation of the rotor, resulting in a dynamic behaviour which can be described by alternating deficit shapes, deficit intensities and deficit positions in all spatial directions. Especially the meandering behaviour of the wake leads to a widening and thus a blurring of the

mean deficit that can be seen as a convolution of the instantaneous deficit. Thus an increase in the local turbulence intensity in a fixed reference frame can be overserved (FFoR) [19]. Due to this complexity, it is difficult to investigate wakes by analytical calculations or numerical simulations only full scale measurements are of importance as well.

The greatest losses and deviations from the calculated power respectively from the calculated loads of turbines occur when these are clustered in wind farms. The positioning in wind farms causes mutual wake shading and is the main disadvantage in form of its negative impact on energy yield. Yield losses due to wake shading were already discussed in wind energy research in the 1970s [20, 21].

Constantly changing inflow conditions causes additional fatigue loads on turbines which are partially or completely influenced by a single or multiple wake [16, 22]. These wake-induced loads are considered to be taken into account within so-called design load cases during the design phase of a wind turbine to ensure its durability according to technical standards [6]. The load cases cover combinations of predefined atmospheric conditions with different operational states of the turbine [23]. The variations in atmospheric conditions refer to clustered combinations of average wind speed, turbulence level or turbulence intensity, wind shear and specific gusts. For the offshore operation, defined hydrodynamic load simulations have been added.

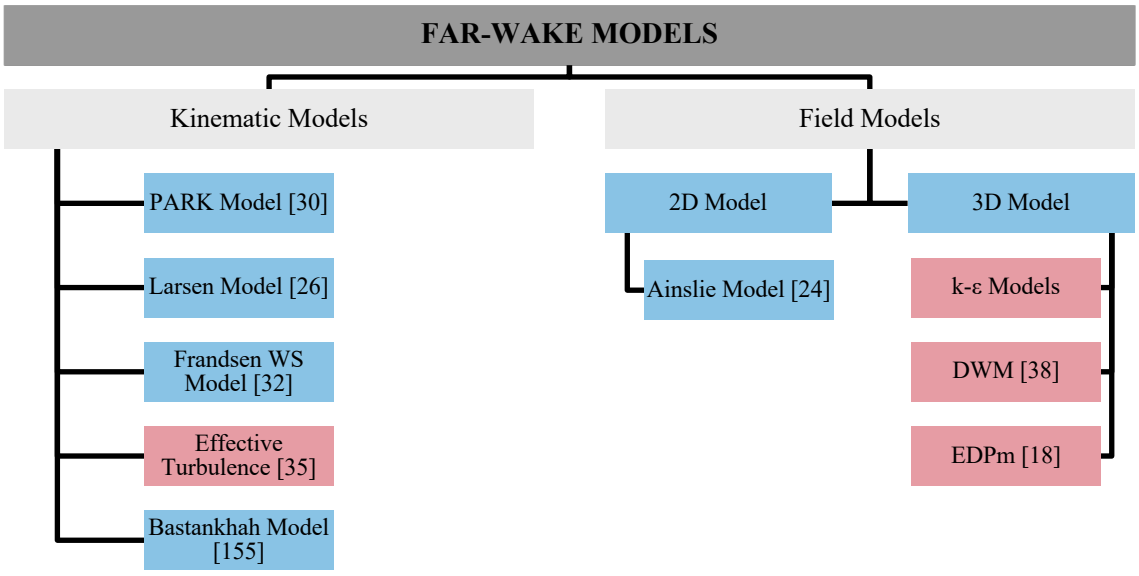

Figure 1.1 Broad overview and categorisation of some selected wake models covering the far-wake region of wind turbines. Blue fields represent models that calculate stationary wind fields, green fields refer to models that include attributes of a dynamic wake behaviour.

1.3 Wake Models

Wake models were developed to simulate the wake behaviour for specific atmospheric conditions with the primal intention of energy yield determination. Over the years, the first models have been further developed on the basis of fluid mechanics, Newton's axioms, empirical approaches and in fact measurements. A known division of far-wake models is made into the category of kinematic models [24] and the field models [25, 26, 27]. Kinematic models base on a self-similar velocity profile, whereas field models solve the Navier-Stokes equations and are further divided into two-dimensional and three-dimensional models, according to Shakoor et al. [28]. Figure 1.1 shows an incomplete overview of far-wake models. For the sake

of clarity, not all the wake modelling options visible in Figure 1.1 are mentioned or explained below.

The division of wake models into their application areas shows that models that spatially resolve the velocity deficit are primarily used to calculate energy yields, while models that map in addition a particular temporal dynamics are used for load calculation. Today, a small number of models have been established in a wide field of application which are briefly summarised in the following. Wake models used for yield prognosis and load calculation represent in their methodology only the far-wake, since current turbine spacings are covered in this region. However, it can be observed that due to the steady growth of the rotor diameter, the available space is quantised into increasingly smaller relative turbine spacings.

1.3.1 PARK Model

One approach for modelling wakes are the simplified fluid mechanics equations of momentum and mass conservation for turbulent flows. Jensen can be classified in the category of kinematic models with the PARK model [29], which assumes a rectangular shape as wind speed profile. Jensen [29] uses the assumption of the continuity equation, which means that the width of the velocity profile increases linearly with the distance to the turbine emitting it. Jensen parameterises the linear expansion with a variable k, which depends on the environmental surface condition in the form of the roughness length. In subsequent studies, the k-value was set to 0.04 in empirical investigations [30]. The intensity of the rectangular velocity deficit depends on the thrust coefficient of the turbine, its rotor diameter and the downstream distance. A significant advantage of the PARK model is its numerical simplicity and the resulting short calculation time, which is suitable for the estimation of the power output of wind farms. Due to the insufficiently detailed resolution of the velocity profile, it is unsuitable for the reproduction of wake wind fields.

1.3.2 Frandsen Models

Also the wake velocity model of Frandsen et al. [31] is based on the equations of conservation of momentum. In contrast to Jensen [29], Frandsen et al. [31] apply these equations three-dimensionally. Frandsen et al. [31] assume that the wake can be regarded as an expanding tube whose volume flow remains the same over its expansion in downstream direction - this implies the incompressibility of the fluid. An advantage of this model is the consideration of multiple wakes, which depend on the ratios of ambient and inflow velocity, the rotor surface to the wake cross-section and the thrust coefficient. In a study by Tong et al. [32], they show that Frandsen et al. [31] overestimate the initial wake expansion and predicts the highest wind velocities compared with other models [33].

Both the Jensen model and the Frandsen model represent the wake in a steady flow state, in which the dynamics and turbulence are not explicitly resolved. Since these influencing factors are of interest for the load calculation, Frandsen [34] postulates an approach for representing the dynamics and turbulence in the wake in the form of an effective turbulence intensity for determining fatigue loads of wind turbines. This effective turbulence intensity refers exclusively to the longitudinal wind speed, while transversal components or a deficit shape are not represented. Frandsen's effective turbulence model [34] is based on the undisturbed hub height wind speed, the standard deviation of the ambient turbulence, the number of adjacent wind turbines, as well as the distance to them and the Wöhler curve exponent. It is a pragmatic

approach, less intended to represent the real turbulence in terms of turbulence intensity than its effects on fatigue loads on the downstream wind turbine. The numerical simplicity and the possibility to calculate load situations of complex wind farm geometries led to the integration of Frandsen [34] calculation model into the IEC standard [35].

1.3.3 Ainslie Model

In the category of field models, the approach of Ainslie [24] is one of the most popular solutions of the Navier-Stokes equations. Ainslie simplifies it to a thin-layer approximation with an axis related rotational symmetry of the flow field by modelling the Reynolds stress with an eddy-viscosity approach. The validity of his model is limited to the far-wake region by balancing pressure gradients as far as possible. To calculate the flow field, a double Gaussian initial velocity profile is assumed, which develops into a single Gaussian profile along the downstream direction. The model also represents the wake in a steady-state state and assumes steady-state environmental conditions. Ainslie discusses the dynamic effect of wake meandering and credits it with a correction of the centreline deficit depending on the wake width, the downstream distance and the standard deviation of the lateral wind speed. A separate term, which combines the wake meandering with the wake width, is not given. By modelling the eddy viscosity, the turbulence intensity in the wake can be inferred, even if it does not claim to represent reality. Thus, the detailed resolution of the wind speed profile beyond a downstream distance of $2D$, with D as the turbine rotor diameter, Ainslie's model is used mainly for yield calculation.

1.3.4 k-ε Models

Another solution of the Navier-Stokes equation is the approach of Crespo and Hernandez [36] using a k-ε approach. They used partial differential equations and describes the development of the turbulent kinetic energy k and the isotopic dissipation rate ε to represent the Reynolds stress. Together with Large-Eddy Simulations (LES), this method of the calculation of wake wind fields is the most advanced and precise way so far. Spatial and temporal restrictions are only limited by the available computing power. k-ε models today form a numerically more favourable calculation possibility of turbulent flow fields compared with Large-Eddy simulations since results of k-ε models simulations are similar detailed and require about three orders of magnitude less computing power [37].

1.3.5 Dynamic Wake Meandering Model

The reproduction of wake dynamics is particularly relevant for load calculations since turbulence increases material fatigue [16]. The Dynamic Wake Meandering (DWM) model by Larsen et al. [38] is dedicated to this topic by covering both small-scale turbulence and atmospheric-scale wake meandering. Similar to Ainslie [24], a stationary flow field is calculated by solving the thin-layer approximation using eddy viscosity modelling, which assumes an initial velocity profile at a distance of two rotor diameters in the downstream direction. In contrast to Ainslie [24], the flow field in Larsen et al. [38] is not calculated in a fixed frame of reference, but in the meandering frame of reference (MFoR).

An example of the calculation of the wake flow fields in the MFoR and FFoR can be seen in Figure 1.2. The visualised wind fields were not created in the course of the wake modelling using the DWM or Ainslie model but consist of corresponding data from a LiDAR measurement

campaign at the offshore wind farm 'alpha ventus' in August 2013. The flow field in the MFoR shows a clearly reduced recovery of the longitudinal wind speed in the axial direction compared with results in the FFoR, which reveals stronger deficit intensities and distinct shear flanks of the velocity profile at commonly used values of the turbine spacings.

Larsen et al. [38] assume that the wake flow behaviour can be represented as a superposition. For this purpose, a scale separation of the ambient turbulence from a frequency of $f_c = \frac{\bar{u}}{2D}$ is introduced, with $\bar{u}$ as the averaged longitudinal wind speed ad D as the rotor diameter. Frequencies below f_c contribute to the wake meandering. For the calculation of a meandering time series, the inflow time series of the vertical and horizontal lateral components are low pass filtered according to f_c. The wake meandering is regarded as the horizontal and vertical movement of planar velocity deficit in a corresponding plane. The wake position on a horizontal-vertical plane a certain downstream distance is calculated by the linear projection of the filtered time series assuming the frozen turbulence [39]. The calculated planar wind speed profile in the MFoR is moved in this plane with the calculated wake position dynamics and is superimposed with a synthetic turbulent wind field. The velocity profile shear-induced turbulence is considered by a turbulence scaling based on the velocity profile shape and position. The DWM model [38] was the first approach to cover temporally resolved wake meandering, which led to a high interest in the model and successive improvements [40, 41, 42].

In the current version of the IEC standard, the DWM is recommended for load calculation [43].

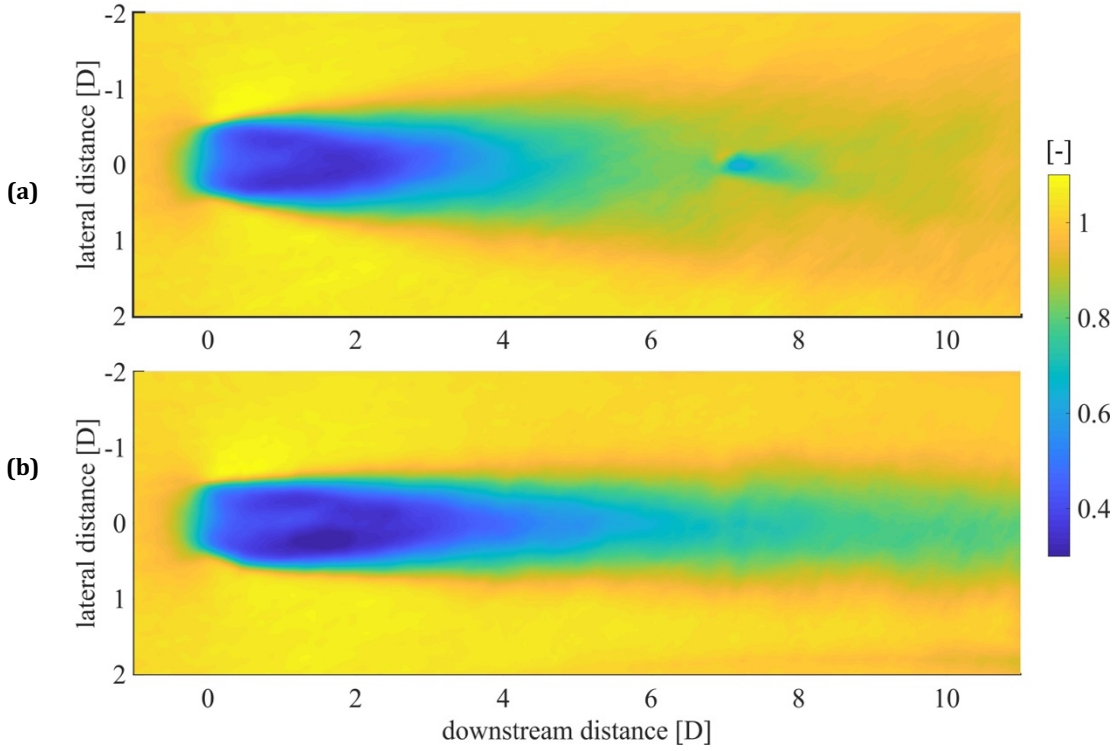

Figure 1.2 Exemplary visualisation of the averaged flow field of total 112 PPI LiDAR scans of the wake of the turbine AV10 (Adwen AD 5-116) in the wind farm ‘alpha ventus’ on 19.08.2013 from 00:15h to 05:45h in **(a)** the fixed frame of reference and **(b)** the meandering frame of reference. The second visible wake in (a) at ca. 7D downstream distance is the nacelle wake of the non-operating turbine AV07.

1.4 LiDAR and LiDAR-measurements

The behaviour of the wind is decisive for the design and operation of wind turbines and wind farms. The more precise measurements can be made, the more accurate assumptions and associated interpretations can be drawn from them. Accordingly, a special level of attention should be paid to the process of measurement, as it constitutes a reference for validation.

The standard instrument in today's resource assessment for determining vertical distributions of the wind speed and wind direction in the free-field is the combination of cup anemometers and wind vanes. A big advantage of this measuring system is the mechanically simple design and the high data availability in relation to the acquisition and measuring costs, which faces the main disadvantage of the inertia of the measurement setup, which limits the possibility to capture turbulent flows in high resolution. A further method of current anemometry is represented in ultrasonic anemometers, which can measure the wind vector in three dimensions or horizontally in two dimensions, depending on the design. This implies a coincident measurement of the wind direction, eliminating the need for a second instrument.

This methods of anemometry are used to determine turbulence characteristics in free-field measurements by small-scale time resolution. For this purpose, meteorological measuring masts must be erected in order to carry out measurements at appropriate heights. For fixed-point measurements, the wind velocities are evaluated via the inflow wind direction. With the aim to analyse time series of wake measurements, the challenge of wake identification has to be considered first. The geometric information of the locations of the wind turbines, the measurement position and wind direction can only be used to determine wake profiles and turbulence intensities for the corresponding downstream distances over time intervals and different inflow conditions with point-measurements [44]. Without the knowledge of the overall flow condition, time series of point-measurements can usually only provide information about a steady flow state. Within this framework, for the first time, remote sensing devices in anemometry made it possible to visualise wake situations quasi-instantaneously over a wide area in free-field measurements.

In recent years, the heterodyne Doppler wind speed LiDAR, in the following only called LiDAR, has been used primarily in wind energy research. In resource assessment, LiDAR measurements are gradually replacing the aforementioned point-measurement systems as a result of the declining acquisition and rental costs. Furthermore, the continuous research on LiDAR systems and LiDAR application leads to new measurement and processing methods, which consider and compensate for the inherent disadvantages of the measurement principle, which will be discussed further in this chapter. This is particularly true for the qualification of potential turbine locations, for wind turbine control, for wake analysis and in combination with conventional anemometry for the certification of power curves.

Two different LiDAR types are mainly used in wind energy. The distinction is usually made by the emission waveform, in continuous wave (CW) and pulsed systems. Both types operate in the near-IR range around 1.55µm [45] and scatter on aerosols contained in the air. The main assumption within LiDAR measurements is the transportation of aerosols with the same speed of the surrounding air like passive particles. It is further presumed, that the composition of aerosols is homogeneous in geometry, backscattering and density. The one-dimensional velocity of the aerosols in the beam direction, the so-called Line-Of-Sight (LOS) velocity, can be determined by backscattering along the laser beam on the basis of the Doppler effect.

The LOS velocity is calculated by determining the Doppler shift by a spectral observation of the backscattered signal. In the resulting spectrum, a ground noise level is present, which is

influenced through saturation processes in the sensors, electrical fluctuations and those of unknown nature. The more homogeneous the velocity distribution within the measurement volume along the laser beam, the clearer the representing peak within the spectrum. To ensure unambiguousness in the peak, the resulting velocity is determined by fitting spectral peaks with a numerical function.

Furthermore, the backscatter intensity is used to calculate the Carrier-to-Noise Ratio (CNR) respectively Signal-to-Noise-Ratio (SNR), which can be seen as a quality indicator for the physical aspects of speed determination. Another quality indicator for wind speed measurement can be found in the evaluation of the velocity peak from the spectrum. The width of the corresponding fitting function, called dispersion, gives information about the numerical quality of the measurement. Both, CNR/SNR and the dispersion may be used as a filter criterion.

Optical losses and variations in the internal processing of the LiDAR cannot be ruled out, as the laser beam is deflected several times within the LiDAR and depending on the specific design and type of LiDAR.

While CW devices have to mechanically set the focus point to a certain distance, pulsed devices can measure quasi-instantaneously at several distances. The distances achieved depend technically on the limitation of the laser safety class. Today's CW-LiDAR measures in the near field up to a distance of a few hundred metres with very high measuring frequencies of up to 400 Hz using the continuous signal. Due to the high measuring frequency with only one focus distance, in most commercial CW-LiDARs the laser beam is deflected opto-mechanically coupled by one or more rotating prisms. Thus it is possible to scan rotationally symmetrical trajectories with one rotating prism or Lissajous pattern with two rotating prisms.

The measurement range of pulsed devices can reach several kilometres by emitting individual pulses one after the other. These require a longer measurement time per measurement to identify and accumulate the pulses. In commercial long-range systems, the maximum measurement frequency is 2 Hz, which is usually achieved in staring mode measurements and rarely in scanning operation mode. The real measurement frequency depends on the appropriate measurement parameter in relation to the atmospheric conditions. The fewer aerosols are present in the air, the less backscattering and the longer the emitted pulses have to be accumulated in order to be able to fit a peak within the spectrum of the backscattering out of the ground noise level of the LiDAR.

When using LiDAR measurements, it should be considered that the resulting data have undergone complex processing. A physical limitation of the measuring principle concerns CW and pulsed measuring systems, since the measurement results do not represent a point-shaped LOS velocity but was measured within the so-called probe volume, along the laser beam. This volume can be assumed approximately as a cylinder and is determined from the geometry of the laser beam and the measurement parameters. In pulsed systems, the pulse shape can be considered as a weighting function within the sample volume, whereby wind speeds within the volume are subjected to volume averaging. The corresponding velocity value is generally assumed to be symmetrical around the centre point. The effect of volume averaging has often been discussed in the literature in connection with the limited possibility of measuring turbulence correctly with LiDAR [45, 46, 47]. A comprehensive review article by Sathe and Mann [48] describes the effects and the research that has been done in this field to date. Especially the measurement of wakes with LiDAR is constrained by this effect, as wake regions are characterised by high turbulence and significant shear which are attenuated by volume averaging in their mapping.

Physical and technical effects influence the signal until it has been digitally quantised. Since commercial systems represent a combination and integration of different electrical components, this may lead to electrical variations within the device or from external sources of interference which may have an effect on the determination of the LOS velocity. To what extent individual influences can be identified in the data depends on the access to LiDAR raw data and system protocols, which not all manufacturers are willing to provide - also considering the enormous amount of data. Thus data from modern LiDAR systems, even if the principle and processing are known, need to be filtered.

Despite the physical, technical and numerical constraints, LiDAR stands out as remote sensing measuring instrument due to its versatile measurement options. Two categories of differentiation have been established in the wind energy sector to date. For primarily logistical reasons or because no other positioning is possible, many LiDAR measurement campaigns are carried out based on the ground and the systems are positioned stationary [49, 50, 51, 52, 53, 54, 55]. Many of the techniques and terminologies used in connection with LiDAR originate from RaDAR (Radio Detection And Ranging) technology, which is similar in its functioning. While measurement approaches such as the Vertical Azimuth Display Method (VAD) from Browning et al. [56] or Doppler-Beam-Swing Method (DBS) [57, 58, 59] for determining wind speeds and wind directions at certain altitudes are designed to measure based on the ground or upwards, other ground-based measurement trajectories have to face additional obstructive measurement inclinations. Quasi-planar flow measurements can be performed with Plan-Position-Indicator scans (PPI) and the Range-Height-Indicator scans (RHI), which have larger inclinations to the main wind speed component due to the difference in height of the near-ground LiDAR to the measuring point. To perform scanning measurements, either the azimuth angle or the elevation angle is fixed, while the other one alters. Due to additional deviations of the laser beam to the wind direction when measuring ground-based, several studies have been published in recent years to investigate the positioning of the LiDAR on the nacelle [13, 62, 63, 64, 65, 66]. Within this framework, CW LiDARs are mostly oriented into the inflow to determine high-frequency inflow situations with the aim of turbine control [61, 63, 66]. Furthermore, LiDAR measurements are carried out in the downstream direction with the focus on wake analysis respectively for the purpose of characterising and validating the wake behaviour. Preferably pulsed systems with a long range are used to capture the wake behaviour in order to obtain a quasi-instantaneous representation of the wake wind speed for multitude of downstream positions. In the research of wake effects, the necessary experience has only accumulated in recent years to enable installation of long-range systems on nacelles. Corresponding research therefore still represents the exception [13, 67]. For instance, Bingöl et al. [68] and Trujillo et al. [69] investigate meandering effects within the near-wake measurements performed by CW LiDAR devices.

Regardless, whether wake measurements are ground or nacelle-based, scanned measurements are used to represent flows over a flat surface. Due to the limitations of the LiDAR technique, the question arises as to how exactly the measurement represents reality. Initial comparisons of so-called staring measurements, in which the laser beam is fixed positioned, and VAD measurements against ultrasonic and cup anemometers showed good matches [70, 71, 72] in average over time [73, 74, 75]. Fluctuations with eddy sizes smaller than the probe volume length are filtered out due to the physic of the measurement principle and cannot be mapped [72, 76].

Since there is no possibility of reference in the free-field to quantise the mapping quality of planar measurements, numerical approaches have been used in recent years to create a transferability of simulated LiDAR data to real LiDAR data. Part of these studies are based on free-flow wind fields [77, 78], while the larger part investigates the interaction of the atmospheric boundary layer (ABL) with wind turbines [55, 79, 80, 81]. With ongoing research into the characteristics of LiDAR velocity data, these can be used to be better understood in the sense of more realistic wind turbine inflow conditions.

1.5 Research Motivation

The precise knowledge of the inflow conditions of wind turbines is essential for their economic operation. This applies not only to the design of the turbine but also to the control during operation, which will not be further discussed in more detail due to the scope of this thesis and the complexity of the topic. In general, it can be stated, that the more precisely wind turbines are designed to their environment, the more efficient the energy yield and the lower the operational outages. Since energy yield and structural loads are calculated on the basis of statistical relevance with a multitude of design cases, knowledge of the interaction of the atmospheric boundary layer (ABL) with the turbine is needed in advance. This amount of necessary data is usually not available during the design phase, which has as the consequence, that inflow data and turbine behaviour have to be simulated.

Nowadays, due to the immense and easily accessible computing power, one of the most promising approaches to simulate the inflow-turbine-interaction in the sense of a verifiable framework is the coupling of Computational Fluid Dynamics (CFD) and aero-elastic calculations. Coupled approaches have become state-of-the-art in science and offer information about the behaviour of the flow, the turbine and their interaction [82, 83, 84, 85]. This combination opens the possibility to calculate wind fields and structural loads in an almost freely selectable spatial and temporal resolution. Due to the complexity of both combined models, the desired quality of the simulation in form of spatial and temporal resolution depends on the numerical infrastructure, expertise and processing time. The amount of required wind fields and concomitant costs are among the main reasons why industrial applications have been the exception until now.

Consequently, more computational-saving models are used which do not explicitly resolve the interaction of the turbine with the flow for load calculation. As an example, the aero-elastic solvers BLADED, HAWC2 and FLEX5 can be mentioned, which solve the interaction of a turbine with a wind field among others with the assumptions of a multibody-problem and the aerodynamic blade element momentum theory (BEM). The degree of abstraction applied in these coupling is in turn a compromise between numerical cost and accuracy. While the numerical representation of the mechanical properties of the wind turbine can be assumed to be accurate to a large extent within the turbine models approved by manufacturers, the more significant uncertainty relates to the modelling of the inflowing wind field.

For the case of undisturbed inflow, the flow field is synthesised with the use of turbulent wind field generators. There are different turbulence generators, which mainly differ in the geometric position of the spatially resolved points in the wind field (depending on the aero-elastic solver), the temporal resolution, the turbulence spectrum and the coherence function used. For the case of wake shading of the rotor area from one or multiple upstream positioned turbines, wake models are additionally used to recreate the corresponding characteristics - as far as the degree of

abstraction of the model permits. The underlying models are themselves numerical compromises, which were created from a large number of corresponding reference measurements or theoretical considerations in order to create a general recallability. Therefore, resulting modelled wake wind field can be seen as conditional parameterised wind field reconstruction, that are accepted based on a statistical assumption. In the following, an overview of wind field reconstruction is addressed.

Comparisons of the application of wake models with free-field measurements show that both the energy yield [86, 87] and, in particular, the predicted loads differ [88, 89]. Possible causes for deviations can be attributed to the inaccuracies in the evaluation, which have their origin, technically in the data set, or logically in the assumptions used. Technical obstacles can be found in the availability of high quality inflow and load data since four-dimensional wind fields and small-scale interactions of these with the rotor cannot yet be measured with sufficient spatial and temporal resolution.

In any case, the lack of suitable and holistic inflow data has the consequence that these have to be compensated by assumptions. The artificial filling represents a source of inaccuracies within the aim to minimise the difference between calculated and real loads and energy yields. To further refine the current calculation possibilities and to be able to map the interaction reality between inflow and turbine more precisely, it is necessary to analyse how far these differ. For this purpose, a new level of comparability of data must be created. Within the framework of comparability of synthetic and real data, the superordinate objective is first, to reproduce the effects of the wind field measured in free-field on a wind turbine and secondly, to compare the results of the simulation with the reconstructed synthetic wind field and the numerical model of the turbine with corresponding measured data. The specific in the wind field reconstruction is the assumption of the unknown information to be filled. Beyond this general definition, specific definitions are given anew in the framework of their application on varying scales of temporal, spatial and flow details.

While in the IEC Standard [6] the comparability was defined as sufficient by the statistical reproduction of flow characteristics in the form of the first two central moments and the spectral energy density within the included turbulence models for undisturbed inflow situations, studies show that the representation of specific wake situations by means of current wake models lead to deviations [88, 89].

With the further development of remote sensing instruments, it has become possible to measure wind fields in the free-field on different length and time scales. The technical achievement opens the possibility to use quasi-instantaneous planar and volumetric wind speed data for a reconstruction beyond the capabilities of stationary anemometry. As already specified in the preamble, short-range LiDAR can measure several hundred meters in upstream direction with high measurement frequencies, which is why they are particularly suitable for providing input for the operational control of wind turbines. While measurements with short-range LiDAR can be performed within the scope of research on turbines with currently sub-average rotor diameters outside the induction zone influenced by the rotor, the reconstruction of the inflow wind field at current average rotor diameters is confronted with the need to map the affected advection speed in the pre-pressure zone without the knowledge of the ambient speed [90].

Long-range LiDAR can record evolution of wind turbine wakes over several kilometres in downstream direction. In the here presented framework, long-range LiDAR are of particular interest when the measurements aim to investigate the wake behaviour of a specific turbine. The

reconstruction of wake wind fields using LiDAR systems seems to be the most promising method to date for the purpose of comparing real and synthetic inflow situations. The difficulty of statistically reproducing wake inflow situations can technically be explained by first, the novelty of the application of LiDAR systems as one-, two- and three-dimensional information-giving measurement techniques, as well as second, logically in the ambiguity of the quantisation and classification of associated flow characteristics of different wake situations. Standardised classification of wake inflow situations is necessary to summarise sufficient measurements or calculations to demonstrate a statistical correlation with a corresponding specific turbine behaviour. However, the representation of these wake classes in models first requires a definition of the classification and delimitation. Due to the variability of the wake, which is influenced by atmospheric, turbines and geographical conditions, an exact normalised categorisation is yet beyond the possibilities of the current state of knowledge and requires as preliminary work the mapping of real inflow situations in the form of reconstructions and simulations in order to recognise unambiguousness and similarities in the wake behaviour for different turbine and rotor geometries, atmospheric conditions, their environment and interactions among them.

As can be read later in Chapter 4, LiDAR measurements are already being used to reconstruct undisturbed and wake wind fields. Since the concept of reconstruction is constantly newly defined from study to study, a broad spectrum of wind field reconstructions is apparent in research. In general, every reconstruction is a certain parametrisation of a model and can therefore never represent the full reality, but only the perspective of the model. Depending on the scientific-pragmatic point of view, studies based on LiDAR measurements can be called per se reconstruction due to the measurements principle, capturing the LOS velocity as the derivative of the aerosol velocity [91]. Here, the inherent reconstruction model is based on the assumptions that aerosols at which the laser refracts are homogeneous in geometry and surface condition and can be seen as passive particles. Even elementary LiDAR measurements (VAD and DBS), as used in site surveys, reconstruct the longitudinal wind velocity and wind direction from the LOS velocities [66, 67, 70, 71, 72, 73] on the basis of the reconstruction assumption that the volume enclosed by the laser beam can be observed stationary. In the reconstruction of Kapp and Kühn [90], the reconstruction method includes the parameterisation of a synthetic wind field employing five parameters in order to achieve the smallest possible deviation from the real inflow field. The reconstruction of the undisturbed flow is particularly challenging concerning the correct mapping of turbulence, as Sathe and Mann [48] describe it, due to the volume averaging.

The reconstruction of wake wind fields is generally more difficult since assumptions about the wake behaviour have to be made for the free flow surrounding the wake. Iungo and Porté-Agel [52] reconstruct wake wind fields by combining volumetric PPI scans and using a 3D Delauny triangulation to bring them to a uniform grid from which they calculate the temporal mean. Iungo and Porté-Agel [52] do not model the wake wind field but use the interpolation as reconstruction assumption. Van Dooren et al. [55] use measurements from two distant LiDAR systems to reconstruct the wake of an offshore turbine to a 2D flow field in the temporal mean under the assumption of the Multiple-Doppler Synthesis and Continuity Adjustment Technique (MUSCAT). They also do not use explicit modelling of the wake but apply MUSCAT reconstruction to all data points in the same way. Fuertes and Porté-Age [80] reconstruct wake wind fields from a synthetic origin (LES) by linearly interpolating PPI, and RHI scans in temporal

average. They investigate the behaviour of the reconstruction error caused by the temporal and spatial quantisation of the scanning behaviour and the projection of the LOS velocities.

A different approach of reconstruction is based on the modal decomposition of the flow field using Proper Orthogonal Decomposition (POD). Both research teams of Bastine et al. [92, 93, 94] and Iungo et al. [95] show that different approaches and implementations of POD can be used to dynamically reconstruct wake wind fields in high precision. In all studies, however, it is described that the reconstruction quality depends on the number and selection of modes.

However, some reconstructions do not aim to reproduce wake wind fields, but only to map properties of the wake. In studies including wake characterisations, the wake motion is mostly reconstructed in the form of the temporal resolved centreline motion to obtain information about the position and/or the atmospheric driven wake meandering [66, 69, 85]. In addition, the recovery of the wind speed deficit in downstream direction and geometric derivatives, such as the wake width, are considered [49, 53, 96, 97].

1.6 Objectives and Structure of the Thesis

As can be concluded so far, remote sensing via LiDAR technology incumbents a central role in wind energy research, since it enables high-resolution, location-independent, point, area and volumetric measurements of the flow situation covering a broad spectrum of spatial and temporal scales. The resultant possibilities extend the capabilities of conventional anemometry and allow a profound insight into the flow behaviour of the wake of wind turbines.

To investigate the effects of wake interaction on wind turbines, numerical models are coupled that calculate the turbine and wake behaviour. In order to improve the transferability of this combination, it is necessary to be able to compare real measurements with simulations at a level of accuracy at which inflow situations are not generated stochastically but are a spatially and temporally deterministic reconstruction of the inflow situation corresponding to real measurements.

Thus, the central topic of this dissertation is the reconstruction of single wind turbine wakes based on long-range LiDAR measurements. The inherent superordinate question of this topic, can be deduced:

How can long-range LiDAR data be used to reconstruct
single wind turbine wake wind fields?

This general question is divided into sub-questions, which will be answered by the following three chapters. These three chapters are partly previously published research articles which, in their sum and synergies, answer the core question. As discussed in the motivation (Section 1.5), the terminology of reconstruction is regularly redefined in the context of its use. The following research includes various approaches that can be unified under the guise of reconstruction and shows the entire processing of wind field reconstruction at different levels: starting with the design of the measurement parameters, data filtering, data preparation and wind field reconstruction. Each of these steps can in turn be regarded as a reconstruction.

The origin of each analysis is the selection of a data set. LiDAR measurements do not reflect the reality, since they are affected by physical, technical and unknown influences as can be deduced from the preamble. Concerning the further processing of the LiDAR data, an exact

filtering of outliers is necessary to enable an as exact as possible mapping of the flow. Otherwise, errors may be amplified in the process chain leading to falsification of the flow characteristics not only in the form of erroneous statistics but also of unrealistic time series. To reduce these influences, filtering the LiDAR data is indispensable. In Chapter 2, the following questions will be addressed:

- *How can a filter method for the unattended and automated application be conceptualised as adaptively and dynamically as possible?*
- *How can LOS velocities be filtered to achieve maximum mapping accuracy*?
- *What are the differences to the reference measurements regarding the filtering of LiDAR data with different methods?*

In Chapter 2, an evaluation will be presented in which different common filtering approaches are applied. Staring-mode LiDAR data is compared with wind speed data of a 3D ultrasonic anemometer from the offshore meteorological mast FINO1. In this framework, a filter method is proposed that reconstruct the flow statistics by minimising the error for stationary and scanning measurements while maximising data availability with the approach of data self-similarity.

For the reconstruction of dynamic wake wind field, temporal and spatially highly resolved planar LiDAR measurements of the wake are favoured for the purpose of analysing and reproducing the flow dynamics as accurately as possible. Due to the space-time dilemma of a scanning measurement, the whole flow field cannot be recorded concurrently using the current LiDAR technology. Consequently and simplified, each measurement is a compromise between good temporal resolution and good spatial resolution, from which it becomes evident that, based on the characteristics of the processes to be mapped, an optimal combination of measurement parameters exists. Depending on the scan speed, angular resolution and the measurement trajectory (among other parameters), scan repetition times of a few seconds to several deca minutes can occur limiting the time scale of the resolvable dynamics. To compensate temporal and spatial limitations, several LiDAR systems are increasingly being used in complex measurement campaigns, most of which perform unsynchronised LiDAR measurements. To cope the requirements of data quality for reconstruction and to overcome technical limitations of scanning measurement with current LiDAR devices, Chapter 3 focuses on the following questions:

- *How can the temporal resolution of scanned measurements be retrospectively improved?*
- *How to synchronise planar scanned LiDAR measurements with another temporal quantisation?*
- *What are the characteristics of the flow statistics that were temporal up-sampled?*

In Chapter 3, a temporal up-sampling method based on a space-time conversion, later called the wind field propagation, is introduced. The up-sampling is the prerequisite for accurate representation and synchronisation of LiDAR scans with external data which in turn is the requirement for wind field reconstruction. Within a bivariant parameter study it is shown first how the scan speed influences the mapping error and secondly how the wind field propagation can reduce the statistical error due to insufficient samples.

The final reconstruction of a dynamic three-dimensional respectively a four-dimensional wake wind field is based on model assumptions in order to satisfy the information that cannot be

recorded by measurements. In Chapter 4, all the research presented afore will be brought together to answer the following questions:

- *How can wake dynamics be captured using todays LiDAR (volumetric-) measurements?*
- *How do LiDAR measurements need to be processed to be used for a dynamic 3D1C wake wind-field reconstruction?*
- *Which assumptions are required for the wake wind-field reconstruction?*
- *What are the characteristics of the reconstruction deviations?*

In Chapter 4, the wind field propagation presented in Chapter 3 is used to up-sample LiDAR data to reconstruct the wake dynamics in a finer temporal resolution than the insufficient measurement scale. Wake assumptions are defined, which are similar to those of the DWM, but exceed the DWM in terms of the number of dynamic tracking parameters. For verifiability, the evaluation of the reconstruction quality the reconstruction method is applied to a data set of a synthetic wake wind field and a numerical LiDAR simulator. Also here a parameter study is shown how the scan speed of the LiDAR affects the reconstruction result.

Chapter 5 concludes the research presented and answer the main question with reference to the individual chapters and place it in the overall context, which leads to an outlook on subsequent and further research.

2 Dynamic Data Filtering of Long-Range Doppler LiDAR Wind Speed Measurements

The content of this chapter is identical to the following journal article:

Beck, H.; Kühn, M.: Dynamic Data Filtering of Long-Range Doppler LiDAR Wind Speed Measurements. *Remote Sensing.* 2017, *9*, 561, doi: 10.3390/rs9060561.

Article

Dynamic Data Filtering of Long-Range Doppler LiDAR Wind Speed Measurements

Hauke Beck* and Martin Kühn

ForWind - University of Oldenburg, Institute of Physics, Küpkersweg 70, 26129 Oldenburg, Germany;
* Correspondence: hauke.beck@uni-oldenburg.de; Tel.: +49-441-798-5069

Received: 24 December 2016 / Revised: 26 May 2017 / Accepted: 31 May 2017 / Published: 4 June 2017

Abstract: Doppler LiDARs have become flexible and versatile remote sensing devices for wind energy applications. The possibility to measure radial wind speed components contemporaneously at multiple distances is an advantage with respect to meteorological masts. However, these measurements must be filtered due to the measurement geometry, hard targets and atmospheric conditions. To ensure a maximum data availability while producing low measurement errors, we introduce a dynamic data filter approach that conditionally decouples the dependency of data availability with increasing range. The new filter approach is based on the assumption of self-similarity, that has not been used so far for LiDAR data filtering. We tested the accuracy of the dynamic data filter approach together with other commonly used filter approaches, from research and industry applications. This has been done with data from a long-range pulsed LiDAR installed at the offshore wind farm 'alpha ventus'. There, an ultrasonic anemometer located approximately 2.8 km from the LiDAR was used as reference. The analysis of around 1.5 weeks of data shows, that the error of mean radial velocity can be minimised for wake and free stream conditions.

Keywords: data density; spatial normalisation; temporal normalisation; carrier-to-noise-ratio; line-of-sight velocity; radial velocity; threshold filter

2.1 Introduction

The basis of any empirical work, whether in the commercial or scientific context, is data that have been acquired through a measurement process. Recording measurement data needs a carefully planned measurement campaign, the selection of suitable instruments with sufficient resolution for the desired purpose and an adequate measurement period. In recent years, the scanning aerosol heterodyne Doppler LiDAR – hereafter LiDAR – has become a standard device when flexible, versatile measurements are needed that go beyond standard point measurements in the wind energy sector [49, 54, 67, 69, 98, 99]. Due to the measurement method of pulsed devices, it is possible to capture a plurality of quasi-instantaneously measurements along the laser beam. The internal processing of the raw measurement data in commercial LiDAR systems can mainly be seen as a black box for standard users. Although the general principle is known [91], manufacturers tend not to publish their exact processing algorithms. Invalid measurement data are occurring due to device-dependent reasons, measuring-dependent influences such as hard targets, measurements outside of the permissible parameter range and those appearing for unknown reasons. Once the measurements are conducted, it is no longer possible to determine whether physical or technical reasons formed the source of errors [100]. Thus, seemingly random outliers can arise despite good measuring conditions. Independently of the objective of analysis, it is necessary to filter valid from invalid measurements to produce accurate results.

While the primary measurement value is the radial speed, the LiDAR devices measure the backscattering intensity as a secondary value. Based on the manufacture, the backscattering is calculated as carrier-to-noise-ratio (CNR), respectively signal-to-noise-ratio (SNR), that can be

interpreted as a quality indicator for the calculation of the radial speed from the spectral raw data. Frehlich [47] state that the accuracy of the radial velocity determination decreases with decreasing mean CNR level. While this conclusion from Frehlich represent a stochastic statement, this does not imply that individual measurement points with low CNR values must be inaccurate or invalid.

Our experiences with LiDAR data show that the CNR baseline is a critical criterion. LiDAR measurements carried out after rain are characterised by low CNR values whereas measurements tend to have increased backscattering in foggy situations because of temporal and spatial variations of the aerosol concentration. Pal et al. [101, 102] state that the aerosol transport and distribution depend on the atmospheric boundary layer (ABL). In combination with local environmental influences, the aerosol distribution varies on timescales in the magnitude from seconds to months and thus represents an influence which justifies the need for an adaptive filtering.

The most common method for filtering LiDAR data is the fixed CNR-threshold filtering based on recommended values [103, 104, 105]. Due to the simplicity and the establishment of common filtering methods, there have been very few studies dealing with the effects of LiDAR filtering to date. The first critical examination of the influence of CNR-filtering on wind speed distributions was presented by Gryning et al. [106]. From Gryning et al. [106] and Pal et al. [101, 102], we interpret that LiDAR data filtering based on a rigid CNR-threshold can lead to inaccurate velocity determination. For quality assurance of the measurement data, a variety of filters may be combined to obtain an outlier free data set [72, 73]. Although many of the filters that Newman et al. [72] and Wang et al. [73] used, are designed, not explicitly for stationary measurements, but are applied point-wise, the question arises how smaller amount of data (for a point in space) influences the filtering in case of non-stationarity. While combinations of filters seem to be a promising approach, their application can mainly be found in scientific related work. Meyer Forsting et al. [107] investigated the adaption of a despiking method from stationary to scanning situations and thus took an important step towards the filtering of scanned LiDAR measurements. Nevertheless, those methods were not specifically designed for an application in LiDAR remote sensing and represent more or less a best practice for general time series processing. Despite these occasional studies, LiDAR data filtering and addressing their impact remain a vacant topic.

Each filter discussed in the following of this paper is based on an assumption to distinguish the validity. Namely, the CNR-threshold filter is based on the accuracy of the radial velocity with respect to the CNR, the interquartile-range filter is based on the data distribution and the standard deviation filters on the assumption of normal distribution. All these assumptions, however, do not rely on factors which affect specifically LiDAR measurements. Atmospheric conditions, but also location-specific incidents such as hard targets, terrain topography or measurement properties such as the trajectory, magnitude of measurement velocity, pulse length and accumulation time influence the data distribution and thereby the filter approach. In consequence, it seems logical to pre-filter measurement data on the basis of purpose. For example, velocity azimuth display (VAD) or Doppler beam swinging (DBS) measurements, which are designed for the calculation of wind speed and wind direction distributions easily exceed the mixing layer height and measure above the ABL. With the knowledge of a significant CNR drop at a certain height, an effective filter approach needs to behave different than a filter for stationary measurement over a constant height.

With the increase of LiDAR devices for research applications and in the future for a stronger commercial use, the amount of data will exceed the capacities of manual verification of processing/filtering results and lead to the need of robust, accurate and highly adaptable routines.

Because the measurement conditions differ with each device, location and time, it seems sensible and necessary to filter LiDAR data in a dynamically adaptive way to ensure high data availability and accuracy of the data set. The simultaneous use of different filter combinations is limited by the available computational power; thus, universal filters are favoured.

While within combined filter approaches methods are applied successively we believe that all measurements outputs may and should be used in a multi-variate manner to satisfy their specific behaviour to determine the measurement data validity. One assumption, we find that adapt to atmospheric and external influences is the self-similarity of the measurement data. To the best of our knowledge, this approach has not been used so far to filter LiDAR data, wherefore we explain this assumption, the advantages and disadvantages in the following of this work.

We introduce a highly self-adapting methodology that demonstrate how line-of-sight velocity measurements of pulsed long-range LiDAR devices can be filtered dynamically to maximise accuracy and data availability of mean radial velocities. The filter approach is designed for determining the mean velocity, and may not be appropriate for turbulence measurement applications. Further, we show that it is possible to decouple the commonly associated data availability of valid measurement data with increasing distances on the assumption of self-similarity using a temporal and spatial normalisation. A validation of the new filter approach based on temporal high resolved, low elevated Leosphere Windcube 200s data in the range of 2864 m has been carried out against ultrasonic anemometer data captured at an offshore meteorological mast in comparison to commonly established and research filters.

2.2 Methodology

In the handling with LiDAR data, we have difficulties to use filters that consider prevailing measurement influences. While the assumption of the LiDAR data behaviour included in every LiDAR data filter may appear to be uncritical for some applications, it seems paradox to filter this data for scientific studies investigating this behaviour. In order to filter LiDAR data in an adaptive dynamic way, we developed two methodologies based on the same approach to identify valid and invalid measurement points in an adaptive, dynamic way. Below, these filters are described along other filters found in the literature.

2.2.1 Threshold Filter

The CNR and SNR, α, are quality indicators of the measurement and extend the data examination from only radial wind speed to two dimensions. Looking at individual measurement points in the radial-speed-carrier-to-noise-ratio diagram ($u_r - \alpha -$ diagram) in Figure 2.1, a correlation of CNR values and validity can be found. It can be seen that data points below the red line indicating a –24 dB level have high deviations in the range of –32 m/s to 32 m/s wind speed, thus, we assume that the points are invalid. The high scattering in this region may be caused by the LiDAR internal peak-fitting-algorithm of the frequency spectrum when there is no significant peak within the background noise. This results in a multimodal data distribution scattered around $u_r =$ 0 m/s forming a comb shape. From this comb-shaped distribution the assumption arises that the peak-fitting-algorithm is not a homogenous process but is more attracted by certain frequencies, leading to a detectable accumulation at corresponding wind speeds.

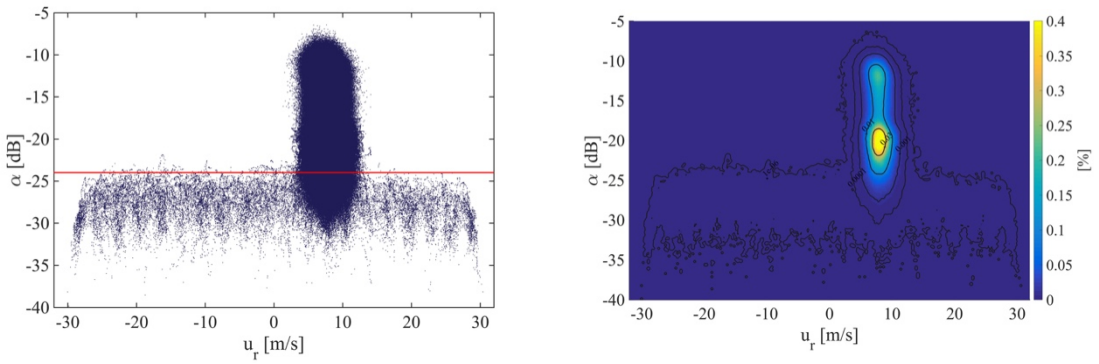

(**a**) (**b**)

Figure 2.1 Example of a staring mode LiDAR measurement in the $u_r - \alpha$ diagram for a duration of 30 min in distances in the range of 361 m to 2911 m. **(a)** Blue points represent single measurements points, the red horizontal line indicates the lower CNR-threshold of −24 dB. **(b)** Visualisation of data density of measurement point distribution. Colours indicate different values of frequency distribution.

While we assume that high data-density regions (HDDR) contain valid measurement points by the assumption of self-similarity and comparing means with the ultrasonic anemometer velocity measurements, here indicated by yellow and green regions in Figure 2.1b, we think that there is no indication based on the measurement distribution that data belonging to HDDR below a lower CNR limit, here $\alpha_{le} = -24$ dB, is invalid (Figure 2.1a).

Main challenge of LiDAR data filters is the distinction of valid data from overlaid invalid scattered data. Outliers could have a real physical meaning, however, they may fall far away from the HDDR.

The threshold filter is commonly applied on CNR values of a data set. Data points beyond a certain range, will be filtered out. The low end edge, α_{le}, indicates the level of signal gain where it is assumed that no information can be extracted anymore, while the upper edge, α_{ue}, filters out hard targets with high backscattering.

$$\alpha_{\mathrm{le}} \leq \alpha \leq \alpha_{\mathrm{ue}}, \qquad \text{Eq. 2.1}$$

where α represents CNR values of a valid measurement points. Depending on the manufacturer, the recommended α_{le} and α_{ue} vary.

2.2.2 Static Standard Deviation Filter

One way of filtering wind speed data, when there is no secondary information such as signal quality or process quality indication, is the application of a standard deviation filter. Looking at the radial speed, all data with a higher scattering around the average radial speed, μ_r, than defined by a standard deviation depending tolerance will be filtered out.

$$\mu_{\mathrm{r}} - \mathrm{n} \cdot \sigma_{\mathrm{r}} \leq u_{\mathrm{r}} \leq \mathrm{n} \cdot \sigma_{\mathrm{r}} + \mu_{\mathrm{r}}, \qquad \text{Eq. 2.2}$$

where u_r is the radial speed of a measurement point and n is a multiplier of the standard deviation σ_r. In a data set, outliers can be eliminated with the right choice of n. With the unsuspectingness of the measurement quality and existence of outliers, the n-sigma interval may lead to a detectable data loss. The influence of different averaging times of μ_r is discussed in Section 2.4.

2.2.3 Iterative Standard Deviation Filter

The static filter standard deviation filter has low computational requirements; thus, it may be applied with multiple parametrisation at the same time. In contrast, the iterative standard deviation approach from Højstrup [108], adapted by Vickers and Mahrt [100] has higher computational costs due to a two looped application.

The standard deviation within a point-wise moving temporal interval is calculated. A measurement point is considered to be an outlier if the value exceeds the range of more than 3.5 standard deviations within the interval. The point is replaced by a linear interpolation. Outliers will not be replenished if four or more consecutive values are detected. This procedure is repeated until no outliers can be found. With each iteration the standard deviation factor will be increased by 0.1.

Appling both types of standard deviation filters imply the assumption of a Gaussian distributed filtering signal.

2.2.4 Interquartile-Range Filter

The interquartile filter or box plot filter descripted by Hoaglin et al. [109] is not based on a specific data distribution. For filtering, the interquartile-range (IQR) is calculated and will be subtracted to the first and added to the third quartiles. It is a threshold filter based on statistical dispersion. We used the following common parametrisation for valid measurement points u_r:

$$u_{r,25} - 1.5IQR \leq u_r \leq 1.5IQR + u_{r,75}, \qquad \text{Eq. 2.3}$$

where $u_{r,25}$ is the first quartile, $u_{r,75}$ is the third quartile and IQR is the interquartile range.

2.2.5 Combined Filter - Newman

A combined filter approach of LiDAR data can be found in the work of Newman et al. [72]. They applied a consecutive CNR-threshold filter and an iterative standard deviation filter described in Section 2.2.4 as quality control.

2.2.6 Combined Filter - Wang

As a second combined filter approach, we would like to mention the quality control of radial speed from Wang et al. [73]. In the original research, a CNR-threshold filter was applied to the data set before filtering with the interquartile-range filter from Section 2.2.5. As a third control body, all absolute radial wind speed differences greater than two IQR of the deviations are removed:

$$|\Delta u_r| > 2IQR_{\Delta u_r}. \qquad \text{Eq. 2.4}$$

2.2.7 Dynamic Data Filtering

The main assumption of the newly proposed filter approach is based on the self-similarity of a measurement at a point in space. Assuming that the technical integrity of the measuring system is given and the measurement parameters are chosen well, we consider that repetitive measurements—stared or scanned—will not change their behaviour in an unpredictable way in a defined time interval.

In an idealised theoretical experiment without atmospheric and error influence a single point would appear in the $u_r - \alpha$ diagram for a steady flow. Taking into account the distance dependency of α adds vertical scattering, while temporal fluctuations of u_r causes horizontal scattering. In reality individual measurements of u_r and α fluctuate around mean values, which depend on the chosen time interval. Valid measurement points are closer to these mean values, while outliers are characterised by a greater distance. This changes the density of the $u_r - \alpha$ data distribution.

In general, it can be said that well parameterised measurements form valid HDDR, which may be overlaid by invalid data. In order to distinguish between those, the dynamic filtering approach is based on two subsequent process steps, temporal & spatial normalisation and data-density calculation. Two different implementations of the density calculation are presented and described in the following sub-chapters.

2.2.7.1 Normalisation

The intention of normalisation is to bring the measurement data to a relative frame of reference to reduce the absolute differences due to time and space. The effect is a compress the data-density distribution. Considering the spatial and temporal dependency of the measurement values α and u_r we apply a corresponding normalisation. The definition of the normalisation time interval Δt can be seen in Figure 2.2.

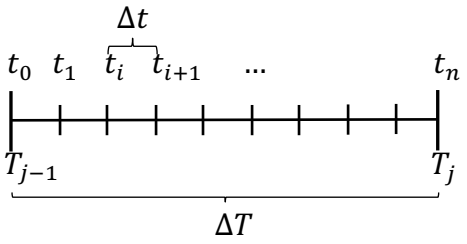

Figure 2.2 Visualisation of segmentation of the overall filtering time interval ΔT in normalisation intervals Δt.

The overall filtering time interval is defined as $\Delta T = T_j - T_{j-1}$, whereas the normalisations interval is set as $\Delta t = t_i - t_{i-1}$. Thus, $T_{j-1} = t_0$, $T_j = t_n$ and $t_i > t_{i-1}$. For each measurement α_k and u_{r_k}, $k \in \{1, \dots, n_d^t\}$, within one time interval t and distance d, we define the normalised values $\alpha_k{}'$ and u'_{r_k}:

$$\alpha_k{}' = \alpha_k - \overline{\alpha_d^t}, \qquad \text{Eq. 2.5}$$

and

$$u'_{r_k} = u_{r_k} - \overline{u_r{}_d^t}. \qquad \text{Eq. 2.6}$$

The calculation of $\overline{\alpha_d^t}$ and $\overline{u_r{}_d^t}$ is based on a one-dimensional Gaussian kernel, which may be expressed as

$$\overline{\alpha_d^t} = \underset{\alpha}{\operatorname{argmax}} \left(\frac{1}{n_d^t} \sum_{k=1}^{n_d^t} \frac{1}{\sqrt{2\pi(\sigma_\alpha)^2}} e^{-\frac{(\alpha-\alpha_k)^2}{2(\sigma_\alpha)^2}} \right), \qquad \text{Eq. 2.7}$$

and

$$\overline{u_r}_d^t = \underset{u_r}{\operatorname{argmax}} \left(\frac{1}{n_d^t} \sum_{k=1}^{n_d^t} \frac{1}{\sqrt{2\pi(\sigma_{u_r})^2}} e^{-\frac{(u_r - u_{r_k})^2}{2(\sigma_{u_r})^2}} \right), \qquad \text{Eq. 2.8}$$

where n_d^t is the amount of measurements within the time interval from t_{i-1} to t_i in the distance d. The calculation of the bandwidth σ_α and σ_{u_r} follows the work of Botev [110]. Thus, each measurement value has been normalised individually based on their distance d and time interval t.

In the following, we consider individually normalised values α'_k and u'_{r_k} in the entire time period T with $k \in \{1,..,n^T\}$, where n^T is the amount of measurements point in the time interval ΔT.

The effect of normalisation can be seen by comparing Figure 2.3 and Figure 2.4. Both are based on the same dataset extracted from the measurement campaign descripted in Section 2.3.1 and represent an example of ΔT = 30 min. Changes of wind speed within this time interval leads to a change of radial velocities, resulting in three HDDR located at different radial speed values (Figure 2.3). The distance dependency of the CNR causes an additional expansion of the data distribution on the α-axis.

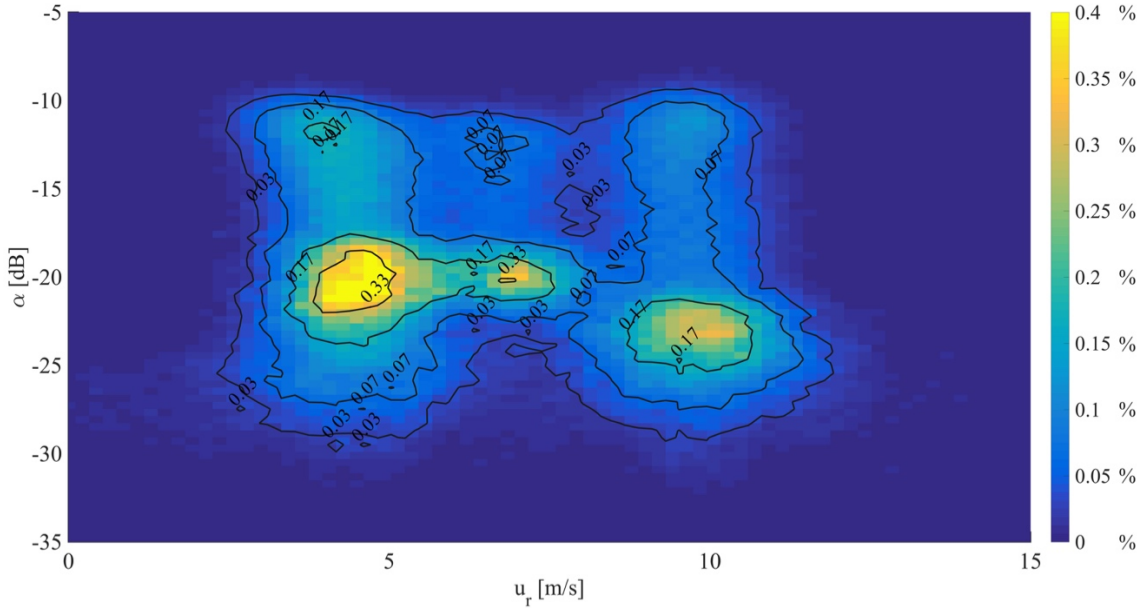

Figure 2.3 Example of data-density distribution of a 30-min time interval of LiDAR staring mode measurements in the original $u_r - \alpha$ frames of reference. Iso-lines show levels of probability of occurrence of the measurement with in a bin of 0.32 m/s width and 0.2 dB height.

Applying the normalisation means switching the reference frame from $u_r - \alpha$ to $u_r' - \alpha'$. This compensates spatial and temporal inhomogeneities and results in a denser data distribution where outliers can be identified with less effort.

The influence of normalisation for different Δt to the data density can be taken from Figure 2.4. In general, it can be said that the data-density distribution becomes softer and wider with increasing Δt. For a better description of this behaviour, we fitted the resulting data density distributions with a bi-variate Gaussian function. We do not assume that the data density behaves in this way but we used the simplicity and reproducibility to characterise the change of parameterisation. The residual can be interpreted as the fitting quality. From Figure 2.5, it can be

seen that the width of the bi-variate Gaussian function increases for $u_r{}'$ and α' with increasing Δt. The maximum value of the data density is subject to exponential decay.

The normalisation is independent of data-density calculation methods which will be presented in the following. The use of the data-density approach may as well be applied without prior normalisation.

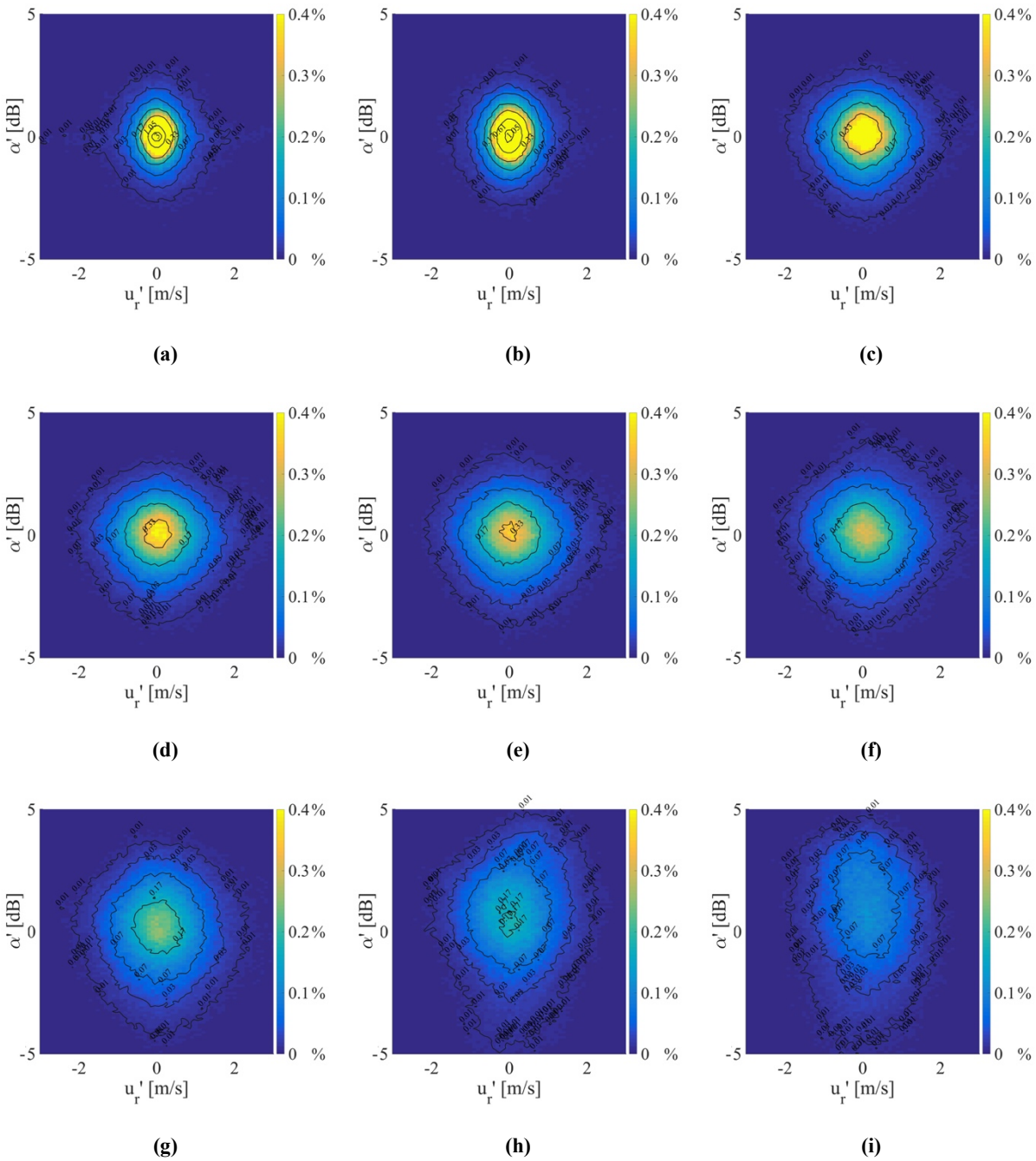

Figure 2.4 Visualisation of different normalisation times Δt of the LiDAR data distribution in the normalised frame of reference (**a**) Δt = 0.5 s, (**b**) Δt = 1 s, (**c**) Δt = 5 s, (**d**) Δt = 15 s, (**e**) Δt = 30 s, (**f**) Δt = 60 s, (**g**) Δt = 120 s, (**h**) Δt = 300 s and (**i**) Δt = 600 s.

2.2.7.2 Histogram-Based Data-Density

The first method to calculate the data-density is based on binning the normalised data in a 2D histogram. A suitable bin width for $u_r{}'$ and α' is given by Scott [111] as

$$h_{n_{u_r}} = \frac{3.49 \cdot \sigma_{u_r'}^{T}}{\sqrt[3]{n^T}}, \qquad \text{Eq. 2.9}$$

and

$$h_{n_\alpha} = \frac{3.49 \cdot \sigma_{\alpha'}{}^{T}}{\sqrt[3]{n^T}}, \qquad \text{Eq. 2.10}$$

where $\sigma_{u_r'}^{T}$ is the standard deviation of $u_r'{}^{T}$, respectively $\sigma_{\alpha'}^{T}$ is the standard deviation of α'^{T}, and n^T is the amount of data points for time interval T.

Scott assumes that the corresponding variable has to be normally distributed to use this parametrisation. Although it has not been proven conclusively that the wind speed is normally distributed, Morales et al. [112] have shown a great consistency of this theory for 10-min time intervals.

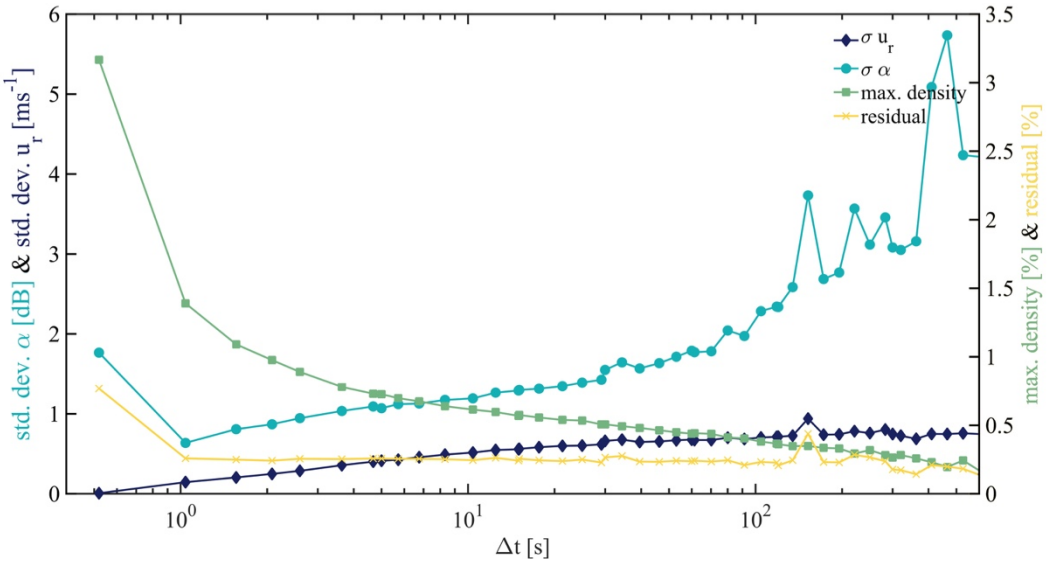

Figure 2.5 Behaviour of parametrisation of fitted bi-variate Gaussian distribution of data density in relation to the different normalisation time intervals Δt. The α-axis fitted standard deviation is shown in turquoise, u_r-axis fitted standard deviation in dark blue, the maximum probability of occurrence in green and the residual of the original and the fitted data distribution.

Instead of normalising the amount of data within a bin with the total number of data points, we normalise with the maximum bin count. Thereby the data distribution dynamically refers to the measurement and requires no absolute values.

The determination of validity is based on a correlation of data in the normalised reference frame $u_r{}' - \alpha'$. Calculating the contours for different densities, iso-lines form almost concentric circular shapes (Figure 2.4). Measurement points within the final contour will be marked as valid. To find the final contour that represents the separation line of valid and invalid data, we define an upper and lower threshold:

The lower threshold value represents the lower percentage limit from which iso-lines will be calculated.

The upper threshold can be seen as the reference shape that is based on the contour shape of the corresponding percentage density value.

By empirical testing, we found a correlation to determine the separation line. The easiest reproducible condition with the least computationally effort is presented in the following:

If the centre of a contour shape within the $u_r'-\alpha'$ reference frame lies within the contour of the referenced shape corresponding to the upper threshold, all data points within this shape are marked as valid.

2.2.7.3 2D-Gaussian Kernel Data-Density

The second method to determine the data density is based on the calculation of a two-dimensional kernel. We assume that u_r and α are subjected to random error processes; thus, their variability can be represented with a bi-variate Gaussian distribution [113], even when the overall behaviour may be non-Gaussian. The validity $v(u_r, \alpha)$ for each measurement point with α_k and u_{r_k} in the time interval T, with $k \in \{1, \dots, n^T\}$, can then be assigned by the normalised data-density kernel in the $u_r'-\alpha'$ reference system:

$$v^T(u_r, \alpha) = \frac{K^T(u_r, \alpha)}{\max\left(K^T(u_r, \alpha)\right)}, \qquad \text{Eq. 2.11}$$

with

$$K^T(u_r, \alpha) = \frac{1}{n^T}\sum_{k=1}^{n^T} \frac{1}{\sqrt{2\pi\left(\sigma_{u_r,\alpha}\right)^2}} e^{-\frac{\left(u_r'_k\right)^2+(\alpha'_k)^2}{2\left(\sigma_{u_r,\alpha}\right)^2}}. \qquad \text{Eq. 2.12}$$

As the one-dimensional case from Section 2.2.7.1, the selection of $\sigma_{u_r,\alpha}$ is based on a Botev-estimator [110].

The distinction between valid and invalid data is now made by the calculation of the validity for each measurement point using Eq. 2.11. The following classification is based on a threshold, v_{th}, which refers to the validity. Measurement point with a validity:

$$v(u_r, \alpha) \geq v_{th}, \qquad \text{Eq. 2.13}$$

may be seen as valid. The Influence of v_{th} to the resulting error is shown in the Appendix 2.A.

2.3 Measurement Setups

The data for this study are drawn from two LiDAR measurement campaigns with different research objectives - an offshore campaign in the research offshore wind farm “alpha ventus” from July 2013 till March 2014 and a nacelle-based onshore campaign in the first half of 2015.

2.3.1 Offshore Ground-Based Comparative Measurement Campaign

In the framework of the German research project “GW Wakes”, three scanning long-range Doppler LiDAR systems of type Leosphere Windcube WLS-200S [54] were operated in the offshore wind farm “alpha ventus” in the German North Sea. The wind farm comprises six 5 MW wind turbines Senvion 5M with rotor diameter of D_S = 126 m hub heights of h_S = 92 m that are located in the northerly two rows and six 5 MW wind turbines Adwen AD5-116, formerly called M5000-116, with rotor diameters of D_A = 116 m and hub heights of h_A = 90 m in the two

southerly rows (Figure 2.6). The LiDAR used for the measurements was operated on the substation of the wind farm in the south east corner. “alpha ventus” is located close to the research platform FINO1 that is equipped with a meteorological mast [114]. In the following, all directions in the context of the offshore measurement campaign refer to the meteorological reference system, if not explicitly mentioned.

2.3.1.1 LiDAR Measurements

The used data was captured from 21.12.2013 15:35h (UTC) till 19.01.2014 7:55h (UTC). During this time period, the LiDAR was operated in a so called staring-mode with a fixed azimuth angle φ and a low elevation angle of θ = 0.2°, aiming at the ultrasonic anemometer at 41.5 m height at FINO1. The measurement frequency was set to f_{stare} = 2 Hz with a pulse repetition frequency of 20 kHz, while capturing 82 equidistant range gates from 361 m to 2811 m with a range step of 30 m and 100 equidistant range gates from 2811 m to 2911 m with a 1 m range step. The pulse length was set to 200 ns or 59.96 m.

Within the measurement duration of 28 days 16 h and 20 min, we were forced to interrupt the measurements for a total of 18 days 8 h and 30 min. The resulting comparable time intervals are comprised of 10 days 7 h and 50 min.

The positioning of the measurement near the anemometer on the FINO1 platform was ensured by an iterative hard-target method. First, we tracked the meteorological mast via horizontal PPI measurements (Plan-Position-Indicator scan) followed by vertical RHI measurements (Range-Height-Indicator scan) to identify the boom with the anemometer. We adjusted the final positioning of the measurement volume with the accuracy of the LiDAR system of 0.1° in azimuth and elevation. When the wind induced movements of the mast-boom-system are neglected, the maximum possible deviation of height of the anemometer and the centre of the range gate can be calculated as:

$$\Delta h_{max} = \pm \sin(0.1°) \cdot 2864\ \mathrm{m} = \pm\ 5.00\ \mathrm{m}. \qquad \text{Eq. 2.14}$$

The inclined measurement of 0.2° in combination with a pulse width of 59.96 m leaded to a negligible height difference within a range gate of 0.21 m. We verified the positioning of the LiDAR device by long term GPS measurements in combination with the geometrical dimensions of the substation. This resulted into an azimuthal orientation referred to the ultrasonic anemometer of φ = 306.47°.

In this data set, wind directions have been measured at FINO1 within a range of 110° and 285°. Due to the fixed measuring geometry of the staring LiDAR, this could only measure the in-beam wind speed component. The result is a cosine behaviour between the wind speed in the wind direction frame of reference, u_{mfr}, and the projected wind speed, u_{lfr} (Eq. 2.17). For an incoming wind direction of 216.47°, the LiDAR measured perpendicular to the wind direction. Thus, the lateral wind speed component tends to become zero in average, which is why the turbulence intensity converges to infinity (Figure 2.9).

2.3.1.2 Ultrasonic Anemometer Measurements

The 3D ultrasonic anemometer used for the comparison with the LiDAR data is a Gill R3-50 mounted at the meteorological mast FINO1 at the height of h = 41.5 m on a 6.5 m long boom orientated at 308°. Vertical wind speed, horizontal wind speed, wind direction and air temperature data have been recorded with a sampling frequency of f_{USA} = 20 Hz. The original wind direction

measurements have been corrected on the basis of the approach of Schmidt, et al. [115] by using staring LiDAR measurement to determine misalignments. The correction of Schmidt, et al., includes the previous correction of the mast influence performed by Westerhellweg, et al. [116]. Figure 2.7 shows the frequency of the wind speed and wind direction distribution within the time period. The temporal change of the wind speed and wind direction can be seen in Figure 2.8. Horizontal lines within Figure 2.8 indicate a possible wake shading of the named turbines for that particular wind direction. Due to simplicity, these wind directions have been calculated on the basis of geometric correlations, and we neglect wake expansion and meandering effects.

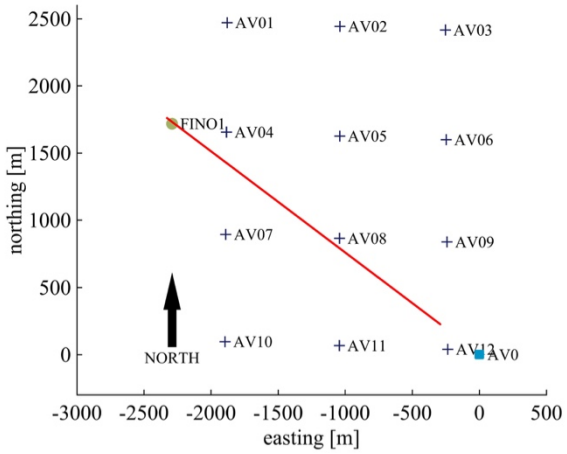

Figure 2.6 Layout of the wind farm “alpha ventus” with measurement geometry of staring mode LiDAR with an azimuthal orientation of 306.47° and an elevation of 0.6° (red). Crosses represent wind turbines, the circle the platform FINO1 and the square the substation AV0. The measurement positions are indicated by the red line.

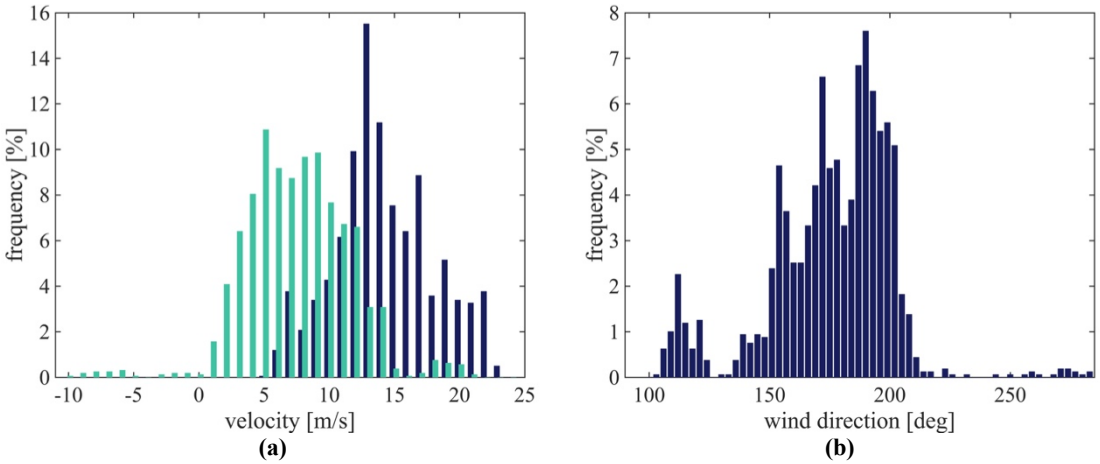

Figure 2.7 Histogram of 10 min averaged ultrasonic anemometer inflow conditions from 21.12.2013 15:35h (UTC) till 19.01.2014 7:55h (UTC) (a) horizontal wind speed in the meteorological reference frame is marked in dark blue, whereas the LiDAR laser beam projected wind speed u_{lrf} (Eq. 2.17) is shown in green. The bin width is 1 m/s, (b) wind direction with a bin width of 3°.

2.3.1.3 Onshore Nacelle-Based Wake Measurements

The second data set was acquired within the German project “CompactWind”, in which two of the previously described LiDAR devices have been installed on the nacelle of an eno114 3.5 MW wind turbine with a rotor diameter D = 114.9 m and a hub height of h = 92 m. The onshore wind farm consists of two wind turbines from the same type and is located near Rostock in the village Brusow. The surrounding terrain is slightly hilly with a compact forest to the east.

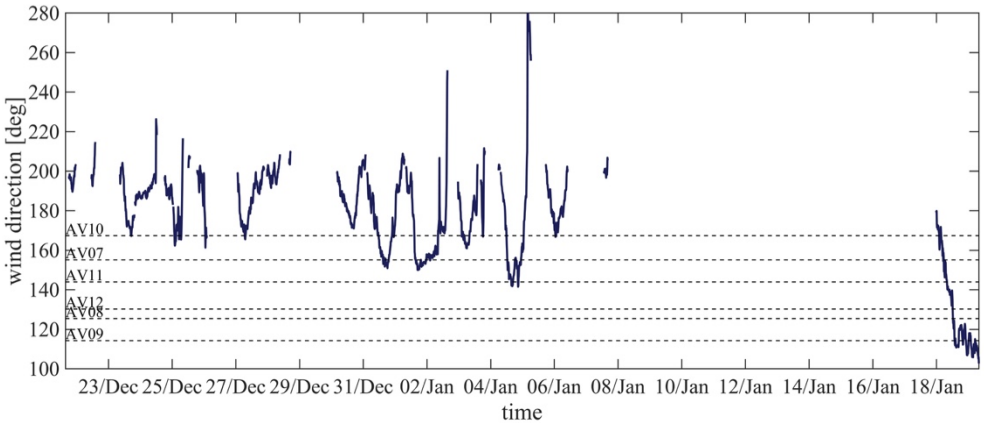

Figure 2.8 Time series of the 10 min averaged wind direction measured by the ultrasonic anemometer from 21.12.2013 15:35h (UTC) till 19.01.2014 7:55h (UTC). Gaps in the plot demonstrate unavailability of LiDAR data. Horizontal lines indicate the wind direction of possible wake shading of the anemometer on FINO1 based on geometrical correlations.

The measurements were performed from 14.05.2015 02:30h (UTC) till 14.05.2015 06:00h (UTC). Here, we show only one LiDAR in measuring horizontal PPI scans with 0° at nearly hub height with a total azimuthal opening angle of 40° centred in downstream direction. Each of the 571 scans took 20 s, resulting in a repetition time of 22 s, including an initialisation time. We parameterised the LiDAR with a pulse length of 200 ns respectively 59.96 m and an accumulation time of 200 ms with a pulse repetition frequency of 20 kHz. In this time period in which the turbine was operating a significant wake was measurable.

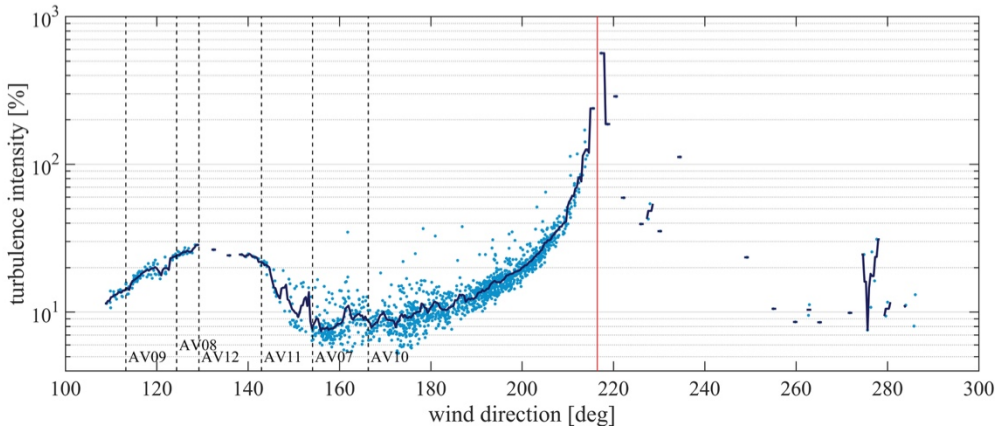

Figure 2.9 Visualisation of the line-of-sight velocity turbulence intensity in dependency of the wind direction measured by the ultrasonic anemometer from 21.12.2013 15:35h (UTC) till 19.01.2014 7:55h (UTC). Gaps in the plot visualise unavailability of anemometer data. Individual 10-min mean values are shown in light blue whereas the binned averaged is marked in dark blue. Black vertical dashed lines indicate the wind direction of possible wake shading of the anemometer on FINO1 based on geometrical correlations. The red line shows the perpendicular wind direction to the azimuthal orientation of the laser beam.

Within the framework of “CompactWind”, we were able to alternate the nacelle mounted LiDAR from the described Leosphere device with a Stream Line XR LiDAR by Halo Photonics. The here used Stream Line XR dataset is shown as an example of general applicability of the dynamic data filtering approach.

The data was captured from 31.10.2016 00:00h (UTC) till 31.10.2016 00:30h (UTC). In that time period, the LiDAR was operating in PPI mode using the above mentioned opening angle,

accumulation time and scan speed. The measurement was parameterised with a pulse length of 100 ns or 29.98 m and a pulse repetition frequency of 10 kHz.

2.4 Results

For the validation and comparison of the new proposed dynamic filtering approach in Section 2.2.7, we applied all described filters on the data of the two measurement campaigns from Section 2.3. The influence of filtering on the data availability and the velocity error regarding the ultrasonic anemometer are shown in the following. Moreover, the behaviour of the velocity error will be discussed.

2.4.1 Evaluation of Filtering Based on Staring Measurements

For the error calculation of ultrasonic anemometer data and the LiDAR data, the initial question arises how different measurement concepts can be mutually compared. The metric used to validate the new and other filters is based on average velocities. We present also results for the velocity standard deviation for sake of completeness. However, we consider that the data available is not adequate for drawing conclusions in our ability to derive turbulence properties. Although both devices measure within a certain volume - in an idealised case, the same volume - this differ in spatial dimensions. While we estimate the ultrasonic measurement volume from technical drawings as a cylinder with $V_{USA} \approx \pi \cdot (0.24\ \mathrm{m})^2 \cdot 0.48\ \mathrm{m}$, the corresponding equivalent for the LiDAR laser beam in the here used configuration is approximately $V_L \approx \pi \cdot (0.1\ \mathrm{m})^2 \cdot 60\ \mathrm{m}$. By this, the LiDAR measurements use around 22 times the ultrasonic anemometer volume. If we consider that the individual ultrasonic transmitter and receiver heads measures on the surface shell of this cylinder, the ratio of V_L/V_{USA} is in the magnitude from 10 to 100. The effect of spatial averaging of LiDAR measurements on the variance of the line-of-sight measurements and the associated challenge of deriving turbulent properties, in a substantial scientific manner, from LiDAR measurements is discussed in a plurality of publications. First, LiDARs filter out high frequencies depending on the effective sampled volume. This distorts the velocity variance. Moreover, Sathe and Mann [48] show that atmospheric conditions play an important role affecting the ability to measure turbulence. Sathe and Mann [48] published an extensive review of turbulence measurements since the beginning of LiDAR based remote sensing in which they show that the variance is very dependent on atmospheric conditions. We conclude from the work of Frehlich [47] and Sathe and Mann [48] that an adequately determination of the wind speed variance is possible, with a comprehensive approach including raw LiDAR data. Such treatment was out of the scope of this work, wherefore we focused in the following inter-comparison of the LiDAR filter on the average wind speed.

To minimise the different volume averaging effects and to comply with other comparisons of LiDAR measurements and met mast anemometers [117, 118, 119, 120, 121], we applied filtering in clustered temporal segments of ΔT = 10 min. We have deliberately refrained a data availability pre-filtering for the calculation of the 10-min average velocity and velocity standard deviation. This is intended to create a greater transparency to the overall filter behaviour.

We evaluated the effect of variable averaging times for all filters with a smaller data set from the already presented campaign. The impact on the total error in combination with the normalisation time Δt for the dynamic data filters can be seen in the Appendix 2.B. We conclude from Figure 2.18, Figure 2.19 and Figure 2.20 that the results of the dynamic data filters vary

depending on the used parametrisation. The parameters should vary with the purpose of data analysis and the desired error calculation, as can be seen in Figure 2.21. For a better readability, we opted for one parameterisation each. The selection of the validity value ν regarding the error behaviour in Appendix 2.A was chosen as a compromise between the average error and the root-mean-square error (RMSE) of each, velocity and velocity standard deviation. The histogram-based dynamic filter has been used with a lower filter threshold of 0.02 % and an upper filter threshold of 0.29 %, through the Gaussian kernel based implementation was set to a validity level of 16.94 %.

The standard deviation filter was used in a two-sigma configuration and the CNR-threshold filter, as well used in the combined filter approaches, in a parametrisation of α_{le} = -24 dB and α_{ue} = -8 dB. To the best of our knowledge, we also porting the filter approach by Wang et al. [73] for the first time to staring mode and horizontally scanned LiDAR data. So far this filter approach has been applied only for VAD measurements. Further, we tested the proposed quality control from Newman et al., with Leosphere Windcube 200s data for distances beyond those in the original publication [72]. In total 4325 10-min time intervals have been processed for the following results.

2.4.1.1 Data Availability

We define the here titled data availability as the ratio of the amount of data for one point in space of the filtered to the unfiltered LiDAR data within a time interval:

$$\lambda = \frac{n_{u_{r\,filtered}}}{n_{u_{r\,unfiltered}}}. \qquad \text{Eq. 2.15}$$

Only 10-min time intervals were considered that amounts the theoretically number of measurement points. A data availability of 100 % within a time interval implies that all measurement points are marked as valid. To calculate the data availability, a spatial based comparison (Figure 2.10) for all ranges and the corresponding closest volume to the ultrasonic anemometer has been made and was summarised in Table 2.1. For the data availability we calculated in non-overlapping time intervals of 10-min.

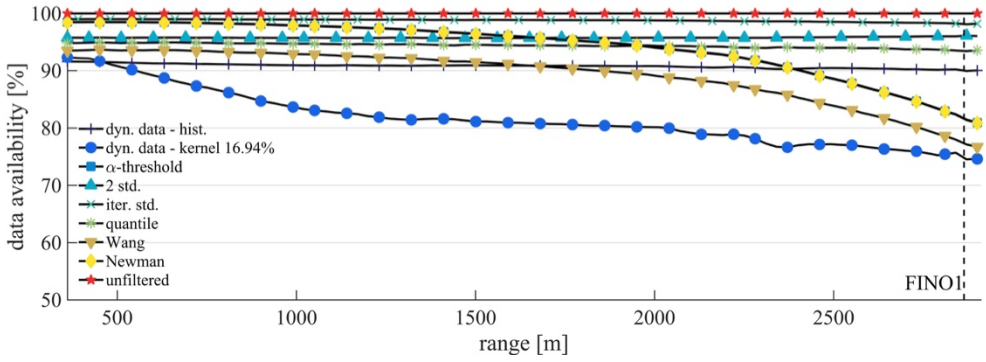

Figure 2.10 Data availability of staring mode measurements for different filter methods. Time dependent behaviour for range at 2864 m and averaged data availability over all ranges. The dashed line marks the distance of the anemometer at FINO1.

While all filters show a consistent mean result above 70 % data availability, the behaviour with respect to the range is dependent on the type of filter. All filters using the CNR-threshold approach show the same decay in availability related to the distance dependency of α. With the

decrease of the CNR over the distance, temporal fluctuations of α are partially filtered out if they exceed the CNR-threshold. By this, the data availability decreases continuously. We assume that the here shown behaviour of all CNR-threshold containing filters is similar to the theoretical and empirically stated data availability decay with increasing distance described by Boquet [122].

It appears that the combined filter by Newman et al. [72] does not show any visible deviation from the CNR-threshold filter even when they applied an addition iterative standard deviation filter that, when applied alone, provides an availability of 98.5 %. It seems that as well the filter approach by Wang et al. [73] leads to a higher data availability compared to a sequential calculation from the individual availabilities. The output of the two-sigma standard deviation filter exhibits an overall availability of over 95 % for the entire distance and increases slightly with more distant range gates. Because it is based on the deviation around the average of wind speed, this behaviour can be explained with the geometric correlation of the measurement setup. From a distance of approximately 2100 m, the laser beam measured outside the wind farm where the flow was not affected by wind turbine wakes. In contrast, the data availability of the iterative standard deviation filter decreases by 1 % over distance. It is shown that the interquartile-range filter produces a smaller availability of 94 % than applied in theory to normal distributions of 99.3 %. This may be an indication that the data distribution within the 10-min intervals does not exactly follow a normal distribution.

If we neglect all filters that do not take into account the distance dependency of α, we can compare all CNR-based filter with the dynamic data filters. It can be seen that the histogram-based filter with nearly constantly 90 % data availability. The kernel-based dynamic data filter shows a drop of data availability in closer distances followed by a constant slight decrease over the distance. From this behaviour it cannot be seen that the data availability of the dynamic data filters follows the decay stated by Boquet [122]. We assume that the main reason for this is based on the temporal and spatial normalisation of the LiDAR data. By normalising α with the most probable value $\overline{\alpha_d^t}$ within the normalisation interval, measurement points close to $\overline{\alpha_d^t}$, which would exceed the CNR-threshold are marked as valid and contribute to high data availability.

Figure 2.11 shows the error distribution of the velocity and the velocity standard deviation in dependency of the data availability on the basis of 10-min means. A high correlation of the general appearance of Figure 2.11a,b suggests a causal connection of the velocity and the velocity standard deviation error. While both standard deviation filters and the interquartile range filter mainly show error values above 80 % data availability the data distributions of the dynamic data filter and CNR-threshold based filters are widely scattered. We see a repeating pattern of data point clusters in Figure 2.11a,b that appears to be individually scaled for each of the dynamic and combined filters.

Although both dynamic data filters use the same normalised dataset, the observed differences in data availability appear for unknown reason. In this test case, the full potential of conservation of data availability by the kernel-based dynamic data filter cannot be seen. We assume that based on the behaviour shown (Figure 2.10), the data availability of the CNR-threshold based filters will drop significantly faster with increasing distances than of the dynamic data filter.

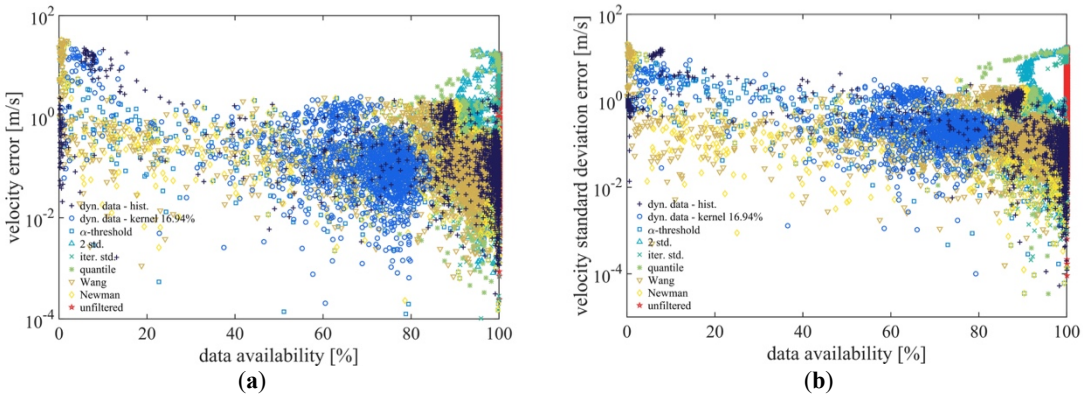

Figure 2.11 Absolute error of staring mode measurements in dependency of data availability. Markers represent 10 min values of **(a)** the velocity error and **(b)** the velocity standard deviation.

2.4.1.2 Comparison of LiDAR and Anemometer Velocity Measurements

In the following sub-chapter, we quantify the accuracy of all filtering methods. For this we assess the discrepancy of estimated velocities taking into account filtered, unfiltered data and the reference data of the ultrasonic anemometers. We distinguish between the average error, which is defined as the Arithmetic mean, and the RMSE. As we mentioned previously the assumption of LiDAR data behaviour is included in every filter. The resulting errors of the following comparison can be seen as a measure of correctness of this filter included LiDAR data behaviour.

Because the fixed LiDAR measurements can strictly measure the in-beam directed wind vector, the ultrasonic anemometer data has been projected to the LiDAR measurement geometry. The original anemometer velocity information has been adjusted on the basis on the study of Westerhellweg [116] to compensate the mast wake. Due to the marginal changes of the wind speed magnitude of the low elevation measurement of the LiDAR of $\theta = 0.2°$,

$$1 - \cos(0.2°) = 5.48 \cdot 10^{-5}, \qquad \text{Eq. 2.16}$$

we used the filtered radial line-of-sight velocities of the LiDAR without additional projection to the horizontal plane. By this assumption, the projection of the ultrasonic anemometer is reduced to a single rotation around the z-axis. The index lrf refers to the LiDAR reference frame, whereas index mrf stands for the meteorological reference frame.

$$\begin{pmatrix} u \\ v \end{pmatrix}_{lrf} = \begin{bmatrix} \cos(\gamma) & -\sin(\gamma) \\ \sin(\gamma) & \cos(\gamma) \end{bmatrix} \begin{pmatrix} u \\ v \end{pmatrix}_{mrf}, \qquad \text{Eq. 2.17}$$

where γ =–53.53° is the directional offset of the LiDAR reference frame and the meteorological reference frame. In advance, we carried out correlations of wind speed time series of each range gate with the ultrasonic anemometer time series to find the closest measurement range gate.

The direct comparison of wind speed and the calculation of deviations of the filter associated time series show that all filters for the greater part behave in a similar manner (Figure 2.12a,b). The CNR threshold and both standard deviation filter did not select all outliers as accurate as the dynamic data and combined filter approaches. High average velocity errors seem to correlate with recognisable peaks in the velocity standard deviation curve (Figure 2.12a,b), which is an indicator of high scattering in the filtered data. This may occur when the invalid data from the “comb”-shaped data distribution (Figure 2.1) is classified as valid.

The velocity error and the velocity standard deviation error over the wind direction show high values for several inflow directions (Figure 2.12c,d). Based on the turbulence intensity distribution from Figure 2.9 and the standard deviation error from Figure 2.12d, it cannot be

differentiated whether the visible increase between 110°–145° is due to the mast shadow or by the wake of the turbines AV09, AV08, AV12 and AV11. Indicated by peaks of the average velocity error (Figure 2.12c) close to the theoretical turbine directions we could conclude that these arise by wake shading. Meandering effects, wake-induction-zone interaction, turbine and wind farm circulation could not be taken into account; thus, the differences in turbine positions and corresponding peaks may occur. The smallest increases can be determined for AV09 in a distance of 2230 m and AV11 (2069 m), whereas significant peaks may be caused by AV10 (1669 m), AV08 (1512 m) and AV07 (916 m). Because AV08 and AV12 are close to each other, we cannot differentiate individual proportion of the wakes to the error.

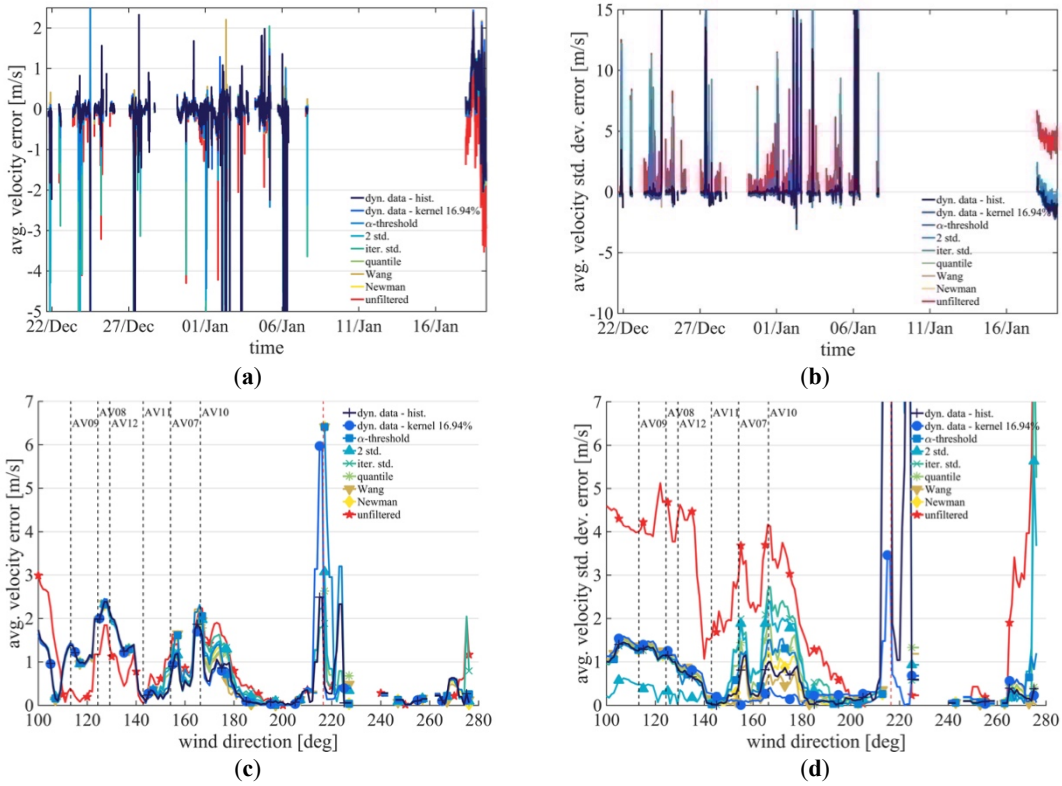

Figure 2.12 Behaviour of the 10 min averaged filtered staring mode measurements of (**a**) the projected wind speed over time; (**b**) the standard deviation over time; (**c**) average wind speed error over wind direction; (**d**) average standard deviation error over wind direction. Vertical dashed lines indicate the wind direction of possible wake shading of the anemometer on FINO1 based on geometrical correlations.

It is surprising that the average error in the mast wake (<145°) is less for unfiltered LiDAR data than for processed ones. This could be indicating that the filters sort out physical reasonable values. While all filters have increased errors in determining the correct velocity standard deviation, the two-sigma standard deviation filter produced noticeably low values in this region. The increase of the errors for this inflow range may be explained due to different measuring volumes. While the anemometer is exposed to increased fluctuation directly in the mast wake, the LiDAR measures a mixed velocity of free and affected flow within the elongated volume. It can further be seen from Figure 2.12c,d that the LiDAR is not capable of capturing perpendicular wind speed components (216° inflow direction) in a good manner. According to the errors shown in Figure 2.12c,d an undisturbed inflow occurred from 180° to 210° and from 220° to 265°.

In Figure 2.13a,b linear correlation of the ultrasonic anemometer data and the LiDAR data has been done for the velocity and the standard deviation. Here, all data are presented without a containment of wind direction. Therefore, these results include situations where the ultrasonic

anemometer, as well the LiDAR measurement is in free flow, in wake flow of the mast and in the wake of the wind farm. We observe regression slopes in the range from 0.866 to 0.974 and regression coefficients from 0.78 to 0.9. These relatively low coefficients are driven by outliers, which are not very frequent, but have a large deviation. These wrong data points evidence in our opinion the discrepancy between point and volumetric flow interrogation in complex flows. In effect these large deviations occur for data in the mast wake predominantly. In the study of Schmidt et al. [115] a subset of these data, specifically restricted to free flow, showed a very high correlation. These results are confirmed here as shown in Table 2.5. Since this is mainly a physical effect, it is impossible for any of the filters to reduce the error. It is to note that the large deviations concentrate in a wind speed range. This is due to the wind conditions during the measurement period, where wind speeds above 6 m/s were found very often for wind directions where the ultrasonic anemometer was shaded by the mast, whereas lower velocities were found in free-flow conditions.

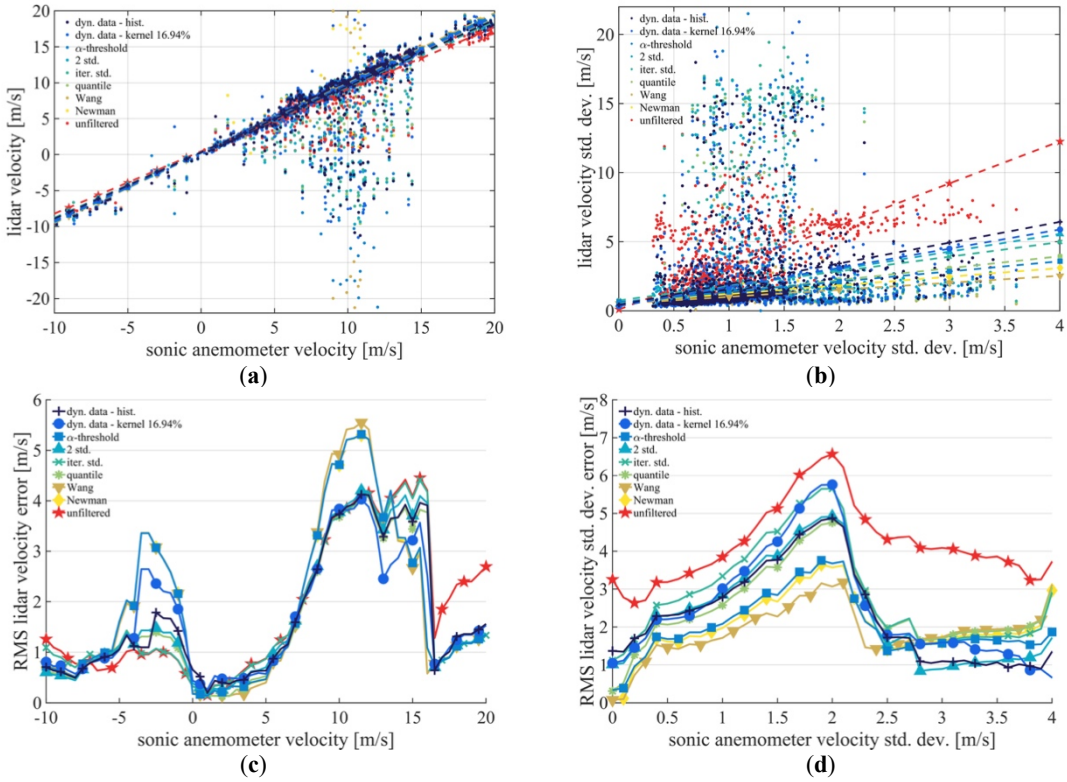

Figure 2.13 Behaviour of the 10 min averaged filtered staring mode measurements of (**a**) the projected wind speed over time, (**b**) the standard deviation over time, (**c**) average wind speed error over time, (**d**) standard deviation error over time.

While the velocities correlate quite well, the regression of the standard deviation is wide spread for the different filters. In combination with Figure 2.13a,b Figure 2.13c,d extend the linear regressions with an uncertainty interval equal to the RMSE. For better visibility, we omit these ranges in Figure 2.13a,b, and plotted them separately in Figure 2.13c,d. It can be recognized that ultrasonic anemometer data in a wide range around 10 m/s is associated with high deviations of LiDAR velocities (Figure 2.13a). A corresponding behaviour is also shown in Figure 2.13c. Even Figure 2.13c,d give the RMSE for specific velocities respectively velocity standard deviations a conclusion about the overall performance need to consider the error frequencies in Figure 2.14. All linear regression parameters are reported in Table 2.2.

In general, it can be said that the application of the combined and dynamic filter approaches filter leads to smaller errors of the velocity and velocity standard deviation compared to other filters. With the exception of the combined filter approach from Wang et al. [73] that was able to reduce the average velocity standard deviation error to 0.0 m/s, both dynamic data filters generated the smallest error in the comparison in three out of four error calculation categories. To give an overview of the overall performance, we distinguish between all wind directions in Table 2.1, wake affected situations, 110°–180° wind direction, and free inflow, 180°–210° wind direction, in Table 2.4 and Table 2.5 in the Appendix 2.C. In each of those data classifications, we see mostly the similar behaviour of the filter in mutual perspective as well in relation to the result in Table 2.1.

2.4.1.3 Error Analysis

In order to gain a better understanding of the error behaviour and insight into the resulting error, we performed an error analysis. For this, the frequency distribution of the errors is calculated.

Figure 2.14 shows histograms for the RMSE of the mean velocity and the velocity standard deviation of all 4325 10-min intervals with a non-constant bin width increasing exponentially. It can be seen that the errors are subject to a double log-normal distribution or Pareto distribution. Explaining the cause of this specific distribution was out of the scope of this paper. Nevertheless, we do a qualitative analysis supported by the cumulative distribution presented in Figure 2.15. While the distribution of absolute average velocity error of the unfiltered LiDAR data (red line) follows this behaviour very well, local deviations of all used filters are shown approximately 3 m/s (Figure 2.14a). The error distribution of the Gaussian kernel dynamic data filter seems to be displaced towards higher errors. We fitted a double logarithm distribution to the histogram to determine the most probable error of the fitted distribution which can be seen in Table 2.3.

The error behaviour of the standard deviation shows double peaks at 0.1 m/s and 4.4 m/s for the unfiltered case and suggests that two functions overlap here. The frequencies of the velocity standard deviation error, for the filtered data, show as well a second peak shifted to ca. 1 m/s.

These error behaviours are also confirmed by Figure 2.15a,b that shows the resulting errors for error values below a certain threshold (x-axis). It turns out that Figure 2.15 is equivalent to the cumulative distribution of error from Figure 2.14. While the resulting RMSEs increase up to 3 m/s error threshold for all filters, this is a turning point followed by a split in behaviour. As expected, the unfiltered LiDAR data results in the highest error up to a threshold of 17 m/s. This error is exceeded from the combined filter approach of Newman et al. [72] and the CNR-threshold filter respectively the combined filter of Wang et al. [73] at the error thresholds of 26 m/s and 29 m/s. While the average error of those three filters are below the unfiltered data, it turns out that the RMSE, as a measure of velocity dynamic accuracy, are the highest with in the test case shown in Table 2.1. A possible explanation may be that all three filters are based on the CNR-threshold filter. While these three filters produce the smallest error up to a threshold of 13 m/s, an enormously increase is followed till the maximum error is reached.

The maximum error can be determined by following the error threshold to the maximum value. By comparing the error behaviour from Figure 2.15a,b with the theoretical accumulated function of a Pareto distribution (root function), the assumption of multiple overlapping distributions may be confirmed. We see the typical increase of a root function several times in Figure 2.15a,b. E.g., the behaviour of the histogram based dynamic data filter standard deviation

curve in Figure 2.14b shows a root functional increase from 0 m/s to 10 m/s and again from 10 m/s to the maximum error. This hypothesis is supported by the second peak of the same graph in Figure 2.14b around about 10 m/s. Similar behaviour can be seen for the remaining filters in Figure 2.14b and Figure 2.15b.

Table 2.1 Comparison of different filtering methods applied on staring mode measurements from 21.12.2013 15:35h (UTC) till 19.01.2014 7:55h (UTC) for all wind directions.

	Avg. Availability FINO1	Avg. Availability All Ranges	Abs. Avg. Velocity Error	RMS Velocity Error	Abs. Avg. Velocity Std. Dev. Error	RMS Velocity Std. Dev. Error
Dyn. data histogram	90.0 %	90.4 %	0.34 m/s	2.38 m/s	0.14 m/s	1.82 m/s
Dyn. data Gauss. kernel	75.1 %	78.2 %	0.30 m/s	2.10 m/s	0.18 m/s	0.90 m/s
CNR threshold	81.9 %	87.6 %	0.45 m/s	3.02 m/s	0.36 m/s	2.24 m/s
Std. dev. two sigma	96.2 %	95.9 %	0.49 m/s	2.50 m/s	0.73 m/s	3.00 m/s
Iterative std. dev.	98.1 %	98.5 %	0.54 m/s	2.54 m/s	0.79 m/s	3.45 m/s
Quartile filter	93.5 %	94.0 %	0.40 m/s	2.42 m/s	0.35 m/s	2.77 m/s
Combined Wang	77.5 %	83.0 %	0.40 m/s	3.10 m/s	0.00 m/s	1.87 m/s
Combined Newman	81.8 %	87.5 %	0.42 m/s	3.02 m/s	0.20 m/s	2.14 m/s
No filter	100 %	100 %	0.76 m/s	2.58 m/s	2.17 m/s	4.10 m/s

Table 2.2 Correlations and residuals of the linear regression between the ultrasonic anemometer and the LiDAR for the velocity and the standard deviation of the velocity. From 21.12.2013 15:35h (UTC) till 19.01.2014 7:55h (UTC) for all wind directions.

	Dyn. Data Hist.	Dyn. Data Gauss.	CNR Thres-hold	Std. Dev.	Iter. Std	Quan-tile	Wang	New-Man	Unfilt-ered
Velocity									
Reg. slope	0.92	0.95	0.96	0.92	0.91	0.93	0.97	0.97	0.86
Offset [m/s]	0.31	0.26	0.22	0.33	0.32	0.32	0.22	0.22	0.44
R^2	0.85	0.84	0.90	0.83	0.79	0.85	0.90	0.90	0.78
Velocity std. dev.									
Reg. slope	1.50	1.39	0.73	1.27	1.05	0.86	0.50	0.62	3.04
Offset [m/s]	0.42	0.33	0.63	0.45	0.74	0.49	0.50	0.58	0.08
R^2	0.06	0.04	0.02	0.04	0.02	0.02	0.01	0.01	0.15

Table 2.3 Most probable velocity and standard deviation error of fitted double log-normal distribution to 10-min error histogram.

	Dyn. Data Hist.	Dyn. Data Gauss.	CNR Thres-hold	Std. Dev.	Iter. Std	Quan-tile	Wang	New-Man	Unfilt-ered
Velocity [m/s]	0.09	0.20	0.09	0.09	0.09	0.10	0.11	0.09	0.11
Vel. std. dev. [m/s]	0.09	0.12	0.06	0.12	0.06	0.10	0.11	0.06	0.07

2.4.2 Evaluation Based on Scanning Measurements

The goodness of the filters must be evaluated in a broad range of applications. The previous staring study does not include the additional spatial effect given in scanning trajectories. Such validation work, is, however, limited by a missing reference. In effect it is very costly to setup an experiment to validate a scanning LiDAR at least at some points in the trajectory. Therefore, such evaluations have to be done at the qualitative level. In this respect we processed the nacelle-based

PPI-scanned measurements analogous to the staring mode measurement data, with the exception of the application of the standard deviation filter and the spatial normalisation within the dynamic data filter. Due to lower spatial measurement frequency of f_{PPI} = 0.045 Hz compared to the staring mode measurements of f_{stare} = 2 Hz, we enlarged the selection of radial wind speed data in beam-wise and azimuthal direction to form an equivalent amount of data to calculate the standard deviation within a 10-min segment. All CNR-threshold based filters have been used with a parametrisation of α_{le} = -25 dB and α_{ue} = -8 dB. The normalisation of CNR and radial speed for PPI-measurements has been extended by calculating the temporal and spatial averages for azimuthal bins of 1°. Thus, we expect to consider different characteristics of the wake regions and allow potential different backscattering properties due to the complex flow structure. All other filters were used as described in referenced publications and thereon applied range- and angle-wise.

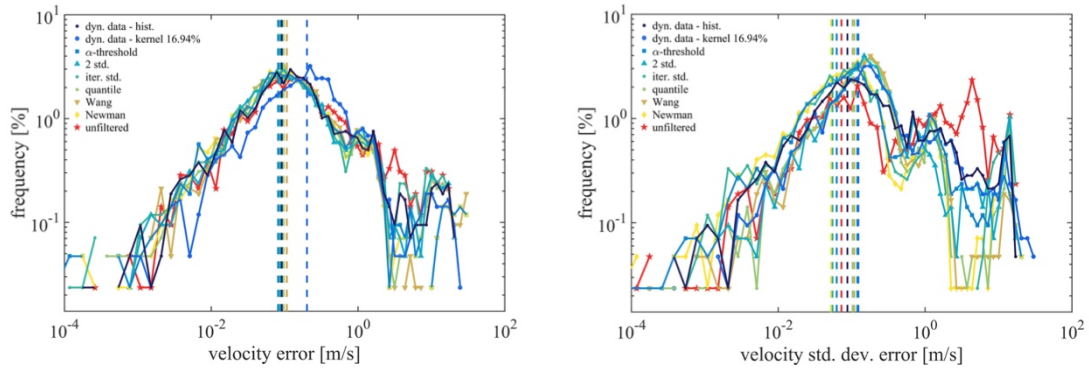

Figure 2.14 Histogram with exponential increasing bin width of the **(a)** absolute average velocity error and **(b)** the absolute velocity standard deviation error. Vertical dashed lines indicate the centre of a fitted Gaussian curve.

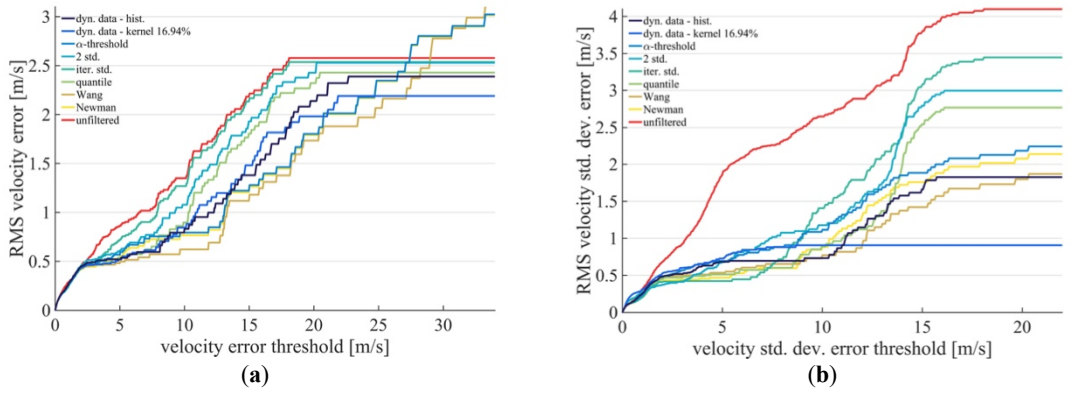

Figure 2.15 Influence of maximum error threshold to the resulting error **(a)** RMS velocity error over velocity error threshold and **(b)** RMS velocity standard deviation error over velocity standard deviation error threshold.

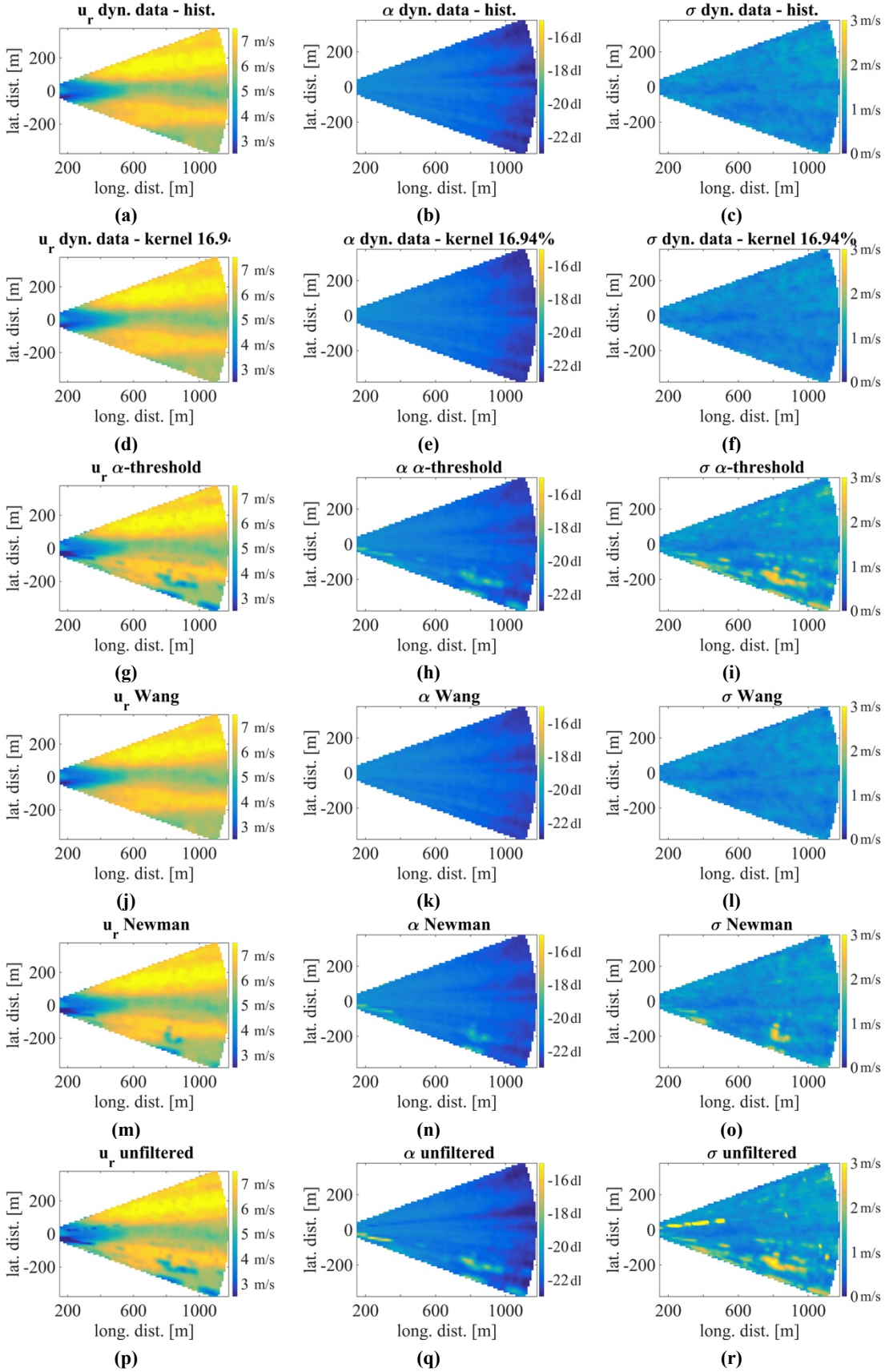

Figure 2.16 Influence of different filtering methods on a 10 min averaged horizontal LiDAR scans. (**1st column**) radial speed, (**2nd column**) CNR mapping, (**3rd column**) standard deviation of radial speed. (**a**–**c**) histogram-based dynamic data filter, (**d**–**f**) Gaussian kernel based dynamic data filter, (**g**–**i**) CNR-threshold filter, (**j**–**l**) combined filter approach by Wang et al., (**m**–**o**) combined filter approach by Newman et al., (**p**–**r**) unfiltered.

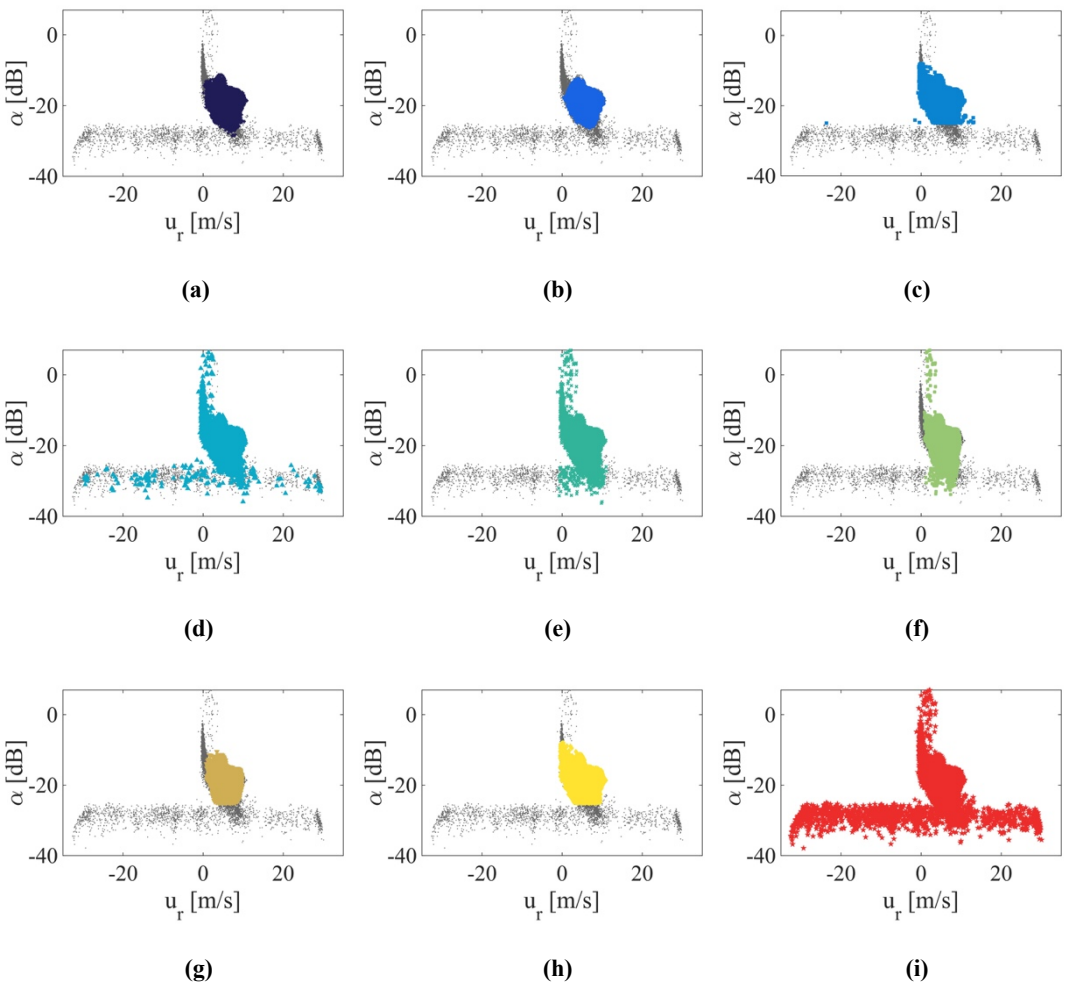

Figure 2.17 Results of application of different filtering methods in the $u_r - \alpha$ diagram. **(a)** histogram-based dynamic data filter, **(b)** Gaussian kernel based dynamic data filter, **(c)** CNR-threshold filter, **(d)** two sigma standard deviation filter, **(e)** iterative standard deviation filter, **(f)** interquartile-range, **(g)** combined filter approach by Wang et al., **(h)** combined filter approach by Newman et al., **(i)** no filtering.

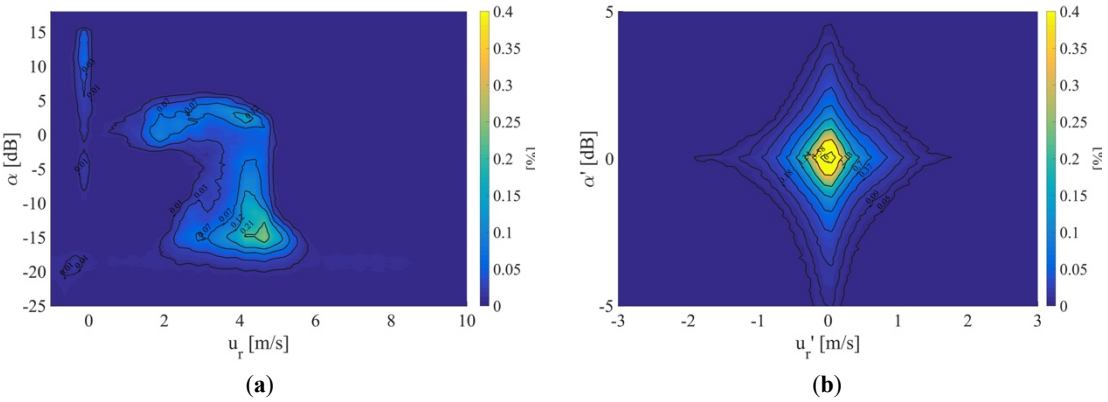

Figure 2.18 Visualisation of the data density distribution of Stream Line XR PPI data from 31.10.2016 00:00h (UTC) till 31.10.2016 00:30h (UTC) in **(a)** $u_r - \alpha$ diagram and **(b)** in the normalised reference frame.

We filtered the PPI scans in 10-min segments and interpolated them scan-wise to a regular Cartesian grid. We averaged the individual scans afterwards to 10-min means.

In the visualisation of the unfiltered data, it can be seen that high CNR-structures (Figure 2.16) correlate with structures in the wind speed (Figure 2.16p) and its standard deviation (Figure 2.16q). The probability of occurrence of those structures in a 10-min averages is improbable. It is unphysical in the sense of a flow field that sharp, irregular structures emerge in the beam direction (Figure 2.16r). Therefore, we assume that these structures occur due to invalid measurements. However, to produce an interference-free data set, we tried to exclude those by filtering.

We may explain those structures regarding the $u_r - \alpha$ diagram and the functioning of the individual filters (Figure 2.17). The data accumulation of measurements points close to 0 m/s in a wide range of α may appear due to partly shading of hard targets or unknown reason. Obstacles, such as meteorological masts, high voltage cables or rotor blades of other turbines influence the laser beam partly, complete or multiple times and affect the backscattering. Therefore, a second distinct peak, besides the one of the wind speed appears in the frequency spectrum. Thus, obstacles causing high-backscattering high-amplitude peaks are fitted as often as the wind speed peaks. Figure 2.17 gives an indication of the functioning of the different filters. It can be seen that only the dynamic data filters and the combined filter approach by Wang et al. [73] managed to eliminate the high scattering of u_r in the "comb"-shaped data distribution and prior described the data accumulation close to 0 m/s.

Regarding Figure 2.16 and Figure 2.17, a relation between mentioned exposed structures and the filtering can be made. Based on this test case of scanned data, we observed that dynamic data filters are capable to identify more outliers than the other filters.

As a proof that the dynamic data filtering approach is not system specific, we want to show an example of PPI data from the second part of the nacelle-based measurement campaign from Section 2.3.1.3 captured with a Stream Line XR. In the following, we will show the data-density distribution in the $u_r - \alpha$ diagram and the normalised LiDAR data in the $u_r' - \alpha'$ reference frame as a proof of similar data behaviour in comparison to the Leosphere LiDAR.

As can be seen from Figure 2.18a, the overall data density of the Stream Line XR dataset shows similar behaviour in comparison to the Leosphere Windcube 200s LiDAR data in Figure 2.3. A horizontal scattering in the radial velocity in combination with a vertical scattering of the CNR is shown in both visualisations. The application of the temporal and spatial normalisation from Section 2.2.7.1 results in a comparable data density distribution.

It is noticeable that the density distribution of the normalised LiDAR data of the Stream Line XR device tend to form a pyramid distribution (Figure 2.17b), whereas the density shown in Figure 2.4 resembles a bi-variate Gaussian distribution. The normalisation shown here was applied with a Δt = 60 s and may therefore be compared with Figure 2.4f. From similar behaviour of forming a dense data distribution in the $u_r' - \alpha'$ reference frame, we see the possibility of application of the dynamic data filter as presented in this paper.

2.5 Conclusions

We introduced a new approach to filter line-of-sight long-range Doppler LiDAR data dynamically. This considers the influences of atmospheric conditions, device dependencies and the measurement setup. The new methods take into account the radial velocity and the signal

quality in a bi-variate manner based upon the assumption of self-similarity of valid data. Here we performed a benchmark of two implementations of the new dynamic filtering approach together with five state-of-the-art filter methods used in research and industry applications. First, a temporal high resolved time series of approximately 1.5 weeks measured in a distance of 2864 m by a minimal inclined long-range LiDAR was compared against an ultrasonic anemometer with means of 10-min to make a quantitative evaluation. Second, we performed a qualitative analysis to infer filter performance for cases of scanning interrogation of the wind field. Within this study the combined research filter approaches by Newman et al., and Wang et al. have been ported to a Leosphere Windcube 200s dataset.

This study shows, that the common practice of using fixed CNR-threshold based filters may lead to unnecessarily reduced data availability. This limitation can be overcome by more elaborated methods, which implementation is technically feasible with low computational cost. We were conditional able to decouple the commonly associated distance dependent data availability on the CNR by introducing a temporal and spatial normalisation of measurement properties within the dynamic data filter approach that includes complex changing flow situations and variations of the CNR over time. However, their general application must be thoroughly studied. Regarding the mean velocity errors, it is shown that high data availabilities do not necessarily lead to good accuracies and lower data availabilities not imply bad agreement with the reference.

The resulting errors of this test case are in the range from 0.30 m/s to 0.76 m/s for the average velocity errors, from 2.1 m/s to 3.1 m/s for the RMS velocity error, from 0.00 m/s to 2.17 m/s for the standard deviation error and from 0.9 m/s to 4.1 m/s for the RMS velocity standard deviation error.

The overall results of all filters and the parametrisation study of the Gaussian kernel based dynamic data filter show, that filtering can be done with the focus on the velocity dynamics in terms of the standard deviation or the average velocity. Moreover, the error evaluation varies whether the average error or the RMSE is considered. In comparison to all filters, both implementations of the new approach show the smallest error in three of four error calculation categories whereas the combined filter approach by Wang et al., was able to diminish the standard deviation velocity error to 0.0 m/s.

Depending on the discipline, the application of wind LiDAR filters and the magnitude of commonly accepted errors vary, wherefore the here shown differences in the results should not be underestimated. Even small differences in the average wind speed can be the decisive argument on the realisation of a wind park in resource assessment. It is up to each user to balance the computational effort with the needed accuracy. The selection of a filter should comply with the analysis requirements. While the commonly used fixed CNR-threshold filter is used for fast and robust results, the histogram based dynamic data filter can be used to increase the data availability resulting high accuracy. Critical applications in which a certain maximum error may not be exceeded require a more stringent filter than applications where the frequency of certain errors is a relevant criterion. The conducted error analysis has shown that the frequency distributions of errors do not show a normal distribution and are very distinct from each other.

In the valuation of filtering results of scanned measurements in full-scale experiments, it was shown on basis of temporal means that special error structures in the flow field and the CNR-mapping were filtered by Wang et al., and the dynamic data filter approach in a good manner.

Due to the behaviour of the dynamic data filter approach within the here presented test cases, we see the assumption of self-similarity to identify valid data points as confirmed. An accompanying limitation within this approach is the need of a certain amount of valid data to form dense clusters for the calculation of the data density. At the same time, this limitation can be seen as an advantage, since large quantities of data can be processed at once and thereby the proportion of valid data can be increased. Because of the applicability of scanned and stared measurement setups we see the dynamic filter approach as a promising tool for all types of LiDAR measurement setups. The results shown here are a further step in the development of filter techniques for explicit LiDAR application and prove that self-similarity can be used as a criterion for LiDAR data filtering. Regarding the reproducibility of the comparison results, further investigations of the behaviour and limitations of this approach should be performed with a plurality of different measurement situations that could not be part of this study.

Acknowledgements: We thank ENO energy systems GmbH for the support during the measurement campaigns and the RAVE consortium. We are also grateful to the reviewers and Juan José Trujillo, Andreas Rott, Marijn Floris van Dooren, Laura Valldecabres Sanmartin and Wilm Friedrichs at the University of Oldenburg for the discussions. The presented work has been funded by the Federal German Ministry for Economic Affairs and Energy of Germany (BMWi) in the framework of projects CompactWind under the contract no. 0325492B and GW Wakes under the contract No. 0325397A.

Author Contributions: Hauke Beck wrote this paper and conducted related research. Intensive review was made by Martin Kühn.

Conflicts of Interest: The authors declare no conflict of interest.

Appendix 2.A

The discretisation of the main averaging interval ΔT in different normalisation intervals Δt changes the data density as shown in Section 2.2.7.1. The calculation of the Gaussian kernel based on different data densities influences the choice of a suitable validity value ν. Based on the entire data set from Section 2.3.1.1, we performed a parameter study that considers the resulting average errors and the RMS of velocity and velocity standard deviation. For this purpose, we used different combinations of Δt, in a range from 0.5 s to 300 s used and validity values from 10 % to 100 % for an averaging interval ΔT = 10 min. The resulting errors can be seen in Figure 2.19.

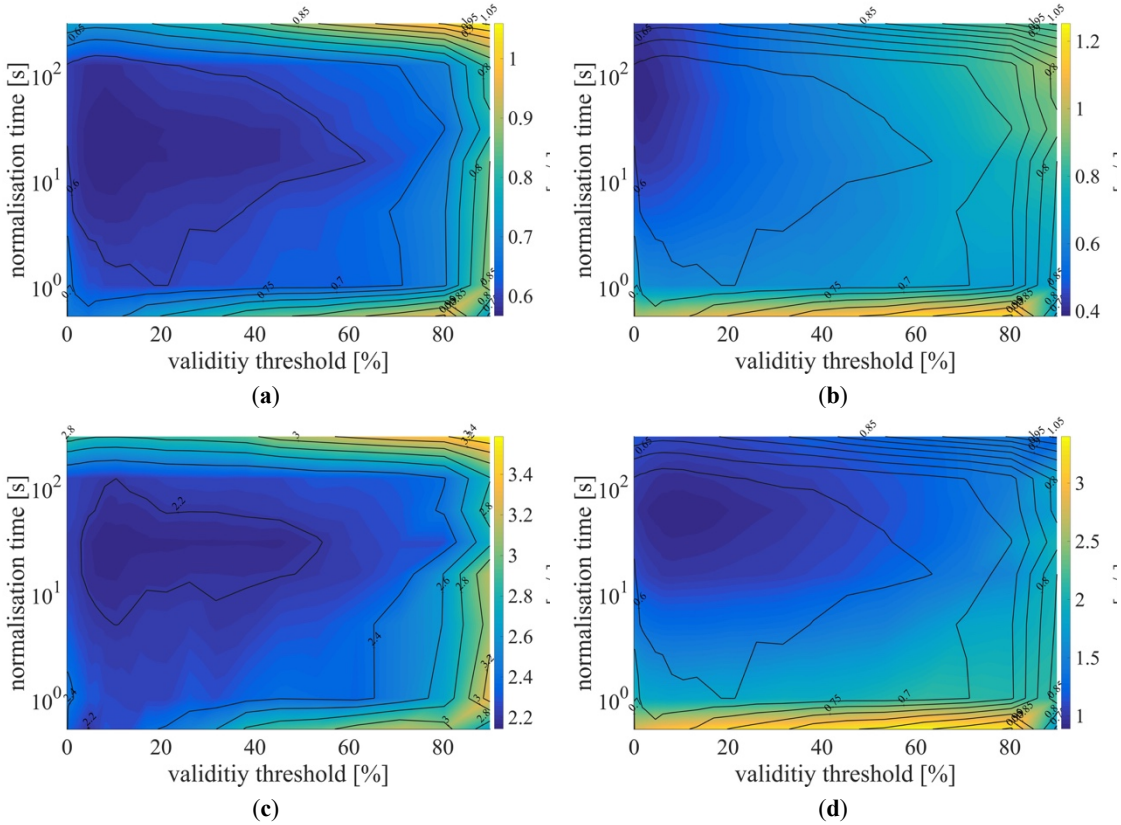

Figure 2.19 Visualisation of the influence of the normalisation time Δt and validity value ν on the resulting total error. Staring mode LiDAR data from 21.12.2013 15:35h (UTC) till 19.01.2014 7:55h (UTC) form the basis for this calculations. **(a)** Average velocity error, **(b)** the average velocity standard deviation error, **(c)** RMS velocity error and **(d)** RMS velocity standard deviation error.

Appendix 2.B

For the investigation of the influence of the averaging time ΔT and the normalisation time Δt on the error, corresponding combinations were calculated (Figure 2.18 and Figure 2.19). We evaluated ΔT for 15 s, 30 s, 60 s, 120 s, 300 s and 600 s and Δt for 0.5 s, 1 s, 5 s, 15 s, 30 s, 60 s, 120 s, 300 s and 600 s with a reduced data set. A time interval of 24 h was selected with the focus to represent a balanced ratio of wake and free-flow situations. The data was captured from 04.01.2014 7:30h (UTC) till 05.01.2014 7:30h (UTC).

Even if all other used filters are defined on prescribed time intervals, we have examined these for variable ΔT. A relation of the non-dynamic data filters to the normalisation time Δt was not given. While the average error and the RMSE behave contrary for the velocity error, there is no clear indication for the velocity standard deviation error. Regarding both implementations of the

dynamic filter, it is only possible to derive a suggested parameter set directly from Figure 2.20a and Figure 2.21a for the average error. The RMS velocity error reduces with increasing average time.

To be able to choose a parameter set from Figures Figure 2.19 and Figure 2.20 that fulfil the compromise of a small error for all calculated error classes, the error behaviours of the histogram-based and the Gaussian kernel based dynamic data filter have been normalised an averaged. The result can be seen in Figure 2.22. For both filters, a parameter set of averaging time and normalisation time can be found that produces the smallest mean error of all errors.

Figure 2.23 Visualisation of the influence of the averaging time ΔT for all filters to the resulting errors. (a) Average velocity error, (b) average velocity standard deviation error, (c) RMS velocity error and (d) RMS velocity standard deviation error. shows the influence of the averaging time ΔT for all filters on the resulting errors. Because the dynamic filters are dependent on the normalisation time, the corresponding value of Δt was chosen from Figure 2.20 and Figure 2.21. While all non-dynamic data filters show relative comparable results for variable averaging times, the strongest impact can be seen for the RMS velocity error which decreases quadratic over ΔT.

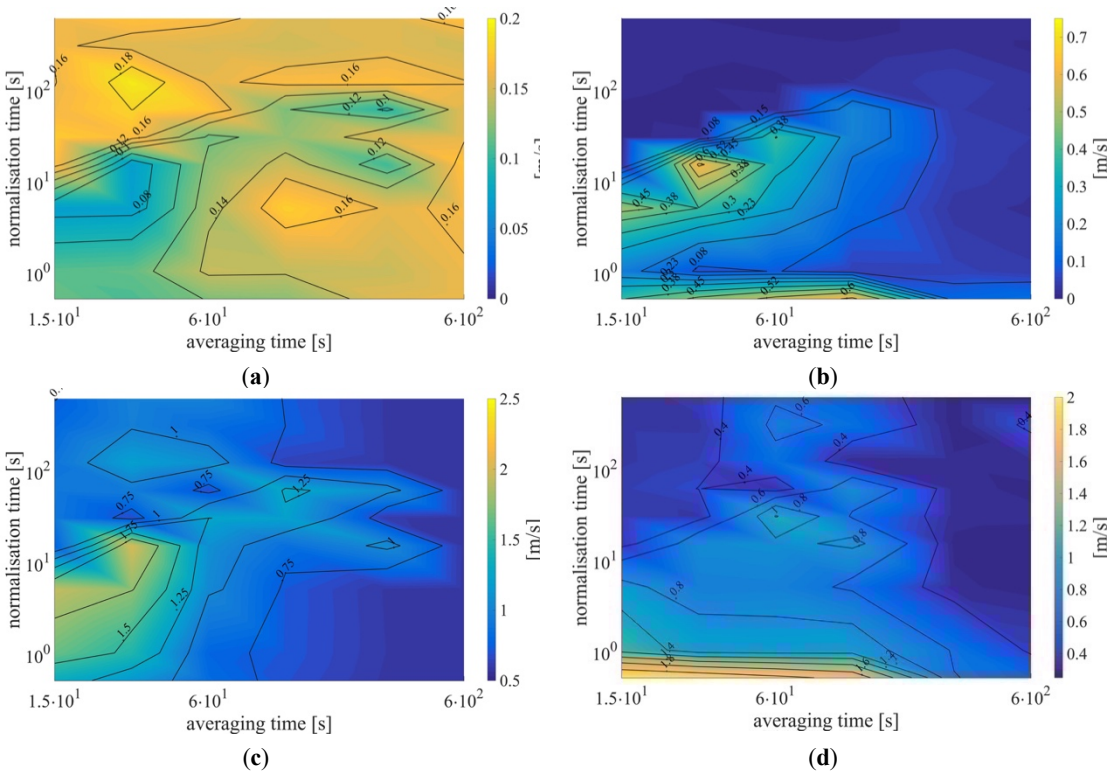

Figure 2.20 Visualisation of the influence of the normalisation time Δt and the averaging time ΔT on the resulting error of staring mode LiDAR data from 04.01.2014 7:30h (UTC) till 05.01.2014 7:30h (UTC) from the histogram-based dynamic data filter **(a)** Average velocity error, **(b)** average velocity standard deviation error, **(c)** RMS velocity error and **(d)** RMS velocity standard deviation error.

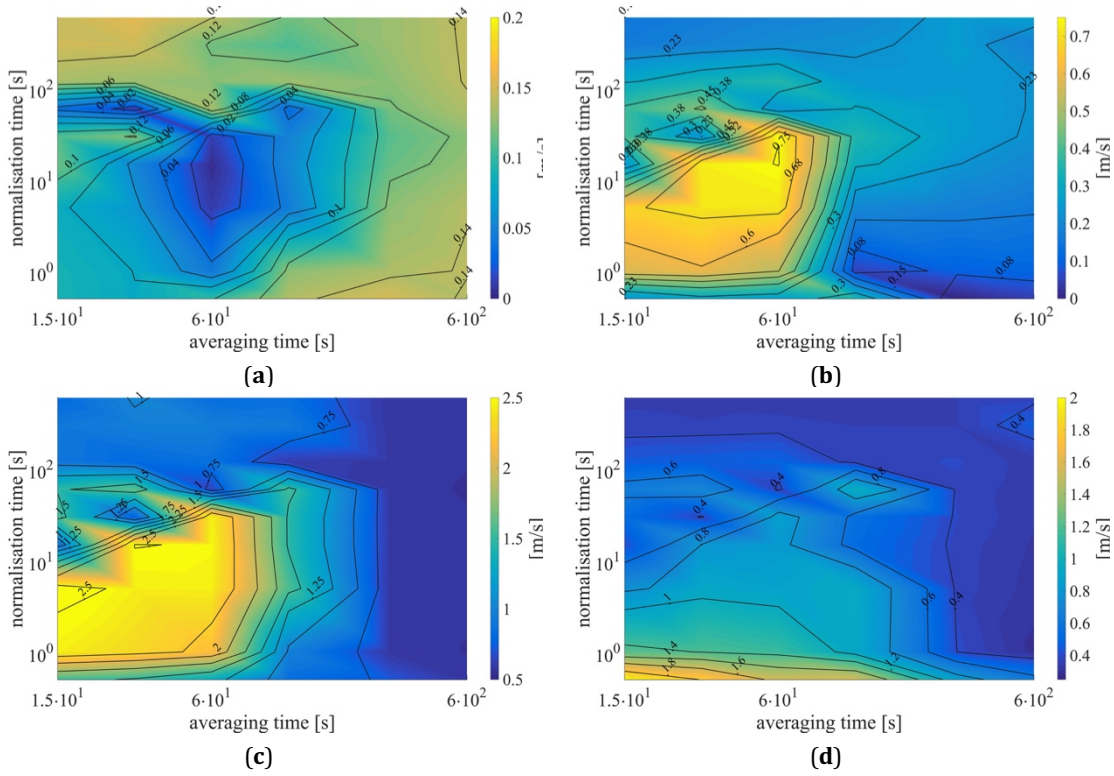

Figure 2.21 Visualisation of the influence of the normalisation time Δt and the averaging time ΔT on the resulting error of staring mode LiDAR data from 04.01.2014 7:30h (UTC) till 05.01.2014 7:30h (UTC) from the Gaussian kernel based dynamic data filter. (**a**) Average velocity error, (**b**) average velocity standard deviation error, (**c**) RMS velocity error and (**d**) RMS velocity standard deviation error.

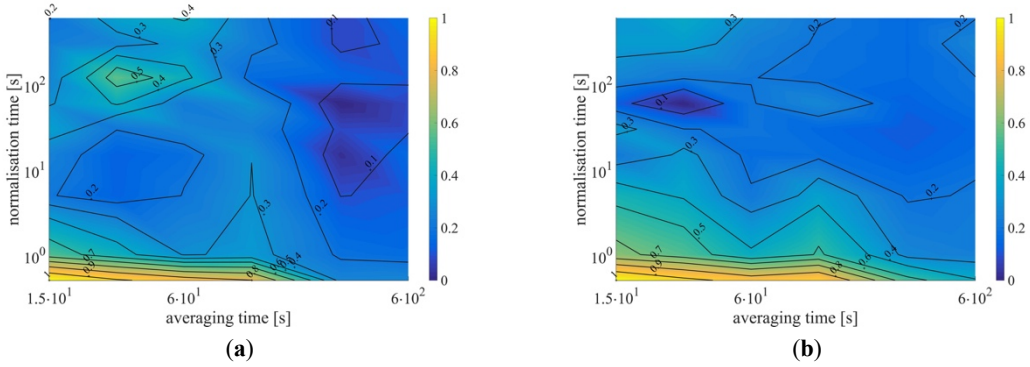

Figure 2.22 Averaged and normalised error behaviour of the average velocity error, the RMS velocity error, the velocity standard deviation error and the RMS velocity standard deviation error of (**a**) the histogram-based dynamic data filter and (**b**) the Gaussian kernel based dynamic data filter. Staring mode LiDAR data from 04.01.2014 7:30h (UTC) till 05.01.2014 7:30h (UTC) form the basis for this calculations.

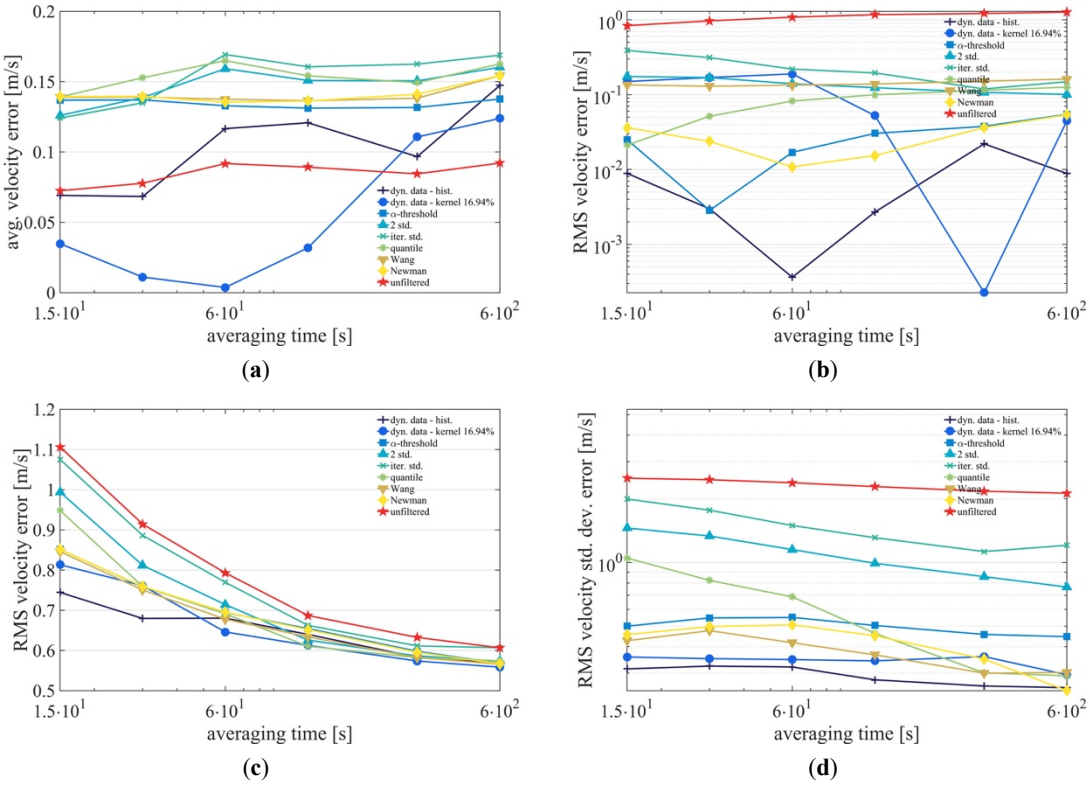

Figure 2.23 Visualisation of the influence of the averaging time ΔT for all filters to the resulting errors. (**a**) Average velocity error, (**b**) average velocity standard deviation error, (**c**) RMS velocity error and (**d**) RMS velocity standard deviation error.

Appendix 2.C

The following results were calculated in analogues way as described in Section 2.4.1.To obtain a better understanding of the filter behaviour, we distinguished between wake and free inflow conditions. We defined waked affected inflow wind direction from 110° to 180° and implied turbine wakes and the mast wake. This results can be seen in Table 2.4.

Free inflow conditions at the ultrasonic anemometer was captured in a wind direction range within 180°–210°. Those results are shown in Table 2.5.

Table 2.4. Comparison of different filtering methods applied on staring mode measurements for wake affected wind directions from 110° to 180°.

	Avg. Availability FINO1	**Avg. Availability All Ranges**	**Abs. Avg. Velocity Error**	**RMS Velocity Error**	**Abs. Avg. Velocity Std. Dev. Error**	**RMS Velocity Std. Dev. Error**
Dyn. data histogram	89.9 %	91.6 %	0.50 m/s	3.13 m/s	0.21 m/s	2.14 m/s
Dyn. data Gauss. kernel	63.6 %	68.5 %	0.47 m/s	2.91 m/s	0.19 m/s	1.10 m/s
CNR threshold	76.1 %	83.5 %	0.75 m/s	4.10 m/s	0.50 m/s	2.68 m/s
Std. dev. two sigma	96.6 %	96.3 %	0.73 m/s	3.28 m/s	1.04 m/s	3.50 m/s
Iterative std. dev.	97.1 %	97.5 %	0.77 m/s	3.26 m/s	1.02 m/s	4.03 m/s
Quartile filter	92.5 %	93.3 %	0.61 m/s	3.17m/s	0.53 m/s	3.28 m/s
Combined Wang	72.1 %	79.3 %	0.68 m/s	4.24 m/s	0.05 m/s	2.24 m/s
Combined Newman	76.0 %	83.4 %	0.70 m/s	4.10 m/s	0.29 m/s	2.56 m/s
No filter	100 %	100 %	1.13 m/s	3.31 m/s	3.14 m/s	4.87 m/s

Table 2.5. Comparison of different filtering methods applied on staring mode measurements for free inflow condition and wind directions from 180° to 210°.

	Avg. Availability FINO1	**Avg. Availability All Ranges**	**Abs. Avg. Velocity Error**	**RMS Velocity Error**	**Abs. Avg. Velocity Std. Dev. Error**	**RMS Velocity Std. Dev. Error**
Dyn. data histogram	89.3 %	90.1 %	0.07 m/s	0.81 m/s	0.04 m/s	1.26 m/s
Dyn. data Gauss. kernel	70.9 %	72.6 %	0.02 m/s	0.91 m/s	0.18 m/s	0.63 m/s
CNR threshold	89.3 %	92.8 %	0.13 m/s	0.90 m/s	0.17 m/s	1.43 m/s
Std. dev. two sigma	96.1 %	96.0 %	0.24 m/s	1.32 m/s	0.32 m/s	2.11 m/s
Iterative std. dev.	99.2 %	99.4 %	0.28 m/s	1.39 m/s	0.45 m/s	2.48 m/s
Quartile filter	94.3 %	94.6 %	0.18 m/s	1.21 m/s	0.09 m/s	1.86 m/s
Combined Wang	84.5 %	87.8 %	0.08 m/s	0.80 m/s	0.10 m/s	1.06 m/s
Combined Newman	89.2 %	92.7 %	0.11 m/s	0.88 m/s	0.05 m/s	1.31 m/s
No filter	100 %	100 %	0.38 m/s	1.44 m/s	1.03 m/s	2.87 m/s

3 Temporal Up-Sampling of Planar Long-Range Doppler LiDAR Wind Speed Measurements Using Space-Time Conversion

The content of this chapter is identical to the following journal article:

Beck, H.; Kühn, M.: Temporal Up-Sampling of Planar Long-Range Doppler LiDAR Wind Speed Measurements Using Space-Time Conversion. *Remote Sensing* 2019, 11, 867, doi: 10.3390/rs11070867

Article

Temporal Up-Sampling of Planar Long-Range Doppler LiDAR Wind Speed Measurements Using Space-Time Conversion

Hauke Beck [1,*] and Martin Kühn [1]

[1] ForWind–University of Oldenburg, Institute of Physics, Küpkersweg 70, 26129 Oldenburg, Germany; martin.kuehn@uol.de
* Correspondence: hauke.beck@uol.de;

Received: 13 March 2019; Accepted: 8 April 2019; Published: 10 April 2019

Abstract: Measurement campaigns in wind energy research are becoming increasingly complex, which has exacerbated the difficulty of taking optimal measurements using light detection and ranging (LiDAR) systems. Compromises between spatial and temporal resolutions are always necessary in the study of heterogeneous flows, like wind turbine wakes. Below, we develop a method for space-time conversion that acts as a temporal fluid-dynamic interpolation without incurring the immense computing costs of a 4D flow solver. We tested this space-time conversion with synthetic LiDAR data extracted from a large-eddy-simulation (LES) of a neutrally stable single-turbine wake field. The data was synthesised with a numerical LiDAR simulator. Then, we performed a parametric study of 11 different scanning velocities. We found that temporal error dominates the mapping error at low scanning speeds and that spatial error becomes dominant at fast scanning speeds. Our space-time conversion method increases the temporal resolution of the LiDAR data by a factor 2.4 to 40 to correct the scan-containing temporal shift and to synchronise the scan with the time code of the LES data. The mean-value error of the test case is reduced to a minimum relative error of 0.13 % and the standard-deviation error is reduced to a minimum of 0.6 % when the optimal scanning velocity is used. When working with the original unprocessed LiDAR measurements, the space-time-conversion yielded a maximal error reduction of 69 % in the mean value and 58 % in the standard deviation with the parameters identified with our analysis

Keywords: improvement; synchronisation; statistics; wakes; scanning measurements; flow solver

3.1 Introduction

The arrangement of wind turbines into dense and efficient clusters is a central challenge in the design of wind farms. The detrimental effect of wake shading decreases energy yield and increases dynamic loads [16, 22]. These additional loads lead to increased fatigue on the turbine components, increasing the likelihood of failure and early maintenance [123, 124]. This additional and unexpected maintenance will deteriorate the economic and energy efficiency of the wind farm [125].

Wake models were developed early in the history of wind-turbine design to account for the loss of yield, wake-induced loads, and to aid in the design of wind turbines. Since single-point measurements are limited to cup anemometers mounted on the turbines themselves or on meteorological masts, reference and validation data can usually only be applied in the form of time averages [24, 29, 31].

Since wakes have highly dynamic behaviour, dynamic wake models have been developed for the sake of simulating how the wake meanders over time, to generate more realistic inflow conditions for load calculations in the design phase or for wind farm control. The dynamic wake meandering model (DWM) of Larsen et al. [38], which is unique in its method for simulating meandering behaviour, has been updated and adjusted to ease comparisons with measured data [40, 126]. However, in Larsen et al. [40], and Churchfield et al. [126], a previously reported

simulation of wake meandering from Larsen et al. [38],was used. Keck et al. [41] introduced a stochastic approach that considers meandering as it is related to atmospheric stability. Validation of these dynamic wake models requires wind velocity data collected with high spatial and temporal resolution, either from suitably recorded measurements or from high-fidelity computational fluid dynamics (CFD) simulations.

One of the most promising measuring devices for understanding wakes in free-field conditions is wind-speed Doppler light detection and ranging (LiDAR). LiDARs are configured as continuous-wave (CW) devices for short distances (<200 m) [127] or as pulsed systems for longer distances (<6,000 m) [54]. Though LiDAR is commonly used for free-field measurements, van Dooren et al. [128] took LiDAR measurements in a wind tunnel under controlled conditions in order to investigate wake behaviour using a synchronised dual-short-range LiDAR setup. Van Dooren et al. [128] captured two-dimensional (2D) flow situations of a model wind farm with three turbines in the range of 20 s per horizontal scan. Bartl et al. [129] investigated how selected yaw misalignments affected wake properties by varying the inflow turbulence and shear in a wind tunnel. In experimental and numerical tests, atmospheric conditions are not trivial to reconstruct, especially the recreation of fluctuations of length scales larger than the turbine. Thus, CFD and wind-tunnel tests cannot replace measurements of a full-scale system in the full field, but instead extend the range of research possibilities.

Due to the measurement principle used, some limitations apply when using a single long-range LiDAR setup for full-scale wake measurements. In Section 3.2, we discuss the constraints due to the one-dimensionality of the measurements, which include the complications in volume averaging due to the laser pulse. We also discuss how all the scanning measurements must strike a compromise between spatial and temporal resolution. These restrictions apply to both CW and pulsed LiDAR systems.

A significant advantage of short-range CW systems over long-range systems is their high measurement frequency, which allows temporal processes to be captured on a shorter time scale. In contrast, pulsed devices can take measurements at multiple quasi-instantaneous positions along the laser beam at long range. This spatial distribution allows the flow pattern of one or many wind turbines to be mapped within one scan.

Depending on the scan-repetition time and the maximum measurement range, characteristic air parcels can be analysed in the form of flow structures at multiple times at different positions with successive scans. Thus, the advection speed of the parcels can be determined and conclusions about their behaviour can be drawn [130]. The reasonableness of the reconstruction must be considered for each application. Resource assessment places more emphasis on time-interval-based values, like 10-min average wind speed and the ambient turbulence intensity [131] than on more fine-grained high-resolution flow dynamics. The numerical and temporal resources required to reconstruct high-resolution flow dynamics are inconsistent with the resulting benefits. In contrast, high-resolution time series are required for the characterisation and validation of models of wake meandering. Larsen et al. [38], Bingöl et al. [68] and Trujillo et al. [69] used LiDAR-based wake wind-speed time series with moderate sampling frequencies, between 0.04 Hz and 0.06 Hz, in order to compare the wake deficit position with wake meander model predictions from the DWM [38].

However, when analysing wake measurements recorded with LiDAR systems, especially in connection with other measurements, high-resolution multidimensional wake measurement data is helpful for the sake of synchronisation and correlation with data about atmospheric or turbine

conditions' information, like stability indicators, wind shear, wind veer, turbine thrust, and turbine loads, measured at specific moments in time [14]. As measurement campaigns tend to become more and more complex to allow detailed analysis of flow situations [14], the limitations of long-range LiDAR systems need to be understood in detail. Specifically, researchers need to know how planar measurement results can be used as time series in addition to the standard mode of statistical averages. To the same end, data-processing methods that can overcome the limitations of individual measurement systems with sufficient accuracy must be improved.

The first objective of this paper is to produce synchronised temporal and spatial high-resolution up-sampled flow data. The secondary objective is to facilitate comparison of this flow data with LES reference data. This comparison requires that the dynamics of planar full-field wake measurements are compatible with data from wind-tunnel experiments or CFD simulations. Further, this full-scale measurement data can be used directly for the evaluation of temporally variable flow structures or dynamic wake models.

To this end, Section 3.2 reports our parametric study of the measurement frequency of numerically simulated LiDAR data from an LES wake flow field, to understand how the measurement parameters influence the mapping quality. In Section 3.3, we present a method for temporal fluid-dynamics interpolation based on space-time conversion, which improves the temporal resolution of long-range planar LiDAR data to a sub-measurement-time scale. With this improvement in the temporal resolution, the time shift within a scan can be corrected, and we can mutually synchronise distinct measurements independent of their sampling time or temporal resolution. In Section 3.4, we show how the mapping error of horizontal and vertical nacelle-mounted wake measurements shifts from a spatial to a temporal nature as the measurement frequency changes. This analysis addresses how the representation of the mean value and standard deviation is affected by retrospectively increasing the temporal resolution of planar long-range LiDAR measurements. The effects of propagation and implied restrictions are discussed in Section 3.5 and conclusions are drawn in Section 3.6. While the paper focuses mostly on the presentation of horizontal measurements, appendices include detailed figures that show the corresponding results for vertical measurements. The effects of temporal up-sampling of LiDAR scans with different angular velocities are detailed in supplementary online video material.

3.2 Planar LiDAR Data

LiDAR systems are subject to limitations inherent to their principle of operation. Single systems can only measure the so-called line-of-sight (LOS) velocity along the direction of the laser beam, which is calculated from the light backscattered from aerosols [91].

A major source of inaccuracy is the spatial resolution of LiDAR, which depends mainly on the pulse length. When using a pulsed laser in commercial devices, the spatial quantisation of the wind speed in the radial direction is in the range of approximately 30 m [45]. This quantisation limit leads to volume averaging within an assumed cylindrical probe volume. This characteristic of LiDAR measurements has already been studied for its effects in turbulence measurement during the early days of LiDAR wind measurements [45, 46, 47]. Depending on the mode of operation, a second volume-averaging effect can build up in the scanning direction while recording planar measurements. During free flow, the associated error is relatively small [74]. In strongly turbulent flow situations that are very inhomogeneous, such as wind-turbine wakes, stronger deviations arise [74]. To understand the errors in this case, Fuertes and Porté-Agel [80]

studied the errors in scanned measurements caused by heterogeneity in temporally averaged wake measurements.

A further restriction on LiDAR technology, which also applies to all scanning measurements systems, is that the spatial and temporal resolution of the measurements is in a trade-off relationship. The slower the selected scan speed, the finer the spatial resolution and the longer the scan-repetition time. Within a scan, the velocities measured at each scan angle correspond to different time stamps within a certain interval. Even though a whole scan may be visualised as a single picture or frame, such an illustration is not physically based and may be misleading. To avoid this effect, planar LiDAR data is usually averaged under the assumption that the time shift within a scan is negligible when compared with the averaging time.

A serious obstacle to using LiDAR for measurements of wind farms lies in the limited temporal resolution, or rather in the ideal combination of temporal and spatial resolutions that cannot yet be achieved with LiDAR systems. When using a very slow scanning speed, flow measurements are not recorded frequently enough to give a sufficient representation of the fluctuating behaviour, which is why the errors are temporal in nature. When using a very fast scan, the quantisation of the flow is too coarse. In this case, small-scale flow structures cannot be mapped with sufficient accuracy, which leads to errors of a spatial nature. Between these extremes lies an optimal parameter set that can clearly depict spatial structures and temporal fluctuations in the flow.

A statistical approach can be used to determine the optimal parameters, and will guarantee that the recorded data is sufficient:

$$N_m \geq \left(\frac{z\,\sigma_m}{e}\right)^2, \qquad \text{Eq. 3.1}$$

where N_m is the required number of scans, z is the confidence interval, e is the maximum tolerable error, and σ_m is the standard deviation of the measurements [132]. The scan resolution or measurement frequency can be derived from the number of scans required to provide a statistical estimation of the mean value. The basic problem here is that the requisite standard deviation (σ_m) is unknown. In practice, this value can be calculated from additional measurements taken by instruments, like sonic or cup anemometers, or it can be estimated from previous LiDAR measurements to select appropriate LiDAR measurement parameters, like the angular-scan resolution.

The theoretical consideration of an optimal parameter set clarifies that many planar LiDAR measurements are recorded sub-optimally and may be statistically under-determined. Furthermore, for continuously optimal measurements, the measurement resolution will need to be adapted continuously to the variability in the flow. This adaptation requires a re-assessment of the data analysis and indicates that complex data-processing methods are in need of development.

In this study, we used simulated LiDAR data synthesised with a large-eddy simulation (LES) run in a LiDAR simulator (Section 3.2.2) to improve the error evaluation. We performed a parametric study of the measurement frequency to address the challenge of optimal measurement settings that can be used in real LiDAR measurement campaigns that may use a broad spectrum of measurement frequencies. The measurement parameters and trajectories used in these simulations were based on a real LiDAR measurement campaign of an onshore wind farm near Brusow in northern Germany, recorded in 2015 [14]. In the following, we first discuss real measurement parameters, as they provide a foundation for the variations that we used to generate LiDAR data from the LES, which are described afterwards.

3.2.1 Measurement Trajectories

During the measurement campaign, we were fortunately able to position two long-range LiDAR devices on a single nacelle. At first, the measurement campaign in Brusow was intended for the improvement of commercial measurements, but instead aimed at a specific investigation of wake deflections caused by specific yaw misalignments. For this purpose, one device was used for horizontal plan position indicator (PPI) scans and the other was used for vertical range height indicator (RHI) scans. This combination of scans forms two unsynchronised perpendicular measurement planes in the downstream direction, which sliced the wake in horizontal and vertical directions, as illustrated in Figure 3.1. The installation of the LiDAR on the nacelle offers the advantage of reducing the measurement elevation for the horizontal scans relative to that of ground-based scans, and avoiding obstacles when adjusting the scan orientation to align with the direction of the wind.

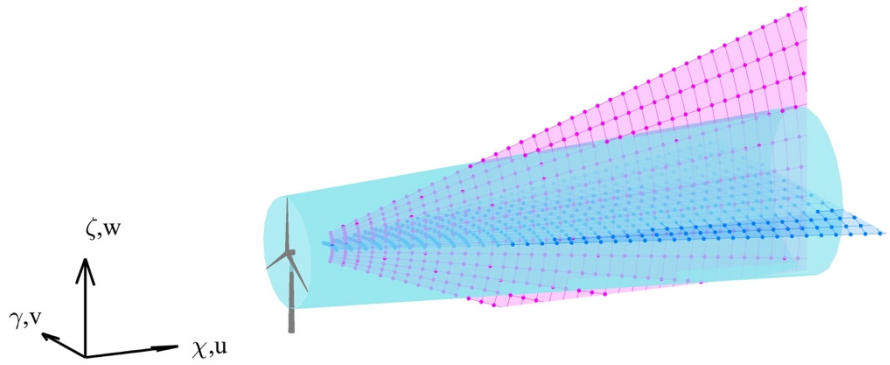

Figure 3.1. Illustration of cross-measurement trajectories. A horizontal PPI scan is shown in dark blue, and a vertical RHI scan is shown in pink. The wake volume is indicated in light blue.

Planar trajectories are executed either by fixing the elevation angle of the scanner (θ) and continuously changing the azimuth angle (ϕ) (PPI) or by fixing the azimuthal scanner orientation while varying the elevation angle (RHI). PPI scans are typically executed with a full 360° azimuth range, and RHI scans are typically executed with a full 180° elevation range. In the configuration used in the present study, we performed only sectoral scan patterns, which we refer to as PPI and RHI below for the sake of readability. Since only sectors were measured, the scanning head requires some reset time (t_r) to return to its initial position. As no previous such measurements or studies about nacelle-based wake measurements were available, the scanning parameters used in the 2015 measurement campaign were not chosen specifically for certain atmospheric conditions, but they were instead chosen for their potential use as universal settings for volumetric nacelle-based wake measurements.

The structure of the LiDAR devices dictates that the measurement data is given in a spherical coordinate system that has the typical characteristics of a polar grid, in which the planar point density decreases as the measurement distance increases. The measurement grid is determined by the radial measurement points along the laser beam and the accumulation time due to the angular velocity in relation to the total opening angles, $\Delta\phi$ and $\Delta\theta$. In the measurement trajectories that are actually executed, the total opening angles are defined symmetrically as:

$$\Delta\phi = |\phi_2 - \phi_1|, \qquad \text{Eq. 3.2}$$

and

$$\Delta\theta = |\theta_2 - \theta_1|. \quad \text{Eq. 3.3}$$

Measurement points were set in the radial direction in a range of 50 m to 1150 m at intervals of 7 m. During the measurements, we tested various accumulation times and found that ϑ_{acc} = 200 ms strikes a good compromise between the backscattering intensity and temporal resolution. The initial configuration for the angular speeds, ω_ϕ and ω_θ, was set to 2°/s, with total opening angles, $\Delta\phi$ and $\Delta\theta$, of 40°. These settings yielded angular resolutions, $\mathcal{R}_\phi$ and $\mathcal{R}_\theta$, of 0.4°.

3.2.2 Synthetic LiDAR Data

A large-eddy simulation based on the parallelized large-eddy simulation model (PALM) [133] and with the actuator line approach (ACL) [134] was used to calculate numerical approximations of the reference wake flow field behind the National Renewable Energy Lab's 5-MW model wind turbine [135] with a rotor diameter (D) of 126 m. We decided to run this LES in an offshore environment since we did not plan to compare the real LiDAR data directly with the synthetic data. Furthermore, the simulation of the LiDAR measurement parameters is not affected by the choice between onshore or offshore conditions. The atmospheric conditions corresponded to a mean wind speed (u_o) of 8 m/s at a hub height of 92 m with an ambient turbulence intensity (I_0) of 5.8 % at neutral stability. In these simulations, we used a 10-min time interval for the entire simulation, which therefore has a temporal resolution of 1 Hz and a spatial resolution of 10 m per grid cell in all three dimensions.

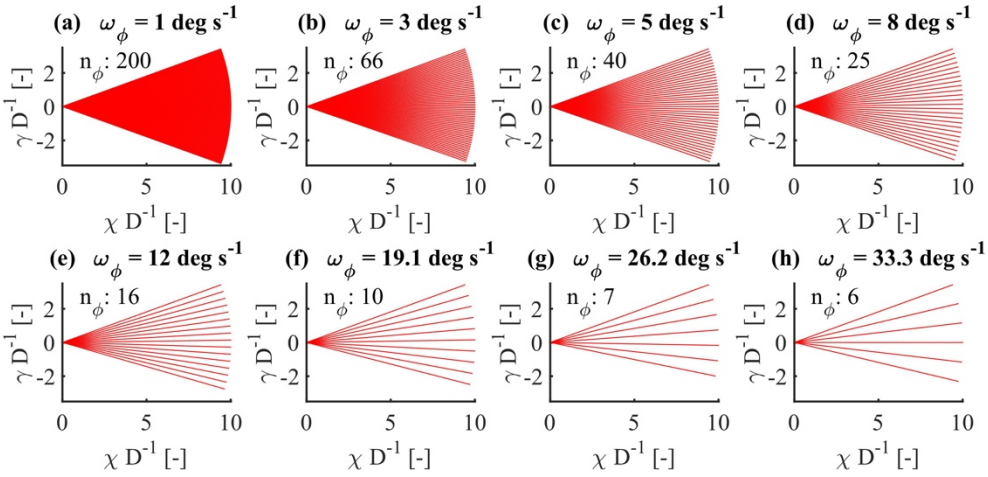

Figure 3.2. Illustration of the polar measurement grid of a PPI scan in the Cartesian χ-γ coordinate system. Each sub-figure plots the grid density for eight out of a total of eleven different angular velocities (ω_ϕ).

The varied parameter for the parametric analysis was the measurement frequency (f_s) as a function of the angular velocities, ω_ϕ and ω_θ. These parameters are listed in Table 3.1. Figure 3.2 shows that the spatial resolution of the measurement grid of the trajectories has a significant effect. To make this data comparable to actual LiDAR measurement campaigns, we chose reasonable and realistic scan durations and extended them to approach the upper physical limits of common commercial long-range LiDAR devices. We selected a total of 11 different angular velocities for each value of ω_ϕ and ω_θ and applied the accumulation time of ϑ_{acc} = 200 ms at the sampling frequencies of 0.024 - 0.417 Hz. The effect on the number of scans for each scan type within a 10-min interval (N_ϕ and N_θ), the number of measurement points (n_{pnt}) for each scan type, the number of angular measurements per scan (n_ϕ and n_θ), the angular resolution ($\mathcal{R}_\phi$ and $\mathcal{R}_\theta$), the

scan duration (T_ϕ and T_θ) and the measurement-time efficiency (η_m), all as a percentage of the total measurement time within a 10-min interval, are listed in Table 3.1. The coordinate system and the wind-speed components, as they are used below, are defined in Figure 3.1.

Table 3.1. Simulated LiDAR trajectories of cross-measurements for $n_r = 180$ and $T = 600$ s.

ω_ϕ, ω_θ	$\Delta\phi$, $\Delta\theta$	N_ϕ, N_θ	n_{pnt}	n_ϕ, n_θ	$\mathcal{R}_\phi$, $\mathcal{R}_\theta$	T_ϕ T_θ	f_s	η_m
1°/s	40°	15	36000	200	0.2°	40.0 s	0.024 Hz	97.2 %
2°/s	40°	29	18000	100	0.4°	20.0 s	0.047 Hz	94.2 %
3°/s	40°	42	11880	66	0.6°	13.3 s	0.068 Hz	91.0 %
4°/s	40°	54	9000	50	0.8°	10.0 s	0.089 Hz	89.2 %
5°/s	40°	66	7920	40	1.0°	8.0 s	0.011 Hz	86.8 %
6°/s	40°	77	6840	33	1.2°	6.7 s	0.127 Hz	84.6 %
8°/s	40°	97	4500	25	1.6°	5.0 s	0.161 Hz	80.6 %
12°/s	40°	133	2880	16	2.5°	3.3 s	0.221 Hz	73.4 %
19.11°/s	40°	183	1800	10	4.0°	2.1 s	0.303 Hz	63.4 %
26.22°/s	40°	221	1260	7	5.7°	1.5 s	0.370 Hz	55.8 %
33.33°/s	40°	250	1080	6	6.7°	1.2 s	0.417 Hz	50.0 %

With the simulated measurement trajectories, we aimed to reproduce measurement points that are comparable to those in the measurement campaign and maintain the radial resolution of 7 m. The related choices result in an overlap of the pulses emitted by the LiDAR as 81.3 % of the probe volume length of ~60 m. This resulted in the total number of radial ranges (n_r) being 180 at the radial distances of 1 to 1260 m. The point density of the Cartesian LES and the polar LiDAR measurement grid differ in the χ-direction because of the radial spread of the angular measurements, which is illustrated in Figure 3.2. Thus, numerical redundancies while interpolating within LES grid cells can only be prevented with an extremely finely discretised wind field and the necessary numerical and temporal capacities were not available within the scope of this study. Since the spatial resolution of the LES with 10 m per grid cell is coarser than the 7 m radial resolution of the LiDAR simulation, the permanent interpolation of the LES grid onto the LiDAR grid restricts our results to realistic behaviours. We expect that the standard deviation of the simulated LiDAR measurement will be lower than that of free-field measurements because of the interpolation from the polar to the Cartesian grid, but the main cause of this difference in the standard deviation is the much lower accumulation time of the LiDAR at $\vartheta_{acc} = 0.2$ s compared to the temporal resolution of the LES at 1 Hz. This difference is critical, so we cannot ensure the absolute transferability of the results presented in Section 3.4 to real LiDAR measurements taken from a free-field. Nevertheless, our analysis of the standard deviations gives some indication of trends in the wake behaviour.

However, to give simulated behaviour that is most similar to the full-scale measurements, we considered the reset time (t_r), which is needed by the LiDAR device to restart the trajectory. During this time, the LiDAR returns to the initial scanner position without recording any measurements. The repetition time of a scan is, therefore, the sum of the scan time (T_ϕ) and the reset time (t_r). The reset time (t_r) was derived from real LiDAR measurements and was set to t_r = 1.2 s for an opening angle of 40°. The following equations explain the formal relationship of the PPI and RHI trajectories. For the sake of brevity, only the PPI case is written out below:

$$\mathrm{T}_{\phi} = \frac{\Delta\phi}{\omega_{\phi}}, \quad \text{Eq. 3.4}$$

$$n_{\phi} = \frac{\mathrm{T}_{\phi}}{\vartheta_{acc}}, \quad \text{Eq. 3.5}$$

$$\mathcal{R}_{\phi} = \frac{\Delta\phi}{n_{\phi}}, \quad \text{Eq. 3.6}$$

$$\mathrm{N}_{\phi} = \left\lceil \frac{\mathrm{T}}{\mathrm{T}_{\phi}} \right\rceil, \quad \text{Eq. 3.7}$$

with $\mathrm{T} = 600\ s$ in the present study.

$$n_{pnt} = n_{\phi} \cdot n_{r}, \quad \text{Eq. 3.8}$$

$$\eta_{m} = 1 - \frac{\mathrm{t}_{r}}{\mathrm{T}_{\phi}}, \quad \text{Eq. 3.9}$$

$$f_{s} = \frac{1}{\mathrm{T}_{\phi} + \mathrm{t}_{r}}. \quad \text{Eq. 3.10}$$

For the calculation of N_{ϕ} and N_{θ}, we rounded up the scans that began in the 10-min interval, but did not finish within the interval. This rounding was not applied when determining η_{m} to visualise how the measurement time efficiency is changed by the different angular velocities.

We also normalised the coordinate system to the wind turbine rotor diameter (D).

We used the defined measurement trajectories listed in Table 3.1 when running the LIXIM LiDAR simulator developed at ForWind by Trabucchi [136], which was used by van Dooren et al. [55] to calculate velocity data from an LES wind field. In total, 2334 synthetic scans representing 11 different angular velocities were simulated within the same 10-min interval of the LES. As with the physical LiDAR measurements, the resulting velocity data are given in radial coordinates.

The limitations and peculiarities of numerically simulated LiDAR measurements have been investigated before. Stawiarski et al. [76] studied the errors that affect a simulated dual-Doppler LiDAR system. They found that the error in the determination of the radial velocity consists of a random error due to measurement inaccuracies caused by the speckle effect and detector noise, a systematic error due to the frequency shift of the laser, non-linear amplifiers, digitising errors and non-ideal noise statistics, and direction errors due to the imperfect adjustment of the LiDAR system and/or scanner movement. Together, these errors cause a projection error, like that described in Eq. 3.14. Träumner et al. [77] used simulated data to investigate the ability of dual-Doppler LiDAR systems to estimate turbulence length scales. The use of a LiDAR simulator in the present study is meant to represent an ideal LiDAR which, apart from volume averaging, does

not consider any other interference, as described by Stawiarski et al. [76]. This ideal simulation emphasises the peculiarities of the space-time conversion method discussed below.

Within the LIXIM software, we used the weighted average of the LOS velocity over the sample volume we considered. To this end, we defined a linear coordinate (s) in the beam direction and varied its orientation as shown in Figure 3.2 with different azimuth/elevation angles. The linear coordinate, s, represents the radial distance from the LiDAR to the measurement point. The range gate length corresponding to the spatial extension ($\Delta p = 36$ m) and the Gaussian-formed laser pulse with intensity, I_p, characterised by a full-width at half-maximum (Δr) of 30 m [137] were used to calculate the LOS velocity:

$$I_p(s) = \frac{1}{\sqrt{\pi}\Delta r} e^{\left(-\frac{s^2}{\Delta r^2}\right)}. \quad \text{Eq. 3.11}$$

The estimated LOS velocity is therefore:

$$\hat{v}_{LOS}(s) = \frac{1}{\Delta p}\int_{-\Delta p/2}^{+\Delta p/2} v_p(s)\, ds, \quad \text{Eq. 3.12}$$

where

$$v_p(s) = \int_{-k_p\frac{\Delta r}{2}}^{+k_p\frac{\Delta r}{2}} v_{r'}(s'-s)\, I(s'-s)\, ds', \quad \text{Eq. 3.13}$$

with $I = \frac{I_p(s)}{\int_{-\infty}^{+\infty} I_p(s)ds}$ and $k_p = 2.56$.

We are aware that the pulse intensity of a real LiDAR differs from the Gaussian representation in Eq. 3.11, but Frehlich used a similar Gaussian distribution [46] Stawiarski et al. [76] and Träumner et al. [77] used a similar weighting function. In other studies, the pulse shape was modelled with other approaches. Mann et al. [71] used an axisymmetric function that, according to Lindöw [138], reasonably approximates the distribution of the pulses emitted by the WindCube LiDAR system. Fuertes et al. [19] built on Mann et al. [71] for the pulse-weighting of a single LiDAR, but they used a 3D Gaussian function to evaluate three synchronised LiDAR measurements.

The choice of the laser pulse function directly affects the calculation of the LOS velocity. As can be deduced from Eq. 3.11, the radial velocity component is a weighted average of the pulse geometry. This averaging in the beam direction affects the resulting velocity, as it is affected by the velocity shear within the pulse geometry. In a wind field with constant laminar wind speed, volume averaging would have no effect. The stronger and faster the velocity shear within the probe volume, however, the greater the error in the accumulated speed. This influences the representation of the mean value and the standard deviation, which will thereby be underestimated in relation to the reference. Depending on the pulse shape that is assumed, volume averaging will have different effects.

As we used it, LIXIM was only able to calculate the spatial average in the radial direction, but not in the scanning direction. This provided deeper insight into step-and-stare measurements, in which the scanner stops and accumulates data for each measurement. This behaviour restricts the transferability of the resulting parameters to on-the-fly measurements, in which the scanner

continuously accumulates data as it moves. LiDAR measurements are usually taken on-the-fly to optimise measurement efficiency in terms of the measurement time. To give some insight into the peculiarities of on-the-fly measurements, we will subsequently introduce a planar average that accounts for this effect in Section 3.4.1.1.

3.3 Method

3.3.1 Wind-Speed Reconstruction

Since LiDAR provides 1D LOS velocities, we assume that horizontal and vertical wind directions are constant within the considered time interval (T) of the flow field. Thus, the streamwise wind-speed component (u) can be constructed relative to an external source of wind direction:

$$u = \frac{\hat{v}_{LOS}}{\cos(\phi')\cos(\theta')}, \qquad \text{Eq. 3.14}$$

where ϕ' is the difference between the horizontal wind direction, Φ, and the azimuth angle, ϕ, and θ' is the difference between the vertical wind direction, Θ, and the elevation angle, θ, as illustrated in Figure 3.3.

With nacelle-based measurements, we can assume that the wind direction tracking of the turbine is sufficiently good if no intentional yaw misalignment is present. Within the synthetic data, the lateral wind-speed component (v) and the vertical component (w) are assumed to average out to zero, though this assumption does not apply in the near-wake region ($\chi D^{-1} \leq 3$). Alternatively, the PPI scans we performed can be used to determine the wind direction at different downstream distances if we use the horizontal velocity azimuth display (VAD) fitting approach. In other cases, Φ and θ can be determined with external wind direction instruments, such as vertical profilers using VAD or Doppler-Beam-Swing (DBS).

Below, we will calculate the average velocity and its standard deviation in the u direction. This calculation applies Eq. 3.14 to the time series of LOS velocities of each point within the measurement area. The resulting statistics do not allow us to reconstruct the exact streamwise wind-speed component statistics. Even so, the implied assumptions are unavoidable when using LiDAR data without other external information or reconstructions based on turbulence spectra. We are aware that our calculation of the standard deviation of the projected wind-speed component (σ_u) differs from the standard deviation of the LOS velocities $\sigma_{\hat{v}_{LOS}}$ for $\phi' \neq 0$ and $\theta' \neq 0$ due to the non-linear dependence of the standard deviation of the LOS velocities $\sigma_{\hat{v}_{LOS}}$ on the standard deviations of the main wind-speed components (σ_u, σ_v, σ_w). Since the standard deviations of all wind-speed components in LiDAR measurements (σ_u, σ_v, σ_w) represent unknowns with no additional external measurements, Eq. 3.14 represents a pragmatic approach for projecting the LOS velocity time series onto the main wind direction, from which the standard deviation (σ_u) can be compared with the standard deviation of the LES ($\sigma_{u_{LES}}$).

The LOS velocities were projected scan-wise, and individual scans were interpolated onto a Cartesian (χ-γ or γ-ζ) coordinate grid using the natural-neighbour interpolation [142].

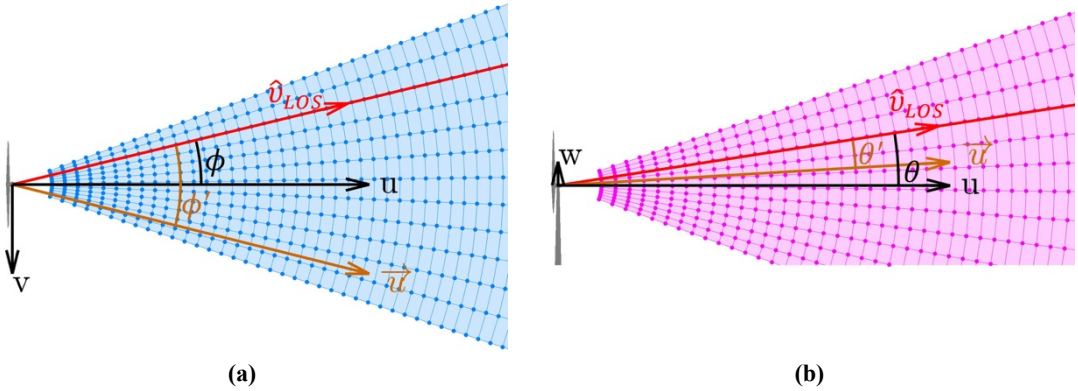

Figure 3.3. Illustration of the measurement geometry, including the wind vector, $\vec{u}$, the azimuth angle, (ϕ), and the elevation angle, (θ), of **(a)** a horizontal PPI scan and **(b)** a vertical RHI scan. The red line indicates the LiDAR laser beam.

3.3.2 Wind-Field Propagation

For most wind speed analyses that aim to give wind speed averages, the recorded scans can be assumed to be quasi-instantaneous. The time shift within a scan is relatively small when compared to the total averaging time. In contrast, if certain dynamics will be calculated or derived from the wind-speed measurements, a high-resolution time series will be needed. If the measurement frequency of points within the measurement region is higher, the conclusions about the dynamics will be more accurate. When analysing scanned wake measurements, special attention must be paid to the temporal shift within a scan, as this temporal shift means that the scan does not show the flow situation at one moment, but instead covers a time interval. When scanning cross-wise in the flow direction, characteristic flow structures are distorted depending on their expansion and flow velocity. If the scan direction is parallel to the flow direction, flow structures may be distorted or may be imaged several times in a single scan, depending on the flow dynamics and scan velocity. This effect is relevant when determining the wake deficit of a wind turbine or when determining the dynamics at the centre of the wake in the downstream direction. Two aspirations are joined with this effect: (1) Our aim is to improve on the temporal resolution and (2) to give a temporally realistic representation of the scanned data. As Section 3.3.3 will show, the improvement of the temporal resolution improves the physical realism of the data.

Table 3.1 shows that planar scans are typically taken over intervals from 1.2 s to 40 s. The scan-repetition time limits the temporal scale of the data that can be analysed and synchronised with simultaneously measured data. As mentioned in Section 3.1, the correlation of flow structures with atmospheric or turbine-measured data is essential for identifying specific synergies in the LiDAR measurements.

The approach used in the following space-time conversion is chosen to meet the requirement that a characteristic flow situation be measured several times in sequence. Depending on the flow velocity and the measurement range, this limits the region in which wind-field propagation can be applied. According to the requirement that a flow situation be measured in two or more consecutive scans, we can use the laws of fluid dynamics to convert the spatial wind velocity information collected in a scan into temporally expressed information. This general idea has been used in other studies to interpolate or extrapolate flow situations from measurements or defined states. Schneiders and Scarano [139] reconstructed instantaneous flow fields from time-resolved

volumetric particle tracking velocimetry (PTV) measurements using multidimensional velocity measurements and their derivatives. Their vortex-in-cell plus (VIC+) method relies on the calculation of vorticity, which in turn requires at least 2D velocity information, which cannot be collected with a single LiDAR system. Like the approach we describe below, Rott et al. [140] used a semi-Lagrangian advection scheme and a stepwise flow solver to estimate the available power during the curtailment of a wind farm by forecasting the flow dynamics and aerodynamic interactions between the turbines. Valldecabres et al. [141] applied the hypothesis of frozen turbulence [39] with local topographic corrections to forecast wind speeds at specific downstream positions from LiDAR measurements taken over the very-short term.

In this chapter, we propose a model that describes how the flow evolves between subsequent scans, which we then apply to achieve continuous closure of planar LiDAR data over time at a specific downstream position. This approach assumes that the measured air parcels evolve downstream along with the local streamwise velocity. This implies that the air parcels do not adhere to Taylor's frozen turbulence hypothesis that assumes advection with a global mean velocity [39]. Like the approach of Rott et al. [140], the following approach can be described using a semi-Lagrangian scheme. At each time step (t), the velocity data on a grid point is interpreted as a parcel of air that is free to move with its own velocity ($u \in \mathbb{R}$) and direction ($\vec{u} \in S^1 \subset \mathbb{R}^2$), with $S^1 \coloneqq \{(\chi, \gamma) \in \mathbb{R}^2 \mid \sqrt{(\chi^2 + \gamma^2)} = 1\}$. This can be understood as an interpretation of Taylor [39] that applies to small spatial and temporal scales.

The advection of each parcel can be approximated in a discretised fashion using the following equation:

$$\frac{\partial u(\chi, \mathrm{t})}{\partial t} = -u(\chi, \mathrm{t}) \cdot \nabla u(\chi, \mathrm{t}), \qquad \text{Eq. 3.15}$$

$$u(\chi, t + \Delta t) = u(\chi, t) - \Delta t \cdot u(\chi, t) \cdot \frac{\delta u(\chi, \mathrm{t})}{\delta \chi}, \qquad \text{Eq. 3.16}$$

$$u(\chi, t + \Delta t) = u(\chi, t) - \Delta t \cdot u(\chi, t) \cdot \frac{u(\chi, t) - u(\chi - \Delta\chi, t)}{\Delta \chi}, \qquad \text{Eq. 3.17}$$

with $\frac{\Delta\chi}{\Delta t} = u(\chi, t)$ respectively $\Delta\chi = u(\chi, t) \cdot \Delta t$. Note that this equation is given in only one dimension because it is projected on the affine subspace $\chi + \lambda\vec{u} \subset \mathbb{R}^2$, with $\lambda \in \mathbb{R}$. This representation gives:

$$u(\chi, t + \Delta t) = u(\chi, t) - \big(u(\chi, t) - u(\chi - \Delta t \cdot u(\chi, \mathrm{t}), t)\big), \qquad \text{Eq. 3.18}$$

$$u(\chi, t + \Delta t) = u(\chi - \Delta t \cdot u(\chi, \mathrm{t}), t), \qquad \text{Eq. 3.19}$$

where $\Delta\chi$ is the distance that the given air packet travels in one time step (Δt). If we define $\chi_{old} \coloneqq \chi - \Delta t \cdot u \cdot \vec{u}$ as the initial position of the packet on the regular Cartesian grid, Eq. 3.19 shows that, at the next time step, $t_{new} \coloneqq t + \Delta t$, each parcel transports its own velocity and direction to its new location via advection ($\chi = \chi_{old} + \Delta t \cdot u \cdot \vec{u}$). This means that parcels on the regular Cartesian grid are displaced to an irregular grid. To resolve the new velocity field in the original grid, the velocities in the intermediate grid are interpolated onto the initial grid using natural-neighbour interpolation [142].

To give an example of this method, we initialise this space-time conversion approach using a scan from Section 3.2.2 at t_n and iterate it with selected temporal resolutions (Δt) to the time interval of the subsequent scan (t_{n+1}). Comparing the iterated and interpolated scans at t_{n+1} with the processed LiDAR scan at t_{n+1}, the flow structures are subjected to numerical diffusion and smoothed out by the subsequent interpolation. To minimise the multiplication of errors with multiple iterations, we applied a mixed propagation approach with the temporal weighted average of forward- and backward-oriented propagations.

In the backwards-oriented propagation, we initialise the process with a negative time step ($-\Delta t$) that causes the air parcel at t_{n+1} to propagate backwards in time to t_n. The sinusoidal function, $w_n(t)$, is used to calculate the weighted average of forward and backward propagations in order to minimise numerical diffusion and to guarantee continuous advection with no unphysical gaps.

We are aware that fluid-mechanical mixing processes are irreversible. We assume, however, that the spatial scale of the mixing process is considerably smaller than the spatial resolution of the measurements, so irreversibility is not a concern. We define $t \in \{\mathbb{R} \mid t_n \leq t \leq t_{n+1}\}$ and:

$$w_n(t) = \begin{cases} 1 & , t \leq m_c - \frac{m_r}{2} \\ \frac{1 + \cos\left(\frac{\pi}{2} + \frac{\pi}{m_r}\left(\frac{t}{t_{n+1}} - m_c\right)\right)}{2} & , m_c - \frac{m_r}{2} < t < m_c + \frac{m_r}{2} \\ 0 & , m_c + \frac{m_r}{2} \leq t \end{cases}. \qquad \text{Eq. 3.20}$$

Thus, the weighting function, $w_n(t)$, has total width of $t_{n+1} - t_n$ and gives variable results in the range from $t > m_c - \frac{m_r}{2}$ to $t < m_c + \frac{m_r}{2}$. The variable, m_c, serves as the point in time between t_n and t_{n+1} at which the weighting functions, $w_n(t)$, for forward propagation and $1 - w_n(t)$ for backwards propagation are in equilibrium. The variable, $m_r = \frac{4}{5}(t_{n+1} - t_n)$, represents the centred window around $m_c = \frac{2}{5}t_n + \frac{3}{5}t_{n+1}$, within which $w_n(t)$ can take values between 1 and 0. Outside of m_r, the weighting function is either 1 or 0. The shift in the centre of the weighting function (m_c) towards t_{n+1} suggests the greater effect of forward propagation compared with the backwards propagation, which accords with the irreversibility of the mixing processes. The behaviour of the weighting functions is illustrated in Figure 3.4. This treatment of $w_n(t)$ and the configuration of m_r and m_c were developed in an unpublished internal study that we will only outline briefly here.

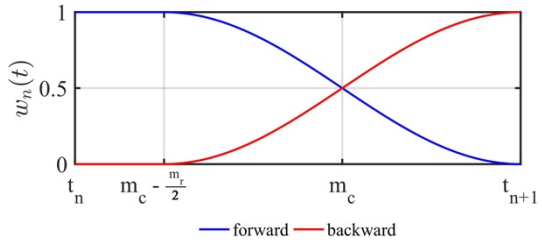

Figure 3.4. Example of the weighting function $w_n(t)$ for forward propagation (blue) and the function $1 - w_n(t)$ for backwards propagation (red).

Different approaches for mixing functions were tested in parametric studies to find the functions that give the smallest error of mixed propagation in comparison to the mean and standard deviation of the LES reference wind-speed values. We tested a linear approach, an

exponential approach, and the trigonometric approach that we eventually used. The exponential increase in the error with each interpolation step was damped the most robustly when using the trigonometric function.

The definition of wind-field propagation implies that Δt is the variable that determines the error. The number of interpolation steps (Π_ϕ,Π_θ) between two subsequent scans depends on this interval. We define the number of propagation steps between two scans as:

$$\Pi_\phi = \left|\frac{T_\phi + t_r}{\Delta t}\right|, \qquad \text{Eq. 3.21}$$

with $\Pi_\phi \in \mathbb{N}$.

3.3.3 Temporal Correction and Data Synchronisation

Since planar LiDAR measurements are recorded with temporally distributed scans, each scan maps the evolution of flow over the scanning period. This temporal shift within the scan increases with longer scan duration, making scanned measurements difficult to compare with measurements that are presented in instantaneous form. The temporal correction method discussed in this chapter is intended to align the temporal shift within a scan so the flow situation at a single moment in time can be expressed. The refinement of the temporal resolution to scales less than that of the measurement, as introduced in Section 3.3.2, lays the foundation for the temporal correction.

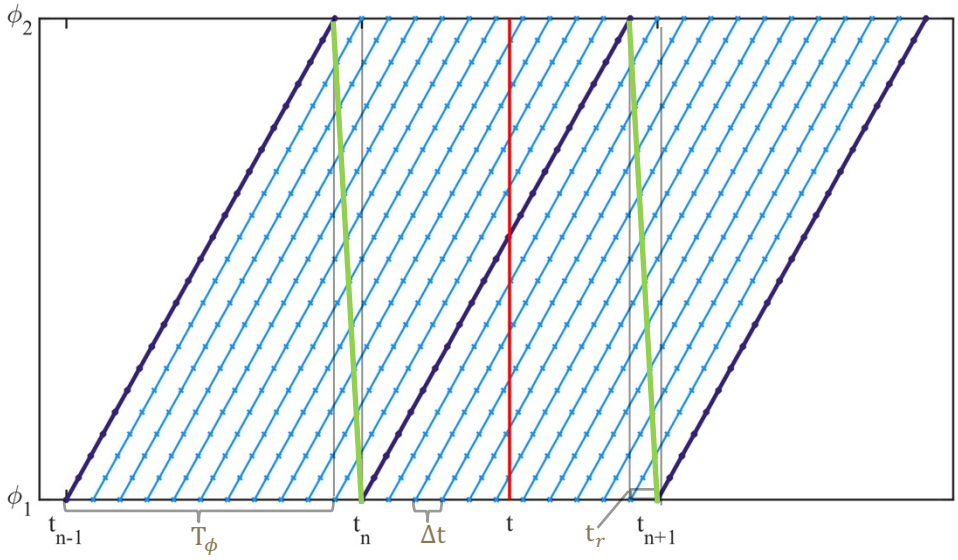

Figure 3.5. Temporal alignment of a PPI scan at time t. Dark-blue lines indicate LiDAR measurements, light-blue lines indicate the propagation steps, green lines indicate the measurement reset time (t_r) and the red line marks the time of interpolation. This example shows $N_\phi = 11$.

The time interval of each scan can be described as $T_n = [t_{n,1}, t_{n,2}] := \{t_{n,\chi} \in T_n \mid t_{n,1} < t_{n,\chi} < t_{n,2}\}$, where $t_{n,1}$ and $t_{n,2}$ are the beginning and end of the scan. Since the azimuth angle (ϕ) and the elevation angle (θ) are functions of time, they can be expressed as $\phi(t_{n,\chi})$ and $\theta(t_{n,\chi})$. As the time gaps between $\phi(t_{n,\chi})$ and $\phi(t_{n+1,\chi})$ and between $\theta(t_{n,\chi})$ and $\theta(t_{n+1,\chi})$ are closed with discrete interpolation steps because of the mixed wind-field propagation, 3D natural-neighbour interpolation can be applied at time t [142]. The first two dimensions represent the scanned measurement area and the third dimension represents time. Figure 3.5 illustrates the temporal correction method and the 3D interpolation in 2D form, and

the measurement area is represented as the scan angle, $\phi(t)$,$\theta(t)$, over time. The propagation steps (light-blue lines) between two consecutive scans (dark-blue lines) are indicated by their slope, such that the measurement result and the refinement of the temporal resolution represent the measurement area over a time interval. By choosing the interpolation time step (Δt) carefully to give an integer number for interpolation (Π), we can exclude the reset time of the scanner (t_r) (green lines), during which no measurements are captured. As shown in Figure 3.5, 3D interpolation is used to give the values of wind speed over the entire measurement area at the moment (t) (red line).

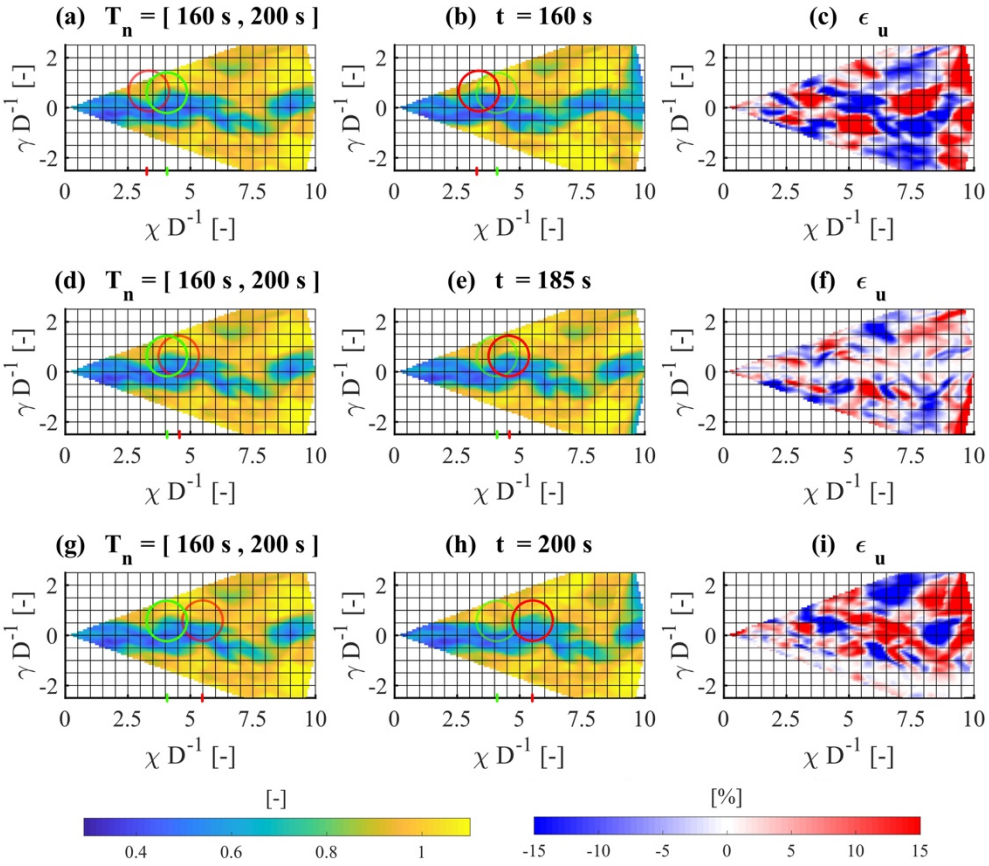

Figure 3.6. Example of the temporal correction for a time shift with a PPI scan. The first column **(a, d, g)** shows the original LiDAR scan in the time interval $T_n = [160\text{ s}, 200\text{ s}]$. The second column **(b, e, h)** shows the temporal improved and corrected data at **(b)** $t = 160$ s, **(e)** $t = 185$ s and **(h)** $t = 200$ s. The third column **(c, f, i)** illustrates the instantaneous wind-speed deviations of the data in the first and second columns. The green circles mark the characteristic wake structure within the original PPI scan. The red circles indicate the propagated position of the same characteristic wake structure within the time-aligned data at the defined time points.

When a smaller value of Δt is chosen, the temporal correction will have finer spatial resolution, since the spatial coverage is time-dependent. With the application of the temporal correction, measurements taken over a period of time can be interpolated into the same time and can thereby be synchronised to a single moment. Next, the RHI and PPI scans are synchronised to match the temporal resolution of the reference LES wind-field data.

The possibility of synchronising time-series data is not entirely novel. Cheynet et al. [143] shifted a time series of pulsed LiDAR data statically to a certain time using Taylor's approach [39] to calculate the data's coherence. While this approach retains the time-series dynamics, our method instead gives a new planar time series of data.

Figure 3.6 shows an example scan with $\omega_\phi = 1°/s$, from which the effect of the temporal alignment can be seen within the planar scans. The first column (Figure 3.6a,d,g) shows the original LiDAR data measured in the time interval, $T_n = [160\ \mathrm{s}, 200\ \mathrm{s}]$. In the second column (Figure 3.6b,e,h), we see the temporal improved and corrected wake velocity data at the start of the scan at $t = 160$ s (Figure 3.6b), at the middle at $t = 185$ s (Figure 3.6e) and at the end at $t = 200$ s (Figure 3.6h). The third column (Figure 3.6c,f,i) visualises the instantaneous wind-speed deviations of the original LiDAR scan to the corrected data. While in the original scans, in Figure 3.6a,d,g, the green marked characteristic wake structures have the same downstream position for the time interval (T_n), it can be seen in the corrected data in Figure 3.6b,e,h that the positions of the red marked structures differ clearly from the green markings at individual points in time (t). We chose these three time points in order to show the effect of temporal alignment using the most common time sampling types, which set the time stamp either at the beginning of the measurement (Figure 3.6a-c), at the middle of the scan (Figure 3.6d–f), or at the end of the scan (Figure 3.6g–i). From the different positions of the green and red markers and with regard to the large wind-speed deviations in Figure 3.6c,f,i, we emphasise the relevance of the temporal correction again. However, the extent to which the temporal correction influences the results of the analysis of dynamic processes, like wake centre tracking or load time-series correlation, was not within the scope of the results in Section 3.4 and should be investigated in other studies.

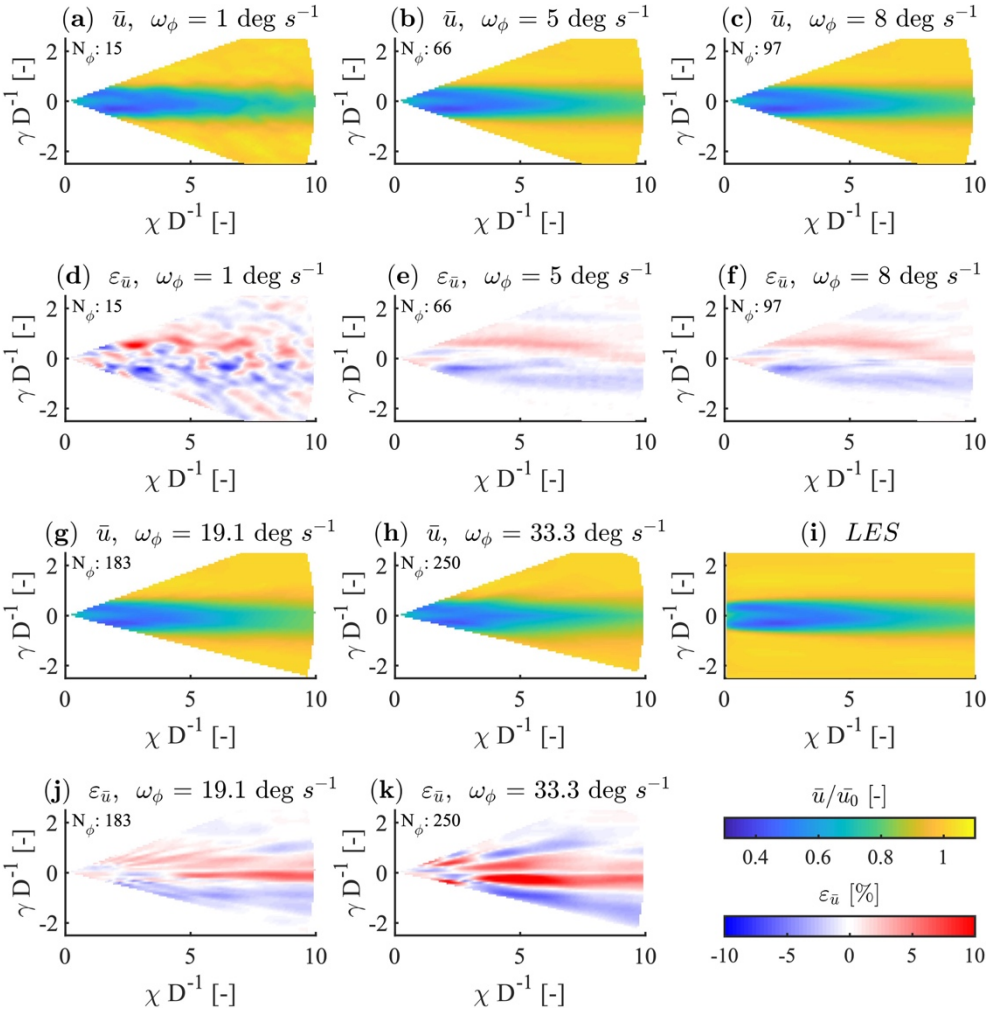

Figure 3.7. **(a–c, g, h)** Visualisation of the normalised 10-min averaged wind-speed component ($\bar{u}$) of the original PPI data and **(d–f, j, k)** the corresponding flow deviations ($\varepsilon_{\bar{u}}$) in comparison to **(i)** the normalised 10-min averaged wind-speed component ($\bar{u}$) of the LES data.

3.4 Results

This section first discusses the results of the synthetic LiDAR data with different angular velocities (ω_ϕ) in Section 3.4.1. These results are related to the angular velocity instead of the measurement frequency, since the angular velocities are easier to differentiate in terms of typography. We describe the effects of the space-time conversion with different propagation time steps (Δt) on the mean wind speed and its standard deviation in Section 3.4.2. For the sake of readability, we do not present detailed results of all the scan velocities we evaluated, instead illustrating only a selection of the data. We report all the results related to the RHI measurements in the appendix. We previously normalised all the wind speeds with a 10-min free-stream average and with the corresponding free-stream wind-speed profile, so the velocities are dimensionless in our presentation.

3.4.1 Calculation of Synthetic LiDAR Data

The LiDAR simulation was applied to synthesise a 10-min wake flow field, yielding the horizontal and vertical measurements summarised in Table 3.1. The resulting scanning times limit both the spatial and temporal resolution. One can see in these results how the choice of different scanning speeds affects the mapping accuracy of successive LiDAR scans. For error analysis, we evaluated the data at downstream distances of $4 \leq \chi D^{-1} \leq 9$ to compare this data with the propagated data described in Section 4.2. The RHI results that correspond to the data in Figure 3.7 and Figure 3.8 are presented in Appendix 3.A . Nevertheless, in this section, we summarised the RHI data in Figure 3.9b.

Slow scan speeds yield fine spatial and coarse temporal resolution and fast scan speeds give the opposite resolutions. These effects are shown in the visualisation of the 10-min averaged wind speeds shown in Figure 3.7 and the distribution of the standard deviations shown in Figure 3.8. The low temporal resolution is indicated by the wavy flow structures along the wake in the plot of average wind speeds in Figure 3.7a,b,d,e and in the standard deviations in Figure 3.8a,b,d,e. These features arise because the number of scans is not sufficient to form a smooth flow field, as stated in Eq. 3.1. In contrast, structural artefacts of quantification by the laser beam along the wake can be seen in Figure 3.7c,f,g,h,j,k, which indicate that the spatial resolution is lower than the LES averages in Figure 3.7i. The strip-shaped structures in the standard deviation (Figure 3.8c,f,g,h,j,k) indicate the limits of the LIXIM LiDAR simulator, which does not reproduce volume-averaging behaviour in the scanning direction. The quantisation of the measurement area with single beams can be seen in the reduction of the standard deviation. Since no measurements are recorded between the individual laser beams, the standard deviation cannot be higher than it is directly on the beams due to the interpolation from inter-polar coordinates to the Cartesian grid. Thus, we see a transition from good spatial to good temporal resolution as the angular velocity changes from 1.00°/s to 33.33°/s. While the variation of the angular velocity apparently has a minor influence on the measurement of the structure of the average wake velocity, the expected under-estimation of the standard deviation caused by volume averaging and the measurement frequency (f_s) can be seen in the wake region as the angular velocity (ω_ϕ) increases (Figure 3.8g and Figure 3.8h).

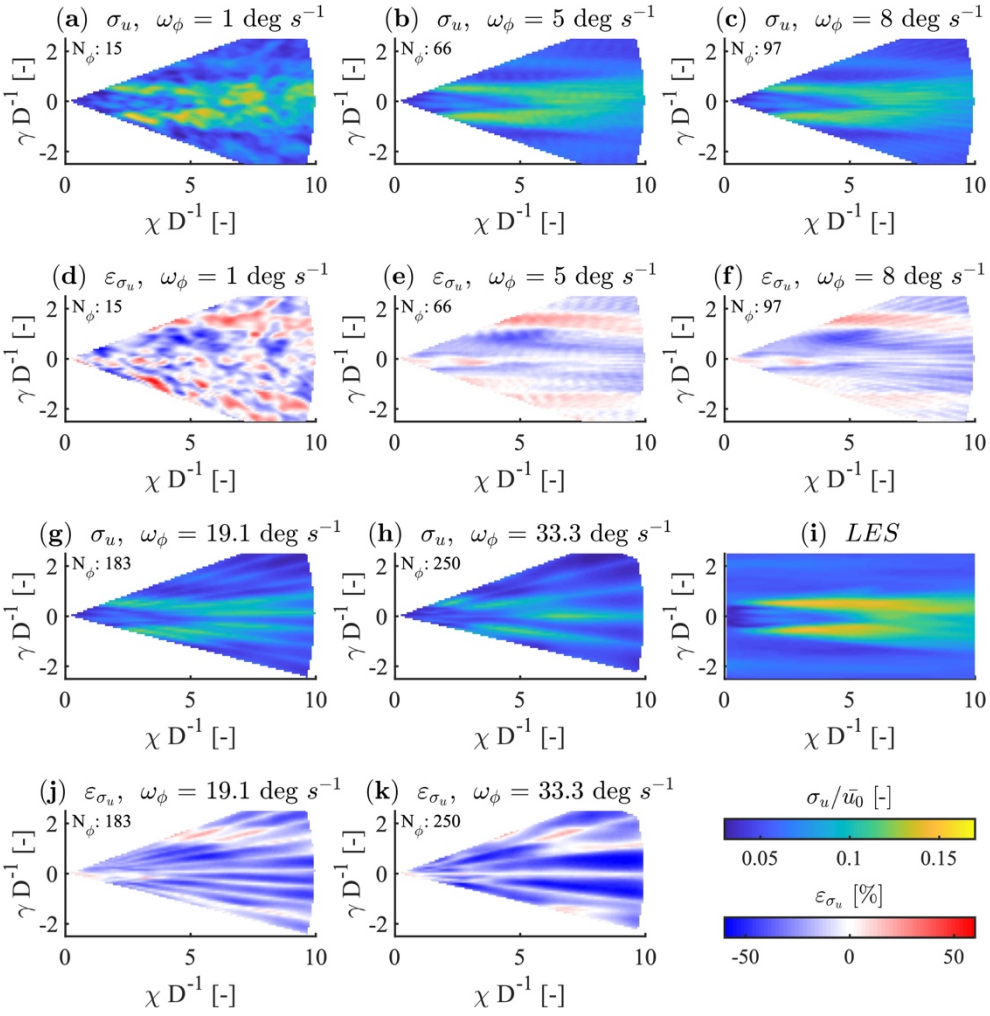

Figure 3.8. **(a–c, g, h)** Visualisation of the normalised 10-min standard deviation (σ_u) of the wind-speed component (u) of the original PPI data and **(d–f, j, k)** the corresponding deviations (ε_{σ_u}) from **(i)** the normalised 10-min standard deviation of the wind-speed component (u) in the LES data.

3.4.1.1 Error Case Discrimination

We determine the deviation from the LES by defining an average velocity error:

$$\varepsilon_{\bar{u}} = \frac{\overline{u_{lidar}} - \overline{u_{LES}}}{\overline{u_{LES}}}, \qquad \text{Eq. 3.22}$$

and the standard-deviation error,

$$\varepsilon_{\sigma_u} = \frac{\sigma_{lidar} - \sigma_{LES}}{\sigma_{LES}}, \qquad \text{Eq. 3.23}$$

where N_{lidar} is the number of velocity points included in the original LiDAR data, while N_{LES} is the number of corresponding velocity points in the LES data. Note that u is normalised before this step, so that $\varepsilon_{\bar{u}}$ and ε_{σ_u} are dimensionless and are given in percentages.

For a more detailed analysis, we distinguished three regions of errors:

- Error at the centreline in the wake: $\gamma D^{-1} = 0$ and $\zeta D^{-1} = 0$.
- Planar wake error: $-1 \leq \gamma D^{-1} \leq 1$ and $-1 \leq \zeta D^{-1} \leq 1$.
- Error in the free stream outside of the wake (opposite the planar wake case).

We introduce these three groups of errors to clarify the added volume-averaging error in the scanning direction. Since this effect is not reproduced in the LiDAR simulator, we attempted to account for it by posteriorly averaging the planar error. The aim of this process was not exactly

to recreate the scan-wise volume averaging in the measured data, but instead to reproduce a similar trend. As a result, the first case, considering data on the centreline, reproduces the step-and-stare measurement behaviour. The second case, planar wake error, resembles the behaviour of on-the-fly measurements. The third case considers free-stream error in the measurements of flow outside of the wake.

The plots in Figure 3.9 show the behaviour of $\varepsilon_{\overline{u}}$ and ε_{σ_u} for each of the three types of error, depending on the scan speeds, ω_ϕ and ω_θ. As mentioned above in Section 3.1, the largest errors occur at the extremes of very slow and very fast measurements. In general, similar behaviour is seen in all the errors in the PPI and RHI measurements. The errors are high at the scanning speed of 1°/s, decrease as the scan speed increases until the minima are reached, and increase again up to the speed of 33.33°/s.

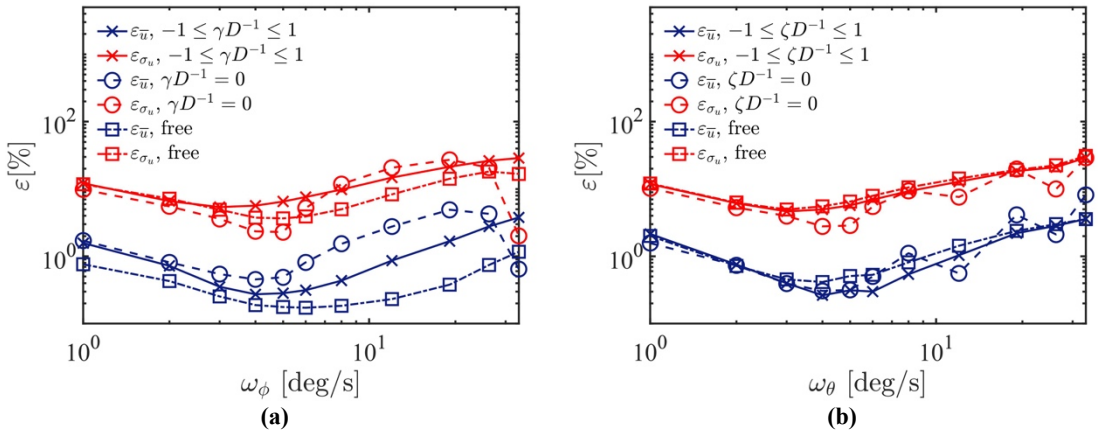

Figure 3.9. Velocity error ($\varepsilon_{\overline{u}}$, blue) and standard-deviation error (ε_{σ_u}, red) of synthetic LiDAR data as compared against the LES for the planar section (crosses), centreline (circles) and free-flow region (squares) of **(a)** PPI scans and **(b)** RHI scans.

Mean-value error ($\varepsilon_{\overline{u}}$) and the standard-deviation error (ε_{σ_u}) emerge along the centreline in the RHI scans, $\zeta D^{-1} = 0$. At the scanning speed of $\omega_\theta = 8°/s$, these errors are more scattered than the other errors. In addition, the centreline errors in the PPI scans show an unexpectedly low value at the scanning speed of $\omega_\phi = 33.33°/s$, which we are unable to explain. The wind-speed data along the centreline is clearly affected the least by the change between the polar and Cartesian coordinate systems, since the scan geometry and the resulting distribution of angular measurements cover this line more consistently than other positions with measurement points. While all errors in the RHI and PPI scans decrease along with increasing angular speeds, the ensemble minimum occurs at approximately 5°/s. The centreline error increases dramatically after 5°/s. The logarithmic representation in these plots makes it difficult to recognise the point symmetry of the error behaviour. The PPI error is symmetric around the minimum at $\omega_\phi = 4°/s$ and $\varepsilon_{\overline{u}}$ = 0.46 %. The minimum of the standard deviation is found at $\omega_\phi = 5°/s$ and ε_{σ_u} = 2.29 %. In the RHI scans, errors of the same magnitude are seen at $\omega_\theta = 4°/s$ with $\varepsilon_{\overline{u}}$ = 0.31 % and at $\omega_\theta = 4°/s$ with ε_{σ_u} = 2.78 %.

By averaging all points in the wake, $-1 \le \gamma D^{-1} \le 1$ and $-1 \le \zeta D^{-1} \le 1$, the representation of wind speed with the LiDAR measurements is improved. The average wind-speed error ($\varepsilon_{\overline{u}}$) is smaller than the centreline error in the PPI and RHI scans. However, since the standard-deviation error (ε_{σ_u}) is more pronounced than the mean wind-speed error ($\varepsilon_{\overline{u}}$), we conclude that volume averaging of the LiDAR measurements and the associated time shift within

the scans accurately reproduces the mean wind speed, although the measured values are widely dispersed. In this case, the minimal error of the standard deviation is $\varepsilon_{\sigma_u} = 5.40$ % at $\omega_\phi = 3°/s$ for the PPI scans and $\varepsilon_{\sigma_u} = 4.98$ % at $\omega_\theta = 3°/s$ for the RHI scans. This minimum indicates that the local turbulence intensity averaged over the wake can be reproduced with an accuracy of ~5 % in absolute terms.

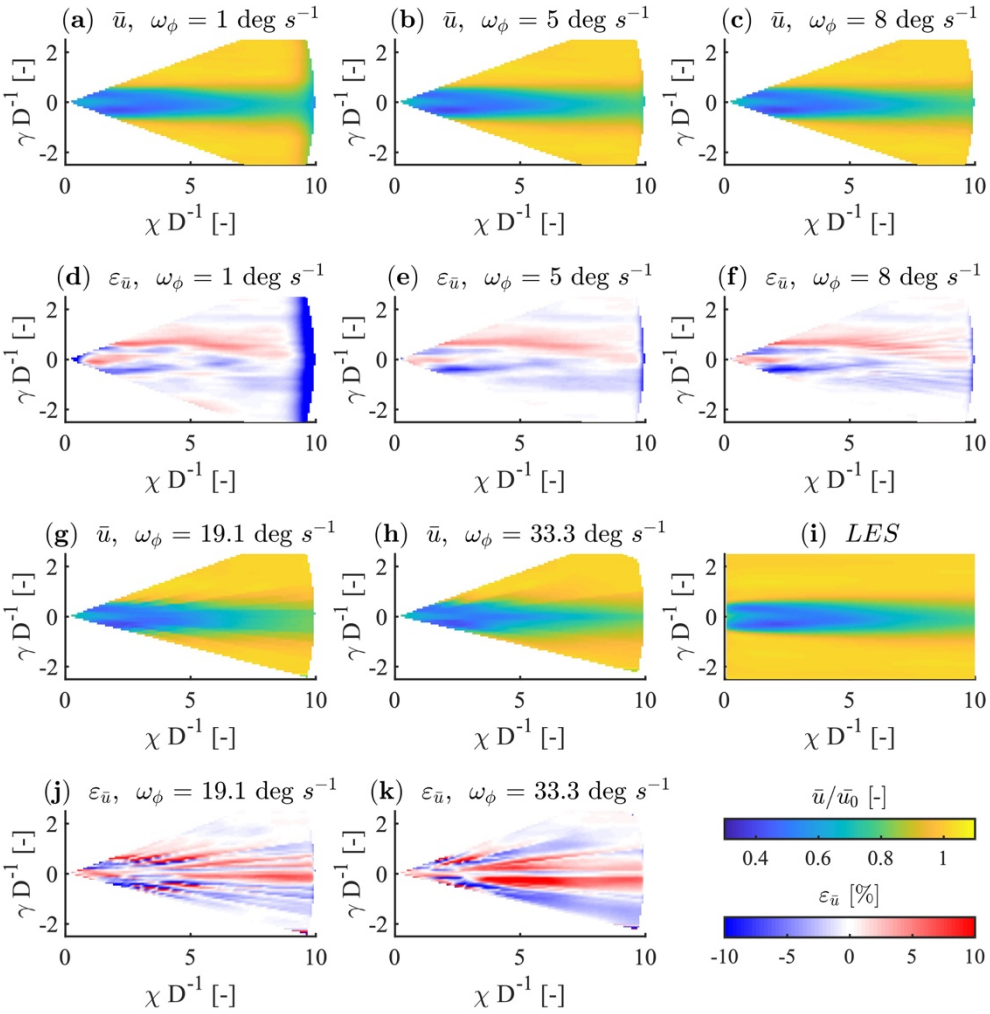

Figure 3.10. Visualisation of the normalised 10-min averaged wind-speed component ($\bar{u}$) of the propagated PPI data and **(d–f, j, k)** the corresponding flow deviations ($\varepsilon_{\bar{u}}$) in comparison to **(i)** the normalised 10-min averaged wind-speed component ($\bar{u}$) of the LES data

As expected, the free-flow errors for the PPI scan are the lowest of any in our analysis. Since the RHI scans mainly map the wake due to the scan geometry (Figure 3.9), free flow could not be defined exactly. These values are given for completeness, but should not be used for drawing generalised conclusions. The PPI free-stream error shows similar behaviour to that of the averaged wake errors, which is likely due to the process of area averaging. The errors are scaled over the scan speeds towards lower values. The minimum of $\varepsilon_{\bar{u}} = 0.17$ % occurs at $\omega_\phi = 6°/s$, and the minimum of $\varepsilon_{\sigma_u} = 3.68$ % occurs at $\omega_\phi = 5°/s$, which are comparable to the centreline errors. Since the turbulence intensity increases considerably compared to the ambient conditions in the high-shear areas of the wakes (Figure 3.8i), we deduce that, with lower turbulence intensities, the mapping error is minimal so the optimal scanning speed is faster. This relationship means that the more a flow fluctuates, measuring spatial structure becomes more important than measuring temporal changes.

The data corresponding to Figure 3.9 is listed in Table 3.4 and Table 3.5 in Appendix 3.B .

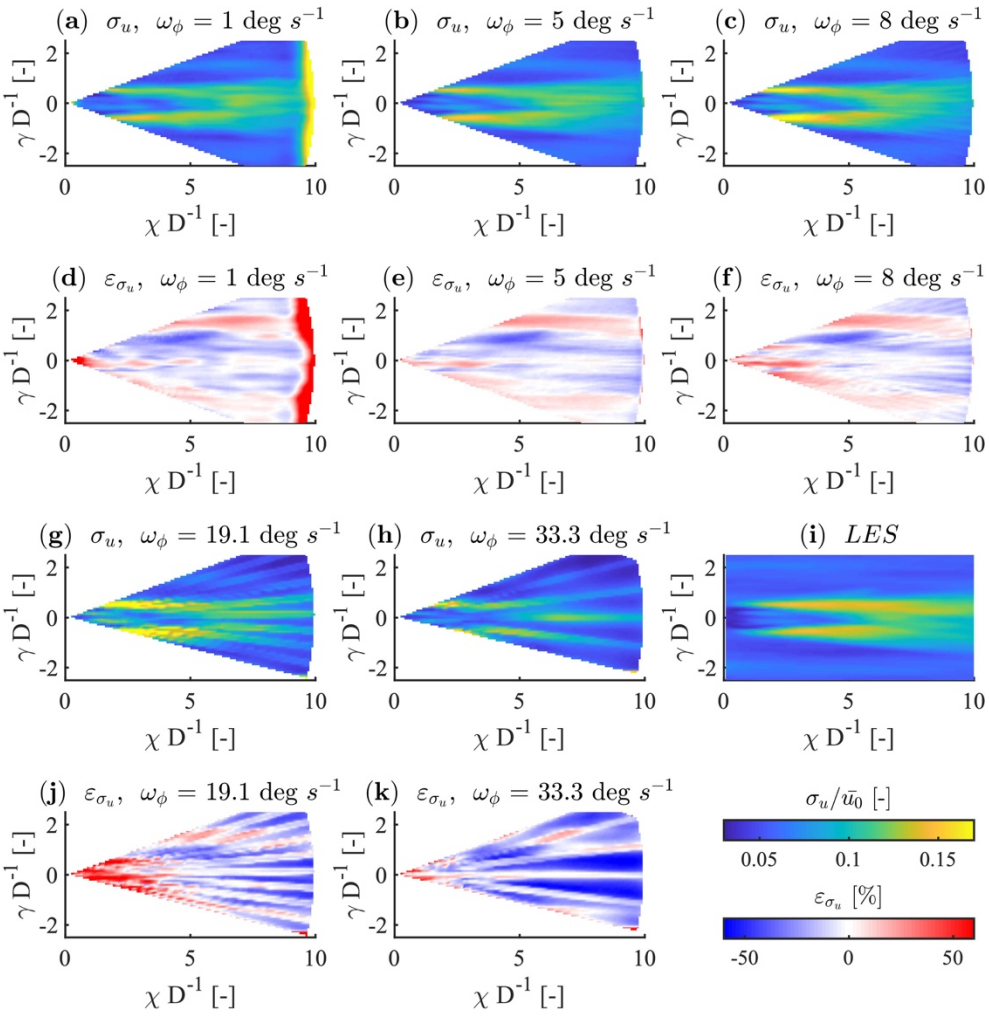

Figure 3.11. Visualisation of the normalised 10-min standard deviation (σ_u) of the wind-speed component (u) of the propagated PPI data and **(d–f, j, k)** the corresponding deviations (ε_{σ_u}) in comparison to **(i)** the normalised 10-min standard deviation of the wind-speed component (u) of the LES data.

3.4.2 Time-Resolution Improvement

To evaluate the effects of increasing the temporal resolution of the synthetic LiDAR data, we first propagated the LiDAR scan backwards and forwards using the wind-field propagation method described in Section 3.3.2 to obtain a mixed and closed space-time conversion. Then, we compared the propagated scans with the reference LES wind field. We corrected the scan-containing time error and synchronised the propagated data with the LES time data. In this sub-chapter, we first discuss the effect of the propagation on the temporally averaged values, like the mean value and the standard deviation, before we address the dynamic behaviour. The following results are based on the averages of the optimal time steps achieved in Section 3.4.3. For the results herein, we used $\Pi_\phi = 16$ as the number of interpolation steps for the PPI data and $\Pi_\phi = 14$ for the RHI data. The influence of $\Pi_{\phi,\theta}$ is discussed in Section 3.4.3. We present all the RHI-related results in Figure 3.17 in Appendix 3.B.

Figure 3.10 illustrates the averaged wind speed ($\bar{u}$) of the propagated PPI data, which are analogous to the original PPI data shown in Figure 3.7. As with the original LiDAR scan discussed in Section 3.4.1, no significant differences in the mean wind speeds of the wake appear.

When considering the differences from the LES data (Figure 3.10d-f,j,k), the same deviation structures occur independently of the angular velocity (Figure 3.11d-f,j,k), even though the structures become coarser because of angular quantisation at faster sampling rates. Compared with Figure 3.7a,b,d,e, in which individual flow artefacts that are caused by the very low number of samples appear, the artefacts in the propagated data in Figure 3.10a,b,d,e are smoothed into the flow direction and are much more like the LES reference data. With propagation and synchronisation with the LES time steps, the number of scans is increased by a factor of 2.4 to 40 within the 10-min time period. Depending on the scanning speed, the structural representation of the flow field is significantly improved.

For the angular velocities, $\omega_\phi = 1°/s$ and $\omega_\phi = 5°/s$ (Figure 3.10a,b,d,e), propagation artefacts are clearly visible at the extremes of the measurement domain around $\chi D^{-1} = 10$. In those cases, the interpolation time (T_ϕ) and the propagation domain create a mixture of wind speeds with boundary conditions in combination with the mean flow velocity, and this blending manifests as a reduction of wind speed. These artefacts can also be seen in the visualisation of the standard deviation of the wind speed shown in Figure 3.11a,b,d,e, which are no longer detectable if $\omega_\phi > 5°/s$.

The effect of the quantisation of the measurement area by individual angular measurements, which is also remarked upon in Section 3.4.1 and Section 3.4.3, is not compensated for by wind-field propagation and is still visible if $\omega_\phi \geq 8°/s$ (Figure 3.11c,f,g,h,j,k).

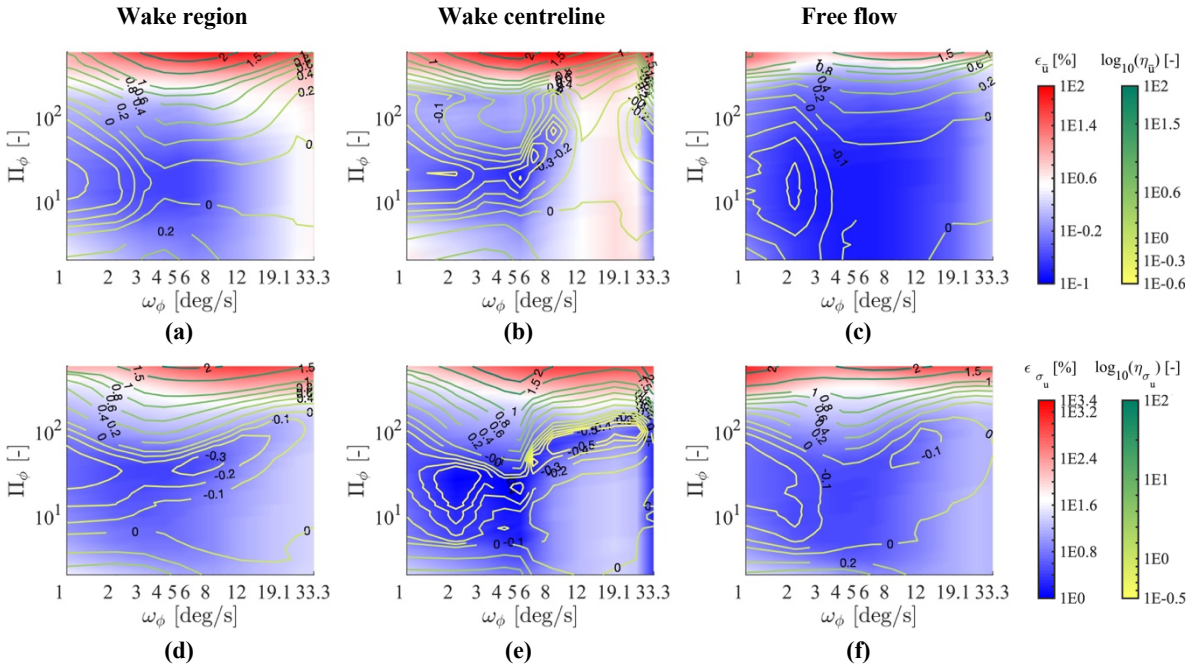

Figure 3.12. Effect of different numbers of interpolation steps Π_ϕ on the error of **(a-c)** the average wind speed $\varepsilon_{\overline{u}}$ and **(d-f)** the error of the standard deviation ε_{σ_u} for **(a,d)** the wake in the range of $-1 \leq \gamma D^{-1} \leq 1$, **(b,e)** along the centreline $\gamma D^{-1} = 0$ and **(c,f)** in free flow of the propagated PPI scans.

To address the dynamic effects of wind-field propagation and to reveal a holistic understanding of the dynamic behaviour, the reader should refer to the supplementary information of Video 3.S1 for horizontal slices and Video 3.S2 for vertical slices. Videos 3.S1 and 3.S2 show the main wind-speed components (u) of the propagated LiDAR data and deviations from the LES reference for different angular velocities, which are analogous to the data in Figure 3.7. As the

angular velocity increases, flow structures are represented with decreasing accuracy because of the decreasing point density of the polar grid. Artefacts due to inconsistent advection velocities during the propagation between two scans can be detected in the errors (ε_u) oriented in the flow direction. These artefacts are most evident at the midpoint between two laser-beam passes (red line) and below the laser beam. In addition, the effect of mixing the boundary conditions with the measured wind speeds appears below the laser beam.

Because of the interpolation method visualised in Figure 3.5, the instantaneous wind-speed error ($\varepsilon_u = \frac{u_{\text{propagated}} - u_{\text{LES}}}{u_{\text{LES}}}$) is lowest around the position of the moving laser beam, since the wind speed in this region corresponds to the un-propagated LiDAR data. The resulting error in the immediate surroundings of the laser beam indicates the volume-averaging error in the beam direction.

3.4.3 Influence of the Interpolation Time Step, Δt, on the Statistical Error

As we discussed in Section 3.3.3, the number of propagation steps (Π) between two measured scans influences the temporal accuracy of the mapping of a scan interpolated at a certain time (t). If Π is too low, the temporal changes in the flow structures are not resolved sufficiently, which increases the temporal error. Since our interpolation method employs a simplistic approach to represent fluid dynamics, the propagation will make the representation diverge somewhat from a realistic physical picture of the flow field. As more steps are interpolated between two scans, the temporal aspect of the reproduction of the flow between each scan will improve. At the same time, the reconstruction error will increase. Since some inaccuracy will arise in the speed of advection between pairs of scans, the position of the flow structures will be shifted somewhat. To investigate the effects of different interpolation steps (Δt) and to determine the parameter configuration that has the lowest statistical errors, we have evaluated different values of Π for each scanning speed, $\omega_{\phi,\theta}$. The corresponding results for RHI scans are presented in Appendix 3.D.

Applying the definition of the averaged error ($\varepsilon_{\bar{u}}$) in Eq. 3.22 and the standard-deviation error ε_{σ_u} in Eq. 3.23 to the temporally improved wind fields with different combinations of ω_ϕ and Π_ϕ (respectively, ω_θ and Π_θ), Figure 3.12 shows resulting three error cases that were reduced above:

- Inside the wake for $-1 \leq \gamma D^{-1} \leq 1$ and $-1 \leq \zeta D^{-1} \leq 1$.
- Along the centreline for $\gamma D^{-1} = 0$ and $\zeta D^{-1} = 0$.
- In the free flow.

The errors are shown in colour, and the iso-lines represent the power of the ratio of the error of the propagated data to the error of the original LiDAR data, $\eta_{\bar{u}} = \frac{\varepsilon_{\bar{u}propagated}}{\varepsilon_{\bar{u}lidar}}$ and $\eta_{\sigma_u} = \frac{\varepsilon_{\sigma u propagated}}{\varepsilon_{\sigma u lidar}}$. For the sake of readability, we have listed the configurations that give minimum errors in Table 3.2.

The results in Figure 3.12 show that an optimal interpolation time step exists for each angular velocity. If we compare these results with those in Figure 3.9, we see that a single optimal angular velocity yields the smallest mapping errors for a set of wake speed and atmospheric conditions. The resulting $\eta_{\bar{u}}$ and η_{σ_u} are plotted as iso-lines in Figure 3.12 to show which value of Π_ϕ most improves the temporal resolution and minimises the absolute error. These values show the

exponent of the decimal expression of $\eta_{\bar{u}}$ and η_{σ_u}. The zero line is a significant feature as it indicates the boundary at which the combination of ω_ϕ and Π_ϕ shifts from reducing to amplifying the mapping error. In all three regions, both the average wind-speed error and standard-deviation error are reduced over the entire range of angular velocities. The most significant improvements are achieved at scanning speeds slower than the optimum, but they do not reflect the absolute smallest error. The results in Figure 3.12 show that for the test case we considered, the error is reduced to the minimum of $\eta_{\bar{u}}$ = 30.5 % of the original $\varepsilon_{\bar{u}}$ and to η_{σ_u} = 42 % of the original ε_{σ_u}. The most significant improvements are outlined in Table 3.3.

Table 3.2. Combinations of ω and Π that give local minima for different error regions in PPI and RHI data

	PPI			**RHI**		
	wake region	**wake centreline**	**free flow**	**wake region**	**wake centreline**	**Free flow**
$\boldsymbol{\omega}$	5 °/s	5 °/s	5 °/s	5 °/s	5 °/s	3 °/s
$\boldsymbol{\Pi}$	16	18	9	14	16	7
$\boldsymbol{\varepsilon_{\bar{u}}}$	0.24 %	0.15 %	0.14 %	0.20 %	0.13 %	0.40 %
$\boldsymbol{\omega}$	4 °/s	5 °/s	4 °/s	4 °/s	5 °/s	3 °/s
$\boldsymbol{\Pi}$	33	21	16	33	26	13
$\boldsymbol{\varepsilon_{\sigma_u}}$	2.89 %	0.60 %	3.02 %	2.79 %	1.61 %	4.53 %

Table 3.3. Combinations of ω and Π that optimise $\eta_{\bar{u}}$ and η_{σ_u} for different cases of PPI and RHI data

	PPI			**RHI**		
	wake region	**wake centreline**	**free flow**	**wake region**	**wake centreline**	**free flow**
$\boldsymbol{\omega}$	1 °/s	2 °/s	2 °/s	1 °/s	1 °/s	1 °/s
$\boldsymbol{\Pi}$	16	21	13	13	16	8
$\boldsymbol{\eta_{\bar{u}}}$	35.5 %	31.0 %	36.9 %	30.5 %	31.2 %	46.5 %
$\boldsymbol{\omega}$	1 °/s	1 °/s	1 °/s	1 °/s	1 °/s	1 °/s
$\boldsymbol{\Pi}$	33	42	37	67	60	26
$\boldsymbol{\eta_{\sigma_u}}$	42.8 %	43.6 %	45.6 %	43.9 %	42.0 %	60.5 %

3.5 Discussion

Scanning LiDAR measurements must strike a compromise between temporal and spatial resolution. Since full-field measurements are usually very expensive, the scan parameters are usually chosen to minimize the scanning time. The greatest obstacle to the choice of effective scanning parameters is the limited availability of adequate validation measurements, so we used synthetic LiDAR data to verify the validity of parameter choices. This synthetic dataset raises questions about transferability and the extent to which the combination of a synthetic wind field and a LiDAR simulator can represent realistic characteristics of full-field LiDAR measurements. As discussed in Section 3.2.2, the lack of volume averaging in the scanning direction limits the direct transferability of synthetic data to step-and-stare LiDAR measurements. In most actual cases [14, 49, 51, 52, 53, 55, 66, 74, 144] scanning measurements are taken on-the-fly to minimize the scanning time. This tendency implies that during the angular movement of the scanner head, backscattering is accumulated continuously, so the velocity measurements are averaged over the traversed volume of air. Real on-the-fly measurements will show a higher reduction in the

standard deviation caused by this additional averaging. Though the data processing within a LiDAR system can be regarded as a non-linear signal process, we compensated for the effects of scanning-volume averaging with retrospective averaging. We considered this missing effect with a separate consideration of the mean and standard-deviation error at the centreline to representing the on-beam behaviour and planar error.

Optics and internal signal processing are also not considered in the LiDAR simulator, as described by Stawiarski et al. [76]. The calculated velocities have the typical device characteristics of one-dimensionality and beam-wise volume averaging, but no indication of the measurement quality, which is usually given by the carrier-to-noise ratio (CNR) or signal-to-noise ratio (SNR). In a real device, the variations in the CNR or SNR and the resulting fluctuations in the wind speed after filtering tend to reduce the data availability [74], which is also not reproduced in the simulation. The test case discussed above therefore represents an idealisation of the measurements in every respect, so it naturally draws attention to the peculiarities of real LiDAR measurements.

The results given above are based on the projection of the LOS velocities in the main wind direction that was described in Section 3.3.1. The assumption of homogeneity in the projection affects the accuracy of the representation of the wind-speed statistics, especially in areas where the assumption does not apply (in the near-wake region ($\chi D^{-1} \leq 3$)). Further, the calculation of the standard deviation from the projected time series of LOS velocities introduces some error due to the non-linear dependency of the standard deviation of the LOS velocities $\sigma_{\hat{v}_{LOS}}$ on the standard deviations of the main wind-speed components (σ_u, σ_v, σ_w). From Figure 3.8 and Figure 3.11, one can see that the error in the standard deviation from deviations in the measurement angle ($\phi' \neq 0$ and $\theta' \neq 0$) in the main flow direction is marginal compared to the error of the standard deviation due to the spatial and temporal quantisation. Otherwise, a clear trend in the error versus the measuring angle would be apparent in Figure 3.8 and Figure 3.11. This statement only applies to the present test case since the difference in the angles of the measurement and the main wind direction (ϕ', θ') are very small because of the nacelle-based measurement setup. We are aware that the projection error increases with increasing ϕ' and θ', but we cannot isolate this effect within the scope of this paper. We do assume that this source of error will have more of an effect if the scanned area is not aligned with the main wind direction, which is confirmed in Fuertes and Porté-Agel [80] for ground-based measurements.

For these reasons, we cannot claim that transfer to real data will results in the same degree of improvement in the mapping accuracy. The basis of data with which this study was conducted is too limited. To consider the general transferability of the propagation method discussed above, more flow situations with variable atmospheric conditions will need to be investigated analogously. These could be combined into a database that would give optimal measurement parameters for a range of atmospheric conditions.

When improving temporal resolution, the space-time conversion proposed above will introduce some error. The results in Section 3.4.3 indicate that this numerical error increases along with the number of interpolations and will produce the minimal mapping error with some combinations of scan parameters. In the present study, we were not able to determine the extent to which the improvement in the mapping accuracy is due to the statistical correlation described in Eq. 3.1.

Regardless of the requirement of statistical independence imposed by Eq. 3.1, we saw an improvement in the mapping quality of the mean values. The improvement in the standard

deviation should be considered more critically and will be analysed again in a future study. A reasonable approach might consider, first, the ratio of the LiDAR accumulation time to the temporal resolution of the LES and, second, the nature of the step-and-stare measurement method. Further studies should evaluate the extent to which improvements to the standard deviation achieved with the wind-field propagation method satisfy turbulence characteristics, or whether this improvement is merely coincidental.

3.6 Conclusion

This paper has presented a space-time conversion method for long-range planar LiDAR data, which achieves temporal interpolation that reflects reasonable approximations of fluid-dynamic processes. This method allowed us to retrospectively improve the temporal resolution of successive scans and to synchronise the scans with measurements collected with different time stamps. This method corrects for time shifts within a scan by applying a sinusoidal weighted average of forward- and backward-propagated wind fields taken from different completed scans, which fills in the unmeasured flow behaviour. We used synthetic LiDAR data generated by a numerical simulator and in an LES wind-turbine wake flow field to evaluate the method in terms of the mean wind speed and standard deviation.

A parametric study of 11 scanning velocities for both PPI and RHI scans was then carried out for a test case with an ambient wind speed of $u_0 = 8$ m/s and a turbulence intensity of $I_0 = 5.8$ %. Using a total of 2334 scans, we revealed how the mapping error in the LiDAR measurements is affected by the angular-scan velocity. This error is temporal in nature at low scanning speeds and shifts to a spatial error at high scanning speeds. The optimal scanning speed is determined by the turbulence intensity and the corresponding spatial variability in the wind-turbine wake. Analysis of 11 different scan velocities showed that, with the careful selection of typical measurement parameters, the compromise between temporal and spatial resolution is well balanced. In the specific test case we considered, the optimal measurements are taken with slower scan speeds and higher spatial resolutions. The use of wind-field propagation increased the volume of synthetic LiDAR data by a factor of 2.4 to 40, allowing synchronisation with the LES reference data. This synchronization led to an improvement of the structural mapping, in terms of both the mean wind speed and the standard deviation.

The interpolation method can be used with various configurations of interpolation steps between two scans, so it can serve as a universal tool for increasing the temporal resolution of planar LiDAR measurements with a minimal increase in statistical errors. This interpolation is particularly useful for the analysis and comparison of wake measurements, for which some wake characteristics might be correlated with data of finer temporal resolution recorded external to the wind turbine, such as load data. In addition to synchronising the data from complex measurement campaigns taken with various LiDAR devices and sensors, the possibility of temporal up-sampling allows for easier processing. In the test case discussed above, the maximum reduction of the error of the mean wind speed was 30.5 % and the standard-deviation error was reduced by 42 %.

Supplementary Materials: The following videos are available online at The following videos are available online at https://zenodo.org/record/2635033#.XK3C0qIRWUk

Video 3.S1: Visualisation of up-sampled horizontal wind-speed data and the wind speed error in comparison to the LES reference for different angular velocities. The red line indicates the scanning laser beam.

Video 3.S2: Visualisation of up-sampled vertical wind-speed data and the wind speed error in comparison to the LES reference for different angular velocities. The red line indicates the scanning laser beam.

Author Contributions: This study was done as a part of H.B.'s doctoral studies supervised by M.K. H.B conducted the research work and wrote the paper. M.K. supervised the research work, advised about the structure of the paper and supplied review and editing.

Funding: This work was funded in part by the Federal Ministry for Economic Affairs and Energy (BMWi) according to a resolution by the German Federal Parliament (project CompactWind, FKZ 0325492B) and in the scope of the ventus efficiens project (ZN3092), through the funding initiative Niedersächsisches Vorab of the Ministry for Science and Culture of Lower Saxony.

Acknowledgments: We thank Davide Trabucchi for help with the implementation of the LiDAR simulator LiXIM and in formulating its formal description. We thank Andreas Rott for initial ideas about the closure of the wind-field propagation. We thank Mehdi Vali for performing LES simulations of the wake wind field.

Conflicts of Interest: The authors declare no conflict of interest.

Appendix 3.A

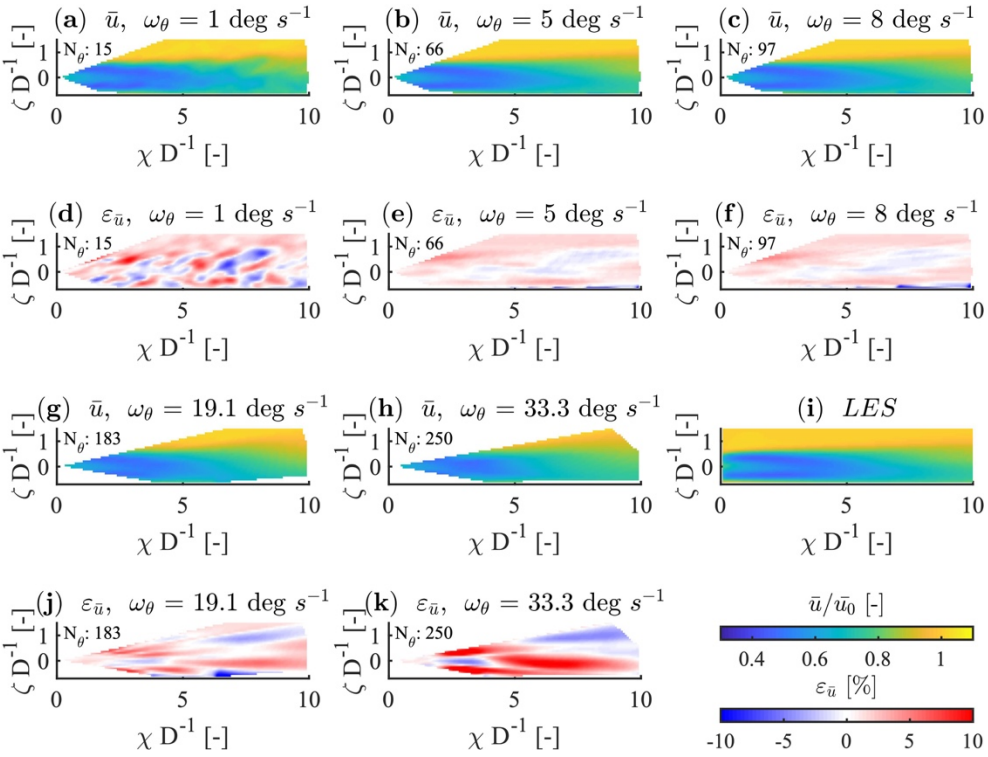

Figure 3.13. Visualisation of the normalised 10-minute averaged wind-speed component $\bar{u}$ of the original RHI data and **(d-f & j-k)** the corresponding flow deviations $\varepsilon_{\bar{u}}$ from **(i)** the normalised 10-minute averaged wind-speed component $\bar{u}$ of LES data.

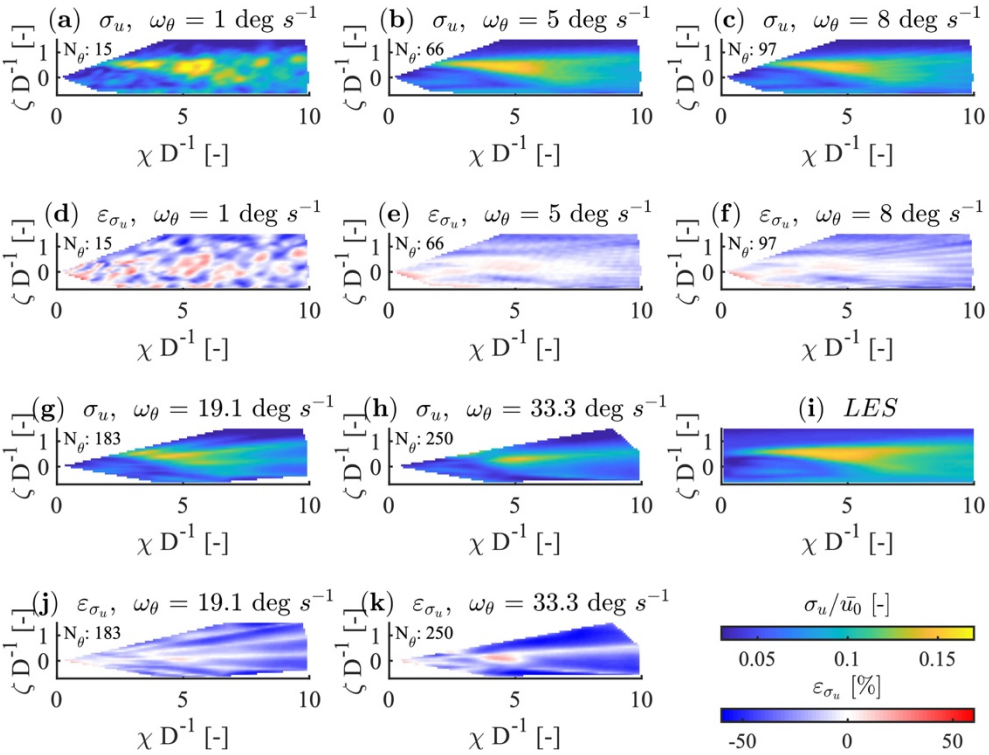

Figure 3.14. Visualisation of the normalised 10-minute standard deviation σ_u of the wind-speed component u of the original RHI data and **(d-f & j-k)** the corresponding deviations ε_{σ_u} from **(i)** the normalised 10-minute standard deviation of wind-speed component u of LES data.

Appendix 3.B

In the following, we list the average wind-speed error and the standard-deviation error of the LiDAR simulator against the LES reference data for different scan speeds ω_ϕ of PPI scans in Table 3.4 and of RHI scans in Table 3.5.

Table 3.4. Average wind speed and standard deviation error against the LES of PPI scans for different angular velocities ω_ϕ

	1°/s	2°/s	3°/s	4°/s	5°/s	6°/s	8°/s	12°/s	19.1°/s	27.2°/s	33.3°/s
wake region $-1 \leq \gamma D^{-1} \leq 1$											
$\varepsilon_{\bar{u}}$	1.68 %	0.72 %	0.36 %	0.29 %	0.31 %	0.35 %	0.49 %	0.99 %	1.99 %	3.17 %	4.21 %
ε_{σ_u}	12.61 %	5.71 %	4.81 %	5.00 %	5.93 %	7.06 %	9.43 %	14.83 %	21.04 %	25.63 %	27.85 %
wake centreline $\gamma D^{-1} = 0$											
$\varepsilon_{\bar{u}}$	1.71 %	0.81 %	0.54 %	0.46 %	0.49 %	0.81 %	1.54 %	2.77 %	4.91 %	4.27 %	0.65 %
ε_{σ_u}	9.81 %	5.54 %	3.59 %	2.36 %	2.29 %	5.23 %	11.87 %	20.65 %	27.09 %	20.72 %	2.01 %
free flow											
$\varepsilon_{\bar{u}}$	0.77 %	0.43 %	0.25 %	0.19 %	0.18 %	0.17 %	0.18 %	0.23 %	0.38 %	0.74 %	1.17 %
ε_{σ_u}	11.78 %	7.19 %	4.91 %	3.77 %	3.68 %	3.90 %	5.00 %	8.34 %	14.22 %	18.15 %	16.69 %

Table 3.5. Average wind speed and standard deviation error against the LES of RHI scans for different angular velocities ω_θ

	1°/s	2°/s	3°/s	4°/s	5°/s	6°/s	8°/s	12°/s	19.1°/s	27.2°/s	33.3°/s
wake region $-1 \leq \zeta D^{-1} \leq 1$											
$\varepsilon_{\bar{u}}$	2.15 %	0.76 %	0.40 %	0.26 %	0.31 %	0.30 %	0.54 %	1.04 %	2.21 %	2.84 %	3.59 %
ε_{σ_u}	11.87 %	6.15 %	4.66 %	4.96 %	5.70 %	6.94 %	9.24 %	12.87 %	18.43 %	21.02 %	29.30 %
wake centreline $\zeta D^{-1} = 0$											
$\varepsilon_{\bar{u}}$	1.58 %	0.73 %	0.39 %	0.31 %	0.32 %	0.50 %	1.11 %	0.56 %	4.13 %	2.11 %	8.20 %
ε_{σ_u}	10.28 %	5.29 %	3.97 %	2.78 %	2.87 %	5.47 %	9.37 %	7.58 %	19.78 %	10.00 %	28.98 %
free flow											
$\varepsilon_{\bar{u}}$	2.01 %	0.72 %	0.45 %	0.42 %	0.51 %	0.53 %	0.81 %	1.44 %	2.39 %	3.00 %	3.58 %
ε_{σ_u}	12.02 %	6.27 %	4.98 %	5.51 %	6.48 %	7.92 %	10.60 %	14.26 %	19.26 %	22.48 %	30.87 %

Appendix 3.C

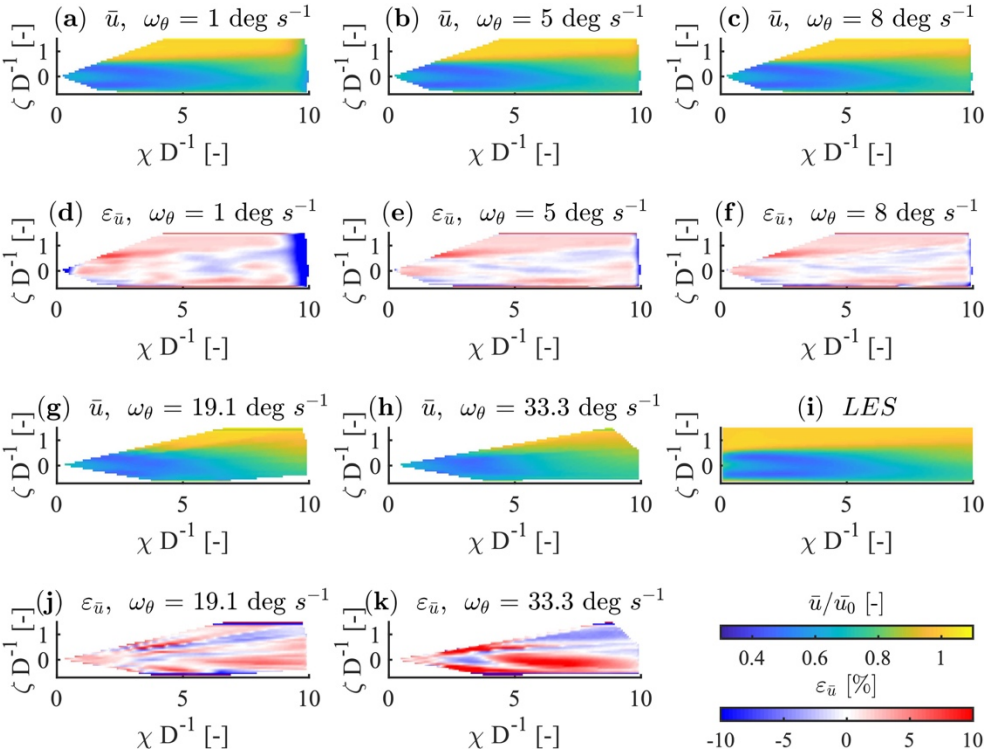

Figure 3.15. Visualisation of the normalised 10-minute averaged wind-speed component $\bar{u}$ of the propagated RHI data and **(d-f & j-k)** the corresponding flow deviations $\varepsilon_{\bar{u}}$ from **(i)** the normalised 10-minute averaged wind-speed component $\bar{u}$ of LES data.

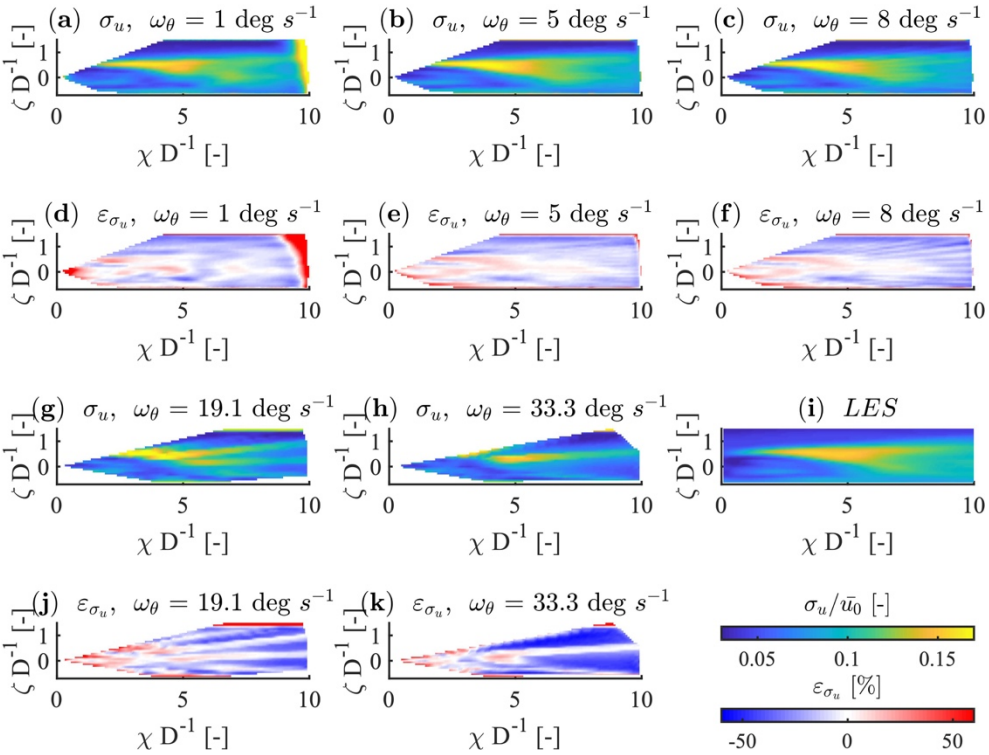

Figure 3.16. Visualisation of the normalised 10-minute standard deviation σ_u of the wind-speed component u of the propagated RHI data and **(d-f & j-k)** the corresponding deviations ε_{σ_u} from **(i)** the normalised 10-minute standard deviation of wind-speed component u of LES data.

Appendix 3.D

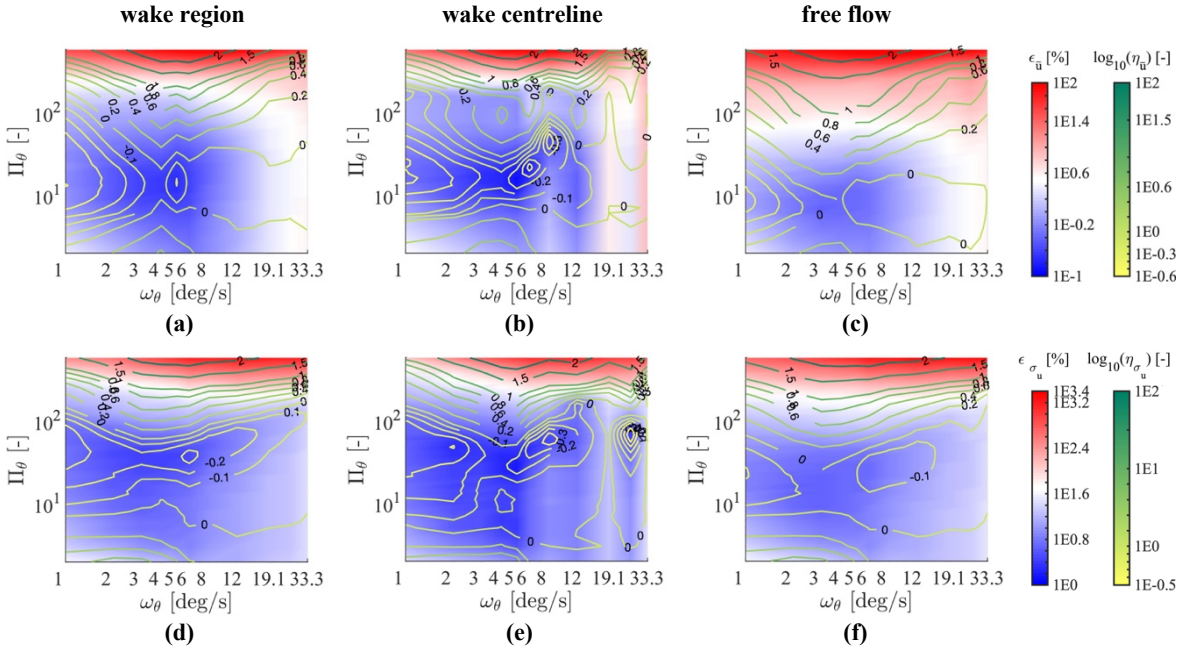

Figure 3.17. Effects of different numbers of interpolation steps (Π_θ) on the error in **(a–c)** the average wind speed ($\varepsilon_{\bar{u}}$) and **(d–f)** the error in the standard deviation (ε_{σ_u}) for **(a, d)** wakes in the range of $-1 \leq \zeta D^{-1} \leq 1$, **(b, e)** along the centreline $\zeta D^{-1} = 0$ and **(c, f)** in the free flow of propagated RHI scans.

4 Reconstruction of Three-Dimensional Dynamic Wind Turbine Wake Wind Fields With Volumetric Long-Range Wind Doppler LiDAR Measurements

The content of this chapter is identical to the submitted journal article:

Beck, H.; Kühn, M.: Reconstruction of Three-Dimensional Dynamic Wind Turbine Wake Wind Fields with Volumetric Long-Range Wind Doppler LiDAR Measurements. *Remote Sensing* 2019, 11(22), 2665, doi: 10.3390/rs11222665.

Article

Reconstruction of Three-Dimensional Dynamic Wind Turbine Wake Wind Fields with Volumetric Long-Range Wind Doppler LiDAR Measurements

Hauke Beck* and Martin Kühn

ForWind – University of Oldenburg, Institute of Physics, Küpkersweg 70, 26129 Oldenburg, Germany;
* Correspondence: hauke.beck@uol.de

Received: 17 September 2019; Accepted: 11 November 2019; Published: 14 November 2019

Abstract: This paper presents a method for reconstructing the wake wind field of a wind turbine based on planar light detection and ranging (LiDAR) scans crossing the wake transversally in the vertical and horizontal directions. Volumetric measurements enable the study of wake characteristics in these two directions. Due to a lack of highly resolved wind speed measurements as reference data, we evaluate the reconstruction in a synthetic environment and determine the reconstruction errors. The wake flow of a multi-megawatt wind turbine is calculated within a 10-min large-eddy simulation (LES) for high-thrust loading conditions. We apply a numerical LiDAR simulator to this wake wind field to achieve realistic one-dimensional velocity data. We perform a nacelle-based set-up with combined plan position indicator and range height indicator scans with eight scanning velocities each. We temporally up-sample the synthetic LiDAR data with a weighted combination of forward- and backward-oriented space–time conversion to retrospectively extract high-resolution wake characteristic dynamics. These dynamics are used to create a dynamic volumetric wake deficit. Finally, we reconstruct the dynamic wake wind field in three spatial dimensions by superposing an ambient wind field with the dynamic volumetric wake deficit. These results demonstrate the feasibility of wake field reconstruction using long-range LiDAR measurements.

Keywords: LiDAR simulator, wind-field propagation, measurement synchronization, space-time-conversion, wake model, error analysis

4.1 Introduction

The ongoing trend toward increased rotor diameters and decreased relative spacing of turbines in wind farms indicates that wind turbine manufacturers, wind farm operators, and researchers need a better understanding of wake-induced load generation. Increased fatigue loads and reduced power output are direct consequences of wake-shading of wind turbines [16, 36]. Uneven load variations from full or partial wake-shading of the swept rotor area can result in increased wear, or even structural damage, of turbines [123, 124]. Thus, when designing turbines and wind farms, wake models are needed to estimate the flow conditions for calculating loads and estimating yields. The interaction of a wind turbine with the atmospheric boundary layer (ABL) causes a highly dynamic wake behaviour, resulting in vertical and horizontal meandering of the wake position and non-symmetric, non-constant velocity-deficit shapes. There is considerable demand for models that can reproduce these dynamics. Because of the limited ability to identify and resolve spatial wake structures with conventional or ultrasonic anemometers, traditional wake models [24, 29, 31] can only be validated using long-term temporally averaged data corresponding to a simplified steady-flow state over 10-min periods. Such models are based on the correlation of statistical analysis of wind turbine operational data, better known as supervisory control and data acquisition (SCADA) data, load measurements, and time-averaged wind speed

point measurements, such as those taken at meteorological towers or the turbine nacelle itself. Through temporal averaging, the wake behaviour's dynamic effects are smoothed out, thus forming a source of inaccuracy that makes it harder to comprehend the occurring loads. Actually, the turbine does not interact with the wider and smoother wake deficit, as known in a stationary reference frame, but rather with a narrower deficit, with a high shear velocity, in the so-called meandering frame of reference (MFoR) [18]. Steady wake models describe the wake as stationary and in a fixed reference frame (FFoR), which does not explicitly resolve the dynamic effects [24, 29]

In contrast to steady wake models, dynamic models were developed that aim to reproduce the meandering behaviour based on a time series of inflow wind speed, wind direction, and wind turbine operational performance. The dynamic wake meandering (DWM) model developed by Larsen et al. [38] and the Extended Disk Particle model (EDPm) by Trujillo [18] can dynamically compute a wake's horizontal and vertical positions at a prescribed downstream distance. Both models describe the horizontal and vertical movements of a constant planar deficit, which is subsequently superimposed on an ambient wind field with both shear and atmospheric turbulence. To address wake-induced turbulence, these models assume a turbulence scaling based on the deficit shape and intensity. A significant difference between the models proposed by Larsen et al. [38] and Trujillo [18] is the assumed advection speed of the wake velocity deficit in the form of air parcels emitted by the rotor. Although the air parcels within the DWM stream with an average velocity of the time series, the parcel velocities in the EDPm are position-dependent and interactively use a stochastic Lagrangian particle model.

An alternative method for coping with realistic dynamic wake conditions is synthesizing high-fidelity wind fields using a computational fluid dynamics (CFD) simulation that can spatially and temporally resolve flow conditions suitably. Large-eddy simulations (LESs) are used to gain a deeper understanding of wakes within the ABL [145, 146]. The coupling of aero-elastic simulations by LESs provides a highly detailed but laborious computation of the interactions between turbines and wakes [14, 84, 147, 148].

Although such approaches are promising, calculating CFD-generated wind fields is still numerically expensive. In addition, the representation of specific atmospheric conditions and the simulation in a complex terrain require expert knowledge and a significant time commitment.

The interaction between modelled wake wind fields and numerical turbine models represents a source of uncertainty, as flow and turbine behaviour are in turn derived from a limited number of measurements and theoretical considerations. In general, the use of models is accompanied by reducing the complexity of circumstances being served. Thus, model results can only depict a model's assumptions and not reality. One indication of a limited modelling accuracy can be found in the verification of turbine loads. Calculating loads with a dynamic wake model is challenging and may lead to load deviations when attempting to match specific inflow conditions [88, 89].

Because the interaction of a turbulent flow field with a turbine is a non-linear process, the representativeness of an extrapolation of coupled model–model calculations should be investigated in comparison to real loads and actual inflow measurements. The resulting challenge involves evaluating and comparing real and modelled effects to quantify the impact of model assumption limitations and overcome them. We find it reasonable to try to avoid modelling inaccuracies as much as possible. Here, we replace the model assumptions with real wake behaviour in the process chain. Concerning the statistically required number of situations, this would require a considerable variety of measurements under different atmospheric conditions.

The requirement for full-field measured dynamic wake behaviours, as well as accurate inflow models that can reconstruct them, is associated with the need for a holistic validation. A promising instrument for full-field wake measurements is a wind-speed Doppler light detection and ranging (LiDAR), hereinafter referred to merely as LiDAR, which was recently established in the wind energy and resource assessment fields as a versatile measurement instrument for research purposes. Investigating wakes mainly uses pulsed scanning long-range devices that can capture many simultaneous measurements along the laser beam. Käsler et al. [49] first published ground-based sectorial scans of a wake along the inflow direction in the full field by alternately fixing and changing the azimuth and elevation angles during the measurements. Aitken et al. [66], conducted planar horizontal scans from a wind turbine nacelle, which represented a significant achievement accompanied by pertinent measurement experience. Their study focused on wake characterization without interference from variable wind direction and measurement inclinations due to ground-based measurement positions. Bromm et al. [14] performed nacelle-based measurements with two long-range LiDARs to investigate the mean wake deflection far downstream with a targeted yaw misalignment. Aubrun et al. [149] investigated the statistical relationship between atmospheric stability and wake characteristics, such as the recovery rate and the lateral meandering, using long-term LiDAR measurements behind two turbines.

Regarding LiDAR measurements, we are confronted with the dilemma of finding a set-up configuration that aims for a compromise between data quality and temporal and spatial resolutions. This dilemma refers to hardware and software settings. Among others, the accumulation time, the angular velocities, and the pulse length, as well as the spectral processing of the backscattering in the form of the pulse repetition frequency, the number of fast Fourier transform (FFT) sampling points, and the peak finder algorithm, influence how spatial and temporal structures of the flow can be resolved and with what quality. Depending on the combinations of measurement settings and flow situations, a mapping error is likely to behave between the extremes of a temporal nature for angular velocities that are too slow and those of a spatial nature when a sector is scanned too quickly [150].

Fuertes and Porté-Agel [80] studied the reconstruction error of measurements with a focus on LiDAR limitations in terms of volume averaging and measurement repetition frequency in the wake region, within a 10-min time interval. Additionally, Beck and Kühn [150] investigated the influence of the planar scanning velocities on the mean value and standard deviation mapping error. To this end, Fuertes and Porté-Agel [80] and Beck and Kühn [150] used numerical LiDAR simulators in an LES wake wind field to achieve a verifiability not yet available with full-field measurements.

The possibility of reconstructing flow situations using LiDAR data was demonstrated in recent years. There is no clear definition of a wind-field reconstruction; thus, reconstructions are performed on varying scales of temporal and spatial detail. Borraccino et al. [152] presented a turbine inflow reconstruction based on temporally averaged short-range LiDAR data that had high accuracy compared to a mast-top-mounted cup anemometer. Kapp and Kühn [90] derived turbine inflow conditions by fitting a five-parameter wind-field model. Towers and Jones [81] used a dynamic wind model to obtain a state estimation based on velocity data from a two-beam nacelle LiDAR system. Other studies used pulsed long-range LiDAR measurements, which mainly differ due to their lower temporal resolutions and extended measurement ranges compared to continuous-wave short-range LiDARs. Iungo and Porté-Agel [52] reconstructed wake flow fields by joining multiple temporally averaged elevated planar scans. Van Dooren et al. [55] used data

from two distant LiDARs to reconstruct a planar two-dimensional time-averaged single-wake flow field.

To achieve reconstructed temporally resolved 3D1C wake wind fields for later use in wake model evaluation or load calculations, we present a comprehensive volumetric nacelle-based LiDAR data processing method in Section 4.3. Firstly, we apply a space–time conversion to retrospectively improve the temporal resolution to a sub-measurement scale to correct the scan containing time shift and mutually synchronize two sets of LiDAR data. Secondly, we reconstruct a temporally resolved 3D1C wake wind field by recreating the dynamic wake behaviour based on the tracked wind speed deficit shapes, deficit intensities, and deficit positions with robust single Gaussian wake tracking. We then evaluate the reconstruction quality using synthetically generated data by using a numerical LiDAR simulator scanning a LES wake wind field, in Section 4.4. For this purpose, we analyse the mean value and standard deviation error for the wake reconstruction, focusing on horizontal and vertical LiDAR scan parameter variations. In Section 4.5, we discuss the introduced reconstruction method with respect to its limitations and further evaluate the possibilities, and we provide conclusions to this research in Section 4.6.

4.2 Nacelle-based LiDAR dataset

The starting point for this research was an actual measurement campaign [14]. Based on these LiDAR measurements, we reconstructed a temporally resolved 3D1C wake wind field. The measurement set-up used for providing insight into the capabilities of commercially available scanning long-range LiDARs is presented in Section 4.2.1. Because no reference data from alternative measurement devices, such as met masts with several anemometers or additional scanning LiDARs, were available, we do not present further details on this campaign's results. The limited and insufficient evaluation possibilities forced us to use synthetic LiDAR data for the systematic methodological development presented in Section 4.3. Therefore, we were restricted to analysing the results of a numerical LiDAR simulator applied on a wake wind field generated by LES, as described in Section 4.2.2.

4.2.1 Onshore LiDAR measurement campaign

Two Leosphere Windcube WLS-200s scanning Doppler long-range LiDARs were installed on the nacelle of a 3.5-MW ENO 114 turbine with 114.9 m rotor diameter (D_{eno}) and 92 m hub height (h_{HH}). These instruments performed temporally and spatially resolved long-range measurements within the time interval of 4:10–4:20 a.m. on 14 May 2015. The mean wind speed was 8.1 m/s, with an average wind direction of 284° at the hub height and a yaw offset of 0°. The determination of the yaw offset, and a detailed description of this measurement campaign are beyond the focus of this paper, but can be found in Bromm et al.'s paper [14].

To obtain volumetric information from these measurements, we chose one of the most straightforward volumetric scan patterns. We programmed a volumetric measurement scenario consisting of horizontal measurements, known as plan position indicator (PPI) scans, for one device and vertical slices, known as range height indicator (RHI) scans, for the other. These measurements were unsynchronized and repeated in a loop. Combining PPI and RHI scans from two perpendicular measurement planes in the downstream direction, slicing the wake in the horizontal and vertical directions, is illustrated in Figure 4.1. Planar trajectories were determined

by either fixing the scanner's elevation angle (θ) and changing its azimuth angle (ϕ) continuously (PPI), or by fixing the scanner's azimuthal orientation while varying the elevation angle (RHI).

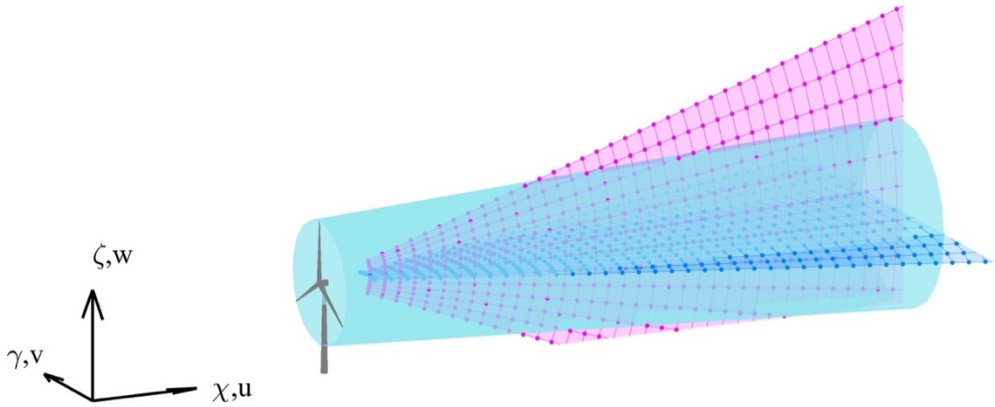

Figure 4.1. Illustration of cross-measurement trajectories and used coordinate system and velocity components. A horizontal PPI scan is shown in dark blue, and a vertical RHI scan is shown in pink. The wake volume is indicated in light blue.

Because of the line-of-sight (LOS) measuring principle of single devices, the data showed inherent one-dimensionality and were recorded by the hemispheric scanner head in a spherical coordinate system, in which the point density decreased with increasing measurement distance. The measurement grid was determined by radial measurement points along the laser beam and the accumulation time due to the angular velocity in relation to the total opening angles, $\Delta\phi$ and $\Delta\theta$. Here, the measurement trajectories and the total opening angles can be expressed as:

$$\Delta\phi = |\phi_2 - \phi_1|, \quad \text{Eq. 4.1}$$

and

$$\Delta\theta = |\theta_2 - \theta_1|. \quad \text{Eq. 4.2}$$

The measurement points in the free-field [14] were set in the radial direction within a 50–1150-m range every 7 m. The resulting 7-m radial resolution was achieved using overlapping pulses. Because of the probe volume length, two measurement points were independent when their radial distance was greater than ~60 m. Each LiDAR, performing either PPI or RHI scans, measured only one repeating trajectory. As shown in Figure 4.1 PPI scans were measured with a 0° elevation, and RHI scans mere measured with a 0° azimuth and an accumulation time (ϑ_{acc}) of 200 ms, an angular speed ($\omega_\phi, \omega_\theta$) of 2°/s, and a total opening angle ($\Delta\phi$, $\Delta\theta$) of 40° symmetrical to the horizontal axis at the hub height, resulting in an angular resolution ($\mathcal{R}_\phi, \mathcal{R}_\theta$) of 0.4°.

4.2.2 Synthetic LiDAR data

We synthesized numerical wind field data offering the possibility of a calculable error for each process step. An LES based on the Parallelized LES Model (PALM) code [133] version 3.10 (r1352) with an actuator line approach (ACL) [134] was used to calculate the wake wind field of an NREL 5-MW wind turbine model [135] with 126 m rotor diameter D_{NREL}. To cope with the sub-grid turbulence effects within PALM, a 1.5th-order closure model based on Deardorff [151] was used. A detailed description of the specific configuration of PALM and an explanation of the flow and wind turbine interactions can be found in Bromm et al.'s paper [85].

We aimed to reproduce the actual atmospheric conditions, resulting in a mean wind speed (u_o) of 8 m/s at a hub height (h_{HH}) of 92 m with an ambient turbulence intensity (I_0) of 5.8 %

for neutral stability. Here, we used a 10-min time interval for the entire simulation, which had a temporal resolution of 1 Hz and a spatial resolution of 10 m per grid cell in all three dimensions.

Because the angular resolutions ($\mathcal{R}_\phi$ and $\mathcal{R}_\theta$) were the main influencing variables for the measurement grid, as they determine point density, we carried out a study to determine the optimum scanning parameters for the later reconstruction [150]. The variation parameters were the angular velocities (ω_ϕ and ω_θ), which significantly influenced the trajectory measurement grid's spatial resolution and the temporal capability of the capturing local flow dynamics. We selected eight angular velocities, resulting in a combination with an accumulation time (ϑ_{acc}) of 200 ms and a sampling frequency of 0.024–0.417 Hz. For a better overview, we summarize the effects of different angular velocities on the following variables in Table 1: the number of scans for each scan type within a 10-min interval (N_ϕ and N_θ), the number of measurement points (n_{pnt}) for each scan type, the number of angular measurements per scan (n_ϕ and n_θ), the angular resolution ($\mathcal{R}_\phi$ and $\mathcal{R}_\theta$), the scan duration (T_ϕ and T_θ), the measuring frequency (f_s), and the measurement time efficiency (η_m), which can be expressed as a percentage of the total net measurement time within a 10-min interval.

$$\eta_m = \frac{T_{\phi,\theta}}{T_{\phi,\theta} + t_r}, \qquad \text{Eq. 4.3}$$

where t_r is time the scanner head needs to return to the restart position. Here, t_r was 1.2 s for a total scan angle of 40°.

Table 4.1. Simulated LiDAR trajectories of cross-measurements for a time interval of 600 s and 180 radial measurement points in the range of 0 m to 1260 m.

ω_ϕ, ω_θ	$\Delta\phi$, $\Delta\theta$	N_ϕ, N_θ	n_{pnt}	n_ϕ, n_θ	$\mathcal{R}_\phi$, $\mathcal{R}_\theta$	T_ϕ T_θ	f_s	η_m
1°/s	40°	15	36000	200	0.2°	40.0 s	0.024 Hz	97.2 %
2°/s	40°	29	18000	100	0.4°	20.0 s	0.047 Hz	94.2 %
4°/s	40°	54	9000	50	0.8°	10.0 s	0.089 Hz	89.2 %
8°/s	40°	97	4500	25	1.6°	5.0 s	0.161 Hz	80.6 %
12°/s	40°	133	2880	16	2.5°	3.3 s	0.221 Hz	73.4 %
19.11°/s	40°	183	1800	10	4.0°	2.1 s	0.303 Hz	63.4 %
26.22°/s	40°	221	1260	7	5.7°	1.5 s	0.370 Hz	55.8 %
33.33°/s	40°	250	1080	6	6.7°	1.2 s	0.417 Hz	50.0 %

The trajectories described in Table 4.1 were used to generate synthetic LiDAR data with the numerical simulator LiXIM developed at ForWind by Trabucchi [136]. A detailed description of LiXIM can be found in van Dooren et al. [55] and Beck and Kühn [150]. In the implementation of the simulator used here, we covered the effect of volume averaging in the beam direction within an assumed cylindrical probe volume, and we did not represent volume averaging in the scanning direction.

In total, 1964 synthetic scans representing eight different angular velocities were simulated within the same 10-min time interval of the LES.

4.3 Method for wind field reconstruction

Our reconstruction method's starting point and reference was the DWM from Larsen et al. [38]. Below, we present the underlying assumptions on which we based the design of the

reconstruction method. These statements do not claim to be absolute, but are rather a logical extension of the parameterization of wake effects in the context of dynamic wake characterization and modelling.

- If we consider a cross-section of a wake wind field in the $\gamma - \zeta$ plane at a certain downstream distance χ, the resulting flow behaviour of the longitudinal wind speed component u of the wake can be described as a superposition of the free flow with a planar (two-dimensional (2D)) longitudinal wind speed deficit, which shows specific transversal dynamics.
- We define these dynamics as temporal changes in the horizontal and vertical positions, the horizontal and vertical velocity deficit shapes, and the velocity deficit intensity, which represents the ratio of the tracked wake velocity at the wake centre to the instantaneous ambient wind speed profile. These dynamics will be described below as the wake centre position, wake width, and wake velocity intensity in 2D and later 3D.
- The wake velocity deficit causes a scaling of the ambient turbulence intensity, which depends on the 2D deficit shape at the downstream position χ. Other than the ambient turbulence intensity scaling, no additional turbulence is added as the meandering of the deficit shape induces turbulence.
- If we apply these considerations continuously in the downstream direction, we can consider the wake region a continuous symmetrical wake volume centred around a spline in space that alters depending on the previously described dynamics.
- The wake velocity deficit intensity is variable in time and space.

To gain a better understanding, we visualised the reconstruction assumptions in Figure 4.2 for one point in time. The wake is shown as a continuous tube that tapers and widens along the wake centreline in the horizontal and vertical directions, respectively. The template for modifying and scaling this tube was a volumetric velocity deficit, which we created from the LiDAR measurements. Different colours within the wake region in Figure 4.2, represent the variable instantaneous intensities of planar deficits at the corresponding downstream positions.

Below, we present the processing steps applied to obtain the wind speed deficit, the shape dynamics, the intensity dynamics, and the position dynamics from LiDAR data for use in wind-field reconstruction.

4.3.1 LiDAR Data Pre-Processing

Because this study represents a further development of Beck and Kühn [150], we used the same data handling in the sense of pre-processing, up-sampling, and synchronization, as well as the same numerical dataset. Therefore, we directly quote the formal description of the dataset and use the essential parts. The complete data processing method can be read in Reference [150].

To deduce the instantaneous longitudinal wind speed component (u_0) from LiDAR radial velocity data ($\hat{v}_{LOS}$), we assumed that within the 10-min interval, the average lateral velocity component ($\bar{v}_0$) and average vertical velocity component ($\overline{w}_0$) were zero. Recognizing that this assumption did not apply near the rotor ($\chi D^{-1} \leq 3$), we calculated u as follows:

$$u_0 = \frac{\hat{v}_{LOS}}{\cos(\phi')\cos(\theta')}, \qquad \text{Eq. 4.4}$$

where ϕ' is the difference between the horizontal wind direction (Φ) and azimuth angle (ϕ), and θ' is that between the vertical wind direction (Θ) and elevation angle (θ).

The projection of LOS velocities was made scanwise and, thus, individual scans were interpolated to a Cartesian (χ - γ , γ - ζ) coordinate grid using the natural neighbour interpolation [142].

Like Beck and Kühn [150], the standard deviation was calculated using the previously calculated LOS velocity projection to the longitudinal wind speed component (u_0). This pragmatic approach had the consequence that not the longitudinal wind speed component's original turbulence intensity (I_0), but only the statistics of the projected LOS velocities ($\hat{v}_{LOS}$), could be constructed.

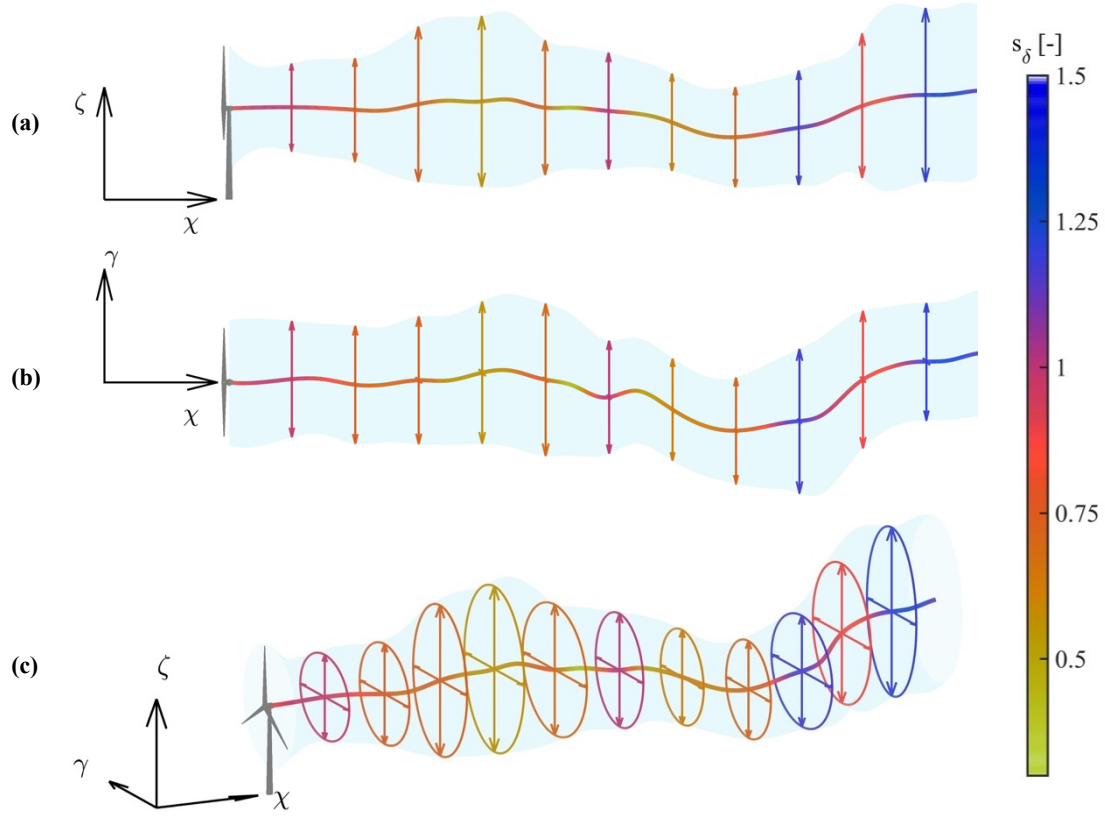

Figure 4.2. Schematic representation of the model assumptions within the reconstruction. Different half axes of the ellipses indicate different scaling of the wake velocity deficit in the horizontal and vertical directions, whereas the colours correspond to scaled wake velocity deficit intensities for one point in time: **(a)** side view; **(b)** top view; **(c)** perspective view.

4.3.2 Temporal Correction and LiDAR Data Synchronisation

Because of the scanning measurements of PPI and RHI scans, it was not possible to capture the entire measurement area at one point in time. This restriction resulted in a representation of the wind field over a time interval of the scan, as shown Table 4.1. Therefore, we did not directly use the measured and projected LiDAR data for further processing. Slower scan speeds resulted in more significant temporal shifts within a scan (Figure 4.3). Furthermore, the temporal resolution of the tracked wake dynamics (Section 4.3.3) became insufficient.

We used Beck and Kühn's [150] temporal up-sampling method to interpolate the synthetic LiDAR data to the LES reference time step. This method uses a simplified 2D Navier–Stokes equation that contains only the advection term implemented using an affine semi-Lagrange interpolation approach. A sinusoidally weighted combination of forward- and backward-oriented

space–time conversions resulted in the closure of each LES grid point of the flow field between two consecutive scans.

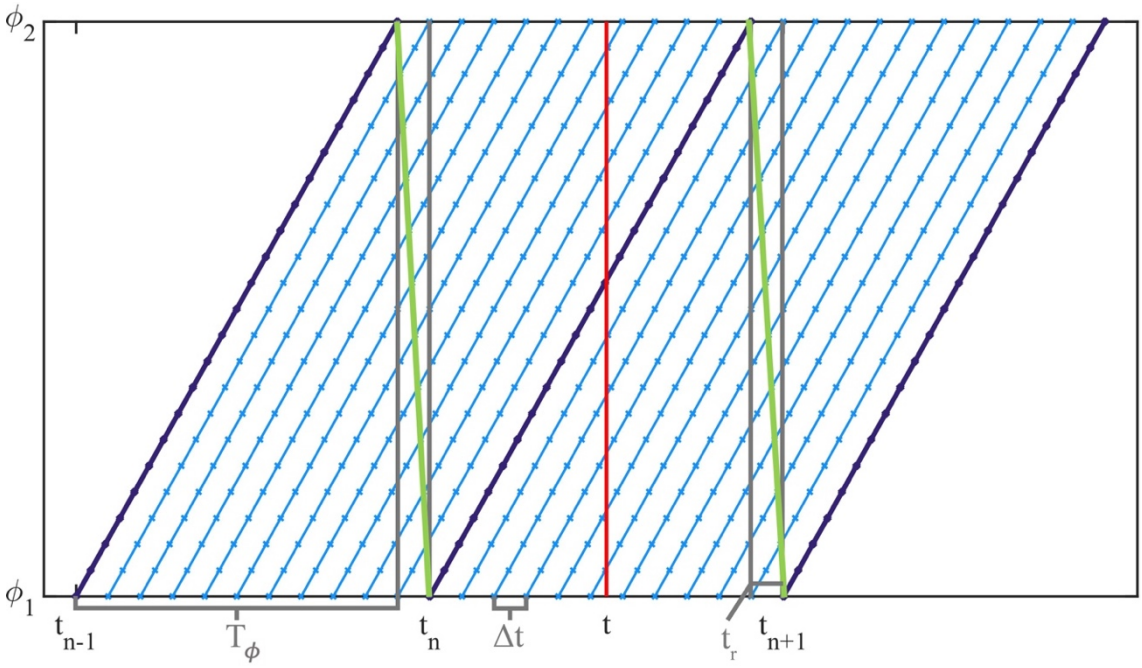

Figure 4.3. Illustration of the time series of the PPI scan azimuth angle, including a visualization of the temporal alignment at time t. Dark-blue lines indicate light detection and ranging (LiDAR) measurements, light-blue lines indicate propagated scans, green lines indicate the measurement reset trajectory during the reset time (t_r)), and the red line represents temporal interpolation at time t. The example shows 11 interpolation steps between two consecutive scans [150].

Figure 4.3 shows how the wind-field propagation minimizes the time shift within one scan (dark blue), where the horizontal axis represents time and the vertical axis indicates the LiDAR measurement's current scan angle. The scanning from ϕ_1 to ϕ_2 is drawn over the scanning period T_ϕ in dark blue. For the return run during the reset time (t_r), the scanner head must start a new trajectory without measuring. The return run is illustrated in green, and the propagated scans are shown in light blue. Applying the wind-field propagation [150] allowed an increase in the number of intermediate steps (light blue) between two consecutive scans by an arbitrary number. To correct the time shift and represent the flow at one point in time (t) and not over the entire time interval (T_ϕ+t_r), we interpolated along the red line using the natural neighbour interpolation [142]. Here, it became apparent that a shorter propagation time step yielded more accurate temporal mapping of a scan.

We up-sampled the LiDAR data based on the scanning velocity and improved the amount of data by factors of 2.4–40, to achieve a resolution of 1 Hz. The wind-field propagation result was a 10-min dataset of 600 planar PPI and RHI scans, which were synchronized mutually and with the LES reference. These data constituted the initial basis for the temporally resolved wake dynamic determination.

4.3.3 Determination of Wake Deficit Dynamics

Two sets of information were needed for wind-field reconstruction: the wind speed deficit and its dynamics. The significant issue here was the characterization of the wake dynamics, namely, the wake position, the wake width, and the velocity deficit intensity over time, as these

data were also used for calculating the velocity deficit shape in the MFoR [18, 38, 69] in Section 4.3.4 and the standard deviation of longitudinal wind speed component u in the MFoR in Section 4.3.5. This led to the reconstruction quality having a direct dependency on the tracked values, with their precision and their expressiveness concerning real flow situations. Like other studies [14, 66, 69], we applied a robust Gaussian curve fitting based on Brent's [153] optimization approach on the temporally aligned and synchronized wind speed dataset. Therefore, we firstly normalized the dataset with the 10-min averaged vertical wind speed profile ($\bar{u}_0(\zeta)$) to obtain $u(\chi, \gamma, \zeta, t)$ as the normalized longitudinal wind speed:

$$u(\chi, \gamma, \zeta, t) = \frac{u_0(\chi, \gamma, \zeta, t)}{\bar{u}_0(\zeta)}. \quad \text{Eq. 4.5}$$

In our study, we obtained this wind speed profile by averaging the LES wind field far upstream of the simulated turbine. In actual LiDAR measurements, one can use downstream measurements well outside of the wake-affected region.

We applied the following functions as the wake-tracking approach:

$$u_{fit,PPI}(\chi, r_\gamma, t) = \beta_\gamma(\chi, t) - \frac{\alpha_\gamma(\chi, t)}{\sigma_\gamma(\chi, t)\sqrt{2\pi}} e^{-\frac{1}{2}\left(\frac{r_\gamma - \mu_\gamma(\chi,t)}{\sigma_\gamma(\chi,t)}\right)^2}, \quad \text{Eq. 4.6}$$

for horizontal scans and

$$u_{fit,RHI}(\chi, r_\zeta, t) = \beta_\zeta(\chi, t) - \frac{\alpha_\zeta(\chi, t)}{\sigma_\zeta(\chi, t)\sqrt{2\pi}} e^{-\frac{1}{2}\left(\frac{r_\zeta - \mu_\zeta(\chi,t)}{\sigma_\zeta(\chi,t)}\right)^2}, \quad \text{Eq. 4.7}$$

for vertical scans, with r_γ and r_ζ as coordinates in the respective transversal in-plane directions relative to the downstream direction χ.

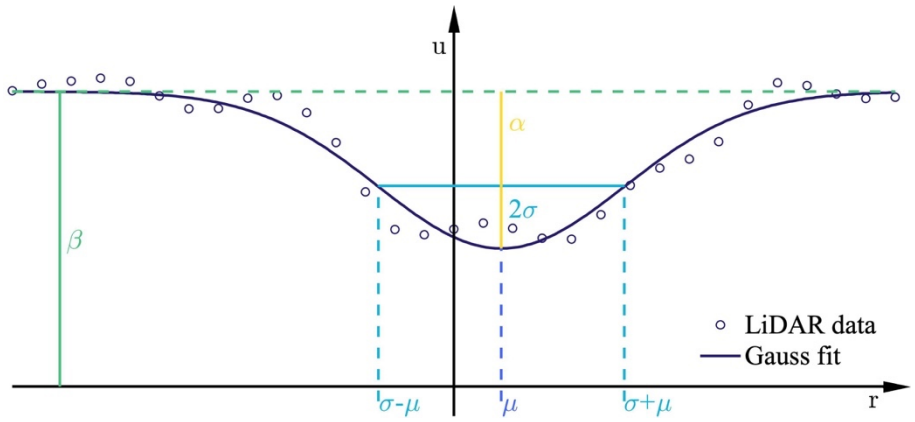

Figure 4.4. Application of Gaussian fitting to a LiDAR measurement of a wake in a downstream distance of five rotor diameters. μ indicates the wake centre position (light blue), σ represents the Gaussian wake width (turquoise), α denotes the intensity of the deficit (yellow), and β labels the ambient longitudinal wind speed levels (green).

For a better understanding of the relationship between the fitting variables and wake velocity, we present a general application of Eq. 4.6 respectively Eq. 4.7 for the RHI and PPI scans in Figure 4.4. μ_γ and μ_ζ depict the wake centre position (light blue), σ_γ and σ_ζ indicate the characteristic wake width (turquoise), α_γ and α_ζ denote the deficit intensity (yellow), and β_γ and β_ζ indicate the ambient longitudinal wind speeds (green). In contrast to Aitken et al. [66] and Bromm et al. [14], who employed a double Gaussian function for the near-wake region ($\chi D^{-1} < 2$) to represent the characteristic deficit form, we used a threshold that does not consider data below a normalized velocity of 0.55. As a result, tracking was robust and numerically faster to calculate, compared to double Gaussian fitting. By omitting velocities up to the threshold, the

algorithm mainly fit the high shear flanks of the wake deficit. The subsequent application of Eq. 4.6 and Eq. 4.7 to the propagated horizontal and vertical data from Section 4.3.2 resulted in a temporal dependency of the tracked values.

4.3.4 Calculation of the Volumetric Wind Speed Deficit

Section 4.3.3 showed how wake tracking was used to determine wake dynamics from temporally up-sampled and synchronized RHI and PPI scans. In this section, we describe how the reconstructed wake deficit is calculated.

To correctly depict the averaged wake deficit at downstream distance χ in the reconstructed wind field, a change in perspective was required to understand why the measured velocities from the RHI and PPI scans could not be directly used within the reconstructed wind field. The averaged wake deficit in the fixed frame of reference ($\overline{\delta^{FFoR}}$) was the convolution of temporally resolved deficits (δ^{MFoR}). Within the DWM model, these temporally resolved deficits are considered constant and observed in the MFoR that moves with the wake centre. In contrast, we regarded temporally resolved deficits (δ^{MFoR}) as variable, with an average deficit ($\overline{\delta^{MFoR}}$) that resulted in an averaged wake deficit in the FFoR ($\overline{\delta^{FFoR}}$) when convoluted according to the wake dynamics. We obtained these wake dynamics in Section 4.3.3; The synchronized RHI and PPI scans constituted the dataset for the average deficit in the MFoR ($\overline{\delta^{MFoR}}$), which in turn was a convolution of the variable temporally resolved deficits in the MFoR (δ^{MFoR}).

In the test case presented here, flow information was available only on the cross-shaped measurement planes. Because the LiDAR-measuring planes were fixed in the FFoR, the wake moved dynamically through them. Therefore, the variable temporally resolved deficits in the MFoR (δ^{MFoR}) were measured at different radial positions in the FFoR, depending on the wake centre position. If we look at a γ-ζ plane at downstream distance χ, only two lines of information are available. To obtain a planar deficit in the γ-ζ plane, we assumed a conditional point symmetry for the wake deficit by rotating the vertical and horizontal LiDAR scans from −90° to 90° (Figure 4.5b). If we extended the consideration of the wake deficit in a γ-ζ plane with a spatial dimension in downstream direction χ, the lines of information became planes of information and the planar deficit became a volumetric deficit (VD).

We used propagated RHI and PPI wind speed data (u), which were combined in a Cartesian (χ, γ, ζ) coordinate system. To obtain volumetric information from planar horizontal data $u_{\mathrm{PPI}}(\chi, \gamma, h_{\mathrm{HH}}, t)$ and planar vertical data $u_{\mathrm{RHI}}(\chi, 0, \zeta, t)$, we assumed a conditional rotational symmetry to create a closed volumetric deficit over downstream distance χ. Thus, we firstly defined the volumetric wind speed average in the MFoR ($\overline{u_{\mathrm{VD}}^{\mathrm{MFoR}}}$). The change from the turbine-based coordinate system to the MFoR can be expressed as:

$$\gamma'(\chi, \gamma, t) = \gamma - \mu_{\gamma}(\chi, t), \qquad \text{Eq. 4.8}$$

and

$$\zeta'(\chi, \zeta, t) = \zeta - \mu_{\zeta}(\chi, t). \qquad \text{Eq. 4.9}$$

To improve the formula's readability, we did not refer further to the dependence of initial variables (γ and ζ), but rather a reference system based on the new variables (γ' and ζ') as a new coordinate system.

The definition of the volumetric wind speed average in the MFoR ($\overline{u_{\mathrm{VD}}^{\mathrm{MFoR}}}$) in Eq. 4.10 aims to describe the average wake wind as emitted from the rotor without meandering effects:

$$\overline{u_{\mathrm{VD}}^{\mathrm{MFoR}}(\chi,\gamma',\zeta')} = \frac{1}{|\mathrm{T}|}\sum_{t\,\in\,T} u_{rot}(\chi,\gamma',\zeta',t) \qquad \text{Eq. 4.10}$$

Although this is clearly visible on the left side, the right side implies the reference frame change by subtracting the wake centre (μ_γ and μ_ζ) from the γ and ζ coordinates within the wind field (Eq. 4.8, Eq. 4.9). From the conditional rotational symmetry (±90°), we defined the wind speed calculation for a corresponding point within the resulting four quadrants:

$$u_{rot}(\chi,\gamma',\zeta',t) = \begin{cases} \big(1-\lambda(\chi,\gamma',\zeta',\mathrm{t})\big)\cdot u_{\mathrm{PPI}}(\chi,\mathrm{sign}(\gamma')\cdot\tau,h_{\mathrm{HH}},t) + & \\ \lambda(\chi,\gamma',\zeta',\mathrm{t})\cdot u_{\mathrm{RHI}}(\chi,0,\mathrm{sign}(\zeta')\cdot\tau,t) & |\ \gamma'\neq 0,\zeta'\neq 0 \\ u_{\mathrm{RHI}}(\chi,0,\zeta',t) & |\ \gamma'=0,\zeta'\neq 0 \\ u_{\mathrm{PPI}}(\chi,\gamma',0,t) & |\ \gamma'\neq 0,\zeta'=0 \\ \frac{1}{2}\big(u_{\mathrm{PPI}}(\chi,0,h_{\mathrm{HH}},t)+u_{\mathrm{RHI}}(\chi,0,0,t)\big) & |\ \gamma'=0,\zeta'=0 \end{cases}, \qquad \text{Eq. 4.11}$$

and

$$\lambda(\chi,\gamma',\zeta',t) = \left|\frac{2\tan^{-1}\left(\frac{\zeta'(\chi,t)}{\gamma'(\chi,t)}\right)}{\pi}\right|, \qquad \text{Eq. 4.12}$$

as the rotational weighting function and

$$\tau = \sqrt[2]{\gamma'^2+\zeta'^2}, \qquad \text{Eq. 4.13}$$

as the radius within the MFoR. Here, T represents a set with $t \in \mathrm{T}$ containing all wind speed information at a discrete time point t within the studied 10-min time interval. The use of dashes in Eq. 4.10 indicates the cardinality of the set T. Eq. 4.10 implies that the wake centre's position was displaced in the γ-direction and ζ-direction with respect to the hub height centreline before the corresponding velocities were rotated and weighted (Eq. 4.11) to calculate the mean value ($\overline{u_{VD}^{MFR}}$). This was the turbine-emitted wake average without any horizontal and vertical meandering effect.

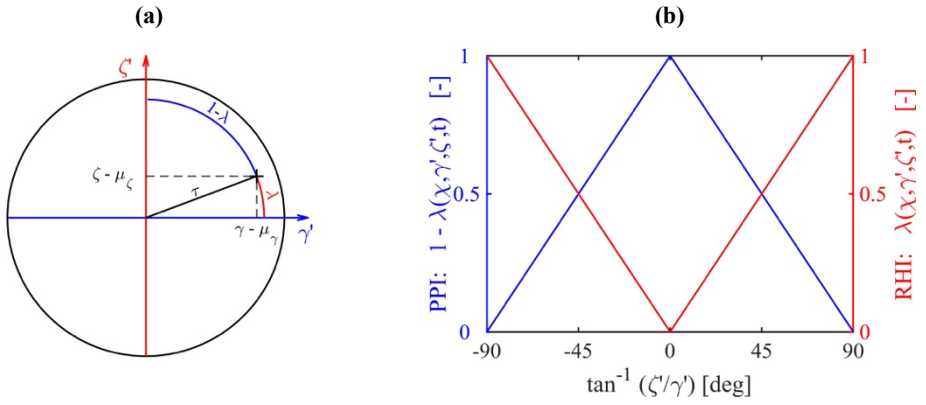

Figure 4.5. Illustration of the rotational assumption of the wake wind-field calculation in the meandering frame of reference (MFoR). **(a)** Geometric relationship of PPI (blue) and RHI scans (red) in the MFoR, and **(b)** weighting of PPI (blue) and RHI (red) wind speed data dependent on positions γ′ and ζ′.

Figure 4.5 visualizes the conditional rotational symmetry introduced in Eq. 4.11. Figure 4.5a shows how the velocity of any point in the MFoR—not only on the measuring axes—was calculated by the weighting factors λ and $1 - \lambda$ from the RHI and PPI data, respectively, depending on the point's position. In Figure 4.5b, we visualize the rotational weighting factor (λ and $1 - \lambda$) as a function of the rotation angle depending on the position in the MFoR.

4.3.5 Calculation of the Volumetric Turbulence Intensity Scaling

Analogous to generating the three-dimensional wake velocity field ($\overline{u_{\mathrm{VD}}^{\mathrm{MFoR}}}$), we calculated the standard deviation of the velocities ($\sigma_{\mathrm{VD}}^{\mathrm{MFoR}}$) in the MFoR as:

$$\sigma_{\mathrm{VD}}^{\mathrm{MFoR}}(\chi, \gamma', \zeta') = \sqrt{\frac{1}{|\mathrm{T}|} \sum_{t \in \mathrm{T}} \left(u(\chi, \gamma', \zeta', t) - \overline{u_{\mathrm{VD}}^{\mathrm{MFoR}}(\chi, \gamma', \zeta')}\right)^2}. \quad \text{Eq. 4.14}$$

where $\sigma_{\mathrm{VD}}^{\mathrm{MFoR}}$ indicates the variability within the meander-free wake velocity field $\overline{u_{\mathrm{VD}}^{\mathrm{MFoR}}}$, and is used to scale ambient turbulence to represent the turbulence induced by the wake itself without meandering-induced turbulence. To generate the turbulence intensity scaling factor ($s_{\mathrm{I}_0}^{\mathrm{MFoR}}$) from $\sigma_{\mathrm{VD}}^{\mathrm{MFoR}}$, we firstly normalized it with $\overline{u_{\mathrm{VD}}^{\mathrm{MFoR}}}$ to obtain the turbulence intensity within the MFoR, and then divided the result by the atmospheric turbulence intensity profile $I_0(\zeta)$:

$$I_{\mathrm{VD}}^{\mathrm{MFoR}}(\chi, \gamma', \zeta') = \frac{\sigma_{\mathrm{VD}}^{\mathrm{MFoR}}(\chi, \gamma', \zeta')}{\overline{u_{\mathrm{VD}}^{\mathrm{MFoR}}}(\chi, \gamma', \zeta')}, \quad \text{Eq. 4.15}$$

$$s_{\mathrm{I}_0}^{\mathrm{MFoR}}(\chi, \gamma', \zeta') = \frac{I_{\mathrm{VD}}^{\mathrm{MFoR}}(\chi, \gamma', \zeta')}{I_0(\zeta')}. \quad \text{Eq. 4.16}$$

4.3.6 Four-Dimensional Wake Wind-Field Reconstruction

In this section, we explain how the wake dynamics determined in Section 4.3.3, the volumetric wake field ($\overline{u_{\mathrm{VD}}^{\mathrm{MFoR}}}$) determined in Section 4.3.4 and the turbulence scaling factor ($s_{\mathrm{I}_0}^{\mathrm{MFoR}}$) determined in Section 4.3.5 were combined to reconstruct a 3D1C wake wind field.

The reconstruction's starting point was a 3D1C ambient flow wind field created by a wind field generator with freely selectable dimensions matching the atmospheric parameters from Section 4.2. We decompose the longitudinal velocity component of the generated wind field (u_a) into a constant part ($\overline{u_a}$) and a fluctuating part (u_t):

$$\mathrm{u}_a(\chi, \gamma, \zeta, t) = \overline{\mathrm{u}_a(\chi, \gamma, \zeta)} + \mathrm{u}_t(\chi, \gamma, \zeta, t). \quad \text{Eq. 4.17}$$

Here, we defined the mean wake deficit in the MFoR as the difference between the wake velocity field and the normalized ambient flow:

$$\overline{\delta_{\mathrm{VD}}^{\mathrm{MFoR}}(\chi, \gamma, \zeta)} = 1 - \overline{u_{\mathrm{VD}}^{\mathrm{MFoR}}(\chi, \gamma, \zeta)}. \quad \text{Eq. 4.18}$$

The average volumetric deficit in the MFoR ($\overline{\delta_{\mathrm{VD}}^{\mathrm{MFoR}}}$) served as a template in the form of a flexible tube that was displaced and scaled by the dynamics ($\mu_\gamma(\chi, t)$, $\mu_\zeta(\chi, t)$, $\sigma_\gamma(\chi, t)$, $\sigma_\zeta(\chi, t)$, $\alpha_\gamma(\chi, t)$, $\alpha_\zeta(\chi, t)$, $\beta_\gamma(\chi, t)$, and $\beta_\zeta(\chi, t)$).

To recreate the original dynamic wake behaviour as a volumetric deficit, we defined three time- and space-dependent scaling factors as follows:

$$s_\gamma(\chi,t) = \frac{\sigma_\gamma(\chi,t)}{\sigma_{\gamma_{\overline{u_{\mathrm{VD}}^{\mathrm{MFoR}}}}}(\chi)}, \qquad \text{Eq. 4.19}$$

which represents the horizontal spatial deficit shape scaling factor;

$$s_\zeta(\chi,t) = \frac{\sigma_\zeta(\chi,t)}{\sigma_{\zeta_{\overline{u_{\mathrm{VD}}^{\mathrm{MFoR}}}}}(\chi)}, \qquad \text{Eq. 4.20}$$

which represents the vertical spatial deficit shape scaling factor; and

$$s_\delta(\chi,t) = \frac{1}{2}\frac{\frac{1}{\sqrt{2\pi}}\left(\frac{\alpha_\gamma(\chi,t)}{\sigma_\gamma(\chi,t)} + \frac{\alpha_\zeta(\chi,t)}{\sigma_\zeta(\chi,t)}\right) + \beta_\gamma(\chi,t) + \beta_\zeta(\chi,t)}{\frac{1}{\sqrt{2\pi}}\left(\frac{\alpha_{\gamma_{\overline{u_{\mathrm{VD}}^{\mathrm{MFoR}}}}}(\chi)}{\sigma_{\gamma_{\overline{u_{\mathrm{VD}}^{\mathrm{MFoR}}}}}(\chi)} + \frac{\alpha_{\zeta_{\overline{u_{\mathrm{VD}}^{\mathrm{MFoR}}}}}(\chi)}{\sigma_{\zeta_{\overline{u_{\mathrm{VD}}^{\mathrm{MFoR}}}}}(\chi)}\right) + \beta_\gamma(\chi) + \beta_\zeta(\chi)}, \qquad \text{Eq. 4.21}$$

which represents the velocity deficit intensity scaling factor. Here, $\mu_{\gamma_{\overline{u_{\mathrm{VD}}^{\mathrm{MFoR}}}}}(\chi)$, $\mu_{\zeta_{\overline{u_{\mathrm{VD}}^{\mathrm{MFoR}}}}}(\chi)$, $\sigma_{\gamma_{\overline{u_{\mathrm{VD}}^{\mathrm{MFoR}}}}}(\chi)$, $\sigma_{\zeta_{\overline{u_{\mathrm{VD}}^{\mathrm{MFoR}}}}}(\chi)$, $\alpha_{\gamma_{\overline{u_{\mathrm{VD}}^{\mathrm{MFoR}}}}}(\chi)$, $\alpha_{\zeta_{\overline{u_{\mathrm{VD}}^{\mathrm{MFoR}}}}}(\chi)$, $\beta_{\gamma_{\overline{u_{\mathrm{VD}}^{\mathrm{MFoR}}}}}(\chi)$, and $\beta_{\zeta_{\overline{u_{\mathrm{VD}}^{\mathrm{MFoR}}}}}(\chi)$ were determined by applying Eq. 4.6 and Eq. 4.7 to the vertical and horizontal slices through the hub height centreline of the 3D $\overline{u_{VD}^{MFoR}}$. Thus, it became apparent that u_{VD}^{MFoR} was only scaled by the three previously defined factors because of its descriptive properties.

This led to the resulting formula for generating the time-dependent 3D1C velocity deficit (δ_{VD}). Here, we applied retransformations from the MFoR on the right sides of Eq. 4.22 and Eq. 4.23, to the FFoR on the left side of these equations, by adding the wake centre position (μ_γ and μ_ζ):

$$\delta_{VD}(\chi,\gamma,\zeta,t) = \overline{\delta_{\mathrm{VD}}^{\mathrm{MFoR}}\left(\chi,\gamma'\cdot s_\gamma(\chi,t)+\mu_\gamma(\chi,t),\zeta'\cdot s_\zeta(\chi,\mathrm{t})+\mu_\zeta(\chi,t)\right)}\cdot s_\delta(\chi,\mathrm{t}), \qquad \text{Eq. 4.22}$$

Analogously, the resulting formula for the four-dimensional (3D1C) turbulence scaling could be expressed as:

$$s_{\mathrm{I}_0}(\chi,\gamma,\zeta,t) = s_{\mathrm{I}_0}^{\mathrm{MFoR}}\left(\chi,\gamma'\cdot s_\gamma(\chi,t)+\mu_\gamma(\chi,t),\zeta'\cdot s_\zeta(\chi,\mathrm{t})+\mu_\zeta(\chi,t)\right)\cdot s_\delta(\chi,\mathrm{t}). \qquad \text{Eq. 4.23}$$

To describe the reconstructed wake field (u_{RC}), we assumed a superposition approach similar to Eq. 4.17. The constant part of the ambient wind field ($\overline{u_a}$) was overlaid with the dynamic wake deficit (δ_{VD}), and the fluctuating part of the ambient wind field (u_t) was multiplied by the dynamic turbulent intensity factor (s_{I_0}). This defined the reconstructed wake field (u_{RC}):

$$u_{RC}(\chi,\gamma,\zeta,t) = \left(\overline{u_a(\chi,\gamma,\zeta)} - \delta_{VD}(\chi,\gamma,\zeta,t)\right) + \left(u_t(\chi,\gamma,\zeta,t)\cdot s_{\mathrm{I}_0}(\chi,\gamma,\zeta,t)\right). \qquad \text{Eq. 4.24}$$

4.4 Results

In this section, we present results of the reconstruction method introduced in Section 4.3 to work with the synthetic LiDAR data described in Section 4.2. To the extent possible, we varied the angular velocities ω_ϕ and ω_θ to determine their influences on reconstruction quality, thereby finding an optimal parameter set for the test case.

4.4.1 Determination of Wake Dynamics

We determined the wake dynamics by applying the Gaussian wake tracking method from Section 4.3.3 on the propagated LiDAR and LES wind speed data. The determined wake dynamics appeared to be the most influencing factors for reconstruction as the corresponding results were also used to calculate the deficit shape. To evaluate the wake tracking quality from

the propagated LiDAR scan data, we referred to the LES wind field. Thus, we applied Equations Eq. 4.6 and Eq. 4.7 to the LES data and estimated the wake centre position dynamics, which we used as a reference in our analysis.

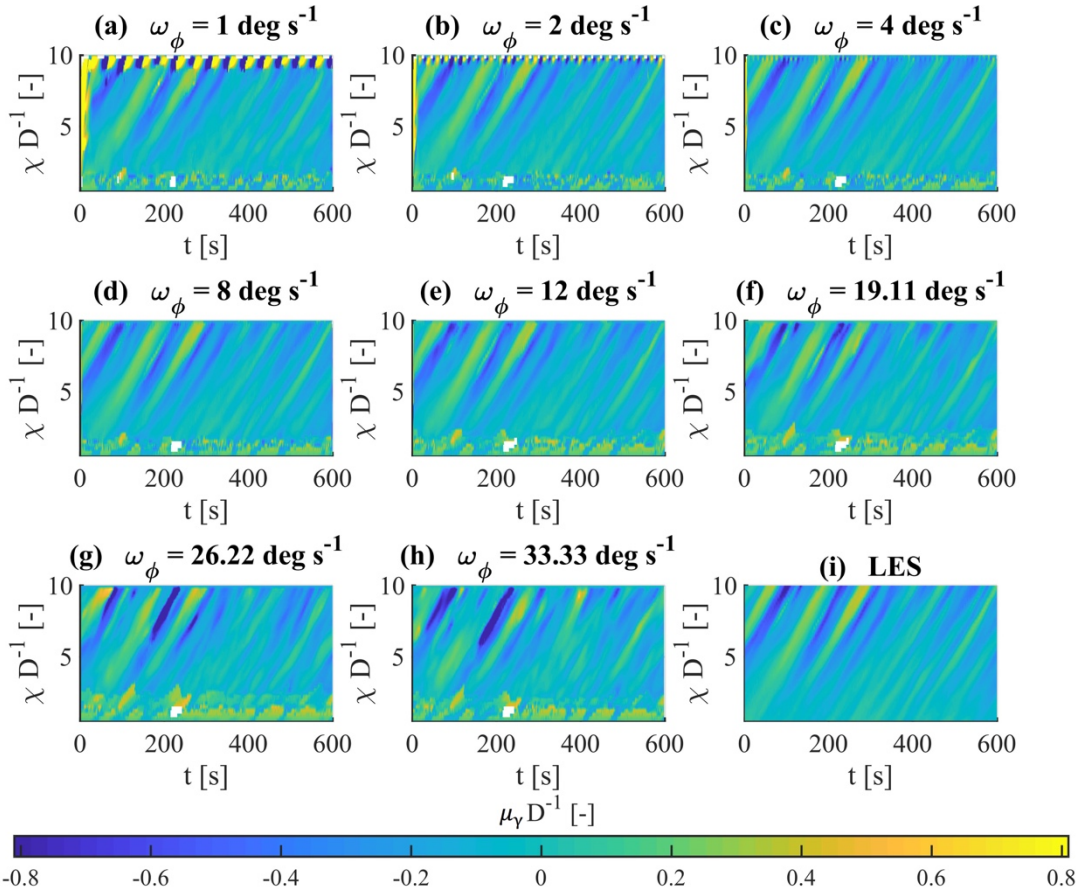

Figure 4.6. Visualisation of the tracked horizontal wake centre μ_γ in the FFoR in dependency of time t and downstream distance χ, **(a-h)** show the effect of different angular velocities on the tracking, **(i)** shows μ_γ based on LES data.

Figure 4.6 shows a visualization of the tracked wake centre depending on time and the dimensionless downstream position χD^{-1}. Figure 4.6i shows a consistent mapping of the wake path and depicts lateral meandering effects over the downstream direction χ and time t. Unphysical jumps or fractures, which indicate that the chosen method cannot be representative or that the chosen spatial and temporal resolutions are insufficient, were not visible. Individual flow structures tracked in the downstream direction over time, which we refer to as meander events, are shown as curved stripes in Figure 4.6. As expected, meander events were characterized by increasing lateral deflections and advection speeds with increased downstream distance.

Noisy behaviour can be recognized for all angular velocities up to a distance of $\chi D^{-1} \approx 3$ for the wake centre data $\mu_\gamma D^{-1}$ in Figure 4.6a-h, This noise occurred due to the insufficient data availability in the γ-direction outside of the scanned area, which was determined by the scanning opening angle $\Delta\phi$.

Because of the influences of the wind-field propagation boundary condition, the wind speed was reduced at a downstream distance of $\chi D^{-1} \approx 10$. This influence was attributed to the space–time conversion boundary conditions and could also be seen in the wake dynamics determination. Compared to the LES, a significant periodic deviation of the tracked wake centre was visible at the rear edge of the measuring area around $\chi D^{-1} \approx 10$, which distracted the Gaussian fitting

function from the real wake deficit. The frequency and size of this distraction depended on the number of propagation steps and decreased as the number of steps decreased. Gaps in Figure 4.6 show that the Gaussian fitting could not always determine a clear parameterization. The corresponding illustration of the RHI scan-tracked wake centre positions can be found in Appendix 4.A.

Although the influence of the wind-field propagation on the wake dynamic tracking could not be bypassed here, the fitting algorithm's performance in situations with insufficient data, i.e., for $\chi D^{-1} \leq 3$, could be significantly improved by artificially adding data from the corresponding scan. For this purpose, unavailable data in Figure 4.7a outside of the red circular arc-shaped area visible in were added within the χ-direction averaged wind speed values for the corresponding γ-positions from the corresponding scan. For averaging, we considered wind speed 0.25 D from the first available data in the χ-direction for the corresponding γ-positions. Figure 4.7b shows how the artificial data extension (ADE) added spatially averaged data to complement unavailable data due to the opening angle of the measurement.

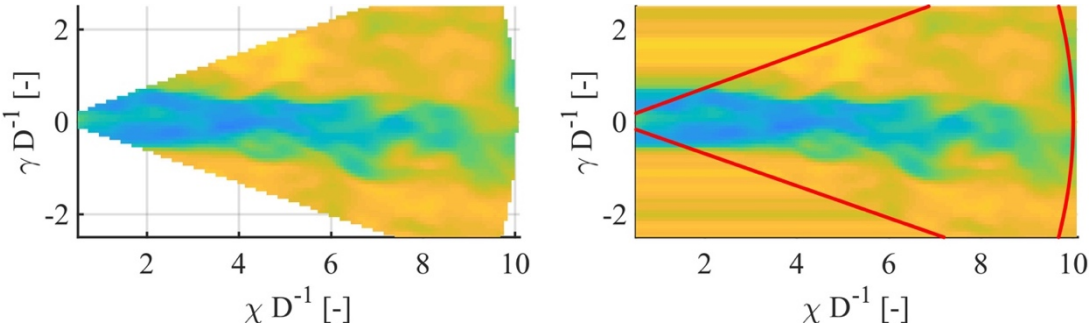

Figure 4.7. Illustration of functioning of the artificial data extension. **(a)** shows the wind speed normalised PPI scan whereas **(b)** depict the result of the method. The scan trajectory outline is marked in red.

Figure 4.8 and Figure 4.9 demonstrate the effects of ADE (Figure 4.8b,d and Figure 4.9b,d) on horizontal tracking results compared to the original data (Figure 4.8c and Figure 4.9c) and provide an overview of the tracked value statistics.

Figure 4.8a,b show the mean value (solid lines) $\overline{\mu_\gamma}$ of the tracked horizontal wake centre μ_γ and its standard deviation (dashed lines) σ_{μ_γ} for different angular speeds, and Figure 4.8c,d display the averaged tracked horizontal wake width (solid lines) $\overline{\sigma_\gamma}$ of σ_γ and its standard deviation (dashed lines) σ_{σ_γ}. An almost linear lateral displacement of the wake centre of approximately 0.17 D could be seen over a downstream distance of 10 D, which corresponded to an approximately 1° deflection angle. Here, the effects of insufficient data and the influence of boundary conditions could be seen in the strong deviations. By applying ADE, we inferred from Figure 4.8b that the wake centre position of the propagated wind speed data could be determined more precisely, not only up to $\chi D^{-1} \leq 3$ but over the entire flow field. This was evident for all angular velocities and could be seen in the mean value $\overline{\mu_\gamma}$ and in the wake centre's standard deviation σ_{μ_γ}. The wake dynamics determination improvements are particularly noticeable in the tracked horizontal wake width in Figure 4.8d. Although the mean wake width $\overline{\sigma_\gamma}$ was accurately represented for downstream distances $\chi D^{-1} > 3$, the most significant improvement was noted in the wake width's standard deviation (dashed lines) σ_{σ_γ}, which was better tracked over all downstream positions.

The videos 4.S1 and 4.S2 (Supplementary Materials) for the horizontal and vertical data, respectively, show not only propagated wind speed data but also the wake tracking results. The black line indicates the wake centre's position based on the propagated data, whereas the white line was based on ADE results. It is clearly visible that the accuracy and variability of the position tracking could be improved with the above presented approach up to $\chi D^{-1} \leq 3$.

We identified, mainly through visual comparison, two factors in tracking vertical wake movements that we found to be more susceptible to interference than in horizontal tracking. Firstly, because vertical velocity data were measured on the centreline, only this wake deficit was displayed on the vertical plane for the horizontal wake profile. It was, thus, not ensured that the tracking algorithm would identify the wake deficit in the case of pronounced horizontal meandering. The effects of limited representativeness of the intersection of the measurement planes and the current wake volume were more evident for vertical measurements than horizontal measurements as the horizontal wake displacement was characterized by greater amplitudes than vertical wake displacement. This different behaviour shows the necessity of wake tracking methods that do not quantify instantaneous wake profile integrally, but rather use a separate method optimized for vertical wake measurements. The amplitude difference cannot be seen in the statistics in Figure 4.8 and Figure 4.9, as they already include effects of limited representativeness of the measured intersection; however, they can be observed in the Videos 4.S1 and 4.S2 (Supplementary Materials).

The second influencing factor was the LiDAR simulator's operating principle. When laser pulses hit the ground, a hard target is simulated, which results in corrupted velocity data. These data gaps result in a reduced amount of data that affect the fitting quality.

As in Figure 4.8, we illustrate vertical wake-tracking statistics in Figure 4.9. Figure 4.9a,b which show the mean value (solid lines) $\overline{\mu_\zeta}$ and its standard deviation (dashed lines) σ_{μ_ζ}. We can see that the wake gradually sank to −0.2 D over the entire downstream distance. This can be clearly observed at a distance of $\chi D^{-1} > 3$, after which the corresponding standard deviation increased almost linearly. At a distance of $\chi D^{-1} > 8$, the accuracy of $\overline{\mu_\zeta}$ of $\omega_\theta \geq 19.11°/s$ decreased due to ADE. A possible explanation for this was the reduced data availability near the ground, which was amplified by the lesser number of angular measurements (Table 4.1).

In Figure 4.9c,d we present the average vertical wake width $\overline{\sigma_{\gamma\zeta}}$ and the standard deviation σ_{σ_ζ}. Here, the difficulties of tracking the vertical wake profile become apparent. If we regard the original the original (Figure 4.9c) and ADE (Figure 4.9d) vertical wake width results, we can find that $\overline{\sigma_{\gamma\zeta}}$ does not reflect a smooth trend, as expected from the horizontal tracking. The ADE data showed a better representation of the wake expansion at $\chi D^{-1} \approx 1$, which could also be found in the LES reference data. Furthermore, the standard deviation of the wake width σ_{σ_ζ} could be improved, especially in the near-wake region of $\chi D^{-1} < 3$.

Within the subsequent reconstruction process steps, we used ADE to represent the wake dynamics.

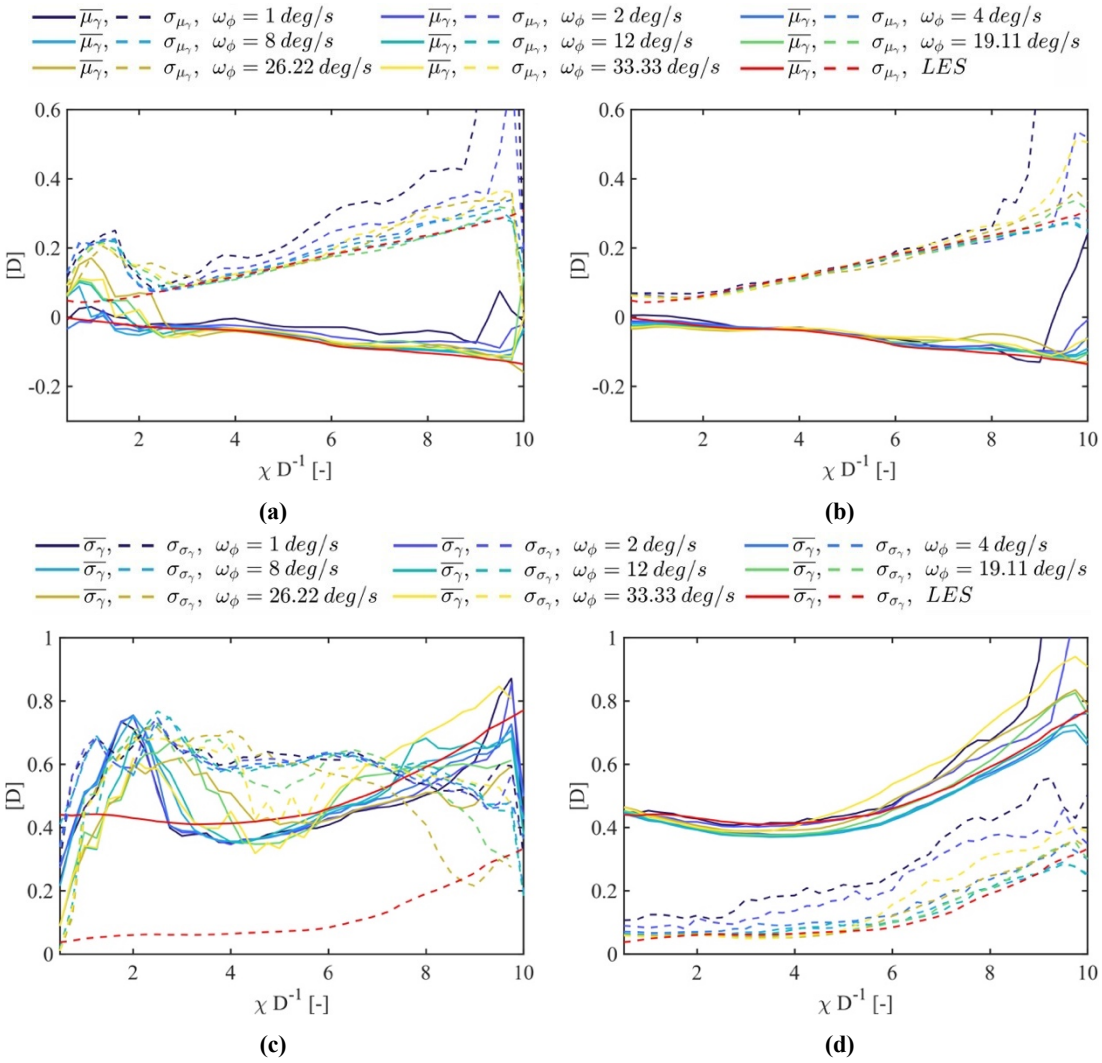

Figure 4.8. Mean value and standard deviation of wake tracking results for propagated PPI data. **(a)** Horizontal wake centre of original data, **(b)** horizontal wake centre based on artificial extended data, **(c)** horizontal wake width of original data and **(d)** horizontal wake width based on artificial extended data.

4.4.2 Four-Dimensional Wake Wind-Field Reconstruction

In this section, we present the 3D1C wake wind-field reconstruction results. Because the comparison of time-dependent wind fields can be quantified using different approaches, we firstly discuss the reconstruction quality's dependence on horizontal and vertical angular velocities as the main influencing factors for spatial and temporal discretization of the wake region. Then, we show the most accurate reconstructed wake wind field. To this end, we differentiated the reconstruction quality into steady and dynamic approaches.

4.4.2.1 Steady Error Quantification

Various methods can be used to quantify the comparability of time series in time-series analysis. One assumption is the consideration of signals as discrete stochastic processes. Central moments can be compared using a finite amount of sample data. Here, we considered the first moment in the form of mean value differences, expressed as:

$$\varepsilon_{\overline{u}} = u_{RC} - u_{LES}, \qquad \text{Eq. 4.25}$$

with index RC representing the reconstructed wake wind field and index LES representing the LES reference wind field. Similarly, we analysed the second moment in the form of standard deviation errors expressed as

$$\varepsilon_{\sigma_u} = \sigma_{RC} - \sigma_{LES}. \qquad \text{Eq. 4.26}$$

We limit the discussion of the following results to an averaged evaluation in the range of $4 \leq \chi D^{-1} \leq 9$ to exclude propagation errors at the outlet of the flow field and in the near rotor area due to the assumption of homogeneity. This choice gives a stronger focus on current commonly used turbine spacing.

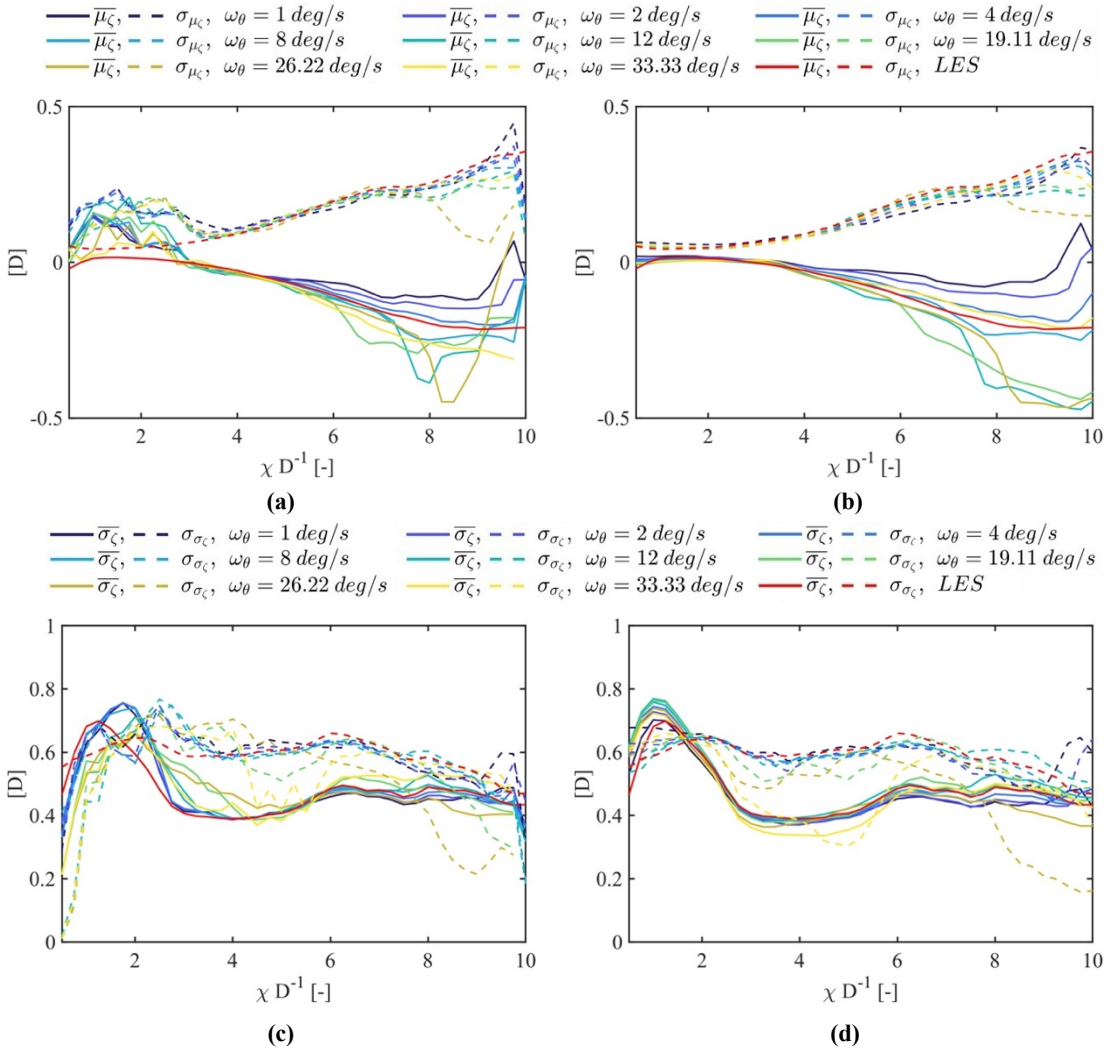

Figure 4.9. Mean value and standard deviation of wake tracking results for propagated RHI data. **(a)** Vertical wake centre of original data, **(b)** vertical wake centre based on artificial extended data, **(c)** vertical wake width of original data and **(d)** vertical wake width based on artificial extended data.

Figure 4.10a, shows the average error of the 3D1C reconstructed wake wind field of corresponding angular velocity combinations with respect to the original LES wake wind field. A clear minimum of $\varepsilon_{\overline{u}} = 2.3\ \%$ can be seen for the combination of $\omega_\phi = 12°/s$ and $\omega_\theta = 19.11°/s$. From this minimum, an exponential increase in error can be detected on both axes, where a greater error increase for ω_θ than ω_ϕ indicates a greater dependency on vertical scanning than horizontal scanning. The standard deviation error distribution in Figure 4.10b indicates that, for $\omega_\phi = 12°/s$ and $\omega_\theta = 8°/s$, it was possible to reconstruct the standard deviation with

$\varepsilon_{\sigma_u} = 0.16$ %. Furthermore, a clear trend can be observed in the error. Combinations showing a small error formed an exponential behaviour for angular velocities of up to $\omega_\phi \leq 12°/s$, after which they mainly depended on ω_θ. This means that reconstructing a wake fluctuation with a low horizontal temporal resolution could be compensated for by using a high vertical temporal resolution. From this behaviour, we deduced a greater dependence of the reconstruction on vertical measurements than horizontal measurements. Figure 4.10a,b show that the reconstruction could be parameterized to minimize either the average wind speed error or standard deviation error. Because of the wake reconstruction method's complexity, we could not provide a detailed justification in this respect and could only evaluate the results as a whole. However, because a major part of the method is based on wake dynamics, we could assume that a wake tracking method that is more representative of the real wake dynamics also provides more precise reconstruction results.

Because we assumed that both the average and the standard deviation should be accurately reflected in the reconstruction, Figure 4.10c presents a combined error behaviour of

$$\varepsilon_{\mathrm{CMB}} = \sqrt{\varepsilon_{\overline{u}}^2 + \varepsilon_{\sigma_u}^2} \qquad \text{Eq. 4.27}$$

to determine a trade-off representing a resulting minimum at $\omega_\phi = 4°/s$ and $\omega_\theta = 19.11°/s$.

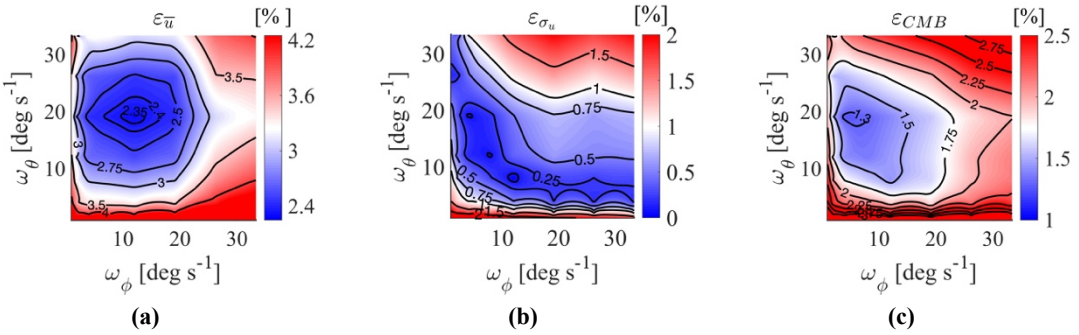

Figure 4.10. Error visualisation of the reconstructed wind field based on the LES wake wind field. **(a)** shows the average wind speed error, **(b)** the standard deviation error and **(c)** a combination of average and standard deviation error. All three in relation of combinations of the vertical and horizontal scanning angular velocities ω_θ and ω_ϕ.

We used this angular velocity combination as a compromise to show differences between the reconstructed wind field and original LES wind field. Therefore, we present $\gamma - \zeta$-planes for different downstream distances in Figure 4.11 and Figure 4.12 to depict the distribution of the wind speed average, the standard deviation, and the related errors $\varepsilon_{\overline{u}}$ and ε_{σ_u}.

The reconstructed wake wind field in Figure 4.11b can represent the expansion and relaxation of the velocity deficit in the downstream direction corresponding to the LES reference in Figure 4.11a. The wind speed error in Figure 4.11c demonstrates an underestimation of the deficit that could be observed for all distances within a structure and was more imposed in the vertical direction. We assumed that this was based on the weaker representation of wake dynamics by the wake tracking method for vertical measurements than horizontal measurements. The importance of this on the overall reconstruction could be seen here.

Because of the conditional rotational symmetry and the limited data availability due to the horizontal and vertical scan opening angles, increased errors were to be expected in the mean wind speed and standard deviation up to $\chi D^{-1} \leq 3$. We first noted this in the velocity deficit of the turbine tower, which could be detected in the first downstream slice at $\chi D^{-1} = 1$ in

Figure 4.11a and Figure 4.12c, but could not be mapped in the reconstruction in Figure 4.11b. Furthermore, it was found in the reconstructed deficit profile in a radial direction up to $\chi D^{-1} \leq 2$. Additionally, it was evident that the distribution of the standard deviation up to $\chi D^{-1} \leq 3$ was strongly underestimated in the wake region (Figure 4.12c). Moreover, the standard deviation in in Figure 4.12a and Figure 4.12b, showed that the areas of increased fluctuation were more strongly affected by errors than the initial horizontal and vertical plane positions because of the rotational symmetry. Figure 4.12c shows this effect in the downstream planes $2 \leq \chi D^{-1} \leq 6$. We surmised that this effect was due to spherical-to-Gaussian sub-grid interpolations.

A further assumption-induced error could be seen up to $\chi D^{-1} \leq 6$ due to the absence of a wake-soil model. The apparent velocity increase near the ground could not be reproduced in the reconstruction. This error could also be seen in the standard deviation differences in Figure 4.12c.

To give an overall impression of the reconstructed wind field behaviour, we present vertical slices at different downstream distances in Video 4.S3 (Supplementary Materials), which shows the wind speed compared to the LES. The reconstructed wind field in Video 4.S3 was calculated using the parameterization of $\omega_\phi = 4°/s$ and $\omega_\theta = 19.11°/s$.

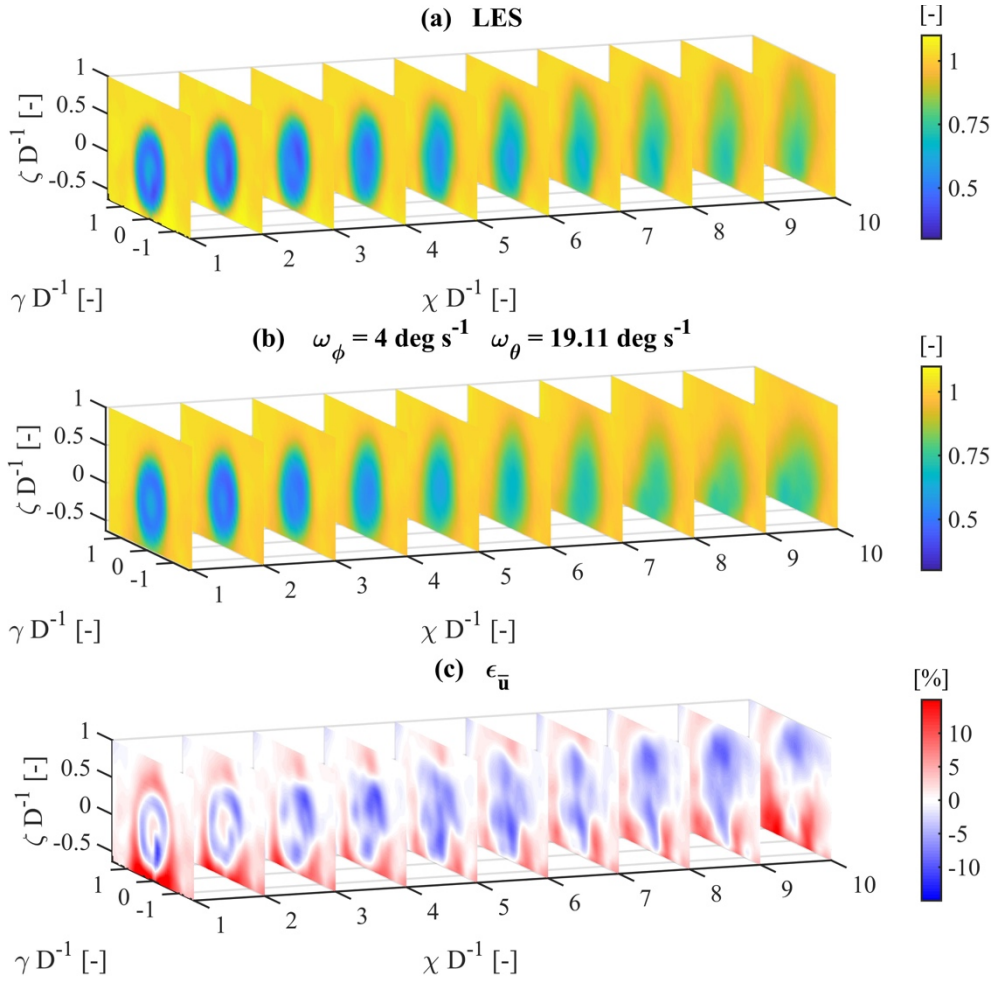

Figure 4.11. Visualisation the normalised wind speed component u of **(a)** the LES wake wind field, **(b)** the reconstructed wind field with $\omega_\phi = 4°/s$ and $\omega_\theta = 19.11°/s$ and **(c)** differences of the LES and the reconstruction.

4.4.2.2 Dynamic Error Quantification

After we examined the steady reconstruction errors in Section 4.4.2.1, we considered how far time-series dynamics could be mapped within the reconstructed wind field. We firstly used

known methods to represent the time-series dynamics reconstruction quality and then presented an approach to quantify the dynamic errors.

To this end, we firstly considered cross-correlations of the original LES time series and reconstructed wind field for each point in space in Figure 4.13a. The correlation of different time series in the wake region was lower than that in the free flow surrounding it. Although the reconstructed wind field reached a nearly perfect correlation in the free stream, a minimum of 0.39 could be found in the wake at $\chi D^{-1} \cong 3$. For downstream distances of $4 \leq \chi D^{-1} \leq 9$, where the previously mentioned propagation errors were lower, we saw correlations greater than 0.65. Apparently, the linear correlation decrease relied on the wake velocity distribution (Figure 4.11b). This effect could be attributed to the decreased average velocity in the wake. Thus, fluctuation differences due to time-delayed meander events had a greater reducing effect on cross-correlation calculations than time-series data within free stream situations.

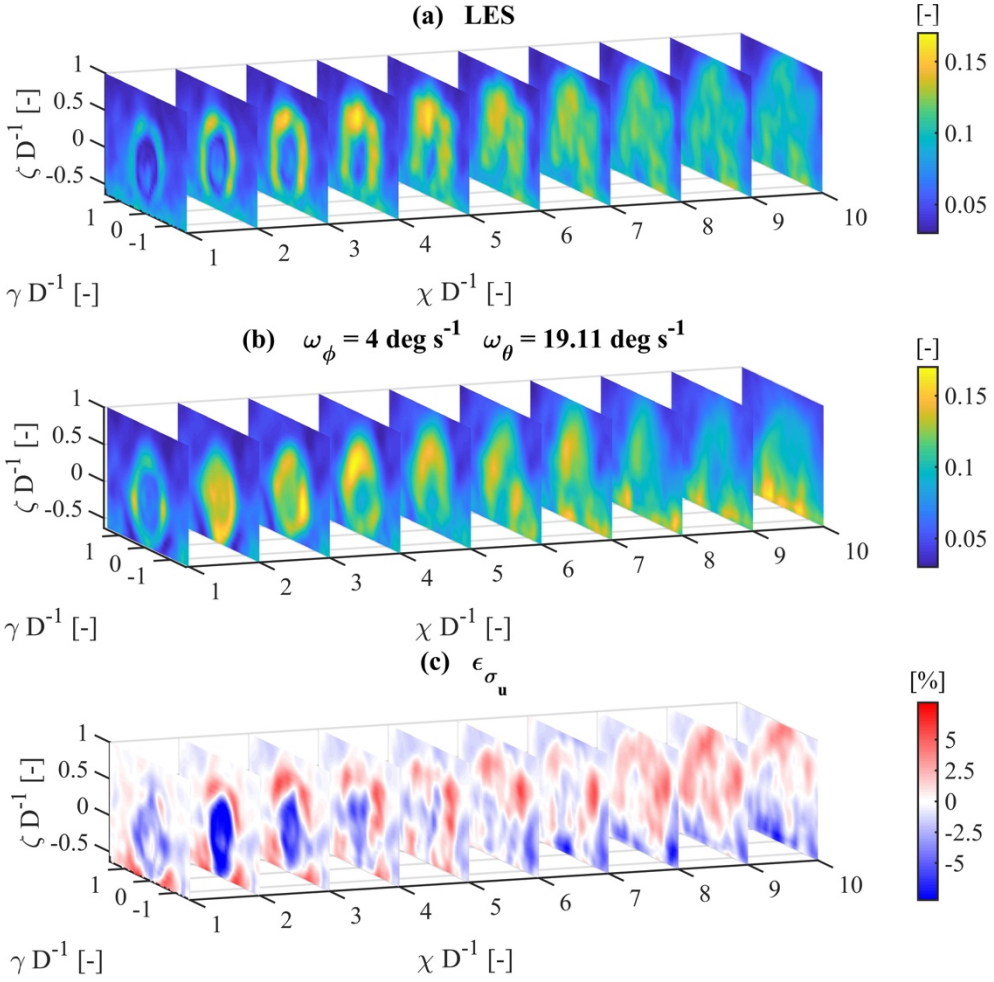

Figure 4.12. Visualisation the standard deviation of the normalised wind speed component u of **(a)** the LES wake wind field, **(b)** the reconstructed wind field with $\omega_\phi = 4°/s$ and $\omega_\theta = 19.11°/s$ and **(c)** differences of the LES and the reconstruction.

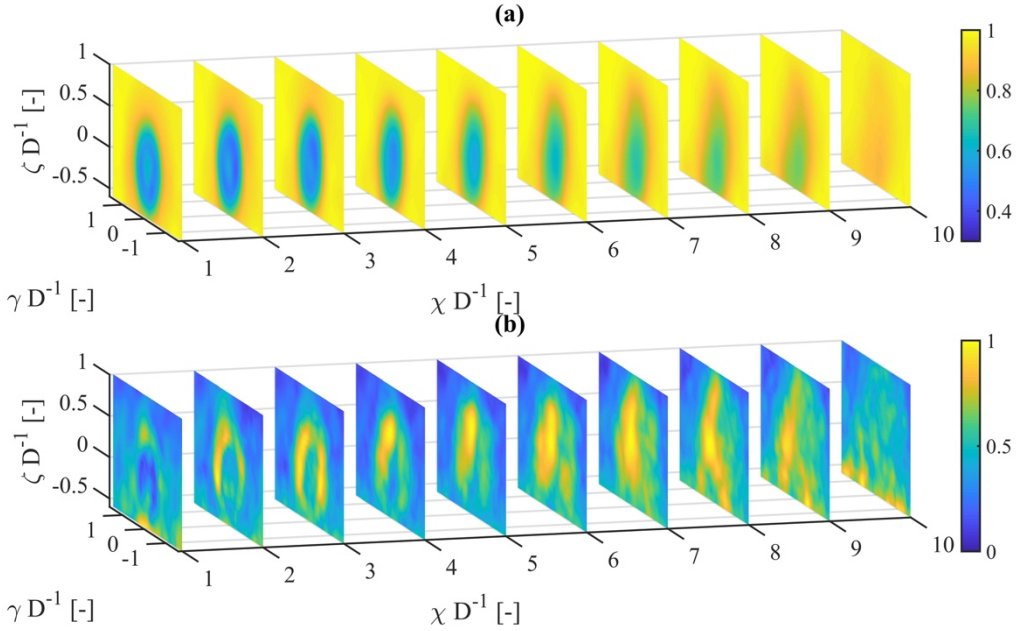

Figure 4.13. Correlation of the LES wake wind field time series with time series of the reconstruction. **(a)** Correlation result based on the time series. **(b)** Correlation result based on average adjusted the time series.

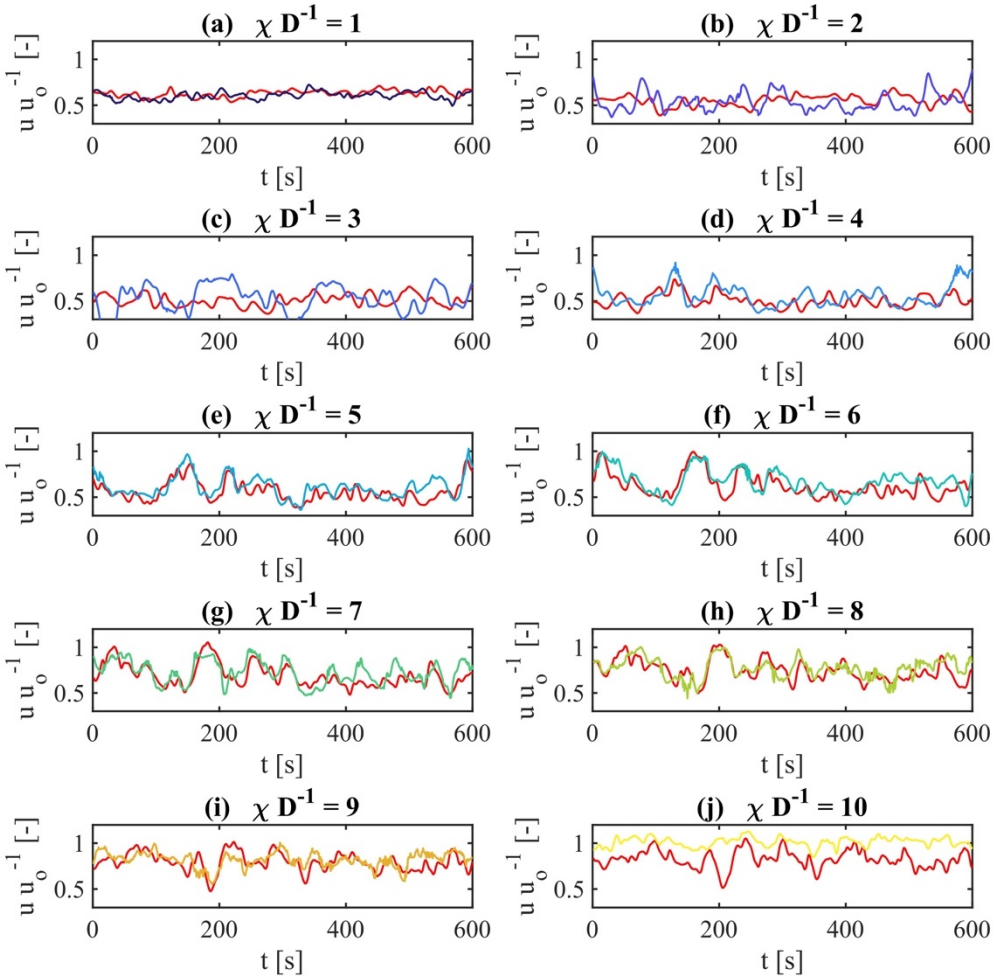

Figure 4.14. Direct comparison of wind speed time series of the LES wake wind field (red) and the reconstructed wind field for different downstream distances along the hub height centreline. Different colours refer to corresponding downstream distances.

It was assumed that flow fluctuations, especially in the wake, were primarily responsible for fatigue loads; therefore, we conducted cross-correlations referring to mean value-adjusted fluctuations (subtraction of local velocity average) of the wind field in Figure 4.13b. The mean-adjusted free flow was only characterized by turbulence; thus, these areas showed a low correlation, as expected. In Figure 4.13b, we further detected that high correlation areas changed with increased downstream distance. Although a round wake shape could be clearly identified up to $\chi D^{-1} \leq 3$, collimated high-correlation areas were visible on the hub height centreline for $\chi D^{-1} > 3$. For both Figure 4.13a and Figure 4.13b, the boundary condition problem's influence by propagation could be recognized at $\chi D^{-1} \approx 10$, as indicated by the lower correlation values.

To further evaluate the similarity of the reconstructed wind field and LES, we used an approach commonly known in the field of speech recognition. Because the cross-correlation considered dynamics of the largest possible time scale of the time series, small-scale signal shifts could not be individually considered. Figure 4.14 shows time-dependent velocity curves at different downstream distances along the centreline of the reconstructed wind field and corresponding LES data (red). As shown in Figure 4.14d-i, the original and reconstructed time series showed similar behaviours in which individual peaks shifted in intensity and time. To describe the reconstruction quality of these individual peak events, we applied dynamic time warping (DTW), which dynamically stretches and compresses signals to minimize the Euclidean distance. Two information groups were generated using DTW. One part of the result was the mutual assignment of each data point of the reconstructed time series to a data point of the original time series. Figure 4.15a illustrates the allocation of velocity data for different downstream distances to the corresponding time index of the original time series. The graph could, thus, be interpreted as an assignment path for both signals. The dashed red diagonal line corresponds to the mapping of two identical signals. As the corresponding allocation paths shifted further from the diagonal, the displacements of single peak events became more pronounced within the time series. We calculated the average mutual time deviation $\varepsilon_{\Delta t}$ of both time series by determining the average of the deviations of the time index of the allocated data points Δt in Figure 4.15b.

We used the average time error $\overline{\varepsilon_{\Delta t}}$ magnitude as a measure of the dynamic reconstruction quality, which we illustrate for all points of the reconstructed wind field in vertical slices in Figure 4.16c. A smaller deviation indicated a more accurate temporal representation of peak events.

Because wind turbine load calculations showed a greater dependence on inflow variability and spectral representation than on a wind speed offset, we saw the mean temporal error $\overline{\varepsilon_{\Delta t}}$ as a pragmatic measure to represent the effects of different dynamics within the time series. The instantaneous temporal error of the reconstructed time series led to a different dynamic of the time series, thus leading to a spectral change in the wind speed. Further studies comparing load calculations of the reconstructed wind fields with those of the LES reference must first evaluate to what extent the mean temporal error can represent differences in time-series dynamics, and then determine to what extent which scalar is suitable for representing the allocation path.

As seen in the results above, the distribution of $\overline{\varepsilon_{\Delta t}}$ indicated an increased error in the near-wake area up to $\chi D^{-1} \leq 3$. From this distance on, the reconstruction quality improved along the centreline, representing an average time error of $\overline{\varepsilon_{\Delta t}} \approx 25\ s$ for the total duration of 600 s within the wake region.

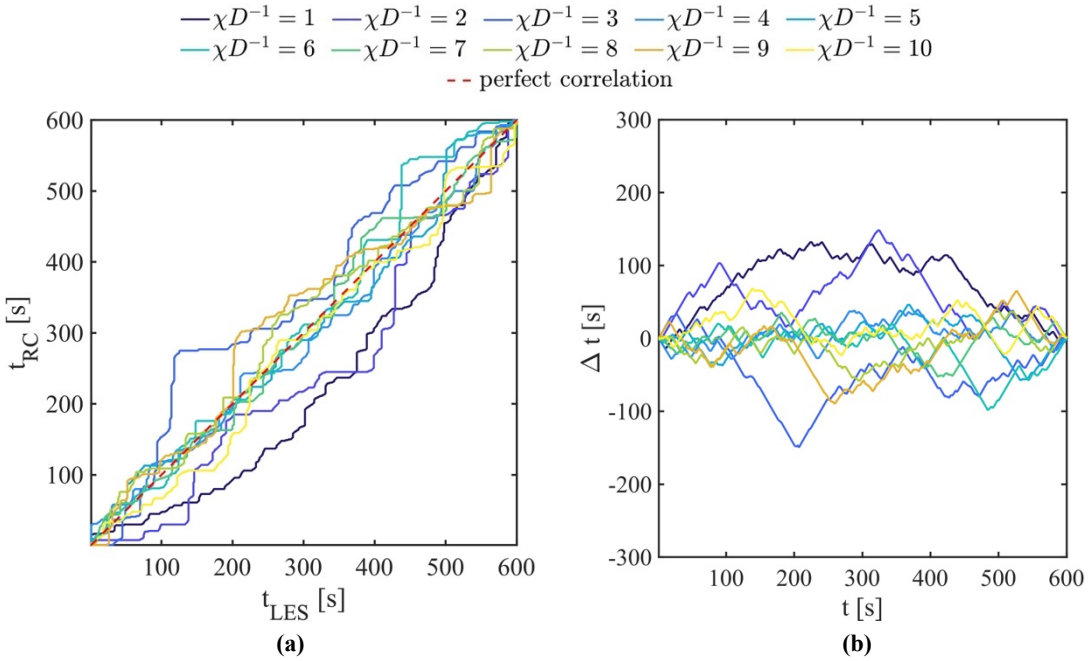

Figure 4.15. Result of the application of the dynamic time warping to the LES wake wind field time series and reconstructed time series. **(a)** Allocation paths of time series and **(b)** the resulting temporal error of peak events along the hub height centreline for different downstream distances.

The second result of the DTW was the time-series Euclidean distance based on the allocated data. The distance of the unadjusted time series in Figure 4.16a is shown in contrast to that of the adjusted time series in Figure 4.16b. At $4 \leq \chi D^{-1} \leq 9$, improvements in velocity error correlated with regions with small average temporal errors. The considerably reduced Euclidean distance seen in the comparison showed the remaining error of the differences in the amplitudes of the new allocated peak events. The average wind speed error in Figure 4.11c could, thus, be divided into its constituent components. One part was an offset and the other was due to different dynamics. With the DTW, we could quantify both components and evaluate the reconstruction. Therefore, we saw this method as a good indicator for evaluating the quality of peak event reconstructions. A smaller average time error (Figure 4.16c), indicated more precise representation of the wake dynamics by wake tracking. Additionally, smaller remaining Euclidean distances (Figure 4.16b), demonstrated a more accurately determined wake deficit in the MFoR, which in turn depended on wake dynamics determination.

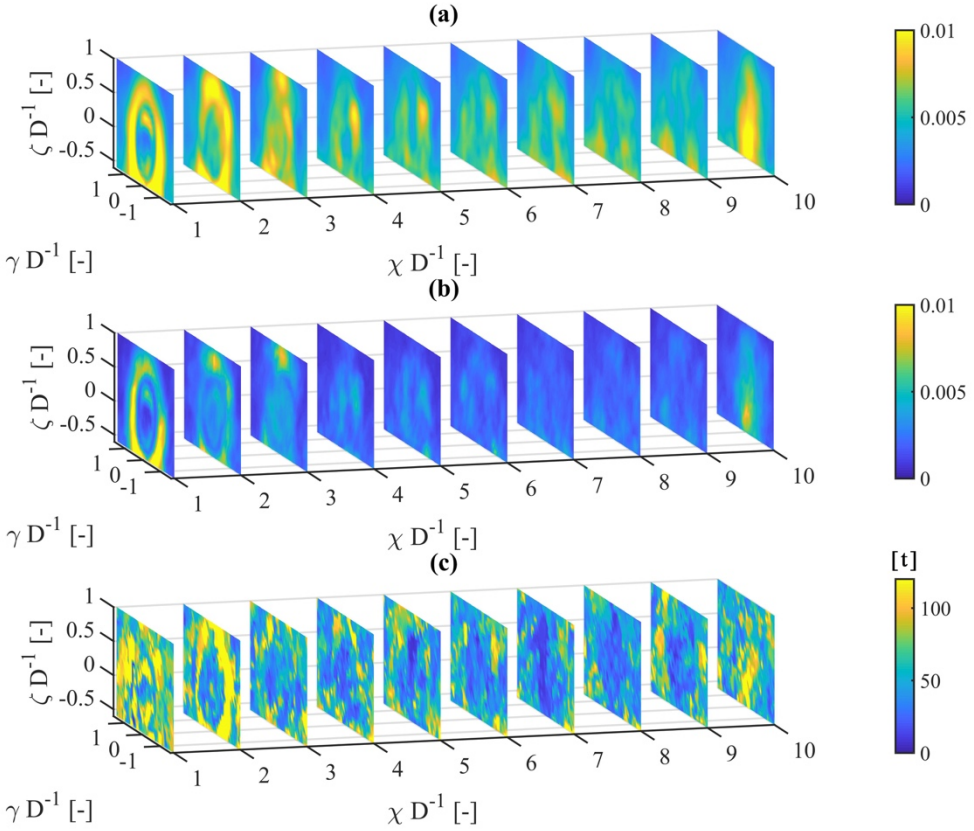

Figure 4.16. **(a)** Visualisation of the Euclidian distance between the time series of the LES and the reconstructed wind field. **(b)** Euclidian distance of the new allocated time series of the LES and the reconstructed wind field after applying the dynamic time warping. **(c)** Resulting average time error of the LES and reconstructed time series by the Application of the dynamic time warping.

4.5 Discussion

In this section, we discuss the introduced method for reconstructing 3D1C wake wind fields from LiDAR measurements and its results.

One significant difficulty with designing a wake reconstruction method is the limited possibility of verification due to a lack of measurement methods needed for a holistic validation. A limited validation of the proposed reconstruction method could still be conducted in full-field measurements. If the corresponding reference data from one or more anemometers in the wake region are available, an evaluation can be performed based on the comparison of statistics or application of DTW, which is a comparison of time series. Nevertheless, the gap of the 3D1C wind speed wake measurements leads to an assumption that simplifications considered in the LiDAR simulation can represent significant full-field LiDAR measurement characteristics. With the way the LiDAR simulator is used here, only step-and-stare LiDAR measurements have direct comparability; however, in application, most scanning measurements are conducted on the fly. Backscattering accumulates during scanning, which leads to additional volume averaging in the scanning direction. Because we cannot reproduce non-linear signal processing within the real LiDAR data, we accommodate this effect using the posterior averaging of wind speed data within the volumetric deficit calculation in the MFoR.

When using physical or simulated long-range LiDAR data, one-dimensional measurements assume vertical and lateral velocity component homogeneity to process them without requiring an additional flow solver for the main wind velocity component. In the near-wake range, the rotor causes complex flows that cannot be mapped using this assumption. As shown in Figure 4.11c, this inaccuracy does not necessarily lead to significant mean wind speed errors; however, it contributes to the mapping of the standard deviation error, as can be seen in Figure 4.12c to $\chi D^{-1} \leq 3$.

We accept a further significant assumption when calculating the volumetric wind velocity deficit in the MFoR. Because of the limited scanning speeds of long-range LiDARs, it is not feasible to volumetrically measure wakes on appropriate time scales. So far, only centreline cross-trajectories were analysed; thus, we introduce the conditional rotational wake symmetry assumption. Although the conditional rotation presented here, which is based on four different quadrants, exceeds a simple axial/point symmetry, deficit shape changes in the diagonal direction must be modelled in further applications. The influence of wind veer on the wake deficit's horizontal distortion in the vertical direction was marginal in this study, and it was compensated for by using a linear displacement approach similar to the advection assumption of the DWM. Because the differences only became apparent in the third decimal place, it is only stated here in the discussion. We find it reasonable to conduct further studies in which X-shaped measurement trajectories are used as a measurement pattern to better capture the potential veer. Studies with corresponding LES wind fields show the extent to which this effect can be achieved with significant height-dependent wind direction differences.

The last assumptions we consider are those of reconstruction. The method shown here can be interpreted as an adaptation of the DWM model based on LiDAR measurements. Air parcel advection speed and tracking position are not calculated using a point time series, but rather recreated based on the tracked dynamics from LiDAR scans. Even if the introduced shape and intensity dynamics may represent a more realistic deficit dynamics behaviour, the assumption that the velocity deficit can be seen as a homogeneous structure on small time scales can only be justified to certain downstream distances.

Despite the many simplifications used, we are encouraged in our assumptions to derive and determine wake dynamics using long-range LiDAR data, because of the good representativeness of the reconstructed wind field shown. The extent to which the reconstructed wake wind fields can produce realistic turbine loads and how turbulence characteristics on time scales smaller than the temporal resolution of the measurements are satisfied by this approach will be discussed in the future.

4.6 Conclusions

This paper presented a method for reconstructing spatially and temporally high-resolution 3D1C wind-turbine wake wind fields from volumetric long-range LiDAR data. The method's evaluation used a numerical LiDAR simulator that calculates 1D LOS velocities from an LES wake wind field. The scan parameters used were taken from a real nacelle-based measurement campaign using two LiDARs, and extended by a parameter study of how far different scan speeds influence wake dynamics representation. Eight different scanning speeds were evaluated for each planar horizontal and vertical measurement. To determine the wake dynamics, the temporal shift within each LiDAR scan was firstly corrected and then mutually synchronized. For this purpose,

we propagated LiDAR measurements using a space–time conversion approach to retrospectively improve the temporal resolution to a sub-measurement scale. From this high-resolution temporal data, we derived the wake dynamics for position, shape, and intensity by using a Gaussian curve fitting. We calculated the volumetric wake deficit in the MFoR, which we displaced and scaled with the tracked dynamics to reconstruct the dynamic wake behaviour. Finally, we superimposed a synthetic turbulent wind field that was scaled based on the tracked wake dynamics.

In the comparison of the reconstructed and original LES wind fields, multiple results could be observed for horizontal and vertical scanning velocity combinations. Although an apparent minimum of 2.3% of the ambient wind speed could be found for the average wind speed reconstruction, the standard deviation followed an exponential trend of horizontal and vertical angular velocity combinations. The maximum accuracy of the standard deviation reconstruction was 0.18–0.3%. We showed that either the averaged wind speeds or their standard deviations could be accurately mapped.

In particular, the good results of dynamic wake behaviour reconstruction indicate that wake characterization and modelling using long-range LiDAR measurements that are not optimally resolved in time are possible if the space–time conversion used here is applied.

With ongoing research in wind-field propagation, a more precise determination of the wake behaviour is possible. Furthermore, increased wake tracking accuracy will directly improve the reconstruction quality and the understanding of wake behaviour.

Supplementary Materials: The following are available online at The following are available online at http://www.mdpi.com/2072-4292/11/22/2665/s1:

Video 4.S1: Propagation and wake tracking results of horizontal wind speed data for variable angular velocities.

Video 4.S2: Propagation and wake tracking results of vertical wind speed data for variable angular velocities.

Video 4.S3: Comparison of the reconstructed wake wind field with the LES reference wake wind field.

Funding: This work was partially funded by the Federal Ministry for Economic Affairs and Energy (BMWi) according to a resolution by the German Federal Parliament (project CompactWind, FKZ 0325492B) and in the scope of the ventus efficiens project (ZN3092) through the funding initiative Niedersächsisches Vorab of the Ministry for Science and Culture of Lower Saxony.

Acknowledgments: We are also grateful to Juan José Trujillo for valuable discussions. We thank Davide Trabucchi for the implementation of the LiDAR simulator LiXIM. We thank Andreas Rott for the idea and the closure of the wind field propagation. We thank Mehdi Vali for performing the LES simulation of the wake wind field. All colleagues are/were affiliated to the research group Wind Energy Systems at the University of Oldenburg

Author Contributions: This study was done as a part of H.B. doctoral studies supervised by M.K. H.B. conducted the research work and wrote the paper. M.K. supervised the research work, contributed to the structure of the paper and performed review & editing.

Conflicts of Interest: The authors declare no conflict of interest.

Appendix 4.A

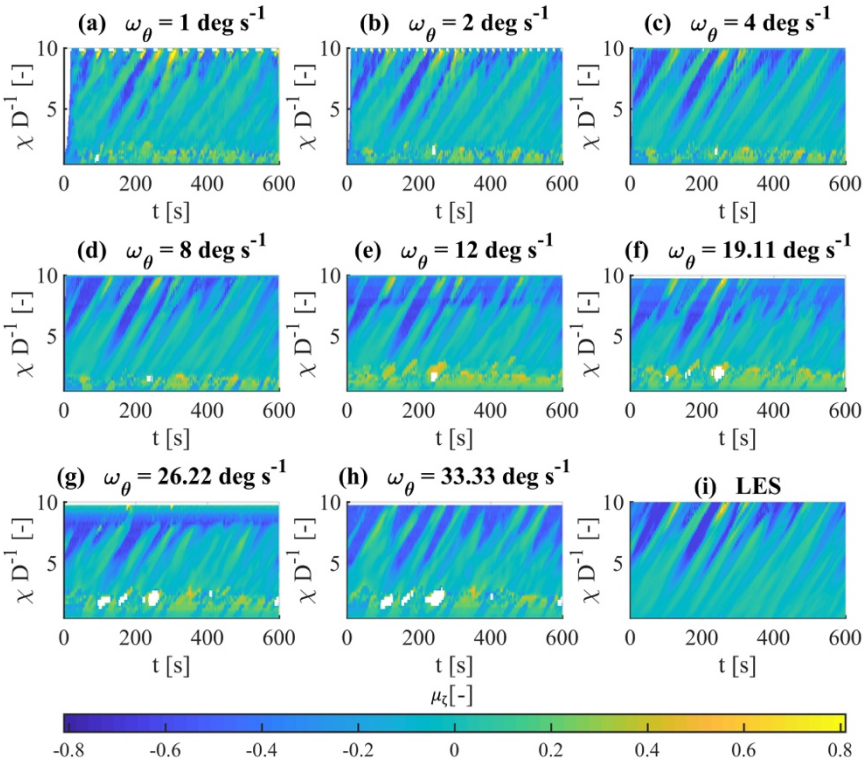

Figure 4.17. Visualisation of the tracked wake centre μ_ζ in dependency of time t and downstream distance χ (a-h) show the effect of different angular velocities on the tracking (i) shows μ_ζ based on LES data.

5 Conclusion & Outlook

At the end of this work, the presented research from Chapters 2 to Chapter 4 will be concluded. The central question from Section 1.6 and the sub-questions will be answered and related to the results shown. Finally, an outlook on further research and the development of the subject areas will be given.

5.1 Conclusion

This dissertation addresses the reconstruction of wake wind fields of wind turbines. The necessity of the reconstruction results from the technical limitations of the used measurement technologies. One of the here presented limitations is based on the technology LiDAR in the dilemma of spatial non-simultaneity. Although the use of long-range LiDAR systems makes it possible to measure at several points over several kilometres along the laser beam at the same time, it does not allow the measurement region to be scanned simultaneously at once. Besides, there are LiDAR and measurement-specific peculiarities, such as the previously discussed volume averaging in the beam and the scanning direction, the correlation of measurement parameters to flow characteristics and those that are known but not quantifiable and those of unknown nature. These current technical limitations make it necessary to make assumptions in order to reconstruct on different levels, from the one-dimensional LOS velocity to 3D1C wake wind fields, as close to reality as possible.

It has been shown at different levels of the process chain which assumptions have to be made and how long-range LiDAR data has to be processed to apply (wake) wind field reconstructions - from the level of the scan parameters, followed by the data filtering, the calculation of the longitudinal wind speed, the time-exact representation and synchronisation of the data set, the temporal up-sampling of the flow field and flow characteristics and the reconstruction of 2D1C and 3D1C wake wind fields.

Concerning the motivation of reconstructing 3D1C wake wind fields for further studies about wake analysis and model evaluation in Section 1.5, Chapter 2 and Chapter 3 can be regarded as essential precursor works which enable the reconstruction in Chapter 4 and contribute to the

overall goal of the comparability of real measured loads in free-field and numerically calculated loads.

The central question posed in Section 1.6, *how long-range LiDAR data can be used to reconstruct single wind turbine wake wind fields*, should rather be seen as a rhetorical means, whose answer is represented by this dissertation. To conclude the main results of this work, each sub-questions asked is discussed chapter by chapter.

Since LiDAR data require filtering for reasons presented in Chapter 2, the question arises how the LOS velocities must be filtered to ensure the most accurate mapping possible. Contrary to the pervasive fixed CNR-Threshold filtering, a dynamic filter approach is presented, which reacts automatically adaptively to atmospheric situations, measurement scenarios and different measuring instruments. Based on self-similarity, here, the new approach filters LiDAR data in a bi-variate manner. CNR and LOS data is first normalised before outliers are identified, based on a data density threshold. This approach shows that the generally associated decreasing distance-dependent data availability can be decoupled from the CNR. This decoupling allows benefiting, especially from long-range measurements, which aim at analysing flow fields over a long spatial range without limiting the temporal resolution. Since the dynamic filter needs a certain amount of valid data to form dense data clusters to calculate the data density, this characteristic can be seen as an advantage to ensure automated processing and thus increased data availability in times of enormous amounts of available measurement data. Compared with commonly used filter methods, both implementations of the new approach generate the smallest error in three of four error categories in the presented test case of a long-term staring mode measurement at the meteorological offshore mast FINO1. Concerning the wind field propagation of scanned LiDAR data in Chapter 3 and of course also for further applications and analyses, the importance of an outlier-free data set is evident. Also applied to scanned measurements, the dynamic data filter shows a robust and accurate behaviour. Disturbances and invalid measurements within a scan would be propagated and lead to an increased deviation of the local flow characteristic which in turn would interfere with the reconstruction of specific flow or meandering events, as read in Chapter 4.

Due to the scanning behaviour within planar LiDAR measurements, the temporal resolution of LiDAR scans is limited by the scan repetition time. To overcome this technical limitation, a method to improve the temporal resolution of planar LiDAR scans was introduced in Chapter 3. Based on a pragmatic space-time conversion using a Lagrangian interpolation approach, it is possible to calculate an arbitrary number of synthetic flow situations between two consecutive scans. By using a mixed propagation approach, which merges the time forward and time backward advection of the flow, a quasi-continuous (limited by the new time resolution) response can be created from the discrete information of two scans. With a spatial interpolation of the intermediate scans over the scan angle, LiDAR scans can be mapped at one point in time, contrary to the usual representation over the scan time interval. The resulting interpolation method can be interpreted as a fluid dynamic specific interpolation and is particularly interesting for the synchronisation of LiDAR measurements with external measurements and for wake analysis. Within sophisticated measurement campaigns like the volumetric measurements in Chapter 4, in which several LiDAR systems scan an overlapping volume, the measurements can be synchronised with the accuracy of the up-sampled temporal resolution. In this test case within a synthetic environment, the bi-

variate parameter study revealed that the temporal up-sampling reduced the statistical mapping error of the wake and the free flow in terms of wind speed mean value and standard deviation. This improvement depends on the angular velocity but could be proven for all scan speeds used. The evaluation showed that the optimal scanning speed of RHI and PPI scans depends on the variability of the flow to be measured. Concerning measurements already carried out, it becomes clear that a significant number of PPI and RHI scans was recorded sub-optimally and thus the mapping error was increased merely by the unmatched scan speed.

In the context of the comparability of real turbine measurement data with simulated turbine data, a 3D1C wake wind field reconstruction method was presented in Chapter 4. In this reconstruction method, unsynchronised nacelle-based RHI and PPI scan are used to map the wake behaviour in the downstream distance volume dynamically. For this purpose, corresponding scan has been synchronised with the space-time conversion presented in Chapter 3 to obtain a volumetric data set. Within the reconstruction, the wake is regarded as a continuous flexible tube in the downstream direction, that changes its position, shape and velocity deficit with spatial and time-dependent dynamics. These dynamics are determined by a robust wake-tracking approach from the temporal up-sampled scans. The velocity deficit is mapped inside the moving tube in the meandering frame of reference calculated from the LiDAR measurements. In order to represent the wake wind speed beyond the two geometry of scan planes, a conditional rotational symmetry is assumed which is here considered by a four-field symmetry. The representation of the wake turbulence is corresponded by a scaling of the local variability generated from the scans. The evaluation of the reconstruction method was carried out with a synthetic wake wind field and a numerical LiDAR simulator as in Chapter 3 in the sense of verifiability. The bi-variate parameter study of the horizontal and vertical scan velocity concerning the reconstruction quality has shown that a general reconstruction with small errors in the wind speed average and the standard deviation is possible. However, the shown reconstruction characteristics indicate that significantly smaller errors can be produced if either the goal of correct average or standard deviation is chosen for corresponding scan velocities for a specific atmospheric situation. The evaluation of the reconstruction quality of time series using the approach of Dynamic Time Warping has shown that the series of so-called peak events in the reconstruction can reproduce the original one in a good manner. Special emphasis is placed on the wake tracking since this is responsible for the representation of the wake dynamics as well as the speed and turbulence mapping within the reconstruction.

The research results shown and combined in this thesis dealt with the topic of wake wind-field reconstruction by means of long-range LiDAR measurements. New possibilities of data processing were introduced, which constitute an essential foundation within the framework of the comparability and transferability of measured inflow wind fields with reconstructed wake wind fields. By the reconstruction of flow characteristics starting with the filtering in Chapter 2, over the time-adjusted representation, the temporal up-sampling as prerequisite for the mutual synchronisation in Chapter 3 up to the combination and modelling of tracking dynamics from the processed LiDAR data within the 3D1C tracking reconstruction in Chapter 4, a comparability not only on statistical but rather on a direct spatially and temporally determined level is possible. This promising opportunity of comparability within the research topic can be applied to the turbine inflow conditions, but also in the combination with aero-elastic load calculations. From today's

point of view, the latter is a promising possibility to reduce the amount of model-specific parameterisations.

The research shown here can be seen as an essential and consequent step to reduce the deviations between the real interaction of wake-influenced wind turbines and simulated results. Thus, within the numerical combination of modelled wind fields and modelled turbine interaction, the uncertainty may be reduced on the side of the flow assumptions. This allows the comparison of real measured and simulated turbine responses and leads to a focus shift towards the analysis of deviations of specific flow events of the numerical representation of the calculation method of the interaction of the wind field and the turbine. The extent to which this research will contribute to the superordinate research question depends on the degree to which the approaches presented can be applied further. Concerning the transferability of these methods from wind energy research to an industry-oriented environment, further evaluations, performance improvements and a reduction of the necessary expertise are needed in order to apply them. The extent to which this is possible and could be realised can be seen in the following section, in which an outlook on further research and overlapping of topic areas is discussed.

5.2 Outlook and Suggestions for Future Research

The results of the research shown so far give a positive picture of the wake reconstruction. However, this dissertation only represents one contribution to the overarching task of improving the modelled numerical representation of the interaction of wind turbines and wake wind fields. The results of the 3D1C wind field reconstruction shown here refer only to one neutral stratified atmospheric situation, which is roughly classify by the combination of atmospheric mean wind speed and turbulence intensity at hub height. The shown reconstruction approach is based on the model assumption of wake behaviour. In general, it can be stated that the reconstruction method is always an equivalent of the quantisation method. A change of perspective on how the wake behaviour can be described will also result in a different and possibly more accurate numerical reconstruction. The reconstruction quality is mainly related to wake tracking techniques that can map the wake dynamics. As one example, a counterpart to the particle-based Extended Disk-Particle wake model of Trujillo [[18] that can calculate the wake dynamics in the form of horizontal and vertical meandering is mentioned. This model has so far only been able to generate wake wind fields based on the statistical average since no particle-based quantisation method has been applied to it. Concerning the wake tracking, it should always be considered that the possibility of mapping the real behaviour within each model is limited. This leads to the idea that different approaches might be applied in order to quantise and reproduce a corresponding behaviour. About the processes acting in the wake, which show up as wake recovery in the downstream direction, it seems reasonable to use different tracking approaches in different areas.

As Bromm et al. [14] and Vollmer et al. [154] postulated, atmospheric influences, especially stability, have a significant influence on the wake behaviour, which has to be represented numerically. The continuation of the investigation of the reconstruction approach shown here with synthetic wind fields with a wide variety of the atmospheric situations would emphasise the reconstruction capabilities and inherent limitations more dominantly. In particular, the reconstruction of situations with prominent veer would answer the question of whether the linear approach of vertical deformation of the velocity and turbulence scaling template can adequately reflect reality. The next step to improve the comparability of real turbine data and simulated data

is the application evaluation of the resulting reconstructed wake wind fields. For this purpose, comparative precursor aeroelastic calculations with the corresponding LES wind fields should first be carried out, before a suitable measurement campaign in the free-field is planned.

The wind fields designed for the mentioned reconstruction evaluation could additionally be used to improve the wind field propagation in Chapter 3 to get a more accurate picture of the flow characteristics caused by the propagation. Especially the influence of turbulence is in the foreground. Furthermore, these synthetically generated wind fields can be used to create a model for calculating the optimal LiDAR measurement parameters for the specific flow characteristics. These results - analogous to Chapter 3 - would not only improve the mapping quality of LiDAR measurements in general but could also replace the current approach for scanned LiDAR measurements. By determining optimal measurement parameters, it would be possible to adjust these parameters through the ongoing measurement continuously. Permanent or stepwise adjustments would have the consequence that the manual evaluation of LiDAR data would also have to be adapted to the increase in complexity through suitable automated evaluation algorithms.

The wind energy research, with its broad thematic areas, is currently, like any other research, confronted with the contemporary perspective of the omnipotence of artificial intelligence (AI), which is becoming more and more important. However, the aim of using AI must be to provide support and assistance for a deeper understanding of the processes to be mapped. Within this framework, a connection of AI with the process chain shown here is reasonable and desirable to extend the domain-specific models. It should never be overlooked that, with the superiority that this technology seems to offer, outstanding results can only be achieved with the appropriate training data, which in turn is handled by humans - so far.

The dynamic LiDAR data filter presented in Chapter 2 should be adapted to include further primary measurement data and measurement parameters - the so-called dispersion as well as spatial information. An adaptation of the self-similarity could be implemented with a machine learning method in the form of a parameterised k-means cluster approach. In general, further filter approaches are required that are explicitly designed for LiDAR measurement. In this context, a categorisation of the filter quality is necessary. For planar measurements and time-specific dynamic applications, such as wind field propagation or wind field reconstruction, the consideration of mean values and standard deviations is not a sufficient measure as a decision criterion.

It seems suitable to investigate further in how far machine learning approaches can be used to apply the projection of the LOS velocity wind field to the main flow component presented in Chapter 3. Additionally, it can be considered whether AI methods will lead to a refinement of the space-time-conversion in areas of significant deviations. Especially in the near wake where the lack of consideration of the pressure is evident and in distances greater than 7D where the inherent spherical coordinate system of the LiDAR leads to a significant coarsening of the spatial resolution by reducing the density of the measuring points.

In general, AI approaches have exceptional potential to categorise and cluster data. Here, their use for the standardised classification of wake situations is reasonable in order to correlate wake-influenced flow situations at wind turbines with their effects and thus make them more reproducible.

Concerning the increasing interest and already use of LiDAR for the control of wind turbines and wind farms it is indispensable that the planning of measurements, their execution, their

quantisation, plausibilisation, analyses and of course the control itself, also independent of AI approaches, become intelligent, robust and autonomous, but above all remains transparent.

REFERENCES

[1] Klaus, G.; Buhr, M.: Philosophisches Wörterbuch. 11. Auflage, Leipzig 1975.

[2] Kosing, A.: Marxistisches Wörterbuch der Philosophie. Verlag am Park, Berlin, 2015.

[3] Wikipedia: Available online: https://de.wikipedia.org/wiki/Wahrheit#cite_ref-Wahrheit_1-0 (accessed on 11.07.2018).

[4] Becker, C.: Lebenszykluskosten (LCC) – Grundlagen und Anwendung bei Serienprodukten. Hrsg.: Schelle, H. et al.: Symposium Life Cycle Cost, München: Gesellschaft für Projektmanagement, Deutschland, 1986.

[5] Wübbenhorst, K.: Lebenszykluskosten. Hrsg: Schulte, C.: Effektives Kostenmanagement - Methoden und Implementierung. Stuttgart: Schäffer Verlag, 1992.

[6] IEC Standard, 61400-1, 2005, Wind turbines - Part 1: Design requirements Guideline International Electrotechnical Commission (IEC).

[7] Nakamura, R.; Arikawa, Y.; Itahashi, T.,: Active Typhoon Control With Space Solar Power Technology. *63rd International Astronautical Congress* 2012, 12, C3, Naples

[8] Schmidt, H.; Wolfrum, R.: Gezielte Eingriffe - Climate Engineering aus klimawissenschaftlicher und völkerrechtlicher Perspektive. Hrsg.: Marotzke, J.; Stratmann, H.: Die Zukunft des Klimas - Neue Erkenntnisse, neue Herausforderungen, ein Report der Max-Planck-Gesellschaft, 183–200, C. H. Beck: München, 2015.

[9] Johnson, K.; Fritsch, G.: Assessment of extremum seeking control for wind farm energy production. *Wind Engineering* 2012, 36(6), 701-716, doi: 10.1260/0309-524X.36.6.701.

[10] Santoni, C.; Ciri, U.; Rotea, M.; Leonardi, S.: Development of a high fidelity CFD code for wind farm control. *American Control Conference* 2015, 1715-1720, doi: 10.1109/ACC.2015.7170980.

[11] Fleming, P. A.; Aho, J.; Gebraad, P. M. O.; Pao, L. Y.; Zhang, Y.: Computational fluid dynamics simulation study of active power control in wind plants. *American Control Conference* 2016, 1413-1420, doi: 10.1109/ACC.2016.7525115.

[12] Clayton, B. R.; Filby, P.: Measured effects of oblique flows and change in blade pitch angle on performance and wake development of model wind turbines. *Proceedings of the 4th BWEA Wind Energy Conference* 1982, 559-572.

[13] Medici, D.; Dahlberg, J. Å.: Potential improvement of wind turbine array efficiency by active wake control (AWC), 2003, 65-84, http://urn.kb.se/resolve?urn=urn:nbn:se:kth:diva-9021 (accessed on 11.06.2017).

[14] Bromm, M.; Rott, A.; Beck, H.; Vollmer, L.; Steinfeld, G.; Kühn, M.: Field investigation on the influence of yaw misalignment on the propagation of wind turbine wakes. *Wind Energy* 2018, 21(11), 1011-1028, doi: 10.1002/we.2210.

[15] Wygnanski, I.; Champagne, F.; Marasli., B.: On the large-scale structures in two-dimensional, small-deficit, turbulent wakes. *Journal of Fluid Mechanics* 1986, 168, 31-71, doi: 10.1017/S0022112086000289.

[16] Vermeer, L. J.; Sørensen, J. N.; Crespo, A.: Wind turbine wake aerodynamics, *Progress in Aerospace Sciences* 2003*,* 39(6-7), 467-510, doi: 10.1016/S0376-0421(03)00078-2.

[17] Sanderse, B.: Aerodynamics of wind turbine wakes, Energy Research Center of the Netherlands (ECN), ECN-E–09-016, Petten, The Netherlands, Technical Report 2009, 5(15), 153.

[18] Trujillo, J. J.: Large scale dynamics of wind turbine wakes, PhD thesis, University of Oldenburg, 2018

[19] Fuertes, F. C.; Iungo, G. V.; Porté-Agel, F.: 3D Turbulence Measurements Using Three Synchronous Wind LiDARs: Validation against Sonic Anemometry. *Journal of Atmospheric and Oceanic Technology* 2014, 31, 1549–1556, doi: 10.1175/JTECH-D-13-00206.1.

[20] Faxen, T.: Wake Interaction in an Array of Windmills – Theory and Preliminary Results. *2nd International Symposium on Wind Energy Systems* 1978**,** 1, B6-59.

[21] Lissaman, P. B. S.: Energy effectiveness of arbitrary arrays of wind turbines, *Journal of Energy* 1979, 3(6), 323-328, doi: 10.2514/3.62441.

[22] Crespo, A.; Hernández, J. S.; Frandsen, S.: Survey of modelling methods for wind turbine wakes and wind farms, *Wind Energy* 1999, 2(1), 1-24, doi: 10.1002/(SICI)1099-1824(199901/03)2:1<1::AID-WE16>3.0.CO;2-7

[23] Natarajan, A.; Hansen, M. H.; Wang, S.: Design Load Basis for Offshore Wind turbines: DTU Wind Energy Report No. E-0133, 2016.

[24] Ainslie, J. F.: Calculating the flowfield in the wake of wind turbines. *Journal of Wind Engineering and Industrial Aerodynamics* 1988, 27(1-3), 213-224, doi: 10.1016/0167-6105(88)90037-2.

[25] Gaumond, M.; Réthoré, P. E.; Bechmann, A.; Ott, S.; Larsen, G. C.; Diaz, A. P.; Hansen, K. S.: Benchmarking of wind turbine wake models in large offshore windfarms.*The science of Making Torque from Wind 2012: 4th scientific conference* 2012.

[26] Larsen, G. C.: A simple wake calculation procedure, Rosklide, Denmark: Risø National Laboratory, Technical report Risø-M-2760, 1988.

[27] Schepers, J.; Van der Pijl, S.: Improved modelling of wake aerodynamics and assessment of new farm control strategies. *Journal of Physics: Conference Series* 2007, 75(1), 012039, doi: 10.1088/1742-6596/75/1/012039.

[28] Shakoor, R.; Hassan, M. Y.; Raheem, A.; Wu, Y. K.: Wake effect modeling: A review of wind farm layout optimization using Jensen′ s model. *Renewable and Sustainable Energy Reviews* 2016, 58, 1048-1059, doi: 10.1016/j.rser.2015.12.229.

[29] Jensen, N. O.: A note on wind generator interaction, Rosklide, Denmark: Risø National Laboratory, Technical Report Riso-M-2411, 1983.

[30] Katic, I.; Højstrup, J.; Jensen, N. O.: A simple model for cluster efficiency, W. Palz, & E. Sesto (Eds.), *EWEC'86 Proceedings* 1989, 1, 407-410, Rome.

[31] Frandsen, S.; Barthelmie, R.; Pryor, S.; Rathmann, O.; Larsen, S.; Hojstrup, J.; Thogersen, M.: Analytical modelling of wind speed deficit in large offshore wind farms. *Wind Energy* 2006, 9(1-2), 39–53, doi: 10.1002/we.189.

[32] Tong, W.; Chowdhury, S.; Zhang, J.; Messac, A.: Impact of different wake models on the estimation of wind farm power generation, *12th AIAA Aviation Technology, Integration, and Operations (ATIO) Conference and 14th AIAA/ISSMO Multidisciplinary Analysis and Optimization Conference* 2012*,* 5430, doi: 10.2514/6.2012-5430.

[33] van Luvanee, D. R.: Investigation of observed and modelled wake effects at Horns Rev using WindPRO, Technical University of Denmark Department of Mechanical Engineering, 2006.

[34] Frandsen, S.: Turbulence and turbulence generated fatigue in wind turbine clusters, Rosklide, Denmark: Risø National Laboratory, Risø Report R-1188, 2003.

[35] IEC Standard, 61400-1, 2010, Wind turbines - Part 1: Design requirements Guideline International Electrotechnical Commission (IEC).

[36] Crespo, A.; Hernandez, J.: Analytical correlations for turbulence characteristics in the wakes of wind turbines. *European Community Wind Energy Conference* 1993, 8-12, Travemünde, Germany.

[37] van der Laan, M. P.; Sørensen, N. N.; Réthoré, P. E.; Mann, J.; Kelly, M. C.; Troldborg, N.; Schepers, J. G.; Machefaux, E.: An improved k-ϵ model applied to a wind turbine wake in atmospheric turbulence. *Wind Energy* 2015, 18(5), 889-907, doi:10.1002/we.1736.

[38] Larsen, G. C.; Madsen, H. A.; Thomsen, K.; Larsen, T. J.: Wake meandering: a pragmatic approach. *Wind Energy* 2008, 11(4), 377-395, doi: 10.1002/we.267.

[39] Taylor, G. I.: The spectrum of turbulence. *Proceedings of the Royal Society of London. Series A: Mathematical and physical sciences* 1938, 164, 476-490. doi: 10.1098/rspa.1938.0032.

[40] Larsen, T. J.; Madsen, H. A.; Larsen, G. C.; Hansen, K. S.: Validation of the dynamic wake meander model for loads and power production in the Egmond aan Zee wind farm. *Wind Energy* 2013, 16(4), 605-624, doi: 10.1002/we.1563.

[41] Keck, R.-E.; Mare, M.; Churchfield, M. J.; Lee, S.,;Larsen, G. C.; Madsen, H. A.: On atmospheric stability in the dynamic wake meandering model. *Wind Energy* 2014, 17(11), 1689-1710, doi: 10.1002/we.1662.

[42] Keck, R.-E.; Mare, M.; Churchfield, M. J.; Lee, S.; Larsen, G. C.; Madsen, H. A.: Two improvements to the dynamic wake meandering model: including the effects of atmospheric shear on wake turbulence and incorporating turbulence build-up in a row of wind turbines. *Wind Energy* 2015, 18(1), 111-132, doi: 10.1002/we.1686.

[43] IEC Standard, 61400-1, 2016, Wind turbines - Part 1: Design requirements Guideline International Electrotechnical Commission (IEC).

[44] Karlsson, C. J.; Olsson, F. Å. A.; Letalick, D.; Harris, M.: All-fiber multifunction CW 1.55 micron coherent laser radar for range, speed, vibration and wind measurements. *Applied Optics* 2000, 39, 3716-3726, doi: 10.1364/AO.39.003716.

[45] Gal-Chen, T.; Xu, M.; Eberhard, W. L.: Estimation of atmospheric boundary layer fluxes and other turbulence parameters from Doppler LiDAR data. *Journal of Geophysical Research* 1992, 97, 18409-18423, doi:10.1029/91JD03174.

[46] Frehlich, R.: Coherent Doppler LiDAR signal covariance including wind shear and wind turbulence, *Applied Optics* 1994, 33, 6472-6481, doi:10.1364/AO.33.006472.

[47] Frehlich, R.: Effects of wind turbulence on coherent Doppler LiDAR performance. *Journal of Atmospheric and Oceanic Technology* 1997, 14, 54-75, doi:10.1175/1520-0426(1997)014,0054:EOWTOC.2.0.CO;2.

[48] Sathe, A.; Mann, J.: A review of turbulence measurements using ground-based wind LiDARs. *Atmospheric Measurement Techniques* 2013, 6, 3147-3167, doi:10.5194/amt-6-3147-2013.

[49] Käsler, Y.; Rahm, S.; Simmet, R.; Kühn, M.: Wake measurements of a multi-MW wind turbine with coherent long- range pulsed Doppler wind LiDAR. *Journal of Atmospheric and Oceanic Technology* 2010, 27, 1529-1532, doi:10.1175/2010JTECHA1483.1.

[50] Kühn, M.: Verifikation von Offshore-Windenergieanlagen (OWEA) : Abschlussbericht des RAVE-Forschungsprojektes. Technischer Bericht der Carl von Ossietzky Universität Oldenburg, 2012, doi: 10.2314/GBV:779674561.

[51] Aitken, M. L., Banta, R. M., Pichugina, Y. L., Lundquist, J. K.: Quantifying Wind Turbine Wake Characteristics from Scanning Remote Sensor Data. *Journal of Atmospheric and Oceanic Technology* 2014, 31(4), 765-787, doi: 10.1175/JTECH-D-13-00104.1.

[52] Iungo, G. V.; Porté-Agel, F.: Volumetric LiDAR scanning of wind turbine wakes under convective and neutral atmospheric stability regimes. *Journal of Atmospheric and Oceanic Technology* 2014, 31, 2035-2048, doi: 10.1175/JTECH-D-13-00252.1.

[53] Banta, R. M.; Pichugina, Y. L.; Brewer, W. A.; Lundquist, J. K.; Kelley, N. D.; Sandberg, S. P.; Alvarez, R. J.; Hardesty, R. M.; Weickmann, A. M.: 3D volumetric analysis of wind turbine wake properties in the atmosphere using high-resolution Doppler LiDAR. *Journal of Atmospheric and Oceanic Technology* 2015, 32, 904-914, doi: 10.1175/JTECH-D-14-00078.1.

[54] Trabucchi, D.; Trujillo, J. J.; Schneemann, J.; Bitter, M.; Kühn, M.: Application of staring LiDARs to study the dynamics of wind turbine wakes. *Meteorologische Zeitschrift* 2015, 6, 557-564, doi: 10.1127/metz/2014/0610.

[55] van Dooren, M. F.; Trabucchi, D.; Kühn, M.: A Methodology for the Reconstruction of 2D Horizontal Wind Fields of Wind Turbine Wakes Based on Dual-Doppler LiDAR Measurements. *Remote Sensing* 2016, 8, 809, doi: 10.3390/rs8100809

[56] Browning, K. A.; Wexler, R.: The determination of kinematic properties of a wind field using Doppler RaDAR. *Journal of Applied Meteorology* 1968, *7*(1), 105-113, doi: 10.1175/1520-0450(1968)007<0105:TDOKPO>2.0.CO;2.

[57] Balsley, B. B.; Gage, K. S.: The MST RaDAR technique: Potential for middle atmospheric studies. *Pure and Applied Geophysics* 1980, 118, 452-493, doi: 10.1007/BF01586464.

[58] Gage, K. S.; Balsley, B. B.: MST RaDAR studies of wind and turbulence in the middle atmosphere. *Journal of Atmospheric and Solar-Terrestrial Physics* 1984, 46, 739-753, doi: 10.1016/0021-9169(84)90055-2.

[59] Rottger, J.: The MST RaDAR technique, MAP Hand Book, 13, 187– 232, University of Illinois Press, 1984.

[60] Schlipf, D.; Fleming, P.; Haizmann, F.; Scholbrock, A.; Hofsäß, M.; Wright, A.; Cheng, P. W.: Field testing of feedforward collective pitch control on the CART2 using a nacelle-based LiDAR scanner. *Journal of Physics: Conference Series* 2014, 555(1), 012090, doi: 10.1088/1742-6596/555/1/012090.

[61] Wagner, R.; Pedersen, T. F.; Courtney, M.; Antoniou, I.; Davoust, S.; Rivera, R. L.: Power curve measurement with a nacelle mounted LiDAR. *Wind Energy* 2014, 17(9), 1441-1453, doi: 10.1002/we.1643.

[62] Harris, M.; Hand, M.; Wright, A.: LiDAR for turbine control, National Renewable Energy Laboratory, Golden, CO, Report No. NREL/TP-500-39154, 2006.

[63] Mikkelsen, T.; Angelou, N.; Hansen, K.; Sjöholm, M.; Harris, M.; Slinger, C.; Hadley,P.; Scullion,R.; Ellis, G.; Vives, G.: A spinner-integrated wind LiDAR for enhanced wind turbine control. *Wind Energy* 2013, 16(4), 625-643, doi: 10.1002/we.1564.

[64] Sjöholm, M.;Angelou, N.; Mikkelsen, T.; Pedersen, A. T.; Kapp, S.; Harris, M.; Slinger, C.: Two- dimensional structures in wind turbine inflow studied by a spinner-mounted LiDAR. *International Symposium for the Advancement of Boundary Layer Remote Sensing* 2014; Auckland, New Zealand.

[65] Medley, J.; Barker, W.; Harris, M.; Pitter, M.; Slinger, C.; Mikkelsen, T.; Sjöholm, M.: Evaluation of wind flow with a nacelle-mounted, continuous wave wind LiDAR, *European Wind Energy Conference & Exhibition* 2014.

[66] Aitken, M. L.; Lundquist, J. K.: Utility-scale wind turbine wake characterization using nacelle-based long-range scanning LiDAR. *Journal of Atmospheric and Oceanic Technology* 2014, 31(7), 1529-1539,doi: 10.1175/JTECH-D-13-00218.1.

[67] Smith, D. A.; Harris, M.; Coffey, A. S.; Mikkelsen, T.; Jørgensen, H. E.; Mann, J.; Danielian, R.: Wind LiDAR evaluation at the Danish wind test site in Høvsøre. *Wind Energy* 2006, 9(1-2), 87-93, doi: 10.1002/we.193.

[68] Bingöl, F.; Mann, J.; Larsen, G. C.: Light detection and ranging measurements of wake dynamics part I: One-dimensional scanning, *Wind Energy* 2010, 13, 51-61, doi:10.1002/we.352.

[69] Trujillo, J. J.; Bingöl, F.; Larsen, G. C.; Mann, J.; Kühn, M.: Light detection and ranging measurements of wake dynamics. Part II: two-dimensional scanning. *Wind Energy* 2011, 14, 61-75, doi:10.1002/we.402.

[70] Courtney, M.; Wagner R.; Lindelöw, P.: Testing and comparison of LiDARs for profile and turbulence measurements in wind energy. *IOP Conference Series: Earth and Environmental Science* 2008, 1(1), 012021, doi: 10.1088/1755-1315/1/1/012021.

[71] Mann, J.; Cariou, J.; Courtney, M.; Parmentier, R.; Mikkelsen, T.; Wagner, R.; Lindelow, P.; Sjöholm, M.; Enevoldsen, K.: Comparison of 3D turbulence measurements using three staring wind LiDARs and a sonic anemometer. *Meteorologische Zeitschrift* 2009, 18(2), 135-140, doi: 10.1127/0941-2948/2009/0370.

[72] Newman, J. F.; Klein, P. M.; Wharton, S.; Sathe, A.; Bonin, T. A.; Chilson, P. B.; Muschinski, A.: Evaluation of three LiDAR scanning strategies for turbulence measurements. *Atmospheric Measurement Techniques* 2016, 9, 1993-2013, doi: 10.5194/amt-9-1993-2016.

[73] Wang, H.; Barthelmie, R.; Clifton, A.; Pryor, S. C.: Wind Measurements from Arc Scans with Doppler Wind LiDAR. *Journal of Atmospheric and Oceanic Technology* 2015, 32, 2024-2040, doi: 10.1175/JTECH-D-14-00059.1.

[74] Beck, H.; Kühn, M.: Dynamic data filtering of long-range doppler LiDAR wind speed measurements. *Remote Sensing* 2017, 9(6), 561, doi: 10.3390/rs9060561.

[75] Sjöholm, M.; Mikkelsen, T.; Mann, J.; Enevoldsen, K.; Courtney, M.: Spatial averaging-effects on turbulence measured by a continuous-wave coherent LiDAR. *Meteorologische Zeitschrift* 2009, 18(3), 281-287, doi: 10.1127/0941-2948/2009/0379.

[76] Stawiarski, C.; Träumner, K.; Knigge, C.; Calhoun, R.: Scopes and challenges of dual-doppler LiDAR wind measurements - an error analysis. *Journal of Atmospheric and Oceanic Technology* 2013, 30, 2044-2062, doi:10.1175/JTECH-D-12-00244.1.

[77] Stawiarski, C.; Träumner, K.; Kottmeier, C.; Knigge, C.; Raasch, S.: Assessment of Surface-Layer Coherent Structure Detection in Dual-Doppler LiDAR Data Based on Virtual Measurements. *Boundary-Layer Meteorology* 2015, 156, 371-393, doi:10.1007/s10546-015-0039-3.

[78] Lundquist, J. K.; Churchfield, M. J.; Lee, S.; Clifton, A.: Quantifying error of LiDAR and SoDAR Doppler Beam Swinging measurements of wind turbine wakes using computational fluid dynamics. *Atmospheric Measurement Techniques* 2015, 8, 907-920, doi:10.5194/amt-8-907-2015.

[79] Mirocha, J. D.; Rajewski, D. A.; Marjanovic, N.; Lundquist, J. K.; Kosovic, B.; Draxl, C.; Churchfield, M. J.: Investigating wind turbine impacts on near-wake flow using profiling LiDAR data and large-eddy simulations with an actuator disk model. *Journal of Renewable and Sustainable Energy* 2015, 7, 043143, doi:10.1063/1.4928873.

[80] Fuertes, F. C.; Porté-Agel, F.: Using a Virtual LiDAR Approach to Assess the Accuracy of the Volumetric Reconstruction of a Wind Turbine Wake. *Remote Sensing* 2018, 10, 721, doi: 10.3390/rs10050721.

[81] Towers, P.; Jones, B.: Real-time wind field reconstruction from LiDAR measurements using a dynamic wind model and state estimation. *Wind Energy* 2016, 19(1), 133-150, doi: 10.1002/we.1824.

[82] Fleming, P. A.,; Gebraad, P. M. O.; Churchfield, M.; Lee, S.; Johnson, K.; Michalakes, J.; van Wingerden, J. W.; Moriarty, P.: SOWFA + Super Controller User's Manual, Tech. rep. NREL/TP-5000-59197. Golden, Colorado, USA: National Renewable Energy Laboratory (NREL) 2013.

[83] Storey, R. C.; Norris, S. E.; Cater, J. E.: An actuator sector method for efficient transient wind turbine simulation. *Wind Energy* 2015, 18(4), 699-711, doi: 10.1002/we.1722.

[84] Vijayakumar, G.; Brasseur, J. G.; Lavely, A.; Jayaraman, B.; Craven, B. C.: Interaction of atmospheric turbulence with blade boundary layer dynamics on a 5MW wind turbine using blade-boundary-layer-resolved CFD with hybrid URANS-LES. *34th Wind Energy Symposium AIAA SciTech* 2015, San Diego, USA, doi: 10.2514/6.2016-0521.

[85] Bromm, M.; Vollmer, L.; Kühn, M.: Numerical investigation of wind turbine wake development in directionally sheared inflow. *Wind Energy* 2017, 20, 381-395, doi: 10.1002/we.2010.

[86] Walker, K.; Adams, N.; Gribben, B.; Gellatly, B.; Nygaard, N. G.; Henderson, A.; Marchante Jiménez, M.; Schmidt, S. R.; Rodriguez Ruiz, J.; Paredes, D.; Harrington, G.; Connell, N.; Peronne, O.; Cordoba, M.; Housley, P.; Cussons, R.; Håkansson, M.; Knauer, A.; Maguire, E.: An evaluation of the predictive accuracy of wake effects models for offshore wind farms. *Wind Energy* 2016, 19, 979-996, doi: 10.1002/we.1871.

[87] Peña Diaz, A.; Hansen, K. S.; Ott, S.; van der Laan, P.: On wake modeling, wind-farm gradients and AEP predictions at the Anholt wind farm. *Wind Energy Science* 2018, 3, 191-202. doi: 10.5194/wes-2017-37.

[88] Schmidt, B.; King, J.; Larsen, G. C.; Larsen, T. J.: Load validation and comparison versus certification approaches of the Risø Dynamic Wake Meandering model implementation in GH Bladed. *Scientific Proceedings European Wind Energy Association (EWEA)* 2011, 249-254.

[89] Larsen, G. C.; Ott, S.; Larsen, T. J.; Hansen, K. S.; Chougule, A.: Improved modelling of fatigue loads in wind farms under non-neutral ABL stability conditions. *Journal of Physics: Conference Series* 2018, 1037(7), 072013, doi: 10.1088/1742-6596/1037/7/072013.

[90] Kapp, S.; Kühn, M.: A five-parameter wind field estimation method based on spherical upwind LiDAR measurements. *Journal of Physics: Conference Series* 2014 , 555(1), 012112, doi: 10.1088/1742-6596/555/1/012112.

[91] Goyer, G. G.; Watson, R.: The Laser and its Application to Meteorology. *Bulletin of the American Meteorological Society* 1963, 44, 564-575, doi: 10.1175/1520-0477-44.9.564.

[92] Bastine, D.; Witha, B.; Wächter, M.; Peinke, J.: POD analysis of a wind turbine wake in a turbulent atmospheric boundary layer. *Journal of Physics: Conference Series* 2014, 524(1), 012153, doi: 10.1088/1742-6596/524/1/012153.

[93] Bastine, D.; Witha, B.; Wächter, M.; Peinke, J.: Towards a simplified dynamic wake model using POD analysis. *Energies* 2015, 8(2), 895-920, doi: 10.3390/en11030612.

[94] Bastine, D.; Vollmer, L.; Wächter, M.; Peinke, J.: Stochastic wake modelling based on POD analysis. *Energies* 2018, 11(3), 612, doi: 10.3390/en11030612.

[95] Iungo, G. V.; Santoni-Ortiz, C.; Abkar, M.; Porté-Agel, F.; Rotea, M. A.; Leonardi, S.: Data-driven reduced order model for prediction of wind turbine wakes. *Journal of Physics: Conference Series* 2015, 625(1), 012009, doi: 10.1088/1742-6596/625/1/012009.

[96] Bodini, N.; Zardi, D.; Lundquist, J. K.: Three-dimensional structure of wind turbine wakes as measured by scanning LiDAR. *Atmospheric Measurement Techniques* 2017, 10(8), doi: 10.5194/amt-10-2881-2017.

[97] Raach, S.; Schlipf, D.; Cheng, P. W.: LiDAR-based wake tracking for closed-loop wind farm control. *Journal of Physics: Conference Series* 2016, 753(5), 052009, doi: 10.1088/1742-6596/753/5/052009.

[98] Grund, C.J.; Banta, R.M.; George, J.L.; Howell, J.N.; Post, M.J.; Richter, R.A.; Weickmann, A.M. High-resolution Doppler LiDAR for boundary-layer and cloud research. *Journal of Atmospheric and Oceanic Technology* . 2001, 18, 376-393, doi:10.1175/ 1520-0426(2001)018,0376:HRDLFB.2.0.CO;2.

[99] Lang, S.; Mckeogh, E.: LIDAR and SODAR Measurements of Wind Speed and Direction in Upland Terrain for Wind Energy Purposes. *Remote Sensing* 2011, 3, 1871-1901,doi: 10.3390/rs3091871.

[100] Vickers, D.; Mahrt, L. Quality control and flux sampling problems for tower and aircraft data, *Journal of Atmospheric and Oceanic Technology* 1997, 14, 512–526, doi: 10.1175/1520-0426(1997)014<0512:QCAFSP>2.0.CO;2.

[101] Pal, S.; Haeffelin, M.; Batchvarova, E.: Exploring a geophysical process-based attribution technique for the determination of the atmospheric boundary layer depth using aerosol LiDAR and near-surface meteorological measurements. *Journal of Geophysical Research: Atmospheres* 2013, 118, 9277-9295, doi:10.1002/jgrd.50710.

[102] Pal, S.; Lee, T. R.; Phelps, S.; De Wekker, S. F. J.: Impact of atmospheric boundary layer depth variability and wind reversal on the diurnal variability of aerosol concentration at a valley site. *Science of the Total Environment* 2014, doi:10.1016/j.scitotenv.2014.07.067.

[103] Hill, M; Calhoun, R.; Fernando, H.J.S. Coplanar Doppler LiDAR Retrieval of Rotors from T-REX. *Journal of the Atmospheric Sciences* 2010*,* 67, 713-729, doi:10.1175/2009JAS3016.1.

[104] Krishnamurthy, R.; Choukulkar, A.; Calhoun, R.; Fine, J.; Oliver, A.; Barr, K. S.: Coherent Doppler LiDAR for wind farm characterization. *Wind Energy* 2013, *16*, 189-206, doi:10.1002/we.539.

[105] Newsom, R. K.; Berg, L. K.; Shaw, W. J.; Fischer, M. L.: Turbine-scale wind field measurements using dual-Doppler LiDAR. *Wind Energy* 2015, 18, 219–235, doi:10.1002/we.1691.

[106] Gryning, S.-E.; Floors, R., Peña, A.; Batchvarova, E.; Brümmer, B.: Weibull Wind-Speed Distribution Parameters Derived from a Combination of Wind-LiDAR and Tall-Mast Measurements Over Land, Coastal and Marine Sites. *Boundary-Layer Meteorology* 2016, 159, 329-348, doi:10.1007/s10546-015-0113-x.

[107] Meyer Forsting, A. R.; Troldborg, N.: A finite difference approach to despiking in-stationary velocity data-Tested on a triple-LiDAR. *Journal of Physics: Conference Series* 2016, 753, 072017, doi:10.1088/1742-6596/753/7/072017.

[108] Højstrup, J.: A statistical data screening procedure. *Measurement Science and Technology* 1993, 4, 153-157, doi: 10.1088/0957-0233/4/2/003.

[109] Hoaglin, D. C.; Mosteller, F.; Tukey, J. W.:Probability and Mathematical Statistics. *Understanding Robust and Exploratory Data Analysis*, 84, 447, Wiley: Hoboken, USA, 1983,

[110] Botev, Z. I.; Grotowski, J. F.; Kroese, D. P.: Kernel density estimation via diffusion. *Annals of Statistics* 2010, 38, 2916-2957, doi:10.1214/10-AOS799.

[111] Scott, D. W.: On optimal and data-based histograms. *Biometrika* 1979, *66*, 605–610, doi:10.1093/biomet/66.3.605.

[112] Morales, A.; Wächter, M.; Peinke, J.: Characterization of wind turbulence by higher-order statistics. *Wind Energy* 2011, 15, 391-406, doi:10.1002/we.478.

[113] Shapiro, S. S.; Wilk, M. B.: An analysis of variance test for normality. *Biometrika* 1965, 52, 591, doi:10.1093/biomet/52.3-4.591.

[114] Bastine, D.; Wächter, M.; Peinke, J.; Trabucchi, D.; Kühn, M.: Characterizing Wake Turbulence with Staring LiDAR Measurements. *Journal of Physics: Conference Series* 2015, *625*, doi:10.1088/1742-6596/625/1/012006.

[115] Schmidt, M.; Trujillo, J. J.; Kühn, M.: Orientation correction of wind direction measurements by means of staring LiDAR. *Journal of Physics: Conference Series* 2016, *749*, doi:10.1088/1742–6596/749/1/012005.

[116] Westerhellweg, A.; Neumann, T.; Riedel, V.: FINO1 Mast Correction. 2012 DEWI Magazin 60–66. Available online: http://www.dewi.de/dewi_res/fileadmin/pdf/publications/Magazin_40/09.pdf (accessed on 9 December 2016).

[117] Sathe, A.; Mann, J.; Gottschall, J.; Courtney, M. S.: Can wind LiDARs measure turbulence? J*ournal of Atmospheric and Oceanic Technology* 2011, 28, 853-868, doi:10.1175/JTECH-D-10-05004.1.

[118] Schneemann, J.; Trabucchi, D.; Trujillo, J. J.; Kühn, M.: Comparing measurements of horizontal wind speed of a 2D Multi-LiDAR and a cup anemometer. *Journal of Physics: Conference Series* 2012, doi:10.1088/1742-6596/555/1/012091.

[119] Klaas, T.; Pauscher, L.; Callies, D.: LiDAR-mast deviations in complex terrain and their simulation using CFD. *Meteorologische Zeitschrift* 2015, 24, 591-603, doi:10.1127/metz/2015/0637.

[120] Pauscher, L.; Vasiljevic, N.; Callies, D.; Lea, G.; Mann, J.; Klaas, T.; Hieronimus, J.; Gottschall, J.; Schwesig, A.; Kühn, M.; Courtney, M.: An Inter-Comparison Study of Multi- and DBS LiDAR Measurements in Complex Terrain. *Remote Sensing* 2016, 8, 782, doi:10.3390/rs8090782.

[121] Peña Diaz, A.; Mann, J.; Dimitrov, N.: Turbulence characterization from a forward-looking nacelle LiDAR. *Wind Energy Science* 2016, 2(1), 133-152, doi:10.5194/wes-2016-47.

[122] Boquet, M.; Royer, P.; Cariou, J.-P.; Matcha, M.: Simulations of Doppler LiDAR Measurements Range and Data Availability. *Journal of Atmospheric and Oceanic Technology* 2016, 33(5), 977-987, doi:10.1175/JTECH-D-15-0057.1.

[123] Osgood, R.; Bialasiewicz, J.; Jakubowski, A: Using wavelet analysis to assess turbulence/rotor interactions. *Wind Energy* 2000, 3, 121-134, doi: 10.1002/we.33.

[124] Hand, M.: Mitigation of wind turbine/vortex interaction using disturbance accommodating control. Ph.D. Thesis, Colorado, USA, 2003, doi: 10.2172/15006832.

[125] Manwell, J. F.; McGowan, J. G.; Rogers, A. L.: Wind energy explained: Theory, design and application. John Wiley & Sons 2010, doi: 10.1002/9781119994367.

[126] Churchfield, M. J.; Lee, S.; Moriarty, P. J.; Hao, Y.; Lackner, M. A.; Barthelmie, R.; Lundquist, J.; Oxley, G. A.: Comparison of the Dynamic Wake Meandering Model, Large-Eddy Simulation and Field Data at the Egmond aan Zee Offshore Wind Plant. *33rd Wind Energy Symposium* 2015, doi: 10.2514/6.2015-0724.

[127] Cheynet, E.; Jakobsen, J. B.; Snæbjörnsson, J.; Angelou, N.; Mikkelsen, T.; Sjöholm, M.; Svardal, B.: Full-scale observation of the flow downstream of a suspension bridge deck. *Journal of Wind Engineering & Industrial Aerodynamics* 2017, 171, 261-272, doi: 10.1016/j.jweia.2017.10.007.

[128] van Dooren, M. F.; Campagnolo, F.; Sjöholm, M.; Angelou, N.; Mikkelsen, T.: Demonstration and uncertainty analysis of synchronised scanning LiDAR measurements of 2-D velocity fields in a boundary-layer wind tunnel. *Wind Energy Science* 2017, 2, 329-341, doi: 10.5194/wes-2-329-2017.

[129] Bartl, J.; Mühle, F.; Schottler, J.; Sætran, L.; Peinke, J.; Adaramola, M.; Hölling, M.: Wind tunnel experiments on wind turbine wakes in yaw: effects of inflow turbulence and shear. *Wind Energy Science* 2018, 3, 329-343, doi: 10.5194/wes-3-329-2018.

[130] Machefaux, E.; Larsen, G. C.; Troldborg, N.; Gaunaa, M.; Rettenmeier, A.: Empirical modeling of single-wake advection and expansion using full-scale pulsed LiDAR-based measurements. *Wind Energy* 2015, 18, 2085-2103. doi: 10.1002/we.1805.

[131] IEC Standard, 61400-1, 2015**,** Assessment of a wind turbine for site-specific conditions.

[132] Stenger, H.: Mehrstufige Stichprobenverfahren. *Metrika* 1974, 21(1), 7-18, doi: 10.1007/BF01893889.

[133] Raasch, S.; Schröter, M.: PALM - A Large-Eddy Simulation Model Performing on Massively Parallel Computers. *Meteorologische Zeitschrift* 2001, 10, 363-372, doi: 0.1127/0941-2948/2001/0010-0363.

[134] Troldborg, N.: Actuator Line Modeling of Wind Turbine Wakes, PhD thesis, Technical University of Denmark - Department of Wind Energy, Risø Campus, 2008

[135] Jonkman, J.; Butterfield, S.; Musial, W.; Scott, G.: Definition of a 5-MW reference wind turbine for offshore system development (No. NREL/TP-500-38060). National Renewable Energy Lab, Golden, USA, 2009

[136] Trabucchi, D.; Trujillo, J. J.; Steinfeld, G.; Schneemann, J.; Machtaa, M.; Cariou, J. P.; Kühn, M.:Numerical assessment of performance of LiDAR WindScanners for wake measurements. *Conference contribution EWEA*, 2011, Brussel.

[137] Peña Diaz, A.; Hasager, C. B.; Lange, J.; Anger, J.; Badger, M.; Bingöl, F.; Bischoff, O.; Cariou, J. P.; Dunne, F.; Emeis, S.; Harris, M.; Hofsäss, M.; Karagali, I.; Laks, J.; Larsen, S. E.; Mann, J.; Mikkelsen, T. K.; Pao, L. Y.; Pitter, M.; Rettenmeier, A.; Sathe, A.; Scanzani, F.; Schlipf, D.; Simley, E.; Slinger, C.; Wagner, R.; Würth, I.: Remote Sensing for Wind Energy; Number DTU Wind Energy-E-Report-0029(EN), DTU 385 Wind Energy, 2013, Chapter 5: Pulsed LiDAR, 131–148.

[138] Lindelöw, P.: Fiber Based Coherent LiDARs for Remote Wind Sensing, PhD thesis, Danish Technical University, 2008.

[139] Schneiders, J.; Scarano, F.: Dense velocity reconstruction from tomographic PTV with material derivatives. *Experiments in Fluids* 2016, 57, doi: 10.1007/s00348-016-2225-6.

[140] Rott, A.; Boersma, S.; van Wingerden, J. W.; Kühn, M.: Dynamic flow model for real-time application in wind farm control. *Journal of Physics: Conference Series* 2017, 854(1), doi: 10.1088/1742-6596/854/1/012039.

[141] Valldecabres, L.; Peña, A.; Courtney, M.; von Bremen, L.; Kühn, M.: Very short-term forecast of near-coastal flow using scanning LiDARs. *Wind Energy Science* 2018, 3, 313-327, doi: 10.5194/wes-3-313-2018.

[142] Sibson, R.: A brief description of natural neighbour interpolation. *Interpreting Multivariate Data*, 21-36, Wiley: New York, USA, 1981, doi: 10.1007/3-540-26772-7_8.

[143] Cheynet, E.; Jakobsen, J. B.; Snæbjörnsson, J.; Mann, J.; Courtney, M.; Lea, G.; Svardal, B.: Measurements of surface-layer turbulence in a wide Norwegian fjord using synchronized long- range Doppler wind LiDARs. *Remote Sensing* 2017, 9, 977, doi: 10.3390/rs9100977.

[144] Smalikho, I. N.; Banakh, V. A.; Pichugina, Y. L.; Brewer, W. A.; Banta, R. M.; Lundquist, J. K.; Kelley, N. D.: LiDAR investigation of atmosphere effect on a wind turbine wake. *Journal of Atmospheric and Oceanic Technology* 2013, 30, 2554-2570, doi: 10.1016/j.egypro.2017.10.367.

[145] Aitken, M. L.; Kosović, B.; Mirocha, J. D.; Lundquist, J. K.: Large-eddy simulation of wind turbine wake dynamics in the stable boundary layer using the Weather Research and Forecasting Model. *Journal of Renewable and Sustainable Energy* 2014, *6*(3), 033137, doi: 10.1063/1.4885111.

[146] Foti, D.; Yang, X.; Guala, M.; Sotiropoulos, F.: Wake meandering statistics of a model wind turbine: Insights gained by large-eddy simulations. *Physical Review Fluids* 2016, 1(4), 044407, doi: 10.1103/PhysRevFluids.1.044407.

[147] Porté-Agel, F.; Wu. Y.-T.; Lu, H.; Conzemius, R. J.: Large-Eddy simulation of atmospheric boundary layer flow through wind turbines and wind farms. *Journal of Wind Engineering and Industrial Aerodynamics* 2011, 99, 154-168, doi: 10.1016/j.jweia.2011.01.011.

[148] Sturge, D.; Sobotta, D.; Howell, R.; While, A.; Lou, J.: A hybrid actuator disc - Full rotor CFD methodology for modelling the effects of wind turbine wake interactions on performance. *Renewable Energy* 2015, 80, 525-53, doi: 10.1016/j.renene.2015.02.053.

[149] Aubrun, S.; Garcia, E. T.; Boquet, M.; Coupiac, O.; Girard, N.: Statistical analysis of a field database to study stability effects on wind turbine wake properties. *Journal of Physics: Conference Series* 2018, 1037(7), 072047, doi:10.1088/1742-6596/1037/7/072047.

[150] Beck, H.; Kühn, M.: Temporal Up-Sampling of Planar Long-Range Doppler LiDAR Wind Speed Measurements Using Space-Time Conversion. *Remote Sensing* 2019, 11, 867, doi: 10.3390/rs11070867.

[151] Deardorff, J.: Stratocumulus-capped mixed layers derived from a three-dimensional model. *Boundary-Layer Meteorology* 1980, 18, 495-527, doi:10.1007/BF00119502.

[152] Borraccino, A.; Schlipf, D.; Haizmann, F.; Wagner, R.: Wind field reconstruction from nacelle-mounted LiDAR short-range measurements. *Wind Energy Science* 2017, 2, 269-283, doi: 10.5194/wes-2-269-2017.

[153] Brent, R. P.: Algorithms for Minimization without Derivatives, Chapter 4, 61-167, 1973.

[154] Vollmer, L.; Steinfeld, G.; Heinemann, D.; Kühn, M.: Estimating the wake defection downstream of a wind turbine in different atmospheric stabilities: an LES study. *Wind Energy Science* 2016, 1(2), 129-141, doi: 10.5194/wes-1-129-2016.

[155] Bastankhah, M.; Porté-Agel, F.: A new analytical model for wind-turbine wakes. *Renewable Energy* 2014, 70, 116-123, doi: 10.1016/j.renene.2014.01.002.

PUBLICATION LIST

This dissertation bases on the following peer-reviewed journal articles.

- **Chapter 2:**
  Beck, H.; Kühn, M.: Dynamic Data Filtering of Long-Range Doppler LiDAR Wind Speed Measurements. *Remote Sensing* 2017, 9(6), 561, doi: 10.3390/rs9060561.

  Hauke Beck performed the related research and wrote the paper. Martin Kühn supervised the research work, advised about the structure of the paper and supplied review and editing.

- **Chapter 3:**
  Beck, H.; Kühn, M.: Temporal Up-Sampling of Planar Long-Range Doppler LiDAR Wind Speed Measurements Using Space-Time Conversion. *Remote Sensing* 2019, 11(7), 867, doi: 10.3390/rs11070867.

  Hauke Beck performed the related research and wrote the paper. Martin Kühn supervised the research work, advised about the structure of the paper and supplied review and editing.

- **Chapter 4:**
  Beck, H.; Kühn, M.: Reconstruction of Three-Dimensional Dynamic Wind Turbine Wake Wind Fields with Volumetric Long-Range Wind Doppler LiDAR Measurements. *Remote Sensing* 2019, 11(22), 2665, doi: 10.3390/rs11222665.

  Hauke Beck performed the related research and wrote the paper. Martin Kühn supervised the research work, advised about the structure of the paper and supplied review and editing.

In addition, publications and presentations are listed, which are related to the thesis and have contributed to the realisation of the research topic.

Peer-reviewed Articles

- Bromm, M.; Rott, A.; Beck, H.; Vollmer, L.; Steinfeld, G.; Kühn, M.: Field investigation on the influence of yaw misalignment on the propagation of wind turbine wakes. *Wind Energy* 2018, 1-18, doi: 10.1002/we.2210.

Conference Proceedings

- Trujillo J. J.; Beck, H.; Müller, K.; Cheng, P. W.; Kühn, M.: A test case of meandering wake simulation with the Extended-Disk Particle model at alpha ventus. *EERA DeepWind*, Trondheim, 2017.
- Beck, H.; Trujillo, J. J.; Kühn, M.: Analysis of wake sweeping effects based on load and long-range LiDAR measurements. *DEWEK2015 Conference*, Bremen, 2015.
- van Dooren, M.; Trabucchi, D.; Beck, H.; Schneemann, H.; Friedrichs, W.; Kühn, M.: Assessment of the global wind and the local wake direction at alpha ventus using long-range scanning LiDAR. *Proceedings of the EWEA Annual Event and Exhibition 2015*, Kopenhagen, 2015.
- Hasager, C.,;Madsen, P. H., P.; Giebel, G.; Réthoré, P.; Hansen, K.; Schaldemose, J.; Badger, J.; Peña Diaz, A.; Volker, P.; Badger, M.; Karagali, I.; Cutululis, N. A.; Maule, P.; Schepers, G.; Wiggelinkhuizen, J.; Cantero, E.; Waldl, I.; Anaya, L.; Olimpo, A.; Attya, A. B.; Svendsen, H.; Palomares, A.; Palma, J.; Gomes, V. C.; Gottschall, J.; Wolken-Möhlmann, G.; Bastigkeit, I.; Beck, H.; Trujillo, J. J.; Barthelmie, R.; Sieros, G.; Chaviaropoulos, T.; Vincent, P.; Husson, R.; Prospathopoulos, J.: Design tool for offshore wind farm cluster planning. *Proceedings of the EWEA Annual Event and Exhibition 2015*, Kopenhagen, 2015.
- Beck, H.; Trabucchi, D.; Kühn, M.: The Ainslie wake model - An update for multi megawatt turbines based on state-of-the-art wake scanning techniques. *EWEA 2014*, Barcelona, 2014.

Conference Presentations

- Trujillo, J. J.; Bastine, D.; Beck, H.; Trabucchi, D.; Schneemann, J.; Vollmer, L.; Witha, B.; Kühn, M.: A new perspective for wake dynamics - Simplified models and their development. *ForWind Symposium 2017*, Oldenburg, 2017.
- Bromm, M.; Rott, A.; Beck, H.; Vollmer, L.; Steinfeld, G.; Kühn, M.: Freifeldversuche zur Nachlaufablenkung. *ForWind Symposium 2017*, Oldenburg, 2017.
- Trujillo, J. J.; Beck, H.; Müller, K.; Cheng, P. W.; Kühn, M.: A test case of meandering wake simulation with the Extended-Disk Particle model at alpha ventus. *EERA DeepWind - 14th Deep Sea Offshore Wind R&D Conference*, Trondheim, 2017.
- Bromm, M.,;Rott, A.; Beck, H.; Vollmer, L.; Steinfeld, G.; Kühn, M.: Field investigation on the influence of yaw misalignment and wind veer on the propagation of a wind turbine wake. *Wind Energy Science Conference 2017*, Lyngby, 2017
- Schmidt, M.; Beck, H.; Trujillo, J. J.; Kühn, M.: Orientation correction of wind direction measurements by means of staring LiDAR. *Wind Europe Summit 2016*, Hamburg, 2016
- Beck, H.; Schmidt, S.; Kühn, M.; Dynamic Data Filtering of Long-range LiDAR wind speed measurements. *ISARS 2016,* Varna*,* 2016.
- Beck, H.; Rott, A.; Trabucchi, D.; Kühn, M.: Volumetric wind field measurements of wind turbine wakes with long-range LiDAR. *EWEA 2015*, Paris, 2015.
- Hasager, C.,;Madsen, P. H., P.; Giebel, G.; Réthoré, P.; Hansen, K.; Schaldemose, J.; Badger, J.; Peña Diaz, A.; Volker, P.; Badger, M.; Karagali, I.; Cutululis, N. A.; Maule, P.; Schepers, G.; Wiggelinkhuizen, J.; Cantero, E.; Waldl, I.; Anaya, L.; Olimpo, A.; Attya, A. B.; Svendsen, H.; Palomares, A.; Palma, J.; Gomes, V. C.; Gottschall, J.;

Wolken-Möhlmann, G.; Bastigkeit, I.; Beck, H.; Trujillo, J. J.; Barthelmie, R.; Sieros, G.; Chaviaropoulos, T.; Vincent, P.; Husson, R.; Prospathopoulos, J.: Design tool for offshore wind farm cluster planning. *EWEA 2015* Kopenhagen, 2015.

- van Dooren, M.; Trabucchi, D.; Beck, H.; Schneemann, J.; Friedrichs, W.; Kühn, M.: Assessment of the global wind and the local wake direction at »alpha ventus« using long-range scanning LiDAR. *EWEA 2015*, Kopenhagen, 2015.
- Beck, H.; Trujillo, J. J.; Wolken-Möhlmann, G.; Gottschall, J.; Schmidt, J.; Peña, A.; Gomez, V.; Lange, B.; Kühn, M.; Hasager, C.: Comparison of simulations of the far wake of alpha ventus against ship-based LiDAR measurements. *RAVE conference*, Bremerhaven, 2015 .
- Schneemann, J.; Bastine, D.; Beck, H.; van Dooren, M.; Hieronimus, J.; Steinfeld, G.; Trabucchi, D.; Trujillo, J. J.; Vollmer, L.; Kühn, M.: Investigation of flow conditions and turbulence characteristics in large offshore wind farms by remote sensing experiments and simulations. *RAVE – offshore wind conference*, Bremerhaven, 2015 .
- Beck, H.; Trujillo, J. J.; Kühn, M.: Analysis of wake sweeping effects based on load and long-range LiDAR measurements. *DEWEK 2015*,Bremen, 2015.
- Schneemann, J.; Bastine, D.; Beck, H.,; van Dooren, M.; Steinfeld, G.; Trabucchi, D.; Trujillo, J. J.; Kühn, M.: GW Wakes - Measurements of Wake effects in »alpha ventus« with synchronised Long-Range LiDAR Windscanners. *DEWEK 2015* Conference proceedings, Bremen, Germany, 2015.
- Beck, H.; Trabucchi, D.; Bitter, M.; Kühn, M.: The Ainslie wake model - An update for multi megawatt turbines based on state-of-the-art wake scanning techniques. *EWEA 2014*, Barcelona, 2014.
- Schneemann, J.; Trujillo, J. J.; Trabucchi, D.; Beck, H.; Unguran, R.; Voss, S.; Kühn, M.: GW Wakes - Measuring wake effects in "alpha ventus" using a long-range multi LiDAR. *FINO Conference*, Kiel, 2013
- Trabucchi, D.; Beck, H.; Schneemann, J.; Trujillo, J. J.; Unguran, R.; Voss, S.; Kühn, M.: Offshore wind farm flow characteristics measured by a long-range multi-LiDAR system: development and preliminary results. *EWEA Offshore*, 2013.
- Trujillo, J. J.; Beck, H.; Kühn, M.: Simulation of Wake Meandering in Convective Atmosphere with the Extended Disk-Particle Model. *The Science of Making Torque from Wind*, Oldenburg, 2012.
- Trujillo, J. J.; Baulig, P.; Beck, H.; Conzelmann, M.; Kuhnle, B.; Rettenmeier, A.; Schlipf, D.; Kühn, M.: Analysis of wake-induced wind turbine loads. *RAVE conference*, Bremerhaven, 2012.
- Schneemann, J.; Brickwell D.; Stoevesandt, B.; Trujillo, J. J.; Trabucchi, D.; Steinfeld, G.; Wächter, M.; Beck, H.; Kühn, M.: GW Wakes - Measuring Wake Effects and Wake Turbulence Characteristics of Very Large Offshore Wind Farms with Synchronized Long-Range LiDAR Windscanners. *DEWEK* 2012, Bremen, 2012.

Seminars and Colloquia

- Bromm, M.; Rott, A.; Beck, H.; Vollmer, L.; Steinfeld, G.; Kühn, M.: Challenges in recording high quality wake flow measurements of a wind turbine in field experiments. *WindTech*, Colorado, 2017

- Beck, H.; Friedrichs, W.; Rott, A.; Schmidt, M.; Schneemann, J.; Seifert, J.; Trabucchi, D.; Tujillo, J. J.; Vera Tudela, L.; Kühn, M.: Some current challenges for robust and systematic analysis of LiDAR data for wind farm research, *EERA JPW Workshop*, Roskilde, 2016.
- Beck, H.; Rott, A.; Trujillo, J. J.; Kühn, M.: Reconstruction of three-dimensional Wind turbine Wakes in forested terrain by long-range LiDAR measurements. *EUROMECH colloquium 576*, Stockholm, 2016.
- Beck, H.; Rott, A.; Trujillo, J. J.; Kühn, M.: Volumetric reconstruction of wind turbine wakes based on long-range LiDAR measurements. *WindPower Monthly 5th annual wind resource assessment forum*, London, 2016.
- Beck, H.: LiDAR data processing for wake wind field reconstruction. *Wind Seminare DTU*, Risø, 2016.
- Beck, H.; Trujillo, J. J.; Wolken-Möhlmann, G.; Schmidt, J.; Diaz, A. P.; Hauge, P.; Hasager, C.; Gomez, V. C.: Comparison results of LiDAR measurements and wind park model simulations. *Workshop at Senvion*, Osterrönfeld, 2015
- Beck, H.; Rott, A.; Schneemann, J.; Trabucchi, D.; Trujillo, J. J.; Unguran, R.; Voss, S.; Kühn, M.: Dynamic multi-LiDAR campaigns for offshore wind farm flow measurements, IEA Wind TEM#78, Lubbock, USA 201.

ACKNOWLEDGEMENTS

At this point, students are delighted to list their family, friends, other scientists and mentors. I could now begin to count in ascending order who has influenced me and how, but I am pretty sure that the appropriate people already know.

Explicit gratitude for inspiration and cooperation has been mentioned in the corresponding chapters.

I would like to express acknowledgements for the financing of my employment, which, on the one hand, came from funded projects and was mentioned in the corresponding chapters. On the other hand, my research was financed by the Wind Energy Systems research group Oldenburg.

And of course, I thank my first examiner Martin Kühn and my second examiner Torben Krogh Mikkelsen for the scientific cooperation and the time and work they invested in the process and the evaluation of this thesis, respectively.

CURRICULUM VITAE

Personal

Name:	Hauke Beck
Place of Birth:	Bünde, Germany

Education

10/2008 - 11/2011	M.Sc., Engineering Physics - Renewable Energies, Carl von Ossietzky University of Oldenburg, Oldenburg, Germany
10/2004 - 09/2008	B.Eng., Mechanical Engineering - Aerospace Engineering, University of Applied Science Bremen, Bremen, Germany

Experience

12/2011 - 12/2017	Researcher at ForWind - Center for Wind Energy Research - Carl von Ossietzky University of Oldenburg
10/2018 - 12/2018	Researcher at ForWind - Center for Wind Energy Research - Carl von Ossietzky University of Oldenburg

EIDESSTATTLICHE ERKLÄRUNG

Hiermit versichere ich, die vorliegende Arbeit selbstständig verfasst, keine anderen als die angegebenen Quellen und Hilfsmittel verwendet und die Leitlinien guter wissenschaftlicher Praxis der Carl von Ossietzky Universität Oldenburg befolgt zu haben.

Die Arbeit hat weder in ihrer Gesamtheit noch in Teilen einer anderen Hochschule zur Begutachtung in einem Promotionsverfahren vorgelegen und im Zusammenhang mit dem Promotionsvorhaben wurden keine kommerziellen Vermittlungs- oder Beratungsdienste in Anspruch genommen.

Teile der Arbeit sind bereits veröffentlicht.

Oldenburg, den 20.12.2019

Hauke Beck